Heat Transfer Flow Regimes of Refrigerants in a Horizontal-Tube Evaporator

J. P. Wattelet, J. C. Chato, B. R. Christoffersen, J. A. Gaibel,
M. Ponchner, P. J. Kenney, R. L. Shimon, T. C. Villaneuva,
N. L. Rhines, K. A. Sweeney, D. G. Allen, and T. T. Hershberger

ACRC TR-55 May 1994

For additional information:

Air Conditioning and Refrigeration Center
University of Illinois
Mechanical & Industrial Engineering Dept.
1206 West Green Street
Urbana, IL 61801

(217) 333-3115

Prepared as part of ACRC Project 37
Effect of Geometric Variables and R-22 Alternatives
on Refrigerant-Side Evaporation and Condensation
J. C. Chato, Principal Investigator

The Air Conditioning and Refrigeration Center was founded in 1988 with a grant from the estate of Richard W. Kritzer, the founder of Peerless of America Inc. A State of Illinois Technology Challenge Grant helped build the laboratory facilities. The ACRC receives continuing support from the Richard W. Kritzer Endowment and the National Science Foundation. The following organizations have also become sponsors of the Center.

Acustar Division of Chrysler
Allied-Signal, Inc.
Amana Refrigeration, Inc.
Brazeway, Inc.
Carrier Corporation
Caterpillar, Inc.
E. I. du Pont de Nemours & Co.
Electric Power Research Institute
Ford Motor Company
Frigidaire Company
General Electric Company
Harrison Division of GM
ICI Americas, Inc.
Modine Manufacturing Co.
Peerless of America, Inc.
Environmental Protection Agency
U. S. Army CERL
Whirlpool Corporation

For additional information:

Air Conditioning & Refrigeration Center
Mechanical & Industrial Engineering Dept.
University of Illinois
1206 West Green Street
Urbana IL 61801

217 333 3115

HEAT TRANSFER FLOW REGIMES OF REFRIGERANTS IN A HORIZONTAL-TUBE EVAPORATOR

Jonathan Wattelet, Ph.D.
Department of Mechanical and Industrial Engineering
University of Illinois at Urbana-Champaign, 1994
John C. Chato, Advisor

ABSTRACT

An experimental study of flow boiling heat transfer of refrigerants in a horizontal-tube evaporator was conducted. A single-tube evaporation test facility was designed and developed to measure the evaporation characteristics of alternative refrigerants. Measurements were made in several instrumented, horizontal copper tubes with inside tube diameters ranging from 0.277 to 0.430 in and lengths ranging from 4 to 8 ft using R-12, R-22, R-134a, and a 60%/40% azeotropic mixture of R-32/R-125.

The two main flow regimes found during objective and visual evaluation of the flow patterns during adiabatic and diabatic flow in smooth, horizontal tubes were wavy-stratified flow and annular flow. High speed pressure and differential pressure measurements were taken for a variety of mass flux and quality combinations, and were analyzed both spectrally and statistically. The normalized power spectral density of these measurements had sharp peaks near zero frequency, indicative of separated flows. Analysis of the standard deviation of pressure drop divided by the mean pressure drop showed that wavy-stratified flow occurred for values above 0.20, while annular flow occurred for values below 0.10.

For annular flow at low heat fluxes, convective boiling was the dominant mode of heat transfer. As heat flux increased, nucleate boiling enhanced the heat transfer coefficient, especially for low qualities and high reduced pressures. For wavy-stratified flows, convective boiling was diminished due to loss of available convective surface area, while nucleate boiling did not appear to be suppressed at higher qualities or lower heat fluxes. The heat transfer coefficients were well correlated using an asymptotic model, which combined the benefits of the "greater of the two" and superposition models for flow boiling heat transfer. A Froude number dependent term accounted for stratification effects on the heat transfer coefficient.

The heat transfer correlation and previously developed pressure drop correlations were combined in a computer program which simulated the two-phase portion of evaporators. This program was used to examine whether an optimum diameter existed for evaporators with fixed air-side resistances and refrigerant mass flow rates. The results revealed that over a wide range of diameters, the required length of the evaporator was relatively insensitive to the tube diameter, but the required surface area had a definite minimum. As the diameter became sufficiently small, pressure drop decreased much of the driving temperature difference, increasing the length of the evaporator dramatically.

Executive Summary

This report on evaporation, together with ACRC TR-57 on condensation, represents the culmination of work done in Project 01 at the ACRC of the University of Illinois on the heat transfer and pressure drop characteristics of pure substances, azeotropes, and near azeotropes; primarily the potentially new refrigerants to be used in refrigeration and air conditioning systems. Some of the work, however, such as the writing of this report, has been performed in Project 37.

The purpose of this work was to obtain experimental, local heat transfer and flow data and to develop from these data appropriate correlations and methods to be used in the design of horizontal-tube evaporators. The emphasis on local values was essential because the evaporation process goes through several different flow patterns as more and more vapor is formed and the refrigerant is forced to accelerate. Thus, the identification of the flow pattern was just as important as the thermal or pressure drop data. We have found that for the range of parameters investigated, which cover primarily refrigerator and air conditioner applications, the two major forces controlling the flow patterns were gravity and vapor shear. At low vapor velocities (low mass flux or quality, or both) gravity dominates and the liquid phase tends to stay at the bottom of the tube; whereas at high vapor velocities (high mass flux or quality, or both) the vapor shear dominates and the liquid phase tends to be uniformly distributed around the entire periphery of the tube with, possibly, some mist also occurring in the central vapor filled space.

Another important aspect of the evaporation process is the presence or the suppression by convective flow of nucleate boiling at the tube surface. Generally, nucleate boiling enhances the heat transfer rates. However, high convective velocities prevent the formation of the vapor bubbles at the surface, unless the heat flux can be raised to sufficiently high levels. Thus, below some level of the heat flux, the heat transfer in convective evaporation is independent of the heat flux. We have successfully correlated these effects by a weighted combination of two heat transfer coefficients, one for nucleate boiling and the other for convective evaporation.

We have accidentally discovered another phenomenon for which we collected data (reported previously) to show its influence but for which no correlation is available. This phenomenon is that the presence of flow oscillations can degrade the heat transfer coefficients very substantially at medium and high qualities and heat fluxes. Our interpretation is that the flow oscillations create corresponding variable thicknesses of the annular liquid film covering the tube surface. At high enough velocities and heat fluxes a thin portion of the liquid layer will actually dry out completely and film boiling will be created with its typically low heat transfer rate. Thus, as a general rule, flow oscillations should be avoided.

The final analysis performed was the development of a method for properly utilizing our correlations for heat transfer and pressure drop in the design of a complete evaporator. The computer model was based on the use of a spreadsheet which considerably simplified the work required. It included the pressure drops created by return bends (reported previously). The results show that the design may be optimized with respect to the minimum surface area required to perform a prescribed refrigeration task.

The details of the work are described in the following order. After the introduction a thorough review of the literature and of the existing theories is presented. Then the experimental work is explained. The results are presented first for the flow patterns, then for the heat transfer, including the development of the correlations. Next, a spreadsheet-based computer model is given for the simulation and design of a complete evaporator. Finally, conclusions and recommendations for future work are described. An extensive bibliography and the appendices containing miscellaneous data close the report.

TABLE OF CONTENTS

LIST OF TABLES

LIST OF FIGURES

NOMENCLATURE

a_α	Acceleration pressure drop variable from Martinelli-Nelson	
A	Area	
A	Constant	
A_l	Liquid surface area	
A_s	Surface area	
A_v	Vapor surface area	
b	Bubble height	
Bo	Boiling number	$= \frac{q''}{Gi_{lv}}$
Bond	Bond number	$= \frac{g(\rho_l - \rho_v)D^2}{\sigma}$
c_p	Specific heat	
c_{p_l}	Liquid specific heat	
C	Constant	
$C_1 - C_7$	Constants	
Co	Convection number	$= \left(\frac{1-x}{x}\right)^{0.8}\left(\frac{\rho_v}{\rho_l}\right)^{0.5}$
$\frac{dp}{dz}$	Pressure gradient	
$(dp/dz)_l$	Liquid alone pressure gradient	
$(dp/dz)_{lo}$	Liquid only pressure gradient	
$(dp/dz)_{TPf}$	Two-phase frictional pressure gradient	
$(dp/dz)_v$	Vapor alone pressure gradient	
$(dp/dz)_{vo}$	Vapor only pressure gradient	
$(dP/dx)_l^s$	Superficial liquid pressure gradient	
$(dP/dx)_v^s$	Superficial vapor pressure gradient	
D	Diameter	
D_b	Bubble departure diameter	

D_h	Hydraulic diameter	
D_{RB}	Return bend diameter	
f	Frequency	
f	Friction factor	
f_{lo}	Frictional factor based on total flow assumed liquid	
f	Function of	
$\bar{f}$	Average frequency	
F	Two-phase multiplier for heat transfer	
F	Modified Froude number	$= \sqrt{\frac{\rho_v}{(\rho_l - \rho_v)}} \frac{j_v}{\sqrt{Dg\cos\alpha}}$
F'	Bennett and Chen modified two-phase heat transfer multiplier	
$\vec{F}_{ext}$	External force vector	
Fr_l	Liquid Froude number	$= \frac{G^2}{\rho_l^2 gD}$
g	Acceleration of gravity	
g_l	Gibb's free energy of the liquid	
g_v	Gibb's free energy of the vapor	
G	Mass flux	
G_l	Liquid mass flux	
G_v	Vapor mass flux	
h	Heat transfer coefficient	
h	Liquid level	
h_{cb}	Convective boiling heat transfer coefficient	$= Fh_l$
h_l	Liquid alone heat transfer coefficient	
h_{nb}	Nucleate boiling heat transfer coefficient	
h_{REF}	Refrigerant-side heat transfer coefficient	
h_{TP}	Two-phase heat transfer coefficient	
i	Summation index	

i_l	Saturated liquid enthalpy	
i_{lv}	Latent heat of vaporization	
I_ϕ	Integral two-phase multiplier variable from Martinelli-Nelson	
j	Summation index	
j_l	Superficial liquid velocity	$=\frac{G(1-x)}{\rho_l}$
j_v	Superficial vapor velocity	$=\frac{Gx}{\rho_v}$
J	Mechanical equivalent of heat	
k	Conductivity	
k_l	Liquid conductivity	
K	Pierre boiling number	$=\frac{Ji_{lv}\Delta x}{L}$
K	Taitel-Dukler wavy-stratified parameter	$=F\left(Re_l^s\right)^{0.5}$
L	Length	
L_T	Loss of turbulence term	
$\dot{m}$	Mass flow rate	
$\dot{m}_l$	Liquid mass flow rate	
$\dot{m}_r$	Refrigerant mass flow rate	
$\dot{m}_v$	Vapor mass flow rate	
M	Molecular weight	
n	Exponent	
n	Nucleation site density	
n	Summation index	
N	Sample size	
Nu_{TP}	Two-phase liquid Nusselt number	$=\frac{h_{TP}D}{k_l}$
Nu	Single-phase liquid Nusselt number	$=\frac{h_lD}{k_l}$
P_l	Liquid pressure	

P_v	Vapor pressure	
P_∞	True power spectral density distribution function	
P_r	Reduced pressure	$= \frac{P_{sat}}{P_{crit}}$
P_{crit}	Critical pressure	
P_{sat}	Saturation pressure	
$P[x, W]$	Probability distribution function	
$\hat{P}(f)$	Normalized power spectral density distribution function	
PDF	Probability density function	
Pr	Prandtl number	$= \frac{\mu c_p}{k}$
$Prob[\ ]$	Probability that	
Pr_l	Liquid Prandtl number	$= \frac{\mu_l c_{p_l}}{k_l}$
q	Heat input rate	
$q_{environment}$	Heat gain from the environment	
q_{latent}	Latent heat gain	
$q_{preheater}$	Electrical heat input rate to the preheater	
$q_{sensible}$	Sensible heat gain	
$q_{test\ section}$	Heat input rate to the test section	
q''	Heat flux	
q''_{ONB}	Heat flux at onset of nucleation	
r	Time delay counter in auto- and cross-correlation	
r_c	Critical cavity radius at onset of nucleation	
r_c	Cavity radius	
r_e	Bubble radius	
$r_{c,max}$	Maximum cavity radius	
$r_{c,min}$	Minimum cavity radius	
R	Bubble radius	

R	Convection reduction parameter	
R'_{AIR}	Air-side thermal resistance per unit length	
R'_{REF}	Refrigerant-side thermal resistance per unit length	
R_{xx}	Sample auto-correlation function	
R_{xy}	Sample cross-correlation function	
Re	Reynolds number	$= \frac{GD}{\mu}$
Re	Single-phase liquid Reynolds number	
Re_{TP}	Two-phase liquid Reynolds number	
Re_l^s	Superficial liquid Reynolds number	$= \frac{\rho_l j_l D}{\mu_l}$
Re_v	Vapor Reynolds number	
Re_{lo}	Liquid only Reynolds number	$= \frac{GD}{\mu_l}$
Re_l	Liquid alone Reynolds number	$= \frac{GD(1-x)}{\mu_l}$
S	Suppression factor	
S_{xx}	Autospectral density	
$\hat{S}_{xx}$	Normalized autospectral density	
St	Stanton number	$= \frac{Nu}{Re\,Pr}$
t	Time	
T	Time period	
T	Taitel-Dukler bubble-intermittent flow parameter	$= \left[\frac{\left\|(dP/dx)_l^s\right\|}{(\rho_l - \rho_v) g \cos\alpha} \right]^{0.5}$
T	Temperature	
T_{AIR}	Air Temperature	
T_b	Bulk fluid temperature	
T_l	Liquid temperature	
$T_{preheater,in}$	Refrigerant temperature at preheater inlet	

$T_{preheater,out}$	Refrigerant temperature at preheater outlet	
T_{REF}	Refrigerant temperature	
T_s	Surface temperature	
T_{sat}	Saturation temperature	
T_v	Vapor temperature	
T_w	Wall temperature	
$(T_w - T_{sat})_{ONB}$	Wall superheat at onset of nucleation	
v_{ave}	Two-phase specific volume	
v_{lv}	difference in specific volume between saturated liquid and vapor	
V_l	Liquid velocity	
V_v	Vapor velocity	
$\vec{V}$	Velocity vector	
W	Amplitude window width	
We'	modified Weber number	$= \frac{x^2 G \mu_l}{\sigma \rho_v} \left(\frac{GD}{\mu_l} \right)^{0.125}$
x	Quality	
x_{cr}	Critical quality for onset of mist flow	
x_i	Inlet quality	
x_o	Outlet quality	
x(t)	Time dependent variable	
$\bar{x}$	Sample mean value of x	
X	Lockhart-Martinelli parameter	$X = \sqrt{\frac{(dp/dz)_l}{(dp/dz)_v}}$
X_{tt}	Turbulent-Turbulent Lockhart-Martinelli parameter	$= \left(\frac{1-x}{x} \right)^{0.9} \left(\frac{\rho_v}{\rho_l} \right)^{0.5} \left(\frac{\mu_l}{\mu_v} \right)^{0.1}$
X(f,T)	Fourier transform of x(t) over record length T	

y	Distance from wall	
z_e	Exit distance	
Z	Property parameter	$=\left(\frac{k_l^{0.6} c_{p_l}^{0.4}}{\mu_l^{0.4}}\right)$
α	Angle of pipe inclination	
α	Void fraction	
α_l	Liquid thermal diffusivity	$=\frac{k_l}{\rho_l c_{p_l}}$
α_o	Inlet void fraction	
α_o	Outlet void fraction	
β	Contact angle	
γ_1	Skewness	
γ_2	Kurtosis	
δ	Change in	
δ	Frequency in which 68% of the energy of $\hat{P}(f)$ is contained between 0 and δ	
δ	Square root of the inside tube diameter to return bend diameter ratio	
δ_t	Edge of thermal boundary layer	
δh	Uncertainty in the heat transfer coefficient	
δq	Heat transfer rate of small quality increment	
δt	Change in time	
ΔL	Change in length	
Δp_i	Differential pressure at observation section i	
Δp_{oi}	Hydrostatic pressure drop at observation section i	
ΔP_a	Two-phase acceleration pressure drop	
ΔP_b	Return bend pressure drop	
ΔP_f	Two-phase friction pressure drop	
ΔP_l	Single-phase liquid alone pressure drop	

ΔP_i	Normalized pressure drop at observation section i	$= \frac{\Delta p_i}{\Delta p_{oi}}$
ΔP_i^*	Matsui void fraction variable at observation section i	$= 1 - \Delta P_i$
ΔP_t	Return bend pressure drop due to turning of the flow	
ΔP_{sat}	Saturation pressure difference	$= P_{sat}(T_w) - P_l$
Δt	Sampling interval	
ΔT	Change in temperature	
ΔT	Wall superheat	$= T_w - T_{sat}$
ΔT_{ONB}	Wall superheat at onset of nucleation	
ΔT_{sat}	Change in saturation temperature	$= T_l - T_{sat}(P_l)$
Δx	Change in quality	
ε	Pressure drop resistance factor	
θ	Frequency in which 68% of $\hat{P}(f)$ is contained between $f \pm \theta$	
θ	Temperature difference	$= T - T_\infty$
θ_b	Temperature difference at top of bubble	$= T_b - T_\infty$
θ_{sat}	Saturation temperature difference	$= T_{sat}(P_l) - T_\infty$
θ_w	Temperature difference	$= T_w - T_\infty$
λ	Property parameter for Baker map	$= \left[\left(\frac{\rho_v}{\rho_a}\right)\left(\frac{\rho_l}{\rho_w}\right)\right]^{0.5}$
μ_l	Liquid viscosity	
μ_n	n-th moment about the mean	
μ_v	Vapor viscosity	
ρ_a	Air density	
ρ_l	Liquid density	
ρ_v	Vapor density	
ρ_w	Water density	
ρ_{xy}	Normalized cross-correlation function	

σ	Standard deviation	
σ	Surface tension	
σ_w	Water surface tension	
τ_w	Shear stress at the wall	
ϕ_l	Two-phase frictional multiplier based on pressure gradient for liquid alone flow	
ϕ_{lo}	Two-phase frictional multiplier based on pressure gradient for total flow assumed liquid	
ϕ_v	Two-phase frictional multiplier based on pressure gradient for vapor alone flow	
ϕ_{vo}	Two-phase frictional multiplier based on pressure gradient for total flow assumed vapor	
φ	Property parameter for Baker map	$=\left(\frac{\sigma_w}{\sigma_l}\right)\left[\left(\frac{\mu_l}{\mu_v}\right)\left(\frac{\rho_w}{\rho_l}\right)^2\right]^{0.33}$
Ω	Property parameter	$=\left(\frac{\rho_v}{\rho_l}\right)^{0.5}\left(\frac{\mu_l}{\mu_v}\right)^{0.1}$

CHAPTER 1. INTRODUCTION

Convective processes associated with phase change are very complex phenomena. Heat transfer to a two-phase fluid occurs either at constant temperature or with relatively small temperature change because there is phase change. This allows large heat transfer rates with small temperature differences. For forced-convective boiling inside a tube, phase change can occur due to evaporation at the liquid-vapor interface or through bubble formation (nucleate boiling) at the tube wall. Both of these phenomena are characterized by several unique features. For convective evaporation at a liquid-vapor interface, mass flux, quality, and vapor to liquid density ratio play important roles in the magnitude of the heat transfer. For bubble formation at a solid-liquid interface, wall superheat, density difference between the liquid and vapor, and surface tension at the liquid-vapor interface of a bubble are a few of the parameters that greatly affect nucleate boiling heat transfer. Combining these two effects, two-phase flow forced-convective heat transfer coefficients are generally much larger than those characteristic of convective heat transfer without phase change. Table 1.1 gives some typical values of heat transfer coefficient for various processes.

Table 1.1. Typical values of the convective heat transfer coefficient [Incropera and DeWitt, 1990]

Process	h (Btu/hr-ft^2-°F)
Free convection	1-5
Forced convection	5-3,500
Convection with phase change	75-20,000

The prediction of heat transfer coefficients and pressure drops during forced-convective boiling is important for a wide range of processes, which include applications relating to the power, chemical process, and refrigeration industries. The first phase of extensive study of heat transfer coefficients during forced-convective evaporation took place during the 1950s and 1960s. Appropriate mechanisms for forced-convective evaporation were identified and dimensionless parameters representing these mechanisms were used in developing correlations. However, magnitudes of resulting terms and transitions between flow regimes were not extensively examined. Later, generalized correlations were developed in the 1970s and 1980s from compiled databases of these earlier studies. Improvements in predicting heat transfer coefficients were made, but the

magnitudes of each mechanism and transitions between these mechanisms were still not clearly defined.

In the 1990s, increasing energy efficiency standards imposed by the federal government along with the replacement of the current generation of CFC refrigerants by alternatives with substantially reduced ozone depleting and global warming potential have led to a need for quick and accurate evaluation of the fluid dynamics and thermal/heat transfer properties of these alternatives. To help facilitate this need, experimental research to measure heat transfer coefficients and pressure drops of these new chemicals has begun, including development of two test apparatuses, one for evaporation and one for condensation, at the Air Conditioning and Refrigeration Center (ACRC) of the University of Illinois.

The present study is concerned with the prediction of heat transfer coefficients for CFC, HCFC, and HFC refrigerants and azeotropic mixtures. Refrigerants used in this study were R-12, R-134a, R-22, and a 60%/40% azeotropic mixture of R-32/R-125. To predict these heat transfer coefficients, the developed correlation will be based on differing flow regimes during the evaporative process. Appropriate dimensionless parameters will be identified for each flow regime and will be used to correlate the results empirically. Special emphasis will be given to the contribution and suppression of nucleate boiling and the effects of transition from annular to mist flow.

Before the heat transfer coefficients can be correlated, identification of the flow regimes in the evaporative process must be properly determined. Various maps have been developed based on properties of the flow to predict these flow regimes, mainly for adiabatic air-water mixtures. Applications of these maps have been based on subjective, visual identification. Objective methods of identifying flow patterns have also been attempted based on X-ray void measurements and both pressure and pressure drop measurements. Previous studies on refrigerants at the Air Conditioning and Refrigeration Center have shown that stratified, wavy, annular, and mist flows exist during horizontal, single-tube evaporation of refrigerants. Varying amounts of slug flow also have been observed to be superimposed with these flow patterns. Transitions between these regimes will be examined using the flow regime maps and spectral and statistical methods to correlate high speed pressure and pressure drop data.

The results of these studies will also be applied to heat exchanger design and simulation. Developed correlations for heat transfer and pressure drop will be applied to a series of heat transfer design conditions for optimum sizing of an evaporator. Special emphasis will be given to the change in heat transfer coefficient due to the presence or suppression of nucleate boiling and the transitions from wavy to annular flow.

A survey of the literature along with theoretical aspects of modeling both the fluid mechanics and heat transfer of forced-convective evaporation will be given in Chap. 2. Flow regime maps will be discussed, including an examination of the parameters for predicting various flow patterns. Objective flow regime indicators will also be analyzed. Special emphasis will be given to high speed pressure and pressure drop measurements. Major scrutiny will be given to heat transfer coefficient correlations developed over the years. This will include in-depth analyses of convective boiling and nucleate boiling theory. Reduced pressure effects, similarity of two-phase and single-phase forced convection, onset of nucleate boiling during pool and flow boiling, and suppression of nucleate boiling will be discussed in detail. Heat transfer coefficient model selection will play a key factor in representing the combined effects of nucleate and convective boiling. The superposition model introduced by Rohsenow [1952] and pioneered by Chen [1966], the "greater of the two" model developed by Shah [1976], and the asymptotic model suggested by Kutateladze [1961] will be examined.

The facility designed and fabricated for this study along with the experimental and data reduction procedures are described in Chap. 3. This is followed by two chapters of results of the flow pattern and heat transfer studies. Chapter 4 will examine the observed flow patterns and predicted flow patterns using several flow regime maps and objective flow regime indicators used to distinguish between flow patterns. Chapter 5 will summarize the important trends in the heat transfer coefficient data and will compare the experimental results with heat transfer coefficient correlations from the open literature. The heat transfer coefficient correlation developed using the experimental data of this study will also be outlined in this chapter and will be compared with data from selected studies from the open literature. Chapter 6 will combine the resulting correlation and flow pattern analysis into a heat transfer design computer program. Pressure drop correlations from previous studies will be included. Parameters within the correlations will be varied to determine optimum sizing of an evaporator. Conclusions and recommendations for future studies are presented in Chap 7. Physical properties and experimental data will be summarized in appendices.

CHAPTER 2. LITERATURE REVIEW AND THEORY

The literature review first focuses on the various flow regimes of two-phase flow inside horizontal tubes. Flow regime maps have been developed over the last several decades which predict flow patterns based on significant flow parameters such as phase velocities, densities, and viscosities. Three of the most important flow regime maps will be reviewed and discussed. Flow regime transitions, such as the transition from wavy to annular flow, will be compared with the flow regime map boundaries. In addition, due to the subjective nature of determining flow patterns based on visual identification, objective flow regime indicators will also be examined. Methods using spectral and statistical analysis of pressure and pressure drop fluctuations will be discussed for both vertical and horizontal flow. Finally, a review of heat transfer coefficient correlations will be given. A chronological summary will be presented along with some detailed discussions of the basic forms of these correlations. The relationship between convective and nucleate boiling will be examined along with the various methods used to predict the onset and suppression of nucleate boiling during forced-convective flow.

2.1. Flow Regimes in Horizontal Two-Phase Flow

To properly predict the variation of heat transfer coefficient in two-phase flow, knowledge of the flow pattern is necessary. This is as important as knowing whether a flow is laminar or turbulent in single-phase flow. Several flow patterns have been identified for two-phase flow. Typical flow patterns observed during two-phase flow are shown in Fig. 2.1. These flow patterns will be described for horizontal concurrent flow with evaporation. Starting with subcooled liquid, the vaporization process may begin with boiling being initiated before the bulk liquid reaches saturation temperature. With the void fraction being low, bubbles begin to form and collect at the top of the tube due to buoyancy. Both vapor and liquid superficial velocities increase as the boiling process continues, changing the flow regime from bubble flow to plug flow. Again, the plugs of vapor remain at the top of the tube due to buoyancy effects. For low mass fluxes and, hence, low superficial liquid and vapor velocities, stratified flow ultimately results. The liquid flowing at the bottom of the tube is separated from the vapor in the upper portion of the tube by a smooth interface. At higher mass fluxes, both superficial liquid and vapor velocities increase and waves begin to form at the liquid-vapor interface. Under certain conditions, these interfacial waves grow to encompass the entire tube cross section, resulting in the formation of liquid slugs that continue down the tube. The vapor separating

these liquid slugs again remains near the top of the tube due to buoyancy effects. This flow regime is called slug flow. Slug and plug flow can also be called intermittent flow.

At higher qualities, the liquid is swept around the tube wall and annular flow occurs. In this flow, an annular liquid ring forms around the tube periphery with a high velocity vapor core moving through the center of the tube. For moderately high mass fluxes, the liquid ring is asymmetric with buoyancy effects thinning the liquid at the top of the tube and thickening it at the bottom of the tube. At high mass fluxes, the liquid flow becomes completely turbulent and strong lateral Reynolds stresses and shear resulting from secondary flows tend to distribute the liquid more evenly around the perimeter [Carey, 1992]. Interfacial waves are ripped off the annular ring and form droplets that are entrained in the vapor core. The annular ring is vaporized as quality increases, leaving only mist flow (also called dispersed or spray flow) with liquid droplets entrained in the vapor core.

2.2. Flow Regime Maps

2.2.1. Baker map

One of the earliest flow regime maps was developed by Baker [1954] for horizontal, adiabatic gas-liquid flow in 1.0, 2.0, and 4.0 in tubes. Baker used results from three separate investigations on both air-water and oil-water flows to develop his map. The coordinates for the map are the gas and liquid mass fluxes multiplied by dimensionless fluid property parameters. For air-water flow, the coordinates reduce to the gas mass flux for the ordinate and the liquid to gas mass flux ratio for the abscissa. The coordinates are as follows:

$$\text{ordinate} = \frac{G_v}{\lambda} \tag{2.1}$$

$$\text{abscissa} = \frac{G_l \lambda \varphi}{G_v} \tag{2.2}$$

where

$$\lambda = \left[\left(\frac{\rho_v}{\rho_a} \right) \left(\frac{\rho_l}{\rho_w} \right) \right]^{0.5} \tag{2.3}$$

and

$$\varphi = \left(\frac{\sigma_w}{\sigma} \right) \left[\left(\frac{\mu_l}{\mu_v} \right) \left(\frac{\rho_w}{\rho_l} \right)^2 \right]^{0.33} \tag{2.4}$$

Subscripts g, l, w, and a are for gas, liquid, water, and air, respectively. Fluid properties for air and water were listed in English units in Baker's original paper. Figure 2.2 is a plot of the flow regime map. Baker stated that the boundaries between flow regimes are not

really lines but bands over which transitions take place. Variations of Baker's map have been developed over the years and have been widely used by the petroleum industry.

2.2.2. Mandhane map

Mandhane et al. [1974] later developed a map based on coordinates of superficial gas and liquid velocities constructed from a large database of several experimental studies. The superficial velocities are defined as follows:

$$j_v = \frac{Gx}{\rho_v} \tag{2.5}$$

$$j_l = \frac{G(1-x)}{\rho_l} \tag{2.6}$$

Superficial velocities were used since improvements in the map using physical property ratios of the fluids in the database were not found. The property parameters resulted in only a small statistical improvement in predicting the proper flow regimes (68.2% versus 67.2% of all the experimental data). Pipe diameters ranged from 0.5 to 6.5 in. The effect of pipe diameter was adequately accounted for using the superficial velocities. Figure 2.3 shows the Mandhane map. Using the superficial velocities defined above, the Mandhane map accurately predicted 67.2% of the experimental data in the compiled database versus 41.5% using the original Baker map. For air-water data only, the original Baker map predicted 61.3% of the data while the Mandhane map predicted 81.8% of the data.

2.2.3. Taitel and Dukler map

Taitel and Dukler [1976] developed models for predicting flow regime transitions in horizontal and near horizontal gas-liquid flow. Utilizing variables such as gas and liquid flow rates, fluid properties, pipe diameter, and inclination angle of the pipe, models were developed for four different flow regime transitions. From the theory, five different dimensionless groups emerged. These groups were used as coordinates for a flow regime map. A generalized flow regime map resulted which was based on physical concepts, not on experimental flow regime data, to predict flow regime transitions.

Figure 2.4 shows the Taitel-Dukler map. The abscissa of the flow regime map for all transitions is the Lockhart-Martinelli parameter defined as follows:

$$X = \left[\frac{\left|(dP/dx)_l^s\right|}{\left|(dP/dx)_v^s\right|}\right]^{0.5} \tag{2.7}$$

The ordinate varies depending on the transition being analyzed. A parameter, Y, is also defined and is based on inclination angle of the pipe and will not be discussed herein. For stratified to intermittent and stratified to annular flow transitions, Kelvin-Helmholtz stability

analysis theory was applied to a wave existing for a stratified liquid sheet between parallel plates and then extended to a round pipe geometry. The analysis determined the superficial gas velocity necessary to overcome the stabilizing effect of gravity. The ordinate that emerged from the theoretical analysis was a Froude number that is modified by a density ratio:

$$F = \sqrt{\frac{\rho_v}{(\rho_l - \rho_v)}} \frac{j_v}{\sqrt{Dg\cos\alpha}} \tag{2.8}$$

Using qualitative arguments, Taitel and Dukler estimated that the Froude number must be greater than the following expression:

$$F \geq \left(1 - \frac{h}{D}\right) f\left(\frac{h}{D}\right) \tag{2.9}$$

Lin and Hanratty [1986] noted that the lack of incorporation of the liquid viscosity for the instability criterion caused the vapor velocity for slug initiation to be overestimated slightly for a given liquid depth. For stratified to slug air-water flow in a rectangular channel, they developed an alternative expression utilizing the void fraction:

$$\frac{j_v}{\sqrt{gh}}\left[\frac{\rho_v}{(\rho_l - \rho_v)}\right]^{0.5} = 1.0\alpha^{1.5} \tag{2.10}$$

For moderately viscous liquids, such as water, the Taitel-Dukler modification to inviscid theory, (1-h/D) in Eq. 2.9, accounted correctly for inertia for air-water flow. However, for liquids other than water and for pipe flow, the correction became a complicated function of fluid viscosity and liquid depth to pipe diameter ratio, h/D. With refrigerants generally tending to have lower viscosities, the transition to slug or annular flow may occur at lower vapor velocities than shown in the Taitel-Dukler map.

When there is not enough of a liquid layer to maintain a slug, the wave is swept around the tube and annular or annular-mist flow is developed, as described by Butterworth [1972]. Again using qualitative arguments, Taitel and Dukler suggested that the transition takes place at a h/D value of 0.5. For liquid levels above this value, intermittent flow (slug or plug flow) will take place. For a constant value of h/D, a single value of X equal to 1.6 accounts for the transition for a horizontal tube. It should be noted that the transition takes place over a band of X since distinguishing between an aerated slug and annular flow with large roll waves is difficult using subjective flow visualization.

The transition from stratified smooth to wavy-stratified regimes was examined using the work of Jeffreys [1925,1926] for wave generation. The transition takes place when pressure and shear work overcome the effects of viscous dissipation in the waves [Taitel and Dukler, 1976]. A dimensionless parameter, K, was defined for this transition,

which is the product of the Froude number and the square root of the superficial liquid Reynolds number as follows:

$$K = F\left(Re_l^s\right)^{0.5} \tag{2.11}$$

Another parameter, T, defines the transition between bubble flow and intermittent flow. T is the ratio of the turbulent to gravity forces acting on the gas and is defined as

$$T = \left[\frac{\left|(dP/dx)_l^s\right|}{(\rho_l - \rho_v)g\cos\alpha}\right]^{0.5} \tag{2.12}$$

Of the three maps discussed above, the Taitel-Dukler map has become the most accepted due to the prediction of the transitions based on theoretical considerations. However, the evaluation of the dimensionless parameters for this map can become more involved, so many use the Mandhane map with its simple superficial velocity coordinates for specific fluids and tube sizes. At varying pressures and smaller line sizes, the Mandhane map's transition lines can shift considerably and care must be taken when comparing flow pattern results for different situations.

2.2.4. Non-ideal effects

It should be noted that the inlet quality for an air conditioning or refrigeration evaporator usually is around 10% to 20%. The Lockhart-Martinelli parameter for refrigerants in this quality range is less than 1.6, and, using the Taitel-Dukler map flow pattern predictions, both the intermittent and dispersed bubble regimes should not be found as flow patterns in the evaporator for the typical conditions used in this study.

Tube bends in evaporators also play an important role, especially for household refrigerator evaporators with low loads and, hence, low refrigerant flow rates. As found in the study of Barnhart [1992] for low flow rates, return bends caused changes in liquid distribution around the tube and slugs of liquid were observed for several diameters after each return bend, especially at lower qualities. These slugs caused pressure fluctuations down the tube and affected droplet entrainment at the superheated conditions of the evaporator outlet. However, the flow patterns returned to their original form previous to the return bend after about 10 pipe diameters, similar to the findings of Zahn [1964].

The tube diameters used in the present study (0.277-0.430 in) are also much smaller than those that were used to develop the flow regime maps. Smaller tube diameters have since been examined in a few studies. Barnea et al. [1980] examined flow patterns for air-water tests in 0.15 to 0.5 in tube diameters. Transitions for annular and wavy-stratified to slug flow were well predicted by the Taitel-Dukler map. Damianides [1987] and Damianides and Westwater [1988] studied air-water flow in 0.04 to 0.20 in tube

diameters and channels of a compact heat exchanger. Utilizing pressure transducers to help differentiate flow patterns in a more objective way, similar trends to the Barnea et al. data were found.

Surface tension effects in small tube diameters have also been examined recently {[Brauner and Maron, 1992],[Galbiati and Andreini, 1992]}. Their results can be summarized using the dimensionless parameter known as the Bond number, defined as follows:

$$\text{Bond} = \frac{g(\rho_l - \rho_v)D^2}{\sigma} \tag{2.13}$$

For tube diameters in the present study (0.277-0.430 in), Bond numbers are much greater than one, indicating that gravitational forces dominate over surface tension forces. Figure 2.5 shows a plot of the Bond number versus inside tube diameter for R-134a, R-12, and R-22. For a Bond number of 1, the tube diameter for typical refrigerant conditions used in this study is approximately 0.04 in.

The effect of high pressure on the flow regime maps will be examined using data from the present study. A 60%/40% azeotropic mixture of R-32/R-125 has pressures near 150 psia for a saturation temperature of 41°F. Shifts in transition lines have been found in flow regime maps using superficial velocities for coordinates for high pressure oil-natural gas data [Taitel and Dukler, 1976].

2.2.5. Mist flow

Another flow regime found near the exit of the evaporator is the mist flow regime. Mist flow occurs when the liquid film wetting the wall dries out. In this regime liquid droplets remain in the vapor core. Whalley [1987] stated that mist flow develops when droplets are stripped from the crests of roll or disturbance waves that form on liquid films above a critical thickness. Barnhart [1992] reviewed several recent papers involving mist flow formation. Significant vapor velocities must be present for this appreciable liquid atomization to occur and the mist flow regime usually follows the annular flow regime. However, Andrisotos et al. [1989] found that atomization can occur during other flow regimes such as wavy-stratified and slug regimes.

Rhee [1972] stated that the onset of mist flow is characterized by a wide fluctuation of wall temperature as the leading edge of the liquid annulus breaks down and dry patches form. Groothius and Hendal [1959] developed a modified Weber number based on the minimum wetting thickness to determine the critical dryout quality. Rhee correlated the dryout quality using this Weber number and used the following expression to predict the transition point between the annular-mist flow and the mist flow regimes:

$$We' = 1.89 \times 10^{-7} Re_v \left(\frac{\rho_l}{\rho_v}\right)^{0.6} \left(\frac{D}{0.0608}\right)^{-0.48} \quad (2.14)$$

where

$$We' = \frac{x^2 G \mu_l}{\sigma \rho_v} \left(\frac{GD}{\mu_l}\right)^{0.125} \quad (2.15)$$

Sthapak, Varma, and Gupta [1976] examined heat transfer coefficients in the dryout region of a water heated horizontal evaporator tube and developed an expression for the critical dryout quality using their experimental data. Dryout was found over the quality range of 0.89 to 0.99 for the wall superheats encountered. The expression for critical dryout quality was as follows:

$$x_{cr} = 7.94\left[Re_v\left\{2.03 \times 10^4 (Re_v)^{-0.81} (\Delta T) - 1\right\}\right]^{-0.161} \quad (2.16)$$

This expression differs from Eq. 2.14 in that wall superheat is included. Figure 2.6 shows the transition qualities using Eq. 2.16 for R-134a as a function of wall superheat for typical flow parameters used in this study.

Wedekind [1971] completed a study which examined the mixture-vapor transition point in a horizontal evaporator tube and found that the transition point experienced fluctuations as large as 1.5 ft, with periods up to 3 seconds. He found that the inlet quality was important for forming slugs near the evaporator inlet, and that these slugs seemed to influence the transition point even though the system maintained a steady flow rate. Figure 2.7 shows some examples of the motion of the mixture-vapor transition point for steady flow conditions.

2.3. Objective Flow Regime Indicators

The accuracy of the flow maps discussed above is limited because of the visual identification of the flow regimes. For adiabatic two-phase flow, several researchers have attempted to objectively identify the flow patterns based on the statistical and spectral properties of the void fraction, pressure signal, or pressure drop signal.

2.3.1. Statistical methods

For vertical flow, Matsui [1984, 1986] measured the pressure drop fluctuations of nitrogen-water mixtures for a variety of flow patterns. The flow regimes were classified by the peculiar features of the statistical properties of the fluctuations. Identification of the flow regimes was made from the configuration of probability density functions, the order of variance, and the average value of the differential pressure drop. Pressure drop was

measured on two scales, the R-scale and the L-scale. The R-scale had a length equal to one tube radius for recognition of spherical cap bubbles and clusters of bubbles. The L-scale had a length of 10 pipe diameters and was selected to identify gas slugs. The arrangement of the observation scales is shown in Fig. 2.8. Differential pressure was normalized with the hydrostatic pressure drop, Δp_{oi}, corresponding to the measurement section as follows:

$$\Delta P_i = \frac{\Delta p_i}{\Delta p_{oi}} \tag{2.17}$$

For cases where the friction and acceleration pressure losses were small compared with $\left(\Delta p_{oi} - \overline{\Delta p_i}\right)$, the quantity $\left(1 - \overline{\Delta P_i}\right)$ approximately represented the average void fraction in the test section, i. Therefore, Matsui used the following statistical variables:

$$\Delta P_i^* = 1 - \Delta P_i \tag{2.18a}$$

$$\mathrm{PDF}\left(\Delta P^*\right)_j = \lim_{\delta\left(\Delta P^*\right)\to 0} \frac{1}{\delta\left(\Delta P^*\right)} \frac{n_j \delta t}{T} \tag{2.18b}$$

Figure 2.9 gives some examples of the differences in the probability density function (PDF) of the variable ΔP_i^* for different flow patterns. Bubble flow showed a single-peaked PDF and a low variance at low ΔP_i^*. Mist flow showed a single-peaked PDF with a low variance at high ΔP_i^*. Annular flow showed a single-peaked PDF and a medium variance at high ΔP_i^*. Slug flow showed a twin-peaked PDF at medium ΔP_i^* for the R-scale. Jones and Zuber [1975] found similar results to those of Matsui using an X-ray void measurement system to identify flow patterns in vertical two-phase flow.

Utilizing the Gram-Charlier series, the configuration of the frequency distributions were approximated. Matsui then used statistical features of the Gram-Charlier series, such as the mean, standard deviation, coefficient of skewness, and coefficient of excess to construct a flow chart which can be used as an objective and automatic identification of flow pattern.

2.3.2. Spectral methods

Hubbard and Dukler [1966] used the spectral distribution of wall pressure fluctuations to characterize the flow regimes for horizontal two-phase flow. Tests were conducted for an air-water system with a 1.5 in inside diameter test section. The power spectral density for a stationary random signal is defined as

$$P_\infty = \lim_{T\to\infty} \frac{1}{T}\left[\int_{-T/2}^{T/2} f(t) e^{-i2\pi ft} dt\right]^2 \tag{2.19}$$

Hubbard and Dukler then defined the normalized the power spectral density with respect to the total power over the entire frequency spectrum, $\hat{P}$, and used this as the objective flow regime indicator.

Flow regimes were grouped into three general areas: separated flow (stratified flow, wavy flow, or annular flow), intermittent flow (slug flow or plug flow), and dispersed flow (bubble flow or mist flow). Separated flow had spectra with distributions centered about zero frequency with amplitudes dropping off rapidly with increasing frequency. Intermittent flows had spectra with sharp peaks at frequencies other than zero. Dispersed flows had more uniform distributions of power over the entire frequency spectrum. Figure 2.10 shows a graphical summary of the above-mentioned flow regime definitions.

Utilizing the spectra of the data for the varying flow patterns, flow regime transitions were characterized by specific features. For the separated flow-dispersed flow transition, a frequency, δ, was defined to account for the variations in the frequencies as follows:

$$\sum_{f=0}^{\delta} \hat{P}(f) = 0.68 \tag{2.20}$$

For δ less than 0.1, the flow regime identified was separated flow with negligible amounts of distribution. For $0.1 < \delta < 1.5$, a transition between separated and dispersed flow occurred with the degree of dispersion roughly characterized by δ. For $\delta > 1.5$, dispersed flow occurred.

The intermittent to dispersed flow transition was characterized by the amount of energy close to the peak of the power spectrum. An average frequency, $\bar{f}$, was defined as follows:

$$\sum_{f=0}^{\bar{f}} \hat{P}(f) = 0.50 \tag{2.21}$$

A frequency band, θ, was also defined in which 68% of the energy is located:

$$\sum_{\bar{f}-\theta}^{\bar{f}+\theta} \hat{P}(f) = 0.68 \tag{2.22}$$

Utilizing the analysis of Dukler et al. [1964], the "no slip" liquid volume fraction, C_l, was used to characterize the transition along with θ. It is defined as

$$C_l = \frac{Q_l}{Q_l + Q_v} \tag{2.23}$$

where Q is the volumetric flow rate. For $\theta/C_l < 11$, the intermittent flow pattern was found to occur with liquid slugs forming a bridge to block gas flow. Transition between the intermittent and dispersed flow regimes occurred for $11 < \theta/C_l < 100$. For $\theta/C_l > 100$, dispersed flow occurred.

The flow regime transition between separated flow and intermittent flow was determined based on the location of the peak of the power spectrum. Separated flow

occurred for spectra with energy peaks around the zero frequency while intermittent flow occurred for spectra with energy peaks at frequencies other than zero.

2.3.3. Pressure traces and records

Weisman et al. [1979] developed simple criteria based on oscilloscope traces of the pressure drop for air-water flow in a horizontal tube with inside tube diameters ranging from 0.5 to 2.0 in. Figure 2.11 shows some examples of the pressure drop fluctuation traces for stratified, wavy, slug, dispersed, and annular flows. Stratified flow essentially showed no pressure fluctuations at all. This can be clearly distinguished from wavy flow, whose pressure fluctuations increased as the gas flow rate increased. The amplitude of the fluctuations remained low, however. Slug flow was characterized by distinctive pressure peaks at regularly spaced intervals. The quiescent part of the trace was at least twice as long as the time scale of the pressure peaks. Annular flow was characterized by increases in the amplitude of the pressure peaks and may be distinguished from wavy flow using this criterion. Dispersed flow (in this case, mist flow) fluctuations were large in amplitude compared with both wavy and annular flows. Again, the amplitude criterion may be used to distinguish between these flow patterns.

Table 2.1 summarizes the criteria for determining flow patterns on the basis of pressure drop fluctuations. The amplitude ratio, R, is defined as the ratio of the observed fluctuation to the fluctuation due to a standard slug at specific water and air mass fluxes. Values for the water and air mass fluxes for the standard slug were 230 klb_m/ft^2-hr and 3 klb_m/ft^2-hr, respectively. In Table 2.1, F stands for frequency defined in terms of cycles per second or Hz.

Damianides [1987], Damianides and Westwater [1988], and Lin and Hanratty [1989] used fast acting pressure transducers to correlate flow patterns based on pressure records for air-water flow. Using methods similar to Hubbard and Dukler [1966], wet-wet pressure transducers with frequency responses ranging from 600 to 2000 Hz were placed 60 diameters apart at the bottom of the flow tube. Damianides and Westwater used tubes with inside diameters ranging from 0.04 to 0.20 in while Lin and Hanratty used tubes with inside diameters of 1.0 and 3.5 in. Figure 2.12 shows examples of pressure records for the three distinctive flow regimes for a 5 mm glass tube. Slug flow was characterized again by an elevation in pressure as the slug passed the pressure tap. Five slugs are shown in Fig. 2.12 with the frequency nearly constant at 0.3 slugs/s. Annular flow showed relatively flat pressure traces compared with the slug flow pressure trace discussed above. No blockage of the tube occurred, which kept the pressure signal fairly constant. These results seem to contrast slightly from those found by Weisman et al. [1979] mentioned

earlier, with their annular flow pressure-time trace having a slightly higher pressure fluctuation.

The dispersed flow in Fig. 2.12 can be described as having a pressure trace that resembles random noise. For the upstream and downstream pressure tap locations, the frequencies were the same, but the magnitudes differed with the downstream pressure measurement recording a slightly lower reading than the upstream tap.

Lin and Hanratty [1989] also noticed a new flow pattern that they called pseudo-slug flow. Figure 2.13 shows the difference between the slug flow pressure signature and the pseudo-slug pressure signature. Large peaks in the h/D signal, measured using conductance probes, were found similar to the slug flow peaks. However, the large pressure fluctuations found in the slug flow pressure signatures were not found in the corresponding pseudo-slug plot. Slugs tended to block the tube and, hence, block the flow of gas along the top of the tube leading to high pressure fluctuations. The pseudo-slugs either did not block the tube entirely or only did so momentarily, allowing the gas to pass through the slug so that a huge pressure build up behind it was not possible. Using the criteria from Table 2.1, the pseudo-slugs would be classified as annular flow.

Table 2.1. Criteria for determining flow patterns on the basis of ΔP fluctuations [Weisman et al., 1979]

Criteria	Flow pattern	Water mass flux range (klb_m/ft^2-hr)	Air mass flux range (klb_m/ft^2-hr)
$R \geq 2.5$	Homogeneous	$105 \leq G_w \leq 10500$	$6 \leq G_a \leq 41$
$R \leq 2.5$	Annular	$105 \leq G_w \leq 10500$	$6 \leq G_a \leq 41$
Pressure peak followed by a quiescent region of twice the length of the peak	Slug	$105 \leq G_w \leq 1050$	$0.75 \leq G_a \leq 7.5$
$R \geq 0.75$	Annular	$10.5 \leq G_w \leq 105$	$10.5 \leq G_w$
$R \leq 0.75$	Wavy	$10.5 \leq G_a \leq 105$	$3 \leq G_a \leq 10.5$
$F \geq 7$ Hz	Homogeneous	$1050 \leq G_w \leq 10500$	$0.105 \leq G_a \leq 1.05$
$F \leq 6.5$ Hz	Plug	$1050 \leq G_w \leq 10500$	$0.105 \leq G_a \leq 1.05$
$R \geq 0.2$	Wavy	$10.5 \leq G_w \leq 105$	$3 \leq G_a \leq 10.5$
$R \leq 0.2$	Stratified	$10.5 \leq G_w \leq 105$	$0.105 \leq G_a \leq 3$

2.4. Pressure Drop Models

A complete treatment of liquid-vapor two-phase flow is extremely difficult. Simplifications can be made through use of time and spatial averaging, but much of the localized behavior is lost. However, a simplified treatment of two-phase flow with a one-dimensional analysis can yield many important results. In this section, a one-dimensional analysis of two-phase flow in a horizontal pipe will be developed. Conservation of mass and momentum will be utilized to develop an expression for pressure drop per unit length of pipe. Aspects of both pressure drop due to acceleration effects and pressure drop due to friction will be examined. For friction pressure drop, the Lockhart-Martinelli model [1947] will be discussed, along with the Martinelli-Nelson model [1948] for two-phase flow pressure drop with phase change. Use of the terminology and concepts in this section will be important for a number of reasons. Later in this chapter, an annular flow analysis will relate the two-phase convective heat transfer coefficient to the pressure drop during two-phase flow. An understanding of the Lockhart-Martinelli parameter is essential here. In addition, the concepts of Lockhart-Martinelli and Martinelli-Nelson are utilized to develop a correlation for pressure drop of the refrigerants used in this study. This correlation will be used in the evaporator simulation chapter along with the developed heat transfer coefficient correlation.

2.4.1. Pressure gradient in horizontal two-phase flow

Figure 2.14 shows stratified flow in a horizontal tube. A one-dimensional analysis of the gas-liquid flow will be considered here [Jabardo, 1991]. Although stratified flow is shown in Fig. 2.14, the relations developed here will apply to any flow regimes discussed in the previous sections within the one-dimensional approximations adopted. Several basic assumptions are made. Uniform properties of both phases in the cross section are assumed, including pressure. The two-phase flow is steady. The fluids are incompressible. Infinitesimals of order 2 or higher are negligible. The integral equations of continuity and momentum will be utilized. Applying the continuity equation,

$$\left(\dot{m}_v\right)_{z+dz} - \left(\dot{m}_v\right)_z - [\text{rate of change of phase}] = 0 \qquad (2.24)$$

$$\left(\dot{m}_l\right)_{z+dz} - \left(\dot{m}_l\right)_z + [\text{rate of change of phase}] = 0 \qquad (2.25)$$

$$d\dot{m}_v = -d\dot{m}_l \qquad (2.26)$$

Using the momentum equation, the external forces on the gas in the z-direction include the pressure effects, the drag on the pipe wall, and the interaction with the liquid. The resulting expression for the external forces is as follows:

$$\left[\sum \vec{F}_{ext}\right]_z = -A_v dp - (\tau_w)_v \rho_v dz + [\text{interaction}]_v \qquad (2.27)$$

The net influx of momentum leaving the gas is a combination of the effects on both cross sections z and z+dz, respectively, plus the effects due to the change of phase. The expression for this integral for the gas phase is as follows:

$$\int_{CS} \rho \vec{V} \vec{V}_r \bullet n dS = \frac{d}{dz}(\dot{m}_v V_v)dz - \left[\begin{matrix}\text{momentum flux due} \\ \text{to change of phase}\end{matrix}\right]_v \qquad (2.28)$$

The final result for the gas phase is

$$-A_v dp - (\tau_w)_v \rho_v dz + [\text{interaction}]_v = \frac{d}{dz}(\dot{m}_v V_v)dz - \left[\begin{matrix}\text{momentum flux due} \\ \text{to change of phase}\end{matrix}\right]_v \qquad (2.29)$$

Similarly for the liquid,

$$-A_l dp - (\tau_w)_l \rho_l dz - [\text{interaction}]_l = \frac{d}{dz}(\dot{m}_l V_l)dz + \left[\begin{matrix}\text{momentum flux due} \\ \text{to change of phase}\end{matrix}\right]_l \qquad (2.30)$$

Adding Eq. 2.29 and Eq. 2.30,

$$-Adp - \left[(\tau_w)_v \rho_v + (\tau_w)_l \rho_l\right]dz = \frac{d}{dz}\left[\dot{m}_v V_v + \dot{m}_l V_l\right]dz \qquad (2.31)$$

Eq. 2.31 can be manipulated into the following form:

$$\left(-\frac{dp}{dz}\right) = \frac{1}{A}\frac{d}{dz}\left[\dot{m}_v V_v + \dot{m}_l V_l\right] + \left[(\tau_w)_v \rho_v + (\tau_w)_l \rho_l\right] \qquad (2.32)$$

$$\left(-\frac{dp}{dz}\right) = \left(-\frac{dp}{dz}\right)_{acceleration} + \left(-\frac{dp}{dz}\right)_{friction} \qquad (2.33)$$

At this point a further assumption is made. Empirical equations from simplified theories will also be allowed to predict the void fraction and two-phase multipliers ϕ_l, ϕ_{lo}, ϕ_v, and ϕ_{vo} from flow parameters. This typical and historical approach relates the two-phase flow pressure drops to corresponding single-phase pressure drops. The basic idea is to correct the single-phase pressure drop using a so called two-phase flow multiplier. The two-phase flow frictional multipliers are defined as follows:

$$\phi_v^2 = \frac{(dp/dz)_{TPf}}{(dp/dz)_v} \qquad (2.34)$$

$$\phi_{vo}^2 = \frac{(dp/dz)_{TPf}}{(dp/dz)_{vo}} \qquad (2.35)$$

$$\phi_l^2 = \frac{(dp/dz)_{TPf}}{(dp/dz)_l} \qquad (2.36)$$

$$\phi_{lo}^2 = \frac{(dp/dz)_{TPf}}{(dp/dz)_{lo}} \tag{2.37}$$

The subscript TPf refers to the two-phase friction pressure drop. The subscripts v and l refer to the pressure drop that would result if the particular phase flowed alone in the pipe at a mass flow rate equal to GxA and G(1-x)A, respectively. The subscripts vo and lo refer to the pressure drop that would result if the particular phase only flowed through the pipe at the same total mass flow rate equal to GA. Using the Blasius form of the single-phase pressure gradient for flow in a circular duct with both the gases flowing in a turbulent or a laminar fashion,

$$\frac{\phi_{vo}^2}{\phi_v^2} = \frac{(dp/dz)_v}{(dp/dz)_{vo}} = \left(\frac{G_v}{G}\right)^{2-n} = x^{2-n} \tag{2.38}$$

or for the liquid,

$$\frac{\phi_{lo}^2}{\phi_l^2} = \frac{(dp/dz)_l}{(dp/dz)_{lo}} = \left(\frac{G_l}{G}\right)^{2-n} = (1-x)^{2-n} \tag{2.39}$$

For values of Reynolds number above 20,000, n is typically given as 0.20 while for Reynolds number below 20,000, n is typically 0.25 [Incropera and DeWitt, 1990].

Acceleration pressure drop in Eq. 2.32 and 2.33 can be evaluated using the definition of void fraction and the continuity equation to yield

$$\frac{1}{A}\left[\dot{m}_v V_v + \dot{m}_l V_l\right] = G^2\left[\frac{x^2}{\rho_v \alpha} + \frac{(1-x)^2}{\rho_l(1-\alpha)}\right] \tag{2.40}$$

and

$$-\left(\frac{dp}{dz}\right)_{accel} = G^2 \frac{d}{dz}\left[\frac{x^2}{\rho_v \alpha} + \frac{(1-x)^2}{\rho_l(1-\alpha)}\right] \tag{2.41}$$

2.4.2. Lockhart-Martinelli-Nelson results

Lockhart and Martinelli [1947] defined a parameter that indicates the relative effects of the phases as follows:

$$X = \sqrt{\frac{\phi_v^2}{\phi_l^2}} = \sqrt{\frac{(dp/dz)_l}{(dp/dz)_v}} \tag{2.42}$$

For turbulent flow of both phases, the Lockhart-Martinelli parameter is designated as X_{tt}. For viscous (laminar) flow of the liquid and turbulent flow of the gas, the parameter is given the subscripts X_{vt}. For the turbulent-turbulent designation using the Blasius form of the pressure gradients with n equal to 0.20, the Lockhart-Martinelli parameter reduces to the following form:

$$X_{tt}^2 = \frac{G_l^{2-n}/(\rho_l \mu_l^{-n})}{G_v^{2-n}/(\rho_v \mu_v^{-n})} = \left(\frac{G_l}{G_v}\right)^{2-n}\left(\frac{\rho_v}{\rho_l}\right)\left(\frac{\mu_l}{\mu_v}\right)^n \tag{2.43}$$

$$X_{tt} = \left(\frac{1-x}{x}\right)^{0.9}\left(\frac{\rho_v}{\rho_l}\right)^{0.5}\left(\frac{\mu_l}{\mu_v}\right)^{0.1} \tag{2.44}$$

Lockhart and Martinelli felt that the friction multipliers defined in Eq. 2.34-2.37 could be exclusively correlated as a function of their parameter. They verified their hypothesis with experimental data for adiabatic air-water and oil-water flow. They developed a simplified separated flow model. Figure 2.15 shows a plot of the two-phase multipliers versus the Lockhart-Martinelli parameter. Chisholm [1968] later curve fitted the data using the following relations:

$$\phi_l^2 = 1 + \frac{C}{X} + \frac{1}{X^2} \tag{2.45}$$

$$\phi_v^2 = 1 + CX + X^2 \tag{2.46}$$

Table 2.2 gives the values of the constant for the four cases of flow encountered for the liquid and gas: turbulent-turbulent, viscous-turbulent, turbulent-viscous, and viscous-viscous.

Table 2.2. Values of the constant for the Lockhart-Martinelli two-phase multiplier correlation [Chisholm, 1968]

Liquid	Vapor	Subscript	C
turbulent	turbulent	tt	20
viscous	turbulent	vt	12
turbulent	viscous	tv	10
viscous	viscous	vv	5

As can be seen from Fig. 2.15, Lockhart and Martinelli also correlated the void fraction as a function of the Lockhart-Martinelli parameter. Butterworth [1975] later curve fitted the results from Lockhart and Martinelli as follows:

$$\alpha = \left[1 + 0.28X^{0.71}\right]^{-1} \tag{2.47}$$

Martinelli and Nelson [1948] developed a correlation technique for pressure drop during flow boiling of water inside tubes. They used the two-phase multiplier ϕ_{lo}^2, and correlated it as a function of quality and pressure using some additional assumptions [Carey, 1992]. First, thermodynamic equilibrium was assumed at each location along the tube in which flow boiling takes place. Next, the two-phase flow always corresponded to

the turbulent-turbulent case for flow boiling. Finally, the frictional contribution to the pressure gradient was the same as an adiabatic horizontal flow of gas-liquid flow under comparable conditions.

Integrating the relations in Eq. 2.33 to determine pressure drop can be difficult and closed-form integration is usually impossible. Numerical integration is generally needed to determine the pressure drop. However, with the assumptions made at the beginning of this section, including a constant cross-sectional area, incompressible fluids, constant properties such as friction factors and densities, an inlet quality of zero, and linear variation of quality with axial length, the pressure drop can be determined as follows:

$$-\Delta P = \frac{2 f_{lo} G^2 z_e}{D_h \rho_l} I_\phi + \frac{G^2}{\rho_l} a_\alpha \tag{2.48}$$

where

$$I_\phi = \left(\frac{1}{x_e}\right)\int_0^{x_e} \phi_{lo}^2 dx \tag{2.49}$$

$$a_\alpha = \left[\frac{x^2 \rho_l}{\alpha \rho_v} + \frac{(1-x)^2}{(1-\alpha)} - 1\right]_{x=x_e} \tag{2.50}$$

Figure 2.16 shows plots of the Martinelli-Nelson steam data for I_ϕ and a_α.

Although the relations of Lockhart-Martinelli-Nelson account for the effects of quality and fluid properties on the two-phase multiplier, the effect of mass flux on the two-phase multiplier was not accounted for. Later, Baroczy [1966] and Chisholm [1968] developed additional expressions that accounted for mass flux variations of the two-phase multiplier for gas-liquid combinations. Variations of these methods were used to correlate the pressure drop data of this study and previous studies for the horizontal single-tube evaporator, and are discussed in Chap. 6.

2.5. Heat Transfer in Flow Boiling

2.5.1. Convective boiling heat transfer

Initial methods were developed for convective boiling heat transfer along a liquid-vapor interface. These methods were based on the premise that the mechanism of heat transfer in forced convection was similar to single-phase forced convection [Chaddock and Noerager, 1966]. By applying the Reynolds analogy that relates the energy transport mechanism to momentum transport in convection, it was shown that the ratio between the two-phase flow and the single-phase liquid heat transfer coefficients could be exclusively correlated by the Lockhart-Martinelli parameter, X_{tt} [Jabardo, 1991].

The relation between the two-phase multiplier for heat transfer and the Lockhart-Martinelli parameter will be derived below. Figure 2.17 shows an annular flow of liquid and vapor flowing in a horizontal tube. The assumptions are as follows: the liquid thickness is small; heat transfer occurs through the liquid film and it is used to vaporize the liquid at the interface; and the flow regimes are the same for the liquid in the film and the liquid flowing alone in the same tube.

As a result of the last assumption,

$$Nu_{TP} = C Re_{TP}^{m} Pr_{l}^{n} \quad : \text{ two - phase} \tag{2.51}$$

$$Nu = C Re^{m} Pr_{l}^{n} \quad : \text{ liquid alone} \tag{2.52}$$

Dividing Eq. 2.51 by 2.52,

$$\frac{Nu_{TP}}{Nu} = \left[\frac{Re_{TP}}{Re}\right]^{m} \tag{2.53}$$

and

$$\frac{Nu_{TP}}{Nu} = \left(\frac{h_{TP}}{h_{l}}\right)\left(\frac{D_{h}}{D}\right) \tag{2.54}$$

where

$$D_{h} = \frac{4A_{l}}{P} = \frac{4(\pi D\delta)}{\pi D} = 4\delta \tag{2.55}$$

$$1-\alpha = \frac{A_{l}}{A} = \frac{\pi D\delta}{\frac{\pi D^{2}}{4}} = \frac{4\delta}{D} \tag{2.56}$$

$$Re = \frac{\dot{m}_{l}}{A}\frac{D}{\mu_{l}} = \frac{G_{l}D}{\mu_{l}} \tag{2.57}$$

$$Re_{TP} = \frac{\dot{m}_{l}}{A_{l}}\frac{D_{h}}{\mu_{l}} = \frac{G_{l}}{(1-\alpha)}\frac{4\delta}{\mu_{l}} = \frac{G_{l}D}{\mu_{l}} \tag{2.58}$$

Comparing Eq. 2.57 and 2.58, the two Reynolds numbers are found to be equal. Therefore, the Nusselt number for the two-phase flow is equal to the Nusselt number as if the liquid flowed alone in the tube. Solving Eq. 2.54 for the heat transfer coefficients,

$$\frac{h_{TP}}{h_{l}} = \frac{D}{D_{h}} = \frac{D}{4\delta} = \frac{1}{1-\alpha} \tag{2.59}$$

From the study of Lockhart and Martinelli [1947] discussed above,

$$(1-\alpha) = f(X_{tt}) \tag{2.60}$$

and

$$\frac{h_{TP}}{h_{l}} = f\left(\frac{1}{X_{tt}}\right) \tag{2.61}$$

Using this form, several researchers developed correlations for forced-convective evaporation in both vertical and horizontal tubes {[Guerrieri and Talty, 1956], [Denglor

and Addoms, 1956], and [Chaddock and Noerager, 1966]}. Table 2.3 shows some examples of early convective correlations. The studies were small in scope and the slopes of the resulting curves were much lower than are found in present studies.

Table 2.3. Early convective correlations

Source	Correlation
Denglor and Addoms [1956]	$\frac{h_{TP}}{h_l} = 3.5\left(\frac{1}{X_{tt}}\right)^{0.5}$
Guerrieri and Talty [1956]	$\frac{h_{TP}}{h_l} = 3.4\left(\frac{1}{X_{tt}}\right)^{0.45}$
Chaddock and Noerager [1966]	$\frac{h_{TP}}{h_l} = 3.0\left(\frac{1}{X_{tt}}\right)^{0.67}$

The heat transfer coefficients for two-phase flow are correlated as a function of the single-phase heat transfer coefficient for the liquid. Two different types of Reynolds numbers have been used in typical single-phase heat transfer coefficient correlations. They are defined below:

$$Re_{lo} = \frac{GD}{\mu_l} \tag{2.62}$$

$$Re_l = \frac{GD(1-x)}{\mu_l} \tag{2.63}$$

Similar to the friction two-phase multipliers, the subscript lo stands for the entire flow as liquid while the subscript l stands for the liquid phase flowing alone in the tube. The two-phase heat transfer coefficient tends to be highly overestimated using Re_{lo}, especially in the higher quality ranges (above 50%). Most correlations developed in the last twenty years utilize the Reynolds number defined in Eq. 2.63. This is because the analogy used to relate two-phase flow heat transfer to single-phase flow heat transfer is based on the liquid alone Reynolds number, which is another name for the film Reynolds number. Physically, this Reynolds number is a measure of the liquid actually left in the tube at the particular quality where the heat transfer coefficient is being evaluated, and it seems to more accurately characterize the variation of the heat transfer coefficient when used in combination with the (1-x) quality term of the Lockhart-Martinelli parameter.

Three single-phase heat transfer coefficients are generally used for turbulent flow inside tubes. These are the Dittus-Boelter correlation [1930], the Petukov correlation

[1970], and the Gnielinski correlation [1976]. The Dittus-Boelter equation is a slight modification of the Colburn equation [1933], which was obtained using the modified Reynolds analogy, similar to the methods used in the two-phase discussion above. This analogy has the form [Incropera and DeWitt, 1990]

$$\frac{f}{8} = St\,Pr^{2/3} = \frac{Nu}{Re\,Pr}Pr^{2/3} \tag{2.64}$$

Using the Blasius form of the friction factor with n equal to 0.20 and substituting into Eq. 2.64,

$$Nu = 0.023 Re^{4/5} Pr^{1/3} \tag{2.65}$$

Dittus and Boelter noticed a difference when correlating their data for heating and cooling situations. They modified Eq. 2.65 using

$$Nu = 0.023 Re^{0.8} Pr^{n} \tag{2.66}$$

with n equal to 0.4 for heating and 0.3 for cooling. The Dittus-Boelter equation has been confirmed experimentally for the range of conditions $0.7 \le Pr \le 120$, $2500 \le Re \le 1.24 \times 10^5$, and $L/D \ge 10$. The Dittus-Boelter equation was the standard correlation used for calculating the single-phase turbulent heat transfer coefficient for heating and cooling for several decades.

Prandtl [1944] developed a theoretical equation for the heat transfer coefficient based on pressure drop as follows:

$$\frac{Nu}{Re\,Pr} = \frac{(f/2)}{1+8.7\sqrt{(f/2)}(Pr-1)} \tag{2.67}$$

Petukov [1970] modified and improved the correlation for $0.5 \le Pr \le 2000$ and $4000 \le Re \le 5x10^6$ as

$$\frac{Nu}{Re\,Pr} = \frac{(f/2)}{1.07+12.7\sqrt{(f/2)}\left(Pr^{2/3}-1\right)} \tag{2.68}$$

Eq. 2.68 was later found by Gnielinski [1976] to overestimate the heat transfer coefficients for $2300 \le Re \le 10{,}000$. Modifying the equation slightly, Gnielinski improved the correlation dramatically in this range. Overall, R.K. Shah [1981] found in a study of several single-phase heat transfer coefficient correlations that the Gnielinski correlation predicted an overall experimental data set of many researchers better than any other. His correlation is given as

$$\frac{Nu}{(Re-1000)Pr} = \frac{(f/2)}{1.07+12.7\sqrt{(f/2)}\left(Pr^{2/3}-1\right)} \tag{2.69}$$

Figure 2.18 is a comparison of the three correlations for R-134a. Ranges for Re_{lo} in the present study are $600 \le Re_{lo} \le 40{,}000$. As can be seen from Fig. 2.18, the Petukov correlation predicts the highest heat transfer coefficient, followed by the Dittus-Boelter and

Gnielinski correlations, respectively, for low Reynolds numbers, and the Gnielinski and Dittus-Boelter correlations, respectively, at high Reynolds numbers.

As described above, the Lockhart-Martinelli parameter is possibly the most important parameter in two-phase flow, both from a pressure drop and convective heat transfer standpoint. The parameter, defined in Eq. 2.44, is listed again here for discussion purposes.

$$X_{tt} = \left(\frac{1-x}{x}\right)^{0.9}\left(\frac{\rho_v}{\rho_l}\right)^{0.5}\left(\frac{\mu_l}{\mu_v}\right)^{0.1} \tag{2.44}$$

The Lockhart-Martinelli parameter is a function of quality, vapor to liquid density ratio, and liquid to vapor viscosity ratio. The viscosity ratio has a very low exponent, and it has been suggested by some to be of very little importance. M.M. Shah [1976] developed a generalized correlation for two-phase heat transfer coefficients in flow boiling. A detailed discussion of his correlation will be given in a following section. In his convective term, he defines a convection number, Co, which is only a function of quality and vapor to liquid density ratio as follows:

$$Co = \left(\frac{1-x}{x}\right)^{0.8}\left(\frac{\rho_v}{\rho_l}\right)^{0.5} \tag{2.70}$$

Figure 2.19 is a comparison of the convection number and Lockhart-Martinelli parameter versus quality for R-134a.

Along these lines, it was also suggested by Cooper [1984] that the density and viscosity ratios in Eq. 2.44 could be exclusively correlated as a function of the reduced pressure, P_r, according to the law of corresponding states. The reduced pressure is defined as

$$P_r = \frac{P_{sat}}{P_{crit}} \tag{2.71}$$

Jung and Radermacher [1989] utilized this format when they correlated their refrigerant heat transfer coefficient data during horizontal flow boiling. For a number of refrigerants, they found that

$$\Omega = \left(\frac{\rho_v}{\rho_l}\right)^{0.5}\left(\frac{\mu_l}{\mu_v}\right)^{0.1} = 0.551P_r^{0.492} \tag{2.72}$$

This parameter, Ω, is plotted for R-134a, R-12, and R-22, in Fig. 2.20. The reduced pressure expression predicts the property ratios from the Lockhart-Martinelli parameter within 5.3% over a wide range of reduced pressure. This simple relation has wide implications for predicting the two-phase multiplier for heat transfer. To predict the heat transfer coefficient for refrigerant data, only knowledge of the quality and pressure are required.

Moving further, the property relations in the Dittus-Boelter equation can also rearranged to yield the following:

$$h_l = 0.023\frac{k_l}{D}\left[\frac{GD(1-x)}{\mu_l}\right]^{0.8}\left(\frac{\mu_l c_{p_l}}{k_l}\right)^{0.4} \tag{2.73}$$

$$h_l = 0.023\frac{[G(1-x)]^{0.8}}{D^{-0.2}}\left(\frac{k_l^{0.6}c_{p_l}^{0.4}}{\mu_l^{0.4}}\right) \tag{2.74}$$

The last property term

$$Z = \left(\frac{k_l^{0.6}c_{p_l}^{0.4}}{\mu_l^{0.4}}\right) \tag{2.75}$$

is normalized with respect to Z for R-12 and is plotted for R-134a, R-22, and R-32/R-125 in Fig. 2.21. This term, Z, is a good parameter to aid in the selection of a good convective heat transfer fluid. For the four refrigerants examined, R-32/R-125 has the highest Z value followed by R-134a, R-22, and R-12.

2.5.2. Nucleate boiling heat transfer

It was also observed that nucleate boiling could occur simultaneously with evaporation along an extensive liquid-vapor interface. A key element to nucleate boiling during forced convection is the superheat required for the onset of nucleation. Bubbles form in imperfections or cavities at the tube wall. Bergles and Rohsenow [1964] developed an analysis based on an assumption that the tube wall has an infinite distribution of cavity sizes. Figure 2.22 shows a representation of one of the cavities. A hemispherical nucleus was assumed to protrude from the cavity mouth. The temperature distribution in the liquid surrounding the nucleus was assumed to be linear with the distance from the wall in the laminar sublayer as follows:

$$T = T_w - \left(\frac{q''}{k_l}\right)y \tag{2.76}$$

A value of superheat for the liquid at the apex of the nucleus was required for bubble growth. This condition was determined from the required superheat to initiate bubble growth of a vapor nucleus in an infinite medium (liquid) [Jabardo, 1991]. Figure 2.23 shows a schematic of this situation. Three equilibrium conditions were required for the bubble to be in stable equilibrium. These conditions were expressed in equation form for thermal, mechanical, and chemical equilibrium, respectively:

$$T_l = T_v = T \text{ [Thermal]} \tag{2.77}$$

$$P_v - P_l = \frac{2\sigma}{R} \text{ [Mechanical]} \tag{2.78}$$

$$g_l(P_{sat}, T) = g_v(P_{sat}, T) \text{ [Chemical]} \tag{2.79}$$

Figure 2.24 shows a qualitative plot of the stable equilibrium curve on a P-T diagram. Several conclusions can be made regarding the stable equilibrium curve. The pressure of the vapor inside the nucleus and the saturation pressure based on the liquid temperature are approximately the same. The vapor, therefore, is approximately at saturated conditions. The liquid is "superheated", which is a condition found for metastable equilibrium.

The superheating of the liquid is defined by the following expression:

$$\Delta T_{sat} = T_l - T_{sat}(P_l) \tag{2.80}$$

An expression was derived for the required superheat to initiate bubble growth by examining the Clausius-Clapeyron equation along the stable equilibrium curve:

$$\left.\frac{dP}{dT}\right|_{sat} = \frac{i_{lv}}{Tv_{lv}} \tag{2.81}$$

Integrating with both i_{lv} and v_{lv} assumed to be constant ($v_{lv} \approx v_v$), which is accurate for high pressures and low values of superheat,

$$\Delta P = \frac{i_{lv}}{v_{lv}} \ln(T)\Big|_{T_{sat}}^{T_l} \cong \frac{i_{lv}}{v_v} - \frac{(T_l - T_{sat})}{T_{sat}} = \frac{2\sigma}{R} \tag{2.82}$$

Rearranging,

$$\Delta T_{sat} = \frac{(2\sigma / R)T_{sat}}{\rho_v i_{lv}} \tag{2.83}$$

Returning to the Bergles and Rohsenow model, the condition for the bubble on the wall to grow was that the liquid temperature at the apex must be larger than the value for T_l determined from Eq. 2.83. Figure 2.25 is a plot of temperature versus distance from the wall and represents the situation mathematically. Each point on the liquid temperature curve given by Eq. 2.83 represents a bubble of a given size. Three different linear temperature distributions for the liquid are shown. Each of these temperature distributions has a fixed wall temperature given as T_W. Condition 1 shows a liquid temperature distribution such that no cavity is activated. The heat flux is too high for the given wall temperature. Condition 2 has a temperature distribution that intersects the curve of Eq. 2.83 at two points. For this situation, there is a range of cavities, from point A to point B, that are active. This situation has a lower heat flux for the same wall temperature as condition 1. Condition 3 is the limit condition for activation. This temperature distribution in the liquid intersects the curve of Eq. 2.83 at only one point. Hence, only one cavity is activated. When the linear temperature distribution from Eq. 2.76 is tangent to Eq. 2.83, the condition for nucleation becomes

$$\frac{dT_l}{dy} = \frac{dT_v}{dy} \tag{2.84}$$

Bergles and Rohsenow used a graphical technique to solve the governing equations described above. They developed an expression based on their results for the onset of boiling for water flowing in a tube as follows:

$$q''_{ONB} = 5.30P^{1.156}\left[1.80(T_w - T_{sat})_{ONB}\right]^{2.41/P^{0.0234}} \tag{2.85}$$

In this equation, the units for q", P, and T are W/m^2, kPa, and °C, respectively. The analysis of Bergles and Rohsenow is plausible only if the surface used has cavity sizes distributed over a wide range. They argued that commercially produced surfaces do produce this result and their analysis should be applicable to many real world applications. For special polished surfaces or for highly wetting liquids, a wide range of cavity sizes may not be present and the analysis described above should be used with extreme caution.

Sato and Matsumura [1964] developed a similar analytical treatment to that of Bergles and Rohsenow and developed the following expression for the onset condition:

$$q''_{ONB} = \frac{k_l i_{lv} \rho_v}{8\sigma T_{sat}}\left[(T_w - T_{sat})_{ONB}\right]^2 \tag{2.86}$$

Davis and Anderson [1966] solved Eq. 2.76, 2.83, and 2.84 analytically to obtain the critical radius, r_c, and wall superheat required to initiate nucleate boiling. The resulting expression for r_c for low surface tension and high pressures was

$$r_c = \sqrt{\frac{2\sigma T_{sat} k_l}{\rho_v i_{lv} q''}} \tag{2.87}$$

For the hemispherical bubble of the above analysis, the Davis and Anderson expression for the wall superheat is the same as Eq. 2.86. Data of Sato and Matsumura [1964], Davis and Anderson [1966], and Rohsenow [1962] agreed well with Eq. 2.86 for water over a wide range of pressure and heat flux.

Frost and Dzakowic [1967] examined the use of this equation for other liquids. They suggested an addition of a Prandtl number squared term to the equation as follows:

$$q''_{ONB} = \frac{k_l i_{lv} \rho_v}{8\sigma T}\left[(T_w - T_{sat})_{ONB}\right]^2 Pr_l^2 \tag{2.88}$$

Figure 2.26 is a plot of the wall superheat versus heat flux curve generated from Eq. 2.88 for R-12, R-134a, and R-22. For a saturation temperature of 41°F, R-134a had the lowest value of required superheat to initiate bubble growth for a given heat flux. Figure 2.27 shows the comparison between the wall superheat values of the Sato and Matsumura correlation and the Frost and Dzakowic correlation for various values of heat flux for R-134a. Refrigerants, in general, have lower required superheat values for onset of nucleation than water, as can be seen from Fig. 2.28.

Hsu [1962] developed a model of the criteria for the onset of nucleate boiling at a wall cavity based on transient conduction of liquid surrounding a bubble during its growth

and release process. He assumed a thermal boundary layer, δ_t, such that, for $y < \delta_t$, transport of heat occurred by diffusion. Above δ_t, turbulent heat transfer resulted in a uniform temperature of T_∞. The edge of the thermal boundary layer was assumed to be fixed. The wall temperature was assumed to be constant. The one-dimensional transient conduction equation was used with the following boundary conditions [Carey, 1992]:

$$\frac{\partial\theta}{\partial t} = \alpha_l\left(\frac{\partial^2\theta}{\partial y^2}\right) \tag{2.89}$$

with

$$\theta = 0 \text{ at } t = 0 \tag{2.90}$$

$$\theta = 0 \text{ at } y = \delta_t \tag{2.91}$$

and for $t > 0$,

$$\theta = \theta_w = T_w - T_\infty \text{ at } y = 0 \tag{2.92}$$

The obtained solution for Eq. 2.89 with the initial and boundary conditions listed above is

$$\frac{\theta}{\theta_w} = \frac{\delta_t - y}{\delta_t} + \frac{2}{\pi}\sum_{n=1}^{\infty}\frac{\cos n\pi}{n}\sin\left[n\pi\left(\frac{\delta_t - y}{\delta_t}\right)\right]e^{-n^2\pi^2\left(\alpha_l t/\delta_t^2\right)} \tag{2.93}$$

The steady state solution is a linear temperature distribution between the wall and the edge of the thermal boundary layer.

Hsu also developed some simple relations between the height of the bubble, b, the radius of the cavity, r_c, and the radius of the bubble, r_e. These were given as

$$b = 2r_c = 1.6r_e \tag{2.94}$$

Using Eq. 2.94 along with Eq. 2.83,

$$\frac{\theta_b}{\theta_w} = \frac{3.2\sigma T_{sat}(P_l)}{\rho_v i_{lv}\delta_t\theta_w(1 - 2r_c/\delta)} \tag{2.95}$$

Hsu postulated that the bubble would grow and the cavity site was active if the temperature of the liquid was equal to or greater than equilibrium superheat from Eq. 2.95. Mathematically, this is stated as

$$\frac{\theta}{\theta_w} = \frac{\theta_b}{\theta_w} \text{ at } y = b = 2r_c \tag{2.96}$$

There are minimum and maximum values of cavity size which the equilibrium value of superheat may be exceeded. These values are the intersection of Eq. 2.95 and, in this case, the steady-state temperature profile, given as

$$\frac{\theta}{\theta_w} = \frac{\delta_t - y}{\delta_t} \tag{2.97}$$

For the onset of nucleation, the curves intersect at only one point. Cavity sizes above $r_{c,max}$ will protrude into the turbulent saturated liquid region and condensation of this vapor may occur. Cavity sizes below $r_{c,min}$ will require too large a wall superheat and will not

grow. The values of $r_{c,min}$ and $r_{c,max}$ are determined by combining Eq. 2.95 and 2.97 to obtain

$$\begin{Bmatrix} r_{c,max} \\ r_{c,min} \end{Bmatrix} = \frac{\delta_t}{4}\left[1 - \frac{\theta_{sat}}{\theta_w}\{\pm\}\sqrt{\left(1-\frac{\theta_{sat}}{\theta_w}\right)^2 - \frac{12.8\sigma T_{sat}(P_l)}{\rho_v i_{lv}\delta_t\theta_w}}\right] \tag{2.98}$$

Values of the cavity radius at the onset of nucleation (one value of r_c) are shown in Fig. 2.29 for a constant wall superheat for R-134a as the convective heat transfer coefficient is varied. Figure 2.30 shows the critical cavity radius for onset of nucleation versus wall superheat for a constant heat transfer coefficient as wall superheat is varied.

The analyses above make a tacit assumption that a wide range of cavity sizes are available. If the cavity sizes are limited, a maximum cavity size exists, and the wall superheat can be recalculated using an expression from convective boiling in the absence of nucleate boiling. From the correlation developed in a later chapter, this expression is

$$\frac{h_{cb}}{h_l} = 1 + 1.925X_{tt}^{-0.83} = F \tag{2.99}$$

This is combined with an intermediate equation that Davis and Anderson [1966] determined for wall superheat as follows:

$$(T_w - T_{sat})_{ONB} = \frac{2\sigma T_{sat}}{\rho_{fg} i_{lv} r_c} + \frac{q''_{ONB} r_c}{k_l} \tag{2.100}$$

The resulting expression is

$$\Delta T_{ONB} = \frac{2\sigma T_{sat} k_l}{i_{lv}\rho_v r_{max}(k_l - Fh_l r_{max})} \tag{2.101}$$

Values for r_{max} are quite scattered in the literature. Brown [1967] measured the active size distributions for several surfaces and found that reasonable numbers of cavity radii exist below 4×10^{-4} in. Davis and Anderson [1966] found reasonable correlation of their data for r_{max} of 4×10^{-5} in. Collier [1981] suggests a value of 2×10^{-5} in on smooth metallic surfaces for refrigerants. Hino and Ueda [1986] and Jung and Radermacher [1989] used a value of 1.1×10^{-5} in to correlate data using a stainless steel tube. The value of r_{max} used in Eq. 2.101 can make a large difference in the value of superheat required for the onset of nucleate boiling. For a value of 1.1×10^{-5} in, a wall superheat of 11.99°F is required for R-134a for the conditions given in Fig. 2.30. For a value of 4×10^{-5} in, the wall superheat is 3.46°F. Using the Sato and Matsumura [1964] and Hsu [1962] analyses, the required wall superheat values are much less than 1.8°F. Figure 2.31 shows a comparison of wall superheat required for onset of nucleation versus maximum cavity size using Eq. 2.101, the Sato and Matsumura correlation, Eq. 2.86, and the Frost and Dzakowic correlation, Eq. 2.88 for R-134a.

Many nucleate pool boiling correlations have been developed over the past several decades. Initial correlations suggested by Chen [1966], such as the Forster-Zuber correlation [1955] for nucleate pool boiling, are difficult to calculate and require knowledge of data such as surface temperatures and surface tension, which are not always available. Their correlation is given as

$$h_{nb} = 0.00122\left[\frac{k_l^{0.79} c_{p_l}^{0.45} \rho_l^{0.49}}{\sigma^{0.5} \mu_l^{0.29} i_{lv}^{0.24} \rho_v^{0.24}}\right] \Delta T_{sat}^{0.24} \Delta P_{sat}^{0.75} \tag{2.102}$$

The lack of surface tension data may become even more important for correlating heat transfer coefficients for zeotropic mixtures.

Several theories regarding the mechanisms of nucleate boiling were also developed. This includes microconvection and thermocapillarity [Mikic and Rohsenow, 1969]. Mikic and Rohsenow developed a correlation based on the thermal boundary layer renewal concept. Their correlation was based on a combination of parameters relating the number of active cavity sites, the bubble departure diameter, and the frequency of bubble departure. The nucleate boiling heat flux in their correlation is given by

$$q'' = 2\sqrt{k_l \rho_l c_{p_l} \pi} \sqrt{f} \left(D_b\right)^2 n \Delta T \tag{2.103}$$

Expressions for each of the parameters were developed based on physical properties of the fluid, such as with the Forster-Zuber correlation [1955]. The Mikic-Rohsenow correlation also incorporated the effects of heat transfer surface characteristics in terms of varying heat flux versus wall superheat relations. Coefficients and exponents of the resulting terms varied based on each surface-fluid pair.

Two recent pool boiling correlations have been developed that are more accurate than some of the original correlations and are easier to evaluate. The Cooper correlation [1984] is based on reduced pressure, heat flux, and molecular weight and is of the same order of accuracy as the Forster-Zuber correlation, but is much easier to evaluate. Physical property relations were correlated as a function of reduced pressure for a number of different fluids and were replaced by the reduced pressure terms below. Molecular weight was added to collapse the results of many different fluids onto a single curve. The correlation is given as

$$h_{nb} = 55 q''^{0.67} M^{-0.5} P_r^{0.12} \left[-\log_{10} P_r\right]^{-0.55} \tag{2.104}$$

Units for the heat flux term must be in W/m^2.

The other recent correlation developed in the literature is that of Stephan and Abdelsalam [1980]. Dimensionless groupings were formulated and the resulting constant and exponents were curve fitted to the experimental data. Their correlation is given as

$$h_{nb} = 207 \frac{k_l}{D_b} \left(\frac{q'' D_b}{k_l T_{sat}} \right)^{0.745} \left(\frac{\rho_v}{\rho_l} \right)^{0.581} (Pr_l)^{0.533} \qquad (2.105)$$

where

$$D_b = 0.0146\beta \left[\frac{2\sigma}{g(\rho_l - \rho_v)} \right] \text{ with } \beta = 35° \qquad (2.106)$$

Both the Mikic and Rohsenow [1969] and Stephan and Abdelsalam [1980] correlations have expressions for bubble departure diameter. Recent studies have been conducted to see if these bubble diameters are accurate for nucleate flow boiling. Klausner et al. [1993] recently conducted a study for the nucleate flow boiling of R-113 over a nicrome heating surface. Their results showed that the measured departure diameter probability density functions were dependent on both mass flux and heat flux. As mass flux was increased, lower departure diameters resulted. As heat flux was increased, larger departure diameters resulted. The predicted bubble departure diameters from the correlation of Cole and Rohsenow [1969] for pool boiling overestimated the experimental data for moderate to high mean liquid velocities.

However, Kedzierski [1993] conducted visual and calorimetric measurements of R-11 and R-123 during nucleate flow boiling in a quartz tube and found that the bubble departure diameter was unaffected by both mass flux and heat flux. They found that the departure diameters predicted by the correlation of Fritz [1935], which is used in both Eq. 2.103 and 2.105 above, are quite accurate for flow boiling conditions for liquid Reynolds number up to 10,000.

Based on the conflicting results of the recent studies above, a conclusion cannot be drawn regarding the applicability of the bubble departure diameters for use in nucleate flow boiling situations. Many flow boiling studies have used pool boiling correlations to obtain reasonable accuracy. The Stephan-Abdelsalam correlation has been generally regarded as the most accurate pool boiling correlation available. However, the use of surface tension in the correlation can make evaluation difficult for newly developed refrigerants and refrigerant mixtures. The Cooper correlation [1984] gives similar accuracy and can readily be evaluated for all fluid if pressure and molecular weight is known.

Correlations were also developed for nucleate flow boiling based on a dimensionless parameter called the boiling number, Bo. It is defined as

$$Bo = \frac{q''}{Gi_{lv}} \qquad (2.107)$$

The boiling number is typically multiplied by the single-phase convective heat transfer coefficient to obtain the nucleate boiling portion of the heat transfer coefficient. This

method is the simplest used to correlate the nucleate boiling portion of the heat transfer coefficient in flow boiling, but also has its limitations. Additional parameters, such as transport properties, pressure, and molecular weight also affect nucleate boiling, and are not properly accounted for using the boiling number. In addition, the variation of the single-phase forced convective heat transfer coefficient and the nucleate boiling heat transfer coefficient versus pressure are opposite in nature. As pressure increases, the nucleate boiling heat transfer coefficient increases while the single-phase heat transfer coefficient decreases. These factors limit the accuracy of using the boiling number to account for the nucleate boiling effects on the heat transfer coefficient in flow boiling. However, as a first approximation, modifications to the boiling number can give fairly accurate results, as will be discussed in the next section.

2.5.3. Flow boiling heat transfer coefficient correlations

Initial methods were developed for convective boiling heat transfer along a liquid-vapor interface. These methods were based on the premise that the mechanism of heat transfer in forced convection was similar to single-phase forced convection [Chaddock and Noerager, 1966]. By applying the Reynolds analogy that relates the energy transport mechanism to momentum transport in convection, it was shown above that the ratio between the two-phase flow and the single-phase liquid heat transfer coefficients could be exclusively correlated by the Lockhart-Martinelli parameter, X_{tt}. The form of this correlation was

$$\frac{h_{TP}}{h_l} = f\left(\frac{1}{X_{tt}}\right) \tag{2.61}$$

Examples of correlations using this form are given in Table 2.3. The Dittus-Boelter correlation was used for the single-phase heat transfer coefficient.

It was also observed that nucleate boiling could occur simultaneously with evaporation along an extensive liquid-vapor interface. Pierre [1956] developed a model for the average heat transfer coefficient over a large quality change using Reynolds number and a modified boiling number as follows:

$$h_{TP} = A\left(Re_{lo}^2 K\right)^n \tag{2.108}$$

where

$$K = \frac{Ji_{lv}\Delta x}{L} \tag{2.109}$$

For an outlet quality less than 90% and $10^9 < Re_{lo}^2 K < 0.7x10^{12}$, A=0.0009 and n=0.5. For 11°F superheat at the exit and $10^9 < Re_{lo}^2 K < 0.7x10^{12}$, A=0.0082 and n=0.4. To

add nucleate boiling effects into the form of Eq. 2.61, Shrock and Grossman [1962] introduced the boiling number, Bo, as follows:

$$\frac{h_{TP}}{h_l} = 7400\left[\mathrm{Bo} + 1.5\times10^{-4}\left(\frac{1}{X_{tt}}\right)^{2/3}\right] \tag{2.110}$$

The Dittus-Boelter correlation was used for the single-phase heat transfer coefficient.

Rohsenow [1952] first proposed an additive model of the nucleate and convective boiling heat transfer coefficients, and Chen [1966] utilized this, based on the superposition of heat transfer coefficients, as follows:

$$h_{TP} = Sh_{nb} + Fh_l \tag{2.111}$$

where S is a suppression factor for nucleate boiling and F is the two-phase convective multiplier for heat transfer as defined on the right hand side of Eq. 2.61. The suppression factor was dependent on the liquid Reynolds number. Collier [1981] later curve fitted the suppression factor curves developed by Chen [1966] as follows:

$$S = \frac{1}{1+2.53\times10^{-6}\,\mathrm{Re}_l\,F^{1.25}} \tag{2.112}$$

F was curve fitted by Kenning and Cooper [1989] for $1/X_{tt} > 1.0$ as follows:

$$F = 1+1.8\left(\frac{1}{X_{tt}}\right)^{0.79} \tag{2.113}$$

The nucleate boiling heat transfer coefficient was evaluated using the Forster-Zuber correlation, defined in Eq. 2.102. The Dittus-Boelter correlation was used for the single-phase heat transfer coefficient. A recent modification to the Chen correlation [1966] is that of Bennett and Chen [1980]. The original Chen correlation was developed for water. To modify the correlation for other fluids, Bennett and Chen added a Prandtl number dependence to Chen's F parameter as follows:

$$F' = F\mathrm{Pr}_l^{0.296} \tag{2.114}$$

Jung and Radermacher [1989] recently used the form of Chen to develop their own model. Their correlation is given in Table 2.4.

Shah [1976] later utilized a different form by developing a generalized correlation using several databases from the literature which broke flow boiling into distinct regions: a nucleate boiling dominated regime, a bubble suppression regime where nucleate boiling and convective boiling are important, and a convective boiling dominated regime. The correlation was in graphical form and was evaluated by taking the larger of the three heat transfer coefficients calculated for the nucleate boiling, bubble suppression, and convective boiling regions. The nucleate boiling term was characterized by the boiling number while the convective boiling term was characterized by the convection number, Co, which is a

modified form of the Lockhart-Martinelli parameter defined in Eq. 2.70. Figure 2.32 shows the graphical form of the Shah correlation. Shah [1982] later put this correlation in equation form. The correlation is given in Table 2.4.

Recognizing that the boiling number could not accurately model the nucleate boiling term alone, Kandlikar [1990] developed a similar correlation that multiplied the boiling number by a fluid specific term which accounted for the different nucleate boiling effects that occurred from fluid to fluid. This can be described as a "greater of the two" (nucleate and convective boiling dominated) method. The correlation is also given in Table 2.4. Table 2.5 shows some examples of the fluid specific parameter of the Kandlikar correlation for various liquids.

The generalized correlations proposed by Shah and Kandlikar also accounted for the loss of tube wetting in horizontal flow for low mass fluxes. For wavy and stratified flows, part of the tube wall remains dry and there is a loss of convective heat transfer area, thereby decreasing the heat transfer coefficient. In these correlations, this loss of tube wetting was accounted for by introducing a Froude number based correction factor to the convective term.

Connecting the Chen and Shah methods is the form Kutateladze [1961] proposed, which is an asymptotic, power-type addition model for the nucleate and convective boiling components:

$$h_{TP} = \left[h_{nb}^{n} + h_{cb}^{n}\right]^{1/n} \tag{2.115}$$

For n equal to 1, the form becomes that of Chen. As n approaches infinity, the form becomes the "greater of the two" method similar to that of Shah and Kandlikar. This method was used by Churchill [1972] to correlate the transition between forced convection and natural convection heat transfer. Bergles and Rohsenow [1964], Steiner and Taborek [1992], and Liu and Winterton [1988] have developed correlations utilizing this form. Choices of n have ranged from 2 to 3. The Liu and Winterton correlation is shown in Table 2.4.

Figure 2.33 shows a comparison of the various two-phase multipliers for heat transfer for the Chen [1966], Jung and Radermacher [1989], Shah [1982], and Kandlikar [1990] correlations for R-134a. A wide variation of F can be seen as quality is varied. The Kandlikar two-phase multiplier is the lowest and the Jung and Radermacher value is the highest among the F parameters chosen. Although these F parameters vary, the overall heat transfer coefficients are similar. This is because the nucleate boiling and convective boiling heat transfer contributions vary quite a bit from correlation to correlation.

Table 2.4. Summary of heat transfer coefficient correlations from the literature

Source	Correlation
Shah (1982)	$h_{TP} = \varphi h_l$ For $Fr_l > 0.04$, $N = Co$; else $N = 0.38\ Fr_l\ Co$; For $N > 1$ $\varphi_{nb} = 230\ Bo^{0.5}$, $Bo > 0.3 \times 10^{-4}$ $\varphi_{nb} = 1 + 46\ Bo^{0.5}$, $Bo < 0.3 \times 10^{-4}$ $\varphi_{cb} = 1.8 / N^{0.8}$, for all N φ is the larger of φ_{nb} and φ_{cb}. For $0.1 < N \leq 1.0$ $\varphi_{bs} = F\ Bo^{0.5} \exp(2.74\ N^{-0.1})$ where $F = 14.7$ for $Bo \geq 11 \times 10^{-4}$; else $F = 15.43$ φ is the larger of φ_{bs} and φ_{cb}. For $N \leq 0.1$ $\varphi_{bs} = F\ Bo^{0.5} \exp(2.47\ N^{-0.15})$ φ is the larger of φ_{bs} and φ_{cb}.
Jung and Radermacher (1989)	$h_{TP} = Nh_{nb} + Fh_l$ $N = 4048 X_{tt}^{1.22} Bo^{1.13}$ for $X_{tt} \leq 1$ $N = 2.0 - 0.1 X_{tt}^{-0.28} Bo^{-0.33}$ for $1 < X_{tt} \leq 5$ $h_{nb} = 207 \frac{k_l}{D_b} \left(\frac{qD_b}{k_l T_{sat}} \right)^{0.745} \left(\frac{\rho_v}{\rho_l} \right)^{0.581} Pr_l^{0.533}$ $D_b = 0.0146\beta \left[\frac{2\sigma}{g(\rho_l - \rho_v)} \right]^{0.5}$ $F = 2.37 \left(0.29 + \frac{1}{X_{tt}} \right)^{0.85}$

Table 2.4. cont'd

Source	Correlation
Kandlikar (1990)	For $Co > 0.65$, $h_{TP} = 1058\ Bo^{0.7} F_{fl} + 0.6683\ Co^{-0.2}$ For $Co < 0.65$, $h_{TP} = 667.2\ Bo^{0.7} F_{fl} + 1.1360\ Co^{-0.9}$ If $Fr_l < 0.04$, then multiply convective term by $(25Fr_l)^{0.3}$
Liu and Winterton (1990)	$h_{TP} = Eh_l + Sh_{nb}\ h_{TP} = \left[(Eh_l)^2 + (Sh_{nb})^2\right]^{0.5}$ $E = \left[1 + x\left(\frac{P}{P_{crit}}\right)\left(\frac{\rho_l}{\rho_v} - 1\right)\right]^{0.35}$ $S = \left[1 + 0.055E^{0.1}(Re_l)^{0.16}\right]^{-1}$ $h_{nb} = 55\ P_r^{0.12}\ (-\log_{10} P_r)^{-0.55}\ M^{-0.5}\ q^{0.67}$

Table 2.5. Fluid specific parameter in Kandlikar correlation [1990] for various fluids

Fluid	F_{fl}
Water	1.00
R-12	1.50
R-22	2.20
R-134a	1.63

Figure 2.34 shows the contribution of the convective and nucleate boiling terms to the overall heat transfer coefficient for R-134a for a typical set of test conditions for the Kandlikar and Jung and Radermacher correlations. The Kandlikar correlation has similar contributions of the two components, while the Jung and Radermacher correlation is made up of mostly the convective term. The Jung and Radermacher correlation suppresses the nucleate boiling contribution at a fairly low quality, while the Kandlikar correlation maintains a significant contribution of the nucleate boiling term over the entire quality range. Overall, the average heat transfer coefficients are within 20% of each other. The contributions of these components, along with the suppression of the nucleate boiling component, need to be more closely examined experimentally.

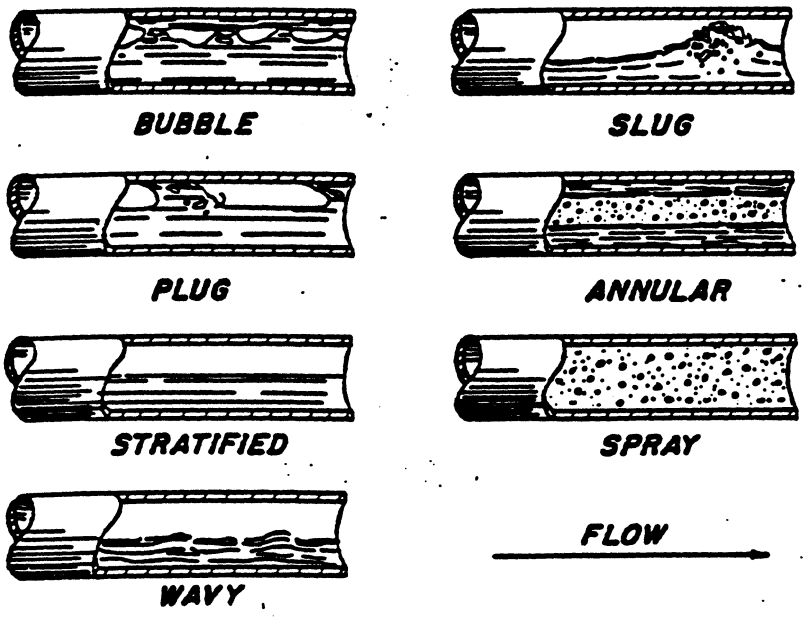

Figure 2.1. Horizontal two-phase flow patterns defined by Alves [Baker, 1954].

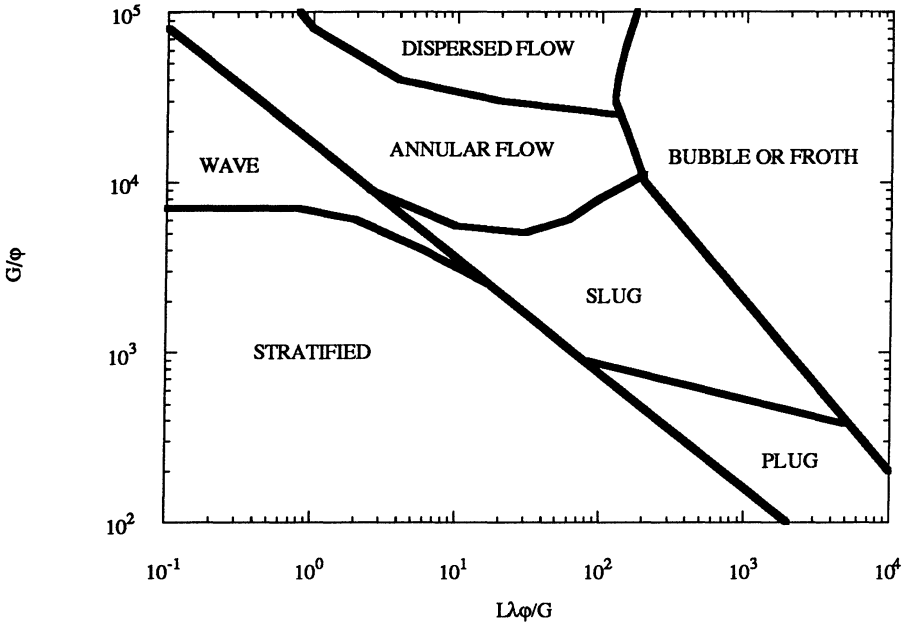

Figure 2.2. Baker map [1954].

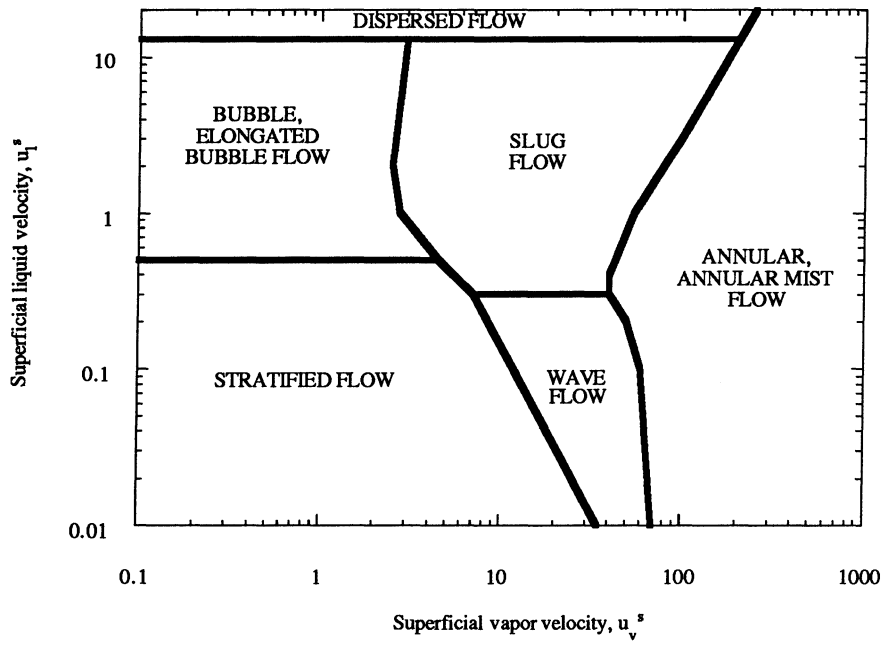

Figure 2.3. Mandhane map [1974].

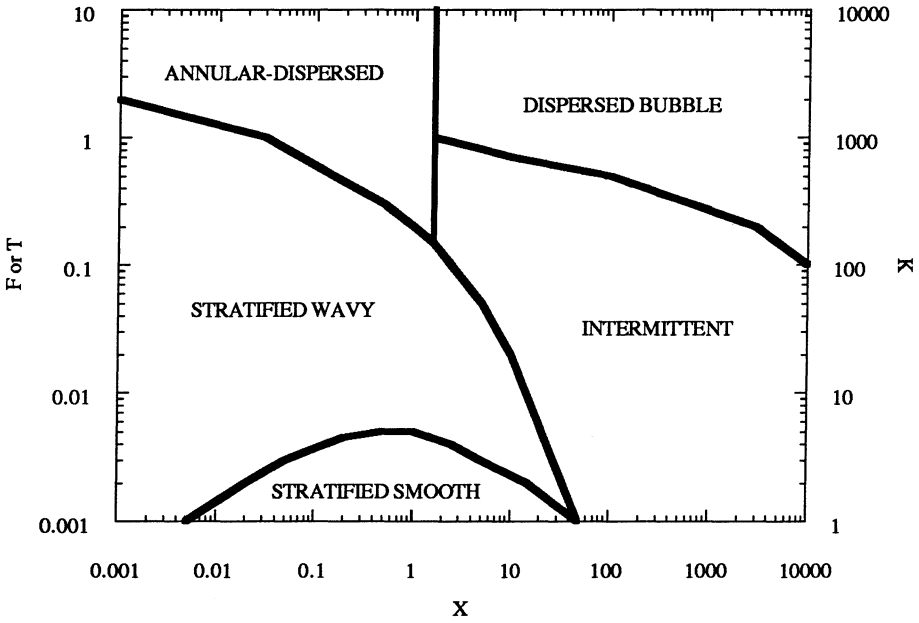

Figure 2.4. Taitel and Dukler map [1976].

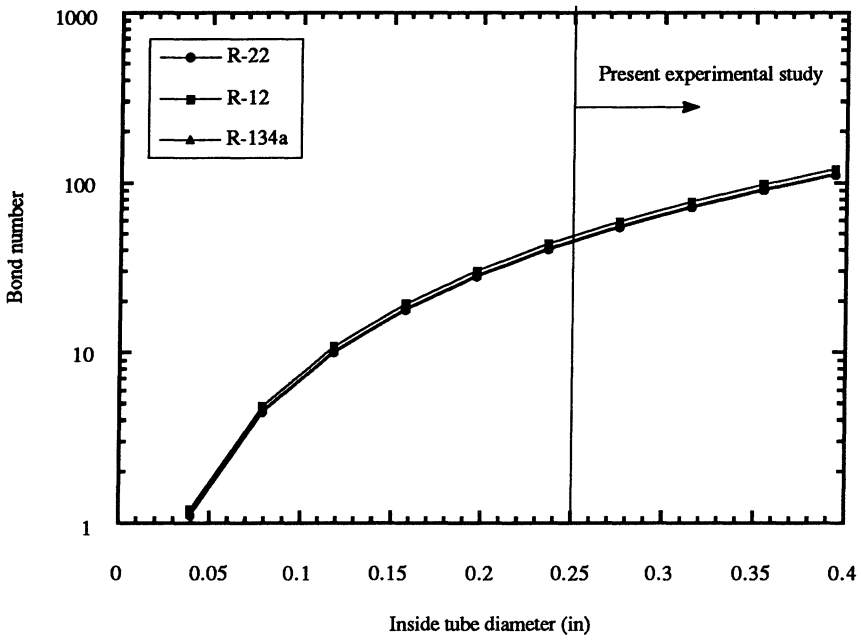

Figure 2.5. Bond number versus tube diameter for R-22, R-12, and R-134a. Saturation temperature, 41°F.

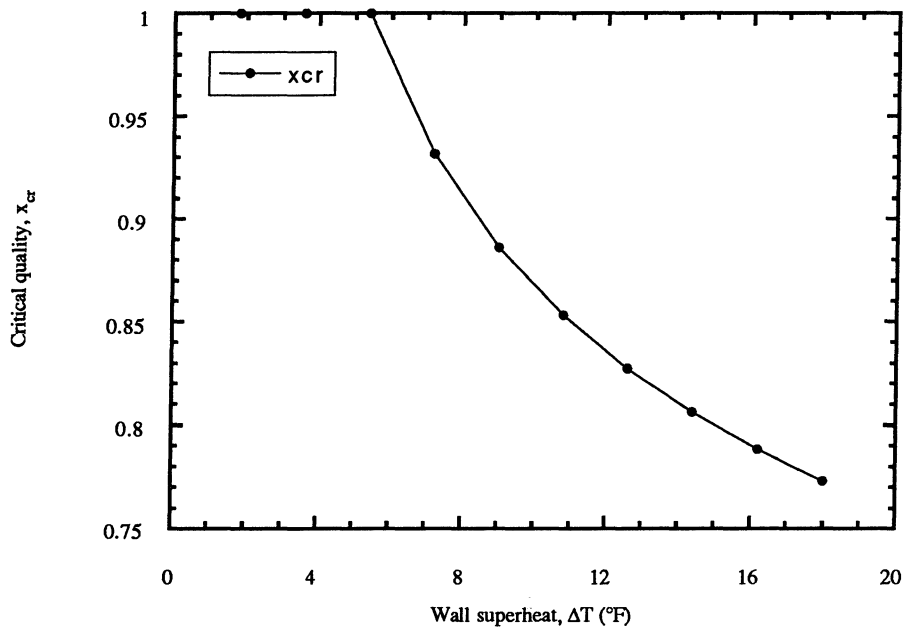

Figure 2.6. Critical transition quality for onset of mist flow versus mass flux for R-134a using Eq. 2.16. Mass flux, 225 klb_m/ft^2-hr. Saturation temperature, 41°F.

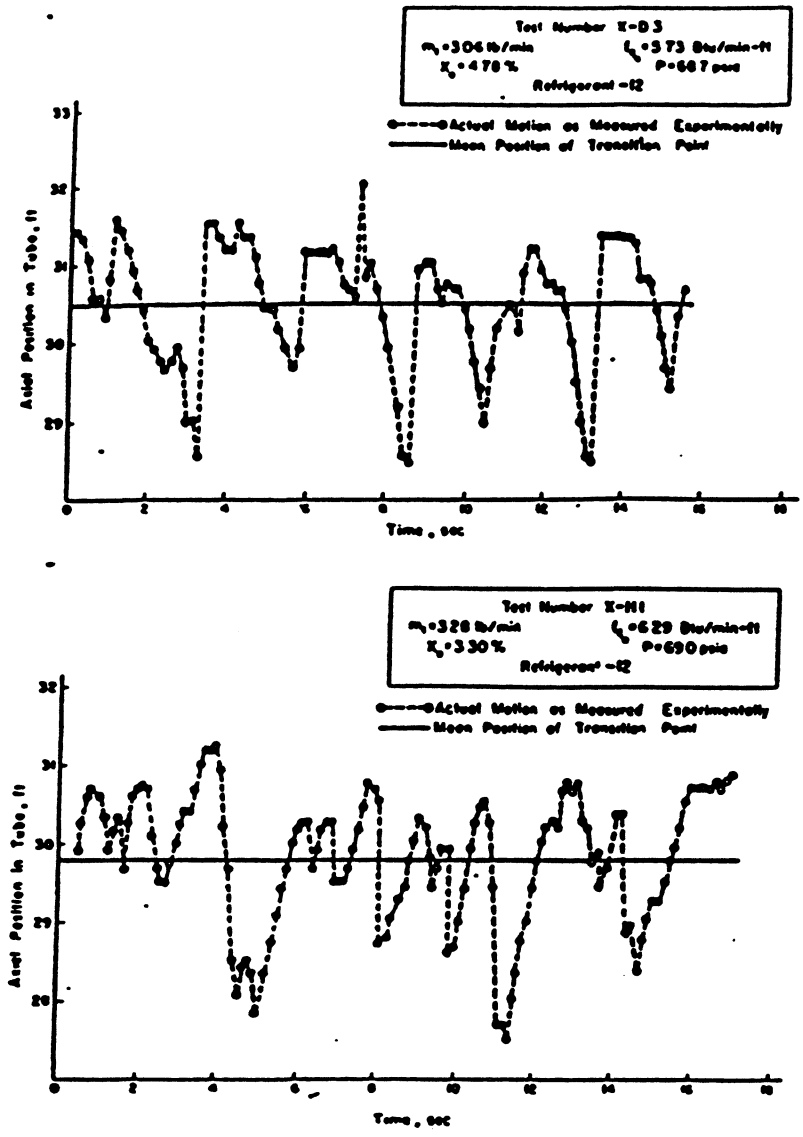

Figure 2.7. Mixture vapor transition point for steady flow conditions [Wedekind, 1971].

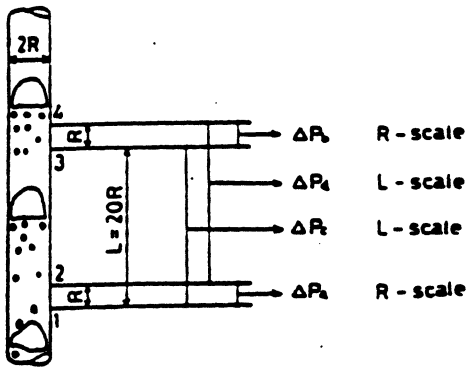

Figure 2.8. Matsui [1984] observation scales.

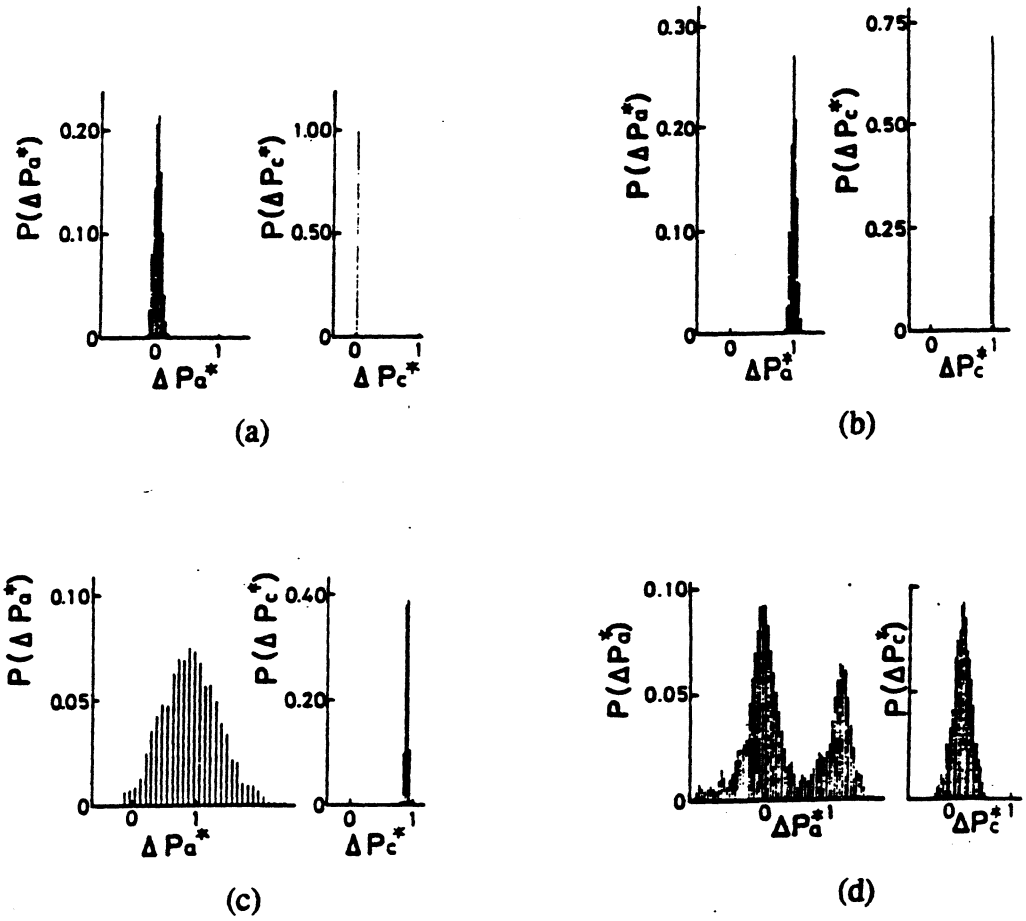

Figure 2.9. Probability density functions for various flow patterns [Matsui, 1984]: (a) bubble flow; (b) mist flow; (c) annular flow; (d) slug flow.

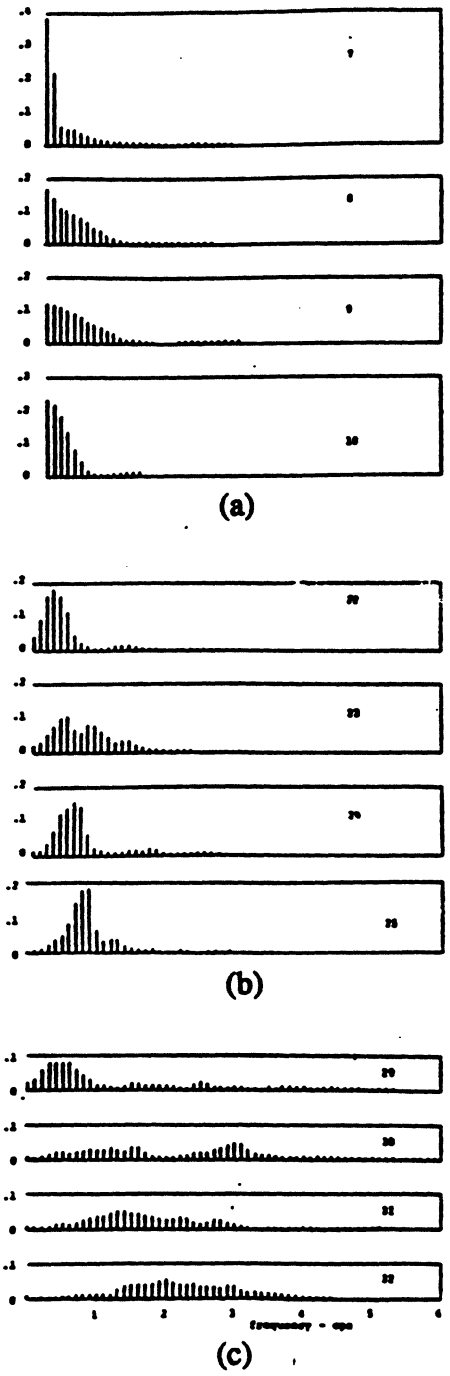

Figure 2.10. Hubbard and Dukler [1966] spectral distributions of wall pressure fluctuations characterizing flow regimes: (a) separated flow; (b) intermittent flow; (c) dispersed flow.

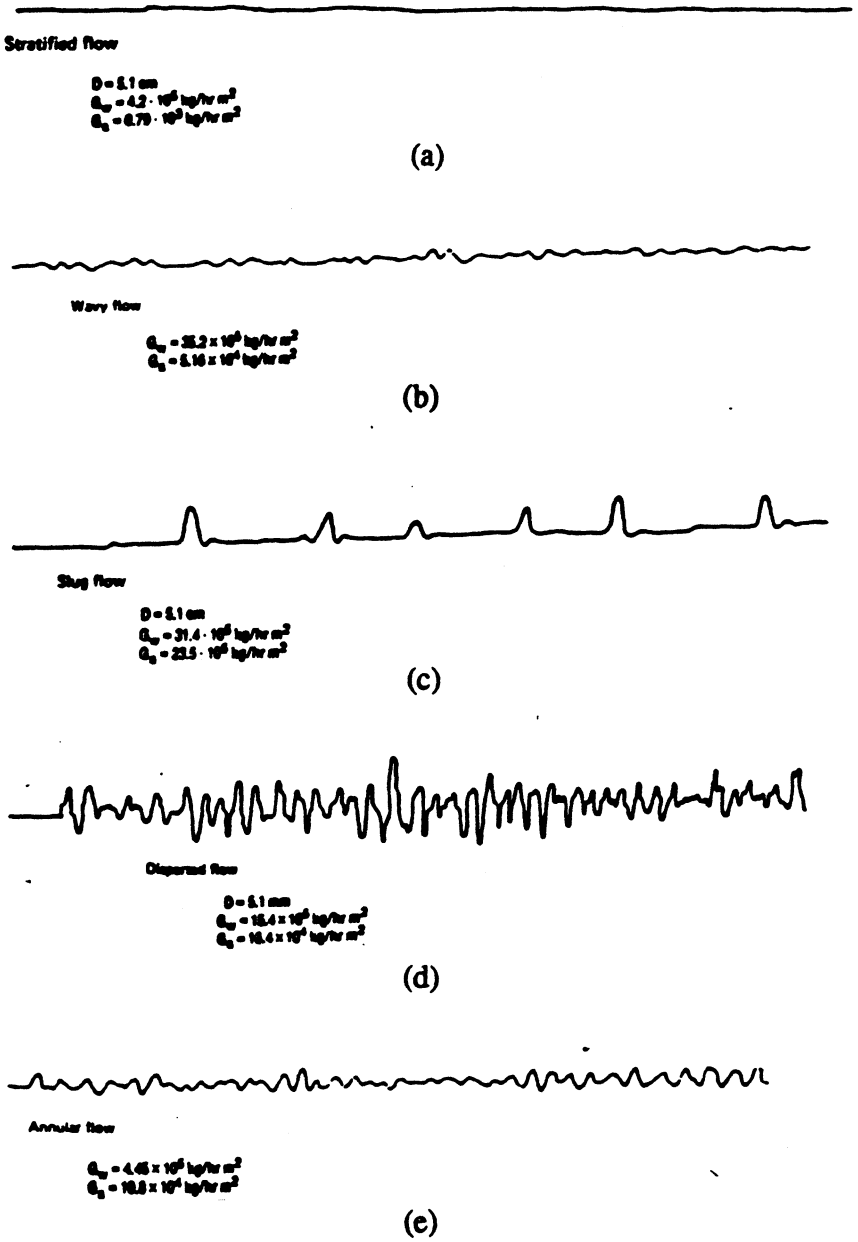

Figure 2.11. Weisman [1979] pressure drop traces: (a) stratified flow; (b) wavy flow; (c) slug flow; (d) dispersed flow; (e) annular flow.

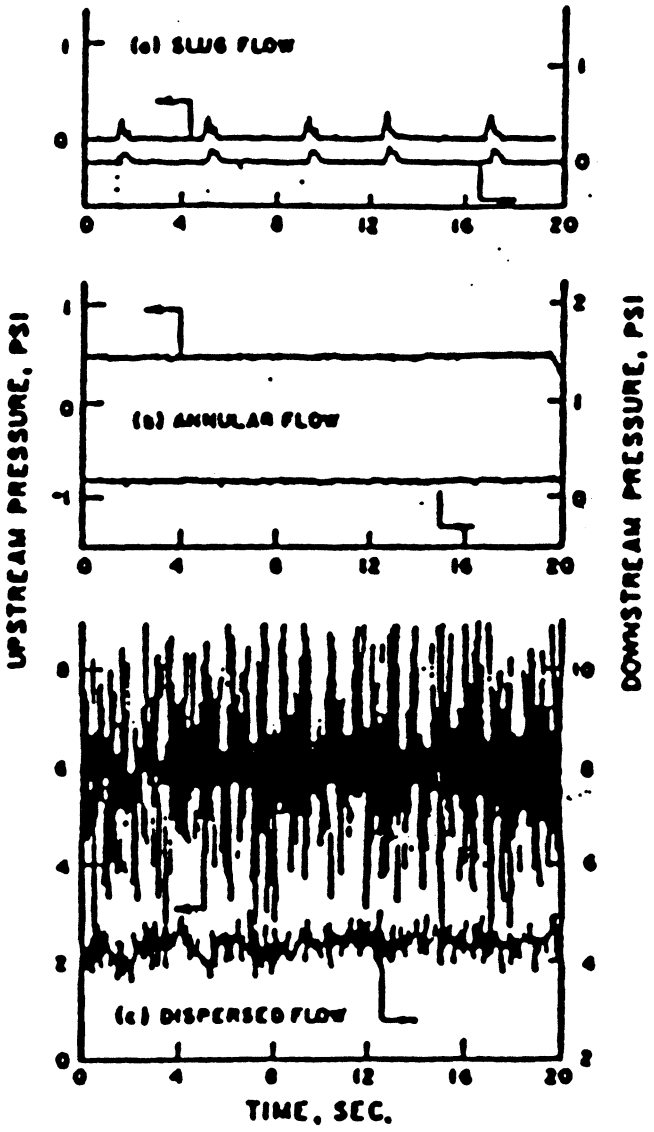

Figure 2.12. Damianides and Westwater [1988] pressure drop records.

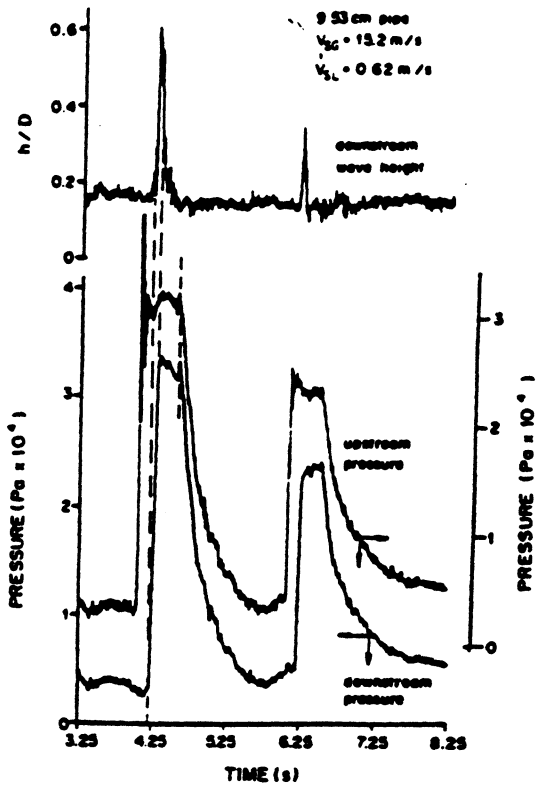

Figure 2.13. Comparison of slug and pseudo-slug pressure records [Lin and Hanratty, 1989]: (a) slug flow; (b) pseudo-slug flow.

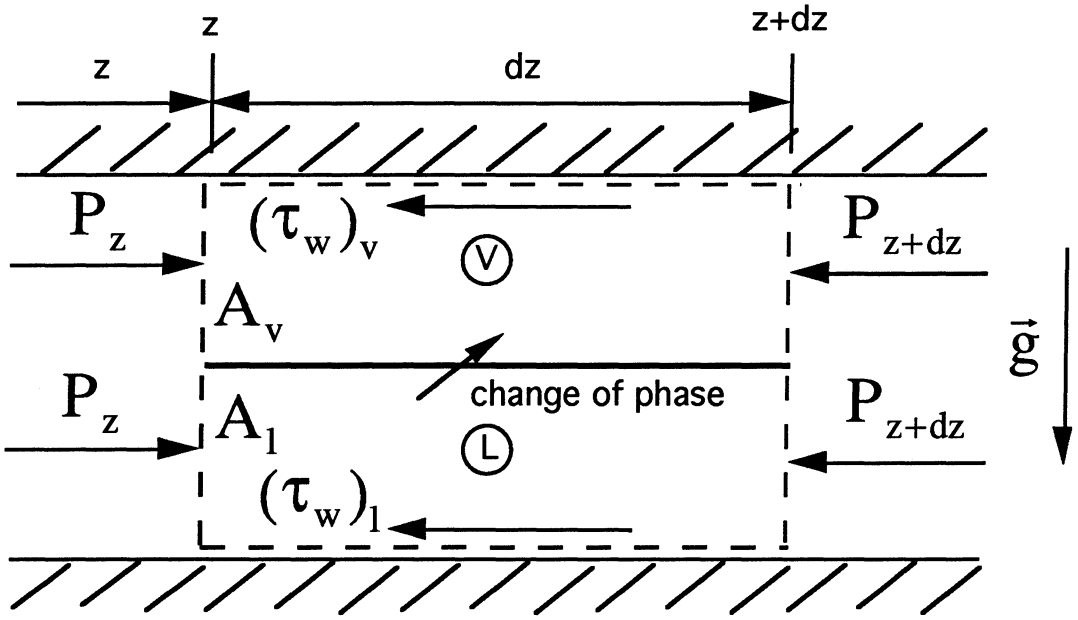

Figure 2.14. Schematic of horizontal, separated flow [Jabardo, 1991].

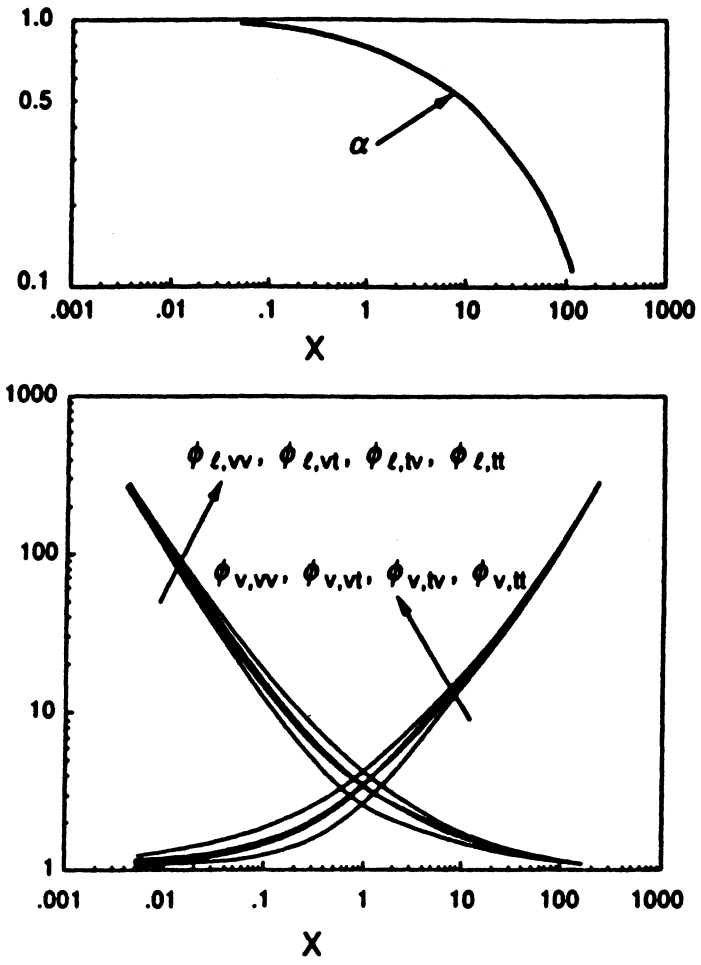

Figure 2.15. Void fraction and friction two-phase multipliers versus Lockhart-Martinelli parameter [Lockhart and Martinelli, 1947].

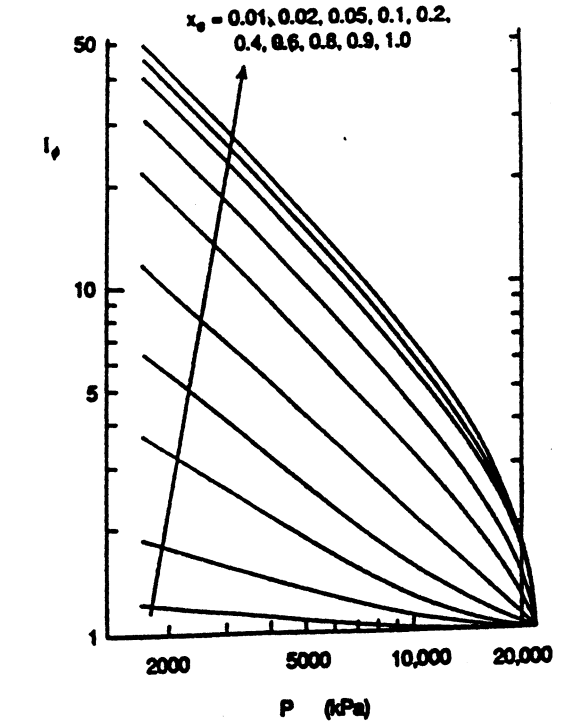

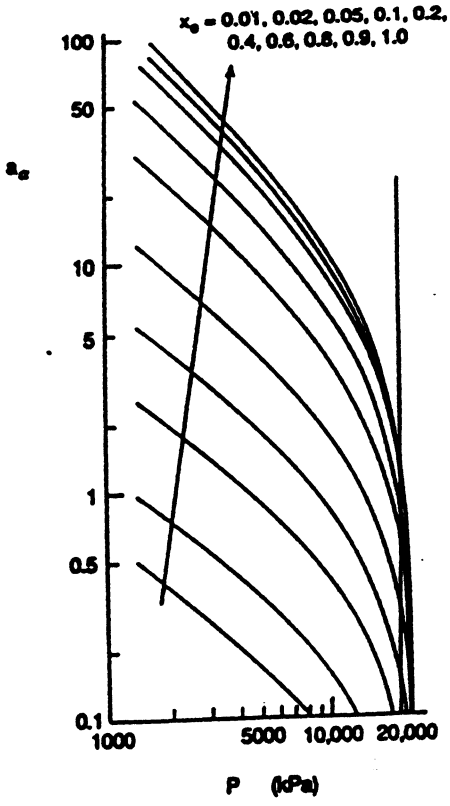

Figure 2.16. Martinelli-Nelson [1948] pressure drop parameters versus pressure.

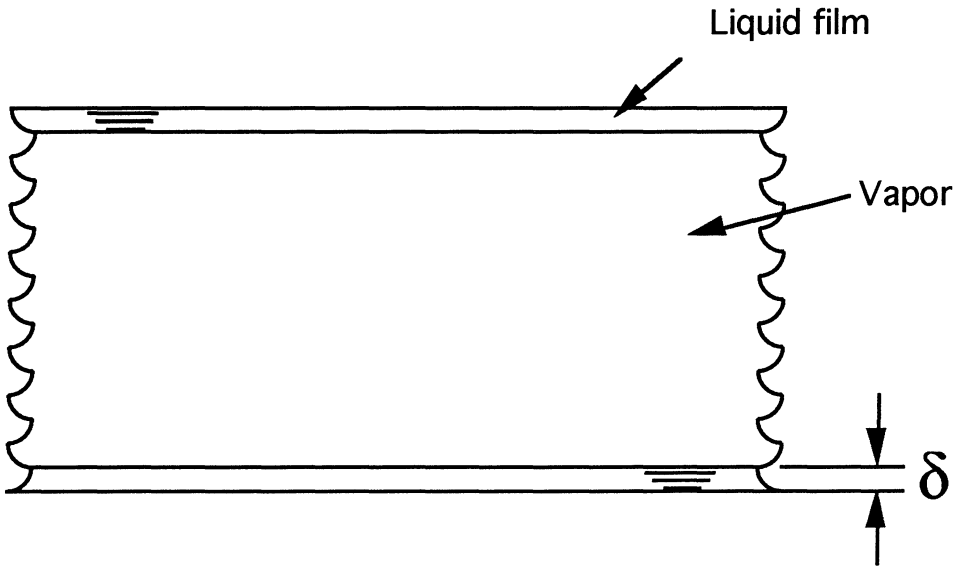

Figure 2.17. Schematic of annular flow for two-phase forced-convective heat transfer analogy [Jabardo, 1991].

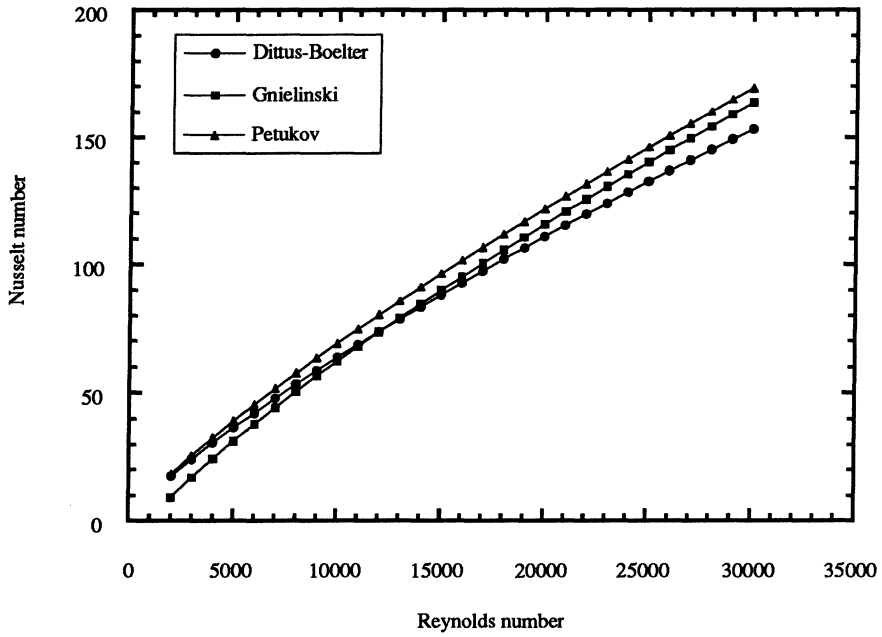

Figure 2.18. Turbulent, single-phase heat transfer correlations versus Reynolds number for R-134a. Saturation temperature, 41°F; Tube diameter, 0.430 in.

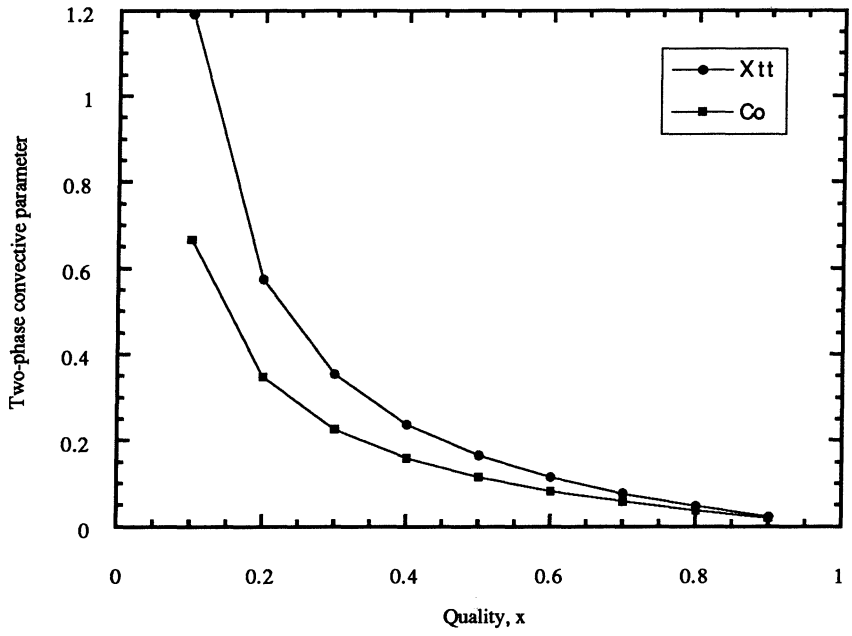

Figure 2.19. Lockhart-Martinelli parameter and convection number versus quality for R-134a. Saturation temperature, 41°F.

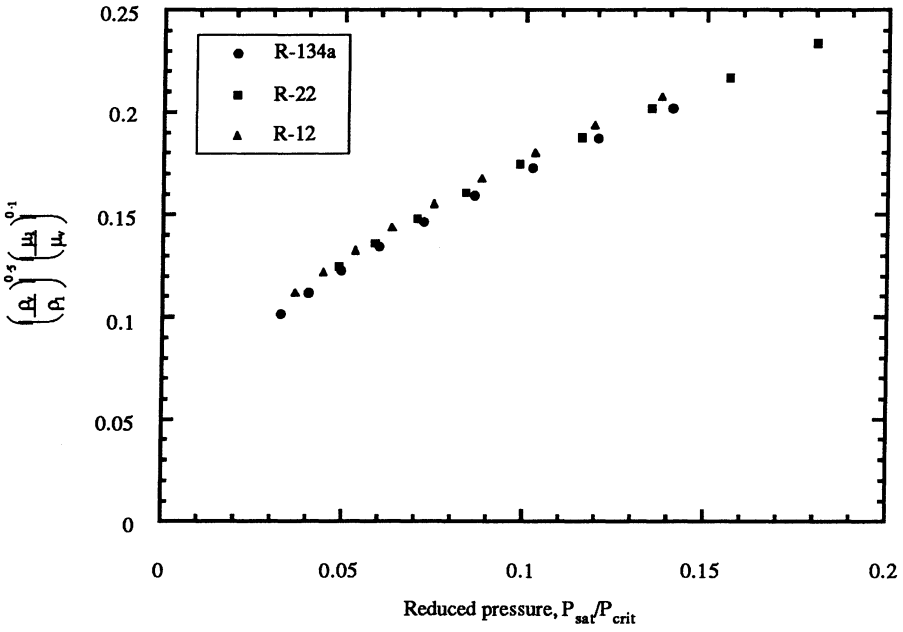

Figure 2.20. Ω versus reduced pressure for R-134a, R-22, and R-12.

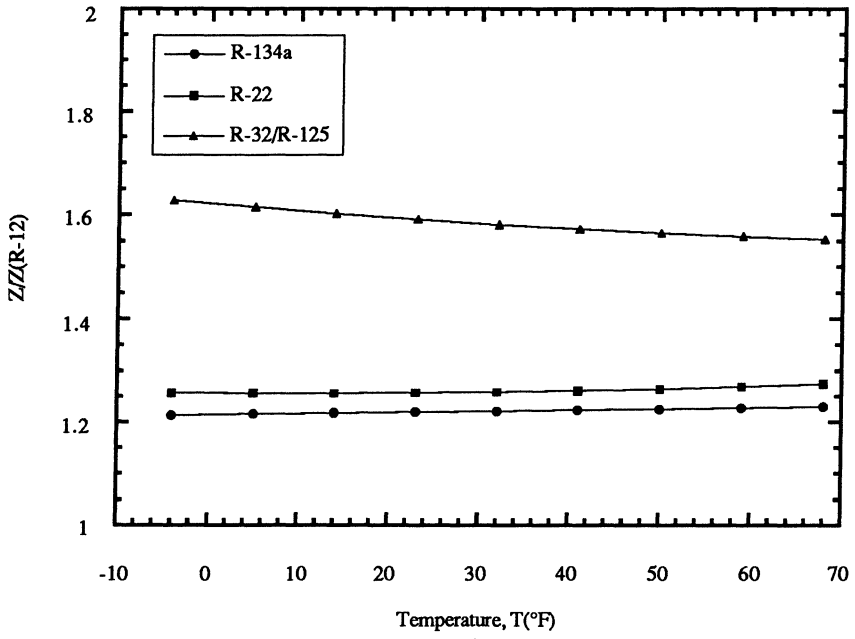

Figure 2.21. Z, the single-phase convective transport term for the Dittus-Boelter correlation, normalized with Z for R-12, versus temperature for R-134a, R-22, and R-32/R-125.

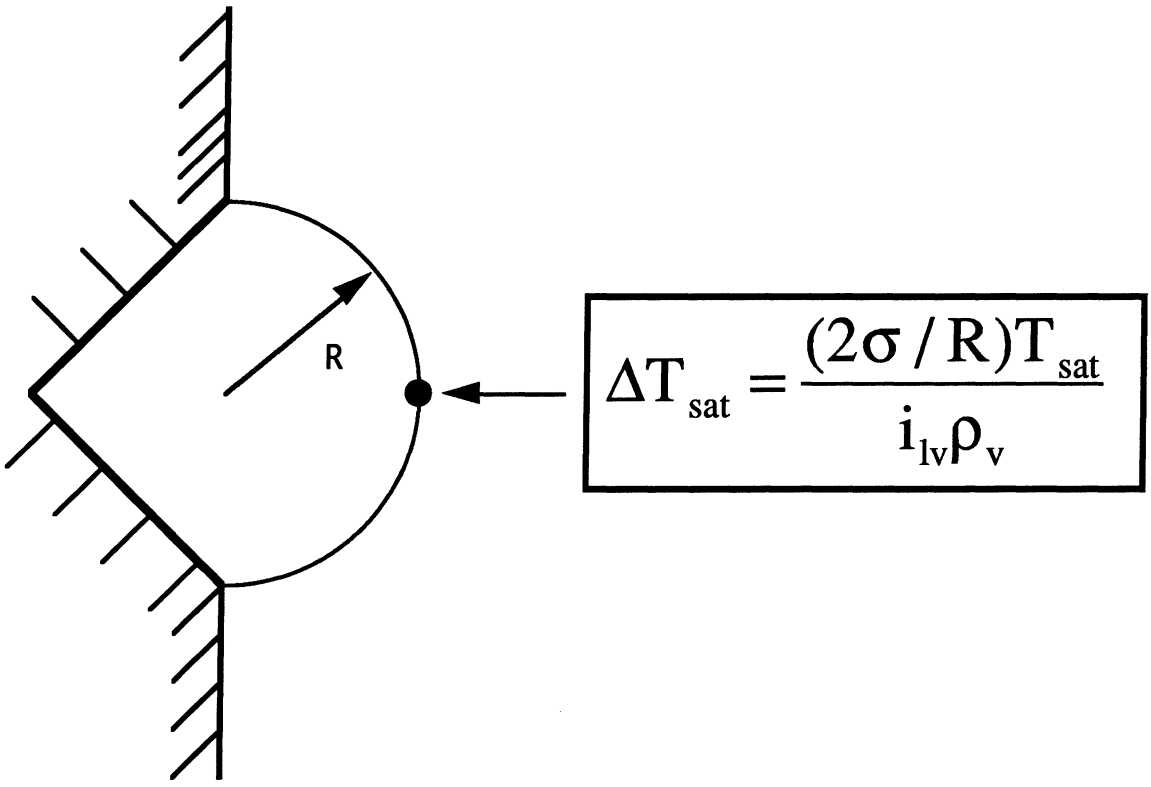

Figure 2.22. Wall superheat required for growth of a hemispherical bubble inside a wall cavity [Jabardo, 1991].

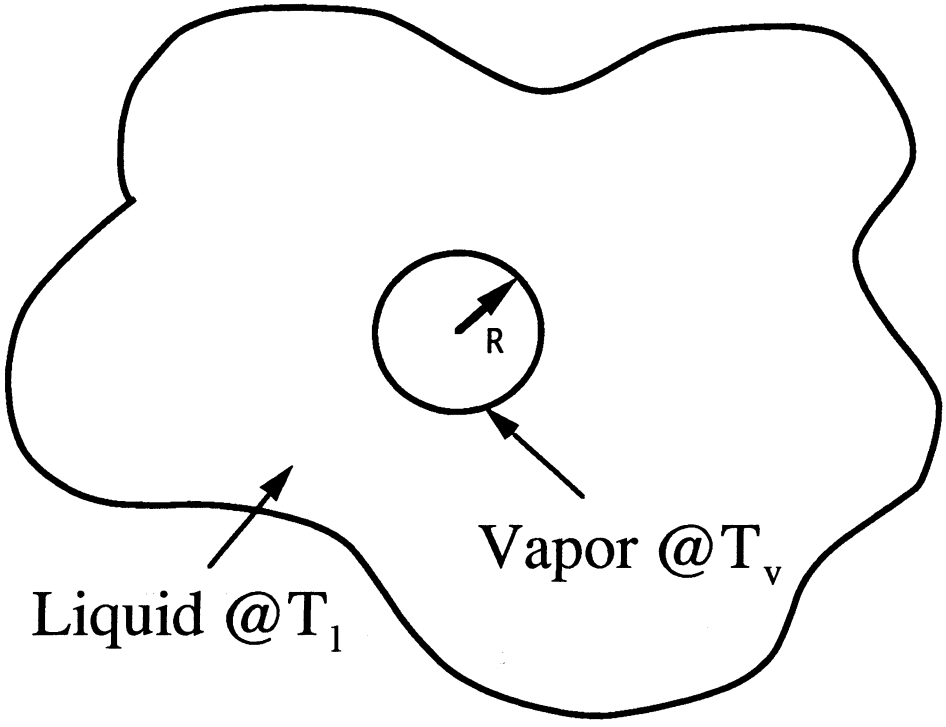

Figure 2.23. Vapor nucleus in an infinite medium (liquid) [Jabardo, 1991].

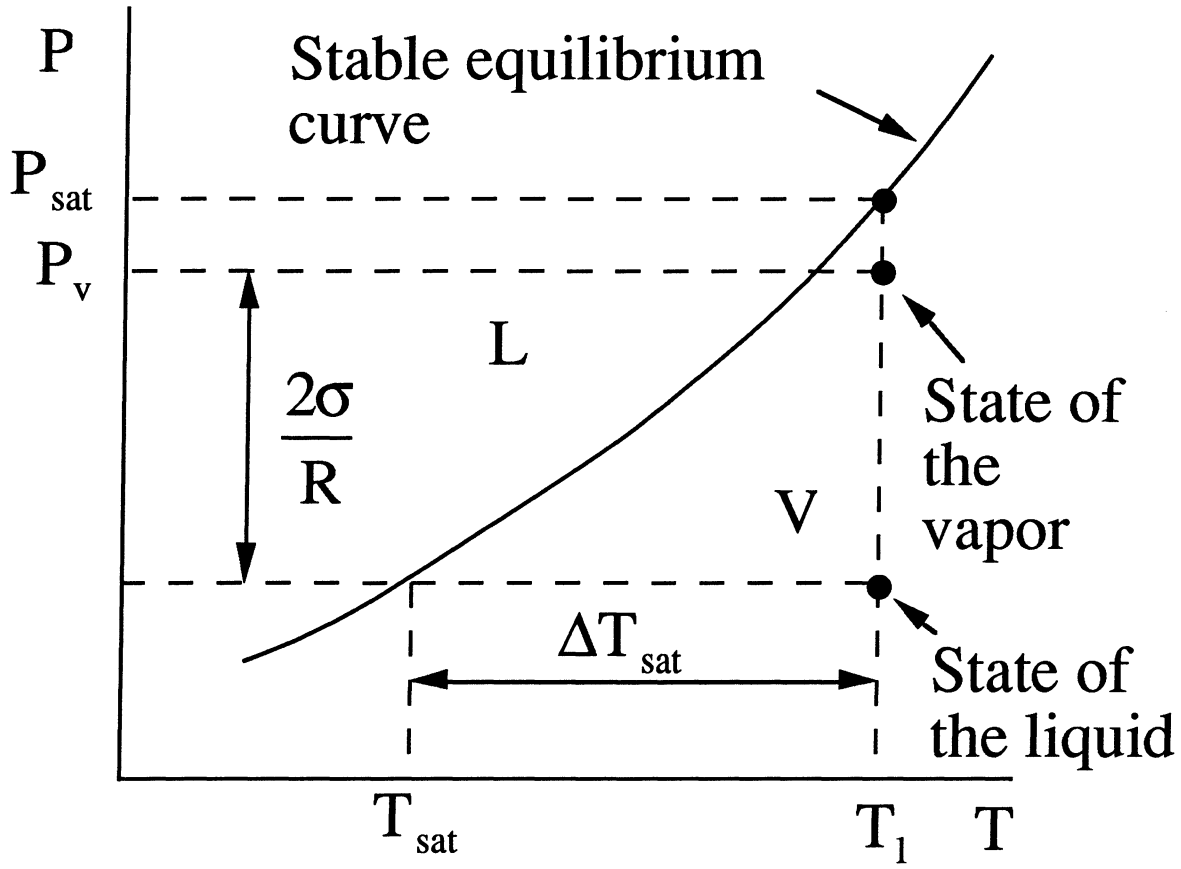

Figure 2.24. Stable equilibrium curve on a pressure-temperature diagram [Jabardo, 1991].

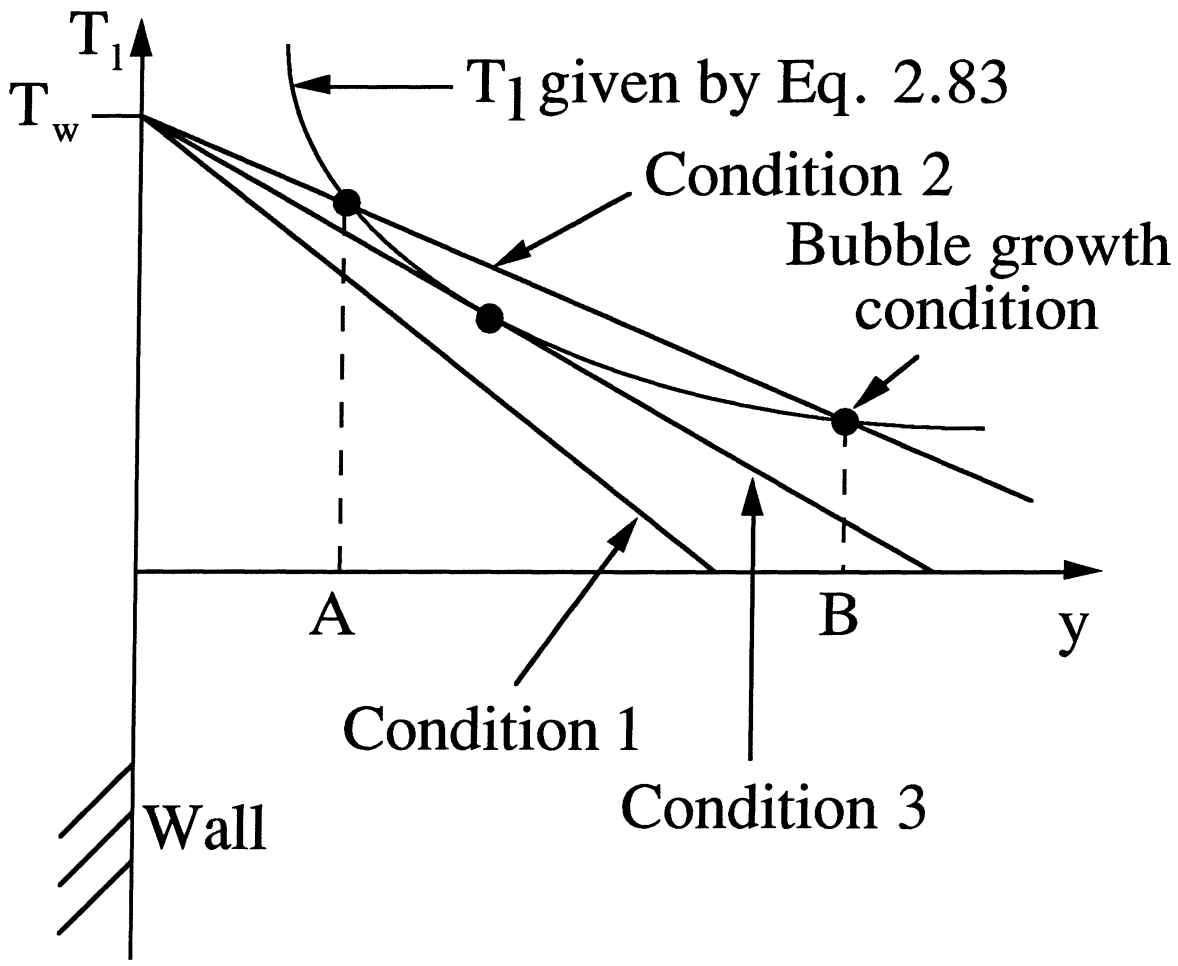

Figure 2.25. Temperature variation versus distance from a heated wall required for onset of nucleation [Jabardo, 1991].

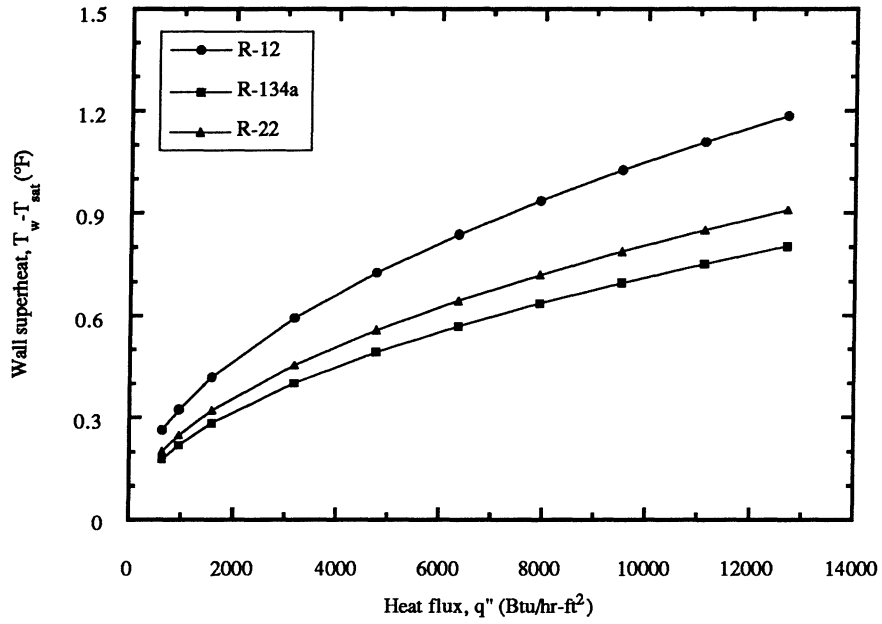

Figure 2.26. Wall superheat for onset of nucleation versus heat flux for R-12, R-134a, and R-22 using the Frost and Dzakowic correlation, Eq. 2.88. Saturation temperature, 41°F.

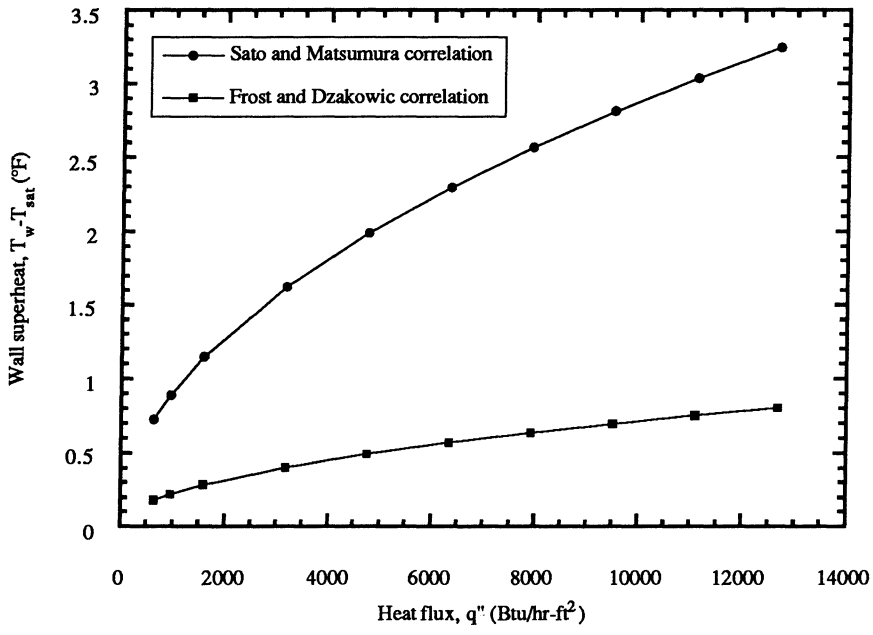

Figure 2.27. Comparison of wall superheat required for the onset of nucleation versus heat flux using the Sato and Matsumura correlation, Eq. 2.86, and the Frost and Dzakowic correlation, Eq. 2.88, for R-134a. Saturation temperature, 41°F.

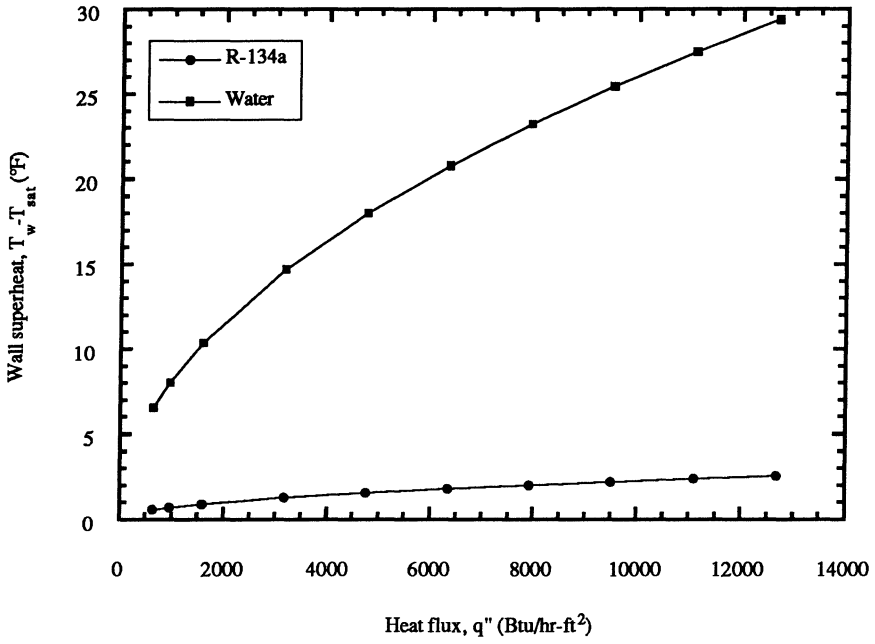

Figure 2.28. Comparison of the wall superheat required for the onset of nucleation versus heat flux for R-134a and water using Eq. 2.86. Saturation temperature, 68°F.

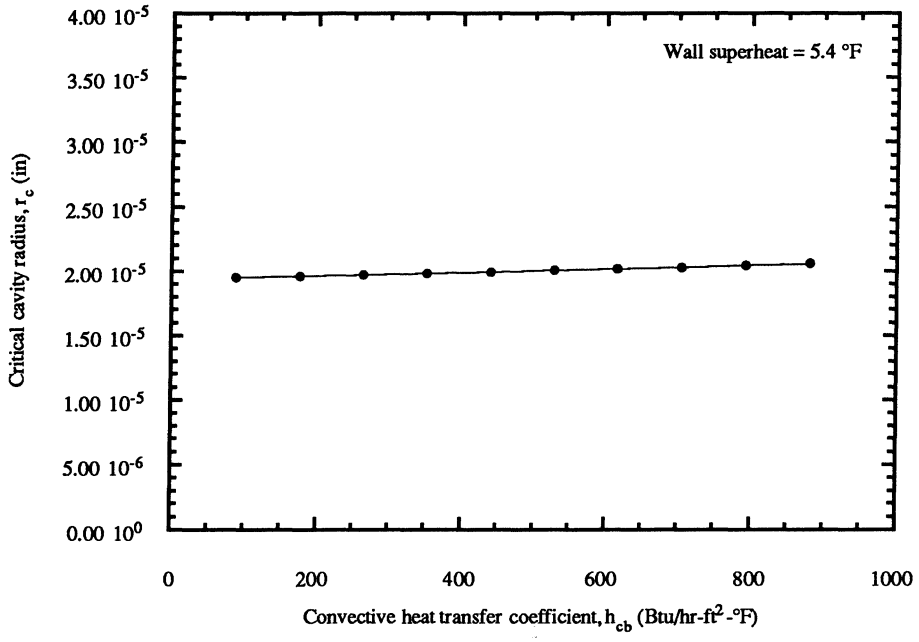

Figure 2.29. Critical cavity radius for onset of nucleation versus convective heat transfer coefficient for R-134a using the Hsu correlation, Eq. 2.98.

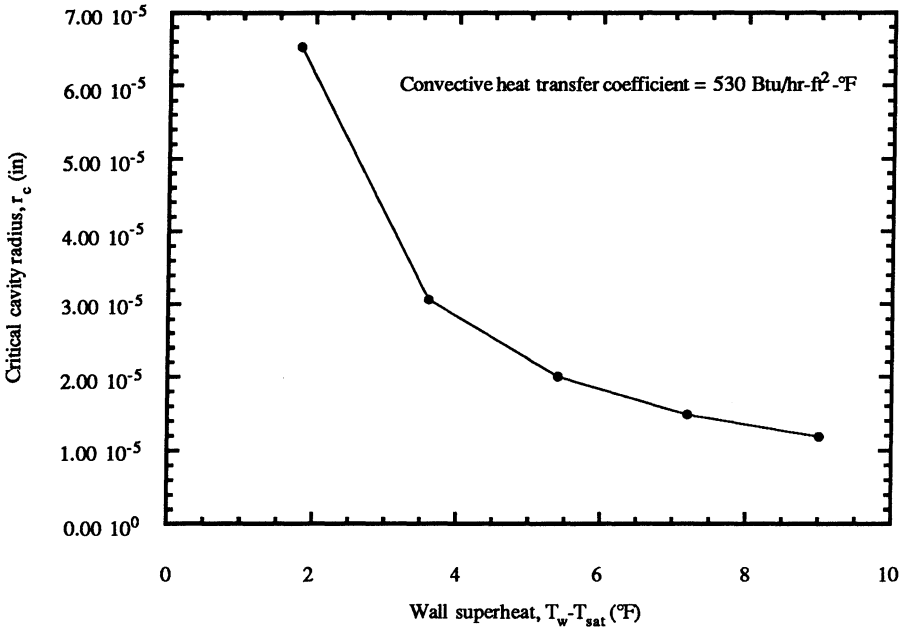

Figure 2.30. Critical cavity radius for onset of nucleation versus wall superheat for R-134a using the Hsu correlation, Eq. 2.98. Saturation temperature, 41°F.

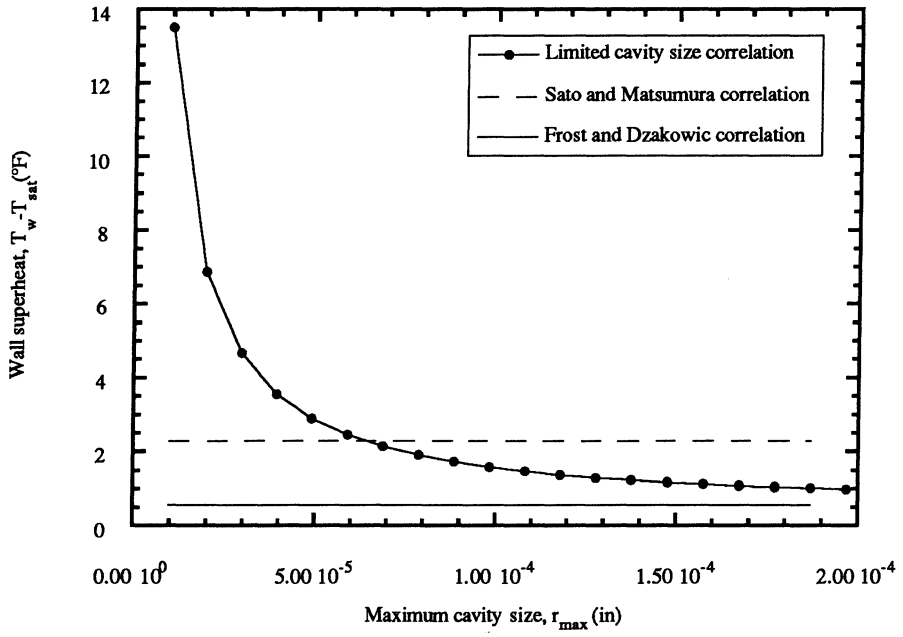

Figure 2.31. Comparison of wall superheat required for onset of nucleation versus maximum cavity size using the limited cavity size correlation, Eq. 2.101, the Sato and Matsumura correlation, Eq. 2.86, and the Frost and Dzakowic correlation, Eq. 2.88, for R-134a. Saturation temperature, 41°F; Heat transfer coefficient, 616 Btu/hr-ft^2-°F.

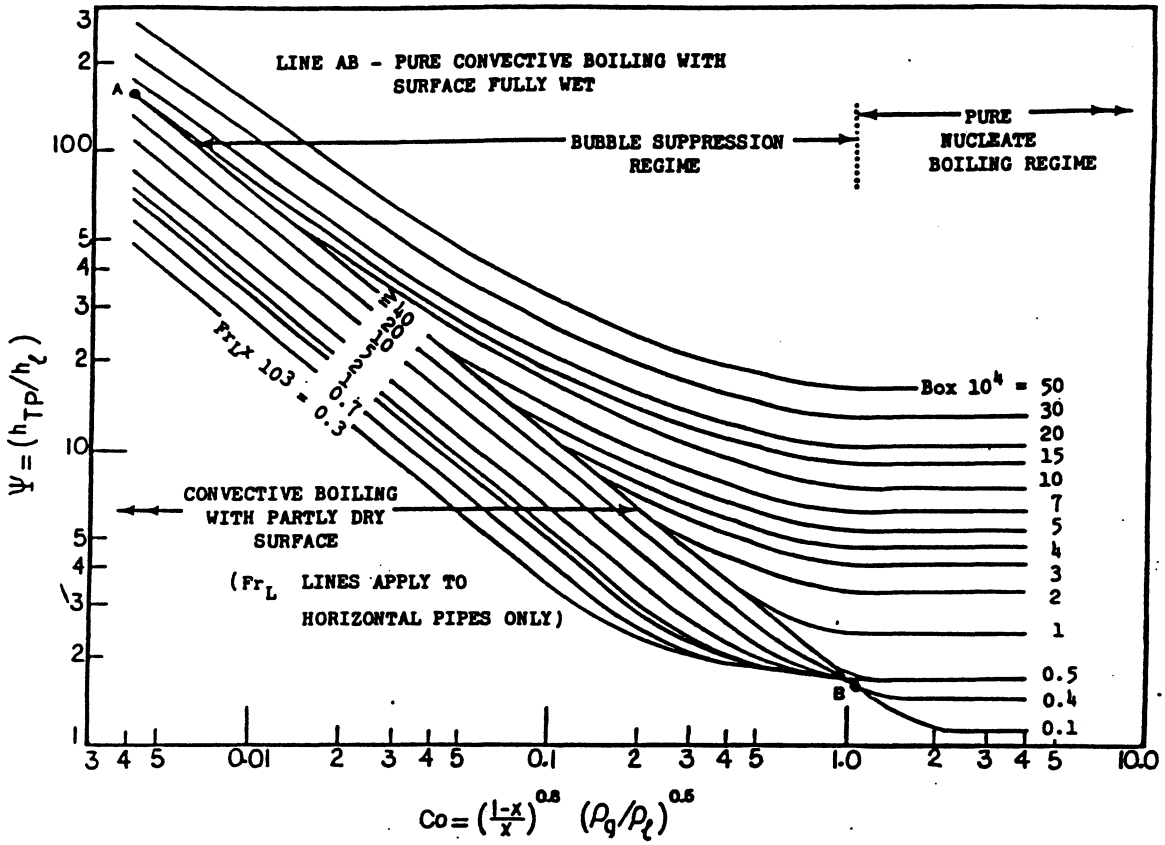

Figure 2.32. M.M. Shah [1982] heat transfer coefficient chart correlation.

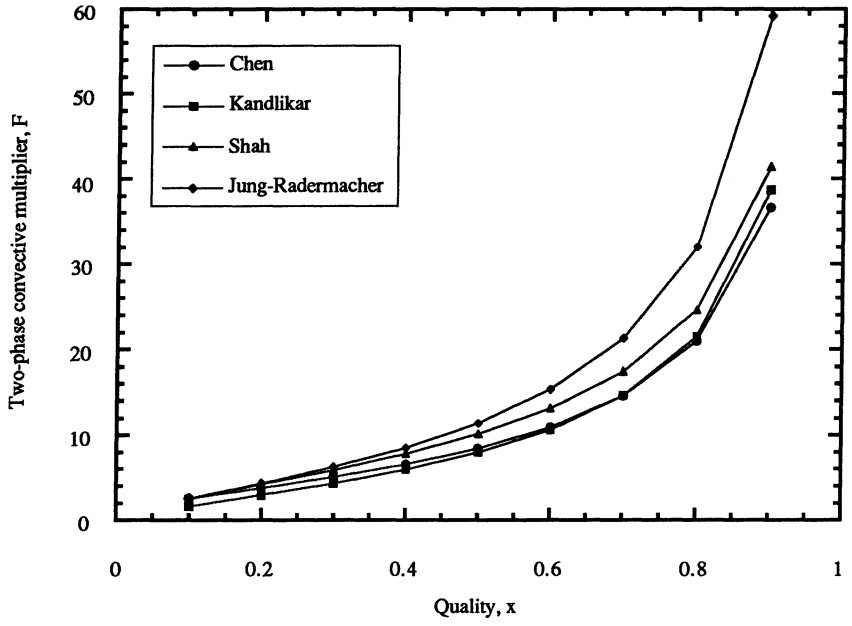

Figure 2.33. Two-phase convective multiplier, F, versus quality, x using the Chen [1966], Kandlikar [1990], Shah [1982], and Jung-Radermacher [1989] correlations. Saturation temperature, 41°F.

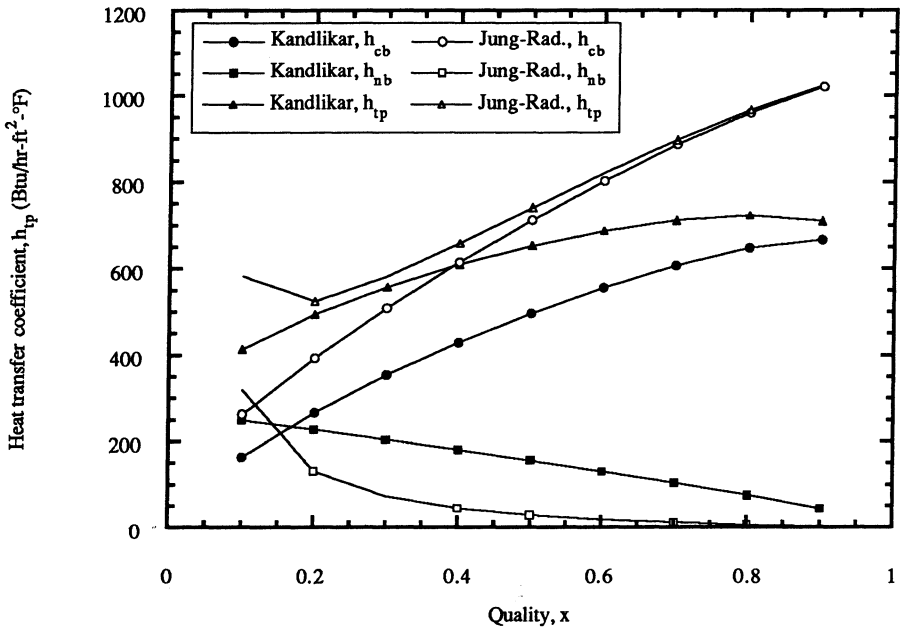

Figure 2.34. Comparison of contributions of convective and nucleate boiling terms in the Kandlikar [1990] and Jung-Radermacher [1989] correlations. Saturation temperature, 41°F; Tube diameter, 0.430 in; Mass flux, 225 klb_m/ft^2-hr.

CHAPTER 3. EXPERIMENTAL FACILITY AND PROCEDURES

In this chapter, the apparatus built and used in this investigation and the experimental and data-reduction procedures followed will be described. A single-tube evaporation test apparatus used to measure heat transfer coefficients and pressure drops will first be outlined. Because the apparatus was extensively documented in Wattelet [1990], Panek [1991], and Christoffersen [1993], only a summary of the main features of the facility will be given. The refrigerant flow loop, horizontal single-tube test section, chiller system, and data acquisition system will be described. System operation will then be summarized including system preparation, operating procedure, and data verification using single-phase liquid testing. Next, the test envelope will be listed. High flow rate heat transfer testing parameter ranges, low flow rate heat transfer testing ranges, high speed pressure measurements, and specialty testing will be discussed. Finally, data reduction procedures will be summarized. This will include heat transfer coefficient calculations, high speed pressure measurement spectral and statistical analysis, and experimental uncertainty analysis.

3.1. Experimental Test Facility

Four basic systems make up the experimental test facility used in this study: the refrigerant flow loop and instrumentation, the horizontal single-tube test section, the chiller system, and the data acquisition system. Major components of each section are outlined. Instrumentation including pressure, temperature, and flow transducers are discussed. The software and hardware components of the data acquisition system are briefly described.

3.1.1. Refrigerant flow loop and instrumentation

Figure 3.1 is a schematic of the experimental test facility. Copper tubing with an outside diameter of 0.5 in connected the various components in the refrigerant flow loop. Subcooled liquid was drawn from the condenser and moved through a Sporlan filter/dryer to a liquid pump. A variable-speed gear pump manufactured by Micropump was used to circulate the refrigerant around the loop, eliminating the need for a compressor and an expansion device found in vapor-compression refrigeration systems. This allowed testing capabilities in a pure refrigerant environment without the influence of the oil from the compressor. A section of bypass tubing circulating a portion of the refrigerant back to either the condenser or the gear pump was also constructed. This was used for fine control

of low refrigerant flow rates without which the speed of the gear pump would have been low enough to cause significant oscillations in the measured flow rate.

The refrigerant next flowed through a Coriolis-type mass flow meter manufactured by Micro-Motion to measure the flow rate. It used a vibrating U-tube to measure the flow. This flow meter had small orifices at the inlet and outlet which also aided in damping any oscillations in the flow. Two meters were mounted in parallel to measure flow rates over the range of conditions tested. A Micro-Motion D6 model was used to measure mass flow rates up to 60 lb_m/hr, and a D12 model was used to measure higher mass flow rates.

Next, the refrigerant moved to the preheater. A 20,000 Btu/hr preheater was used to control inlet qualities to the test section. The preheater was a 3-pass, horizontal, serpentine, copper coil wrapped with Kapton^{TM} heaters manufactured by Minco to provide heat input. The heaters were mounted longitudinally along the serpentine tube. The refrigerant inside the preheater flowed through an annulus with a 0.875 in outside diameter tube and a 0.375 in outside diameter tube mounted inside the larger tube using a steel helix coil. Heat input rates to the preheater were set using a variac and three sets of on/off switches, which were manually controlled. Three of the switches controlled 5000 Btu/hr each, and the other switch controlled 1700 Btu/hr. The variac controlled 3400 Btu/hr. A model PC5-49D watt transducer by Ohio Semitronics monitored the heat input rate of the preheater. This watt transducer generated output signals of 1 VDC for every 3400 Btu/hr of power. The accuracy of the watt transducer was ±0.2% of reading accuracy, which was 1600 Btu/hr. Figure 3.2 shows a schematic of the preheater.

After the preheater, the two-phase refrigerant moved into the horizontal, single-tube test section. Test sections have been both 4 and 8 ft in length. Surface-wrapped, variac-controlled heaters manufactured by Minco provided heat to the test section. The test section was instrumented with thermocouples to measure surface and fluid temperatures. An absolute pressure transducer measured the saturation pressure, and was, hence, an additional check on inlet saturation temperature. A differential pressure transducer measured the pressure drop through the test section. A more detailed discussion of the test section design is given in Sec. 3.1.3.

Absolute pressures were measured at several locations using strain-gage pressure transducers. BEC GWP5-46AW 0 to 50 psi and 0 to 300 psi pressure transducers were selected for the absolute pressure measurement before the preheater and before the test section. A Setra 0 to 1000 psi pressure transducer was used to measure refrigerant pressure at the outlet of the condenser. All pressure transducers were calibrated against a primary standard, a dead weight tester. Uncertainty of the pressure measurement after processing in the data acquisition system was estimated to be ±0.3% of the full scale

reading. Figure 3.3 shows a schematic of the pressure taps. The tap was first soldered to the tube in the proper position. Next, a 0.06 in hole was drilled through the test section wall. The hole was then de-burred using fine emery cloth. To connect the transducer to the pressure tap, 0.125 in o.d. copper tubing was used.

Fluid temperatures were measured using calibrated, type T (copper-constantan) thermocouples. The 0.06 in diameter probes extended into the center of the tube at various locations around the refrigerant loop. The probes were grounded to a stainless steel outer sheath and had 30 gauge instrument grade extension wires. All thermocouple probes were calibrated in a thermostatic bath against NIST traceable precision mercury thermometers. Uncertainty of the temperature measurements after processing in the data acquisition system was estimated to be ±0.36°F.

3.1.2. Chiller system

Heat was removed from the refrigerant using a series of condensers cooled by an ethylene glycol-water mixture from a chiller. Two shell and tube heat exchangers were originally used to condense and subcool the two-phase refrigerant. For low heat removal situations, the condensers were oversized and required a large amount of charge to fill the their unused portion. Valving was constructed so that only one condenser could be used at a time. However, each condenser still required approximately twenty pounds for the low flow rate cases, which was still too much charge for the highly expensive alternative refrigerants being used as potential R-22 replacements. A smaller, more efficient, counterflow, helical condenser was installed. This condenser was used for most refrigerant testing and reduced the charge from twenty pounds to between six and thirteen pounds. Figure 3.4 shows a schematic of the condenser arrangement. One drawback to using the smaller condenser was that charge control became a much more important issue. The larger condensers acted as both condenser and receiver, allowing a large number of tests to be run with one system charge. Using the smaller condenser, charge had to be added or subtracted more frequently to maintain subcooling at the pump entrance and preheater inlet.

Figure 3.5 shows a schematic of the chiller system. The antifreeze loop fluid consisted of a 50/50 solution of ethylene glycol and water. The antifreeze was drawn from a 50 pound storage tank to two Grundfos pumps which circulated the antifreeze to the various condensers. A thermocouple in the storage tank regulated the temperature of the antifreeze and was originally used to prevent the chiller from short cycling. The storage tank was designed so that the temperature varied within ±2.0°F of the set point. The addition of a false load heater in the antifreeze loop, which is described below, altered the

dynamics of the chiller system. In addition, this allowed the charge of antifreeze used in this loop to decrease dramatically below the 50 pound storage tank value, which in turn allowed more efficient use of the chiller system from a time standpoint.

The flow rate of the antifreeze loop was measured using a Flow Technology turbine flow meter. It was connected to a Flow Technology CA03 amplifier which produced a pulse output proportional to the flow rate. The viscosity of the antifreeze was highly dependent on temperature and affected the calibration of the turbine flow meter. The flow meter was calibrated at three different viscosities to account for this effect. Type T thermocouples were attached externally to the insulated, adiabatic sections of the antifreeze tubing at the inlet and outlet of the condensers. The heat removal rate of the condenser in use was monitored using a single-phase energy balance with the outputs from the thermocouples and the flow meter.

A chiller control panel monitored the set point temperature, turned the pumps in the antifreeze loop on and off, and set the maximum heat removal rate of the chiller by changing the expansion valve on the R-502 loop. Two separate thermostatic expansion valves allowed high capacity heat removal rates at high temperatures and lower capacity heat removal rates at lower temperatures. Heat removal rate decreased exponentially as the set point temperature of the antifreeze loop decreased.

The antifreeze loop exchanged its heat through the evaporator of the R-502 loop. The R-502 chiller had a maximum heat removal rate of 60,000 Btu/hr. The chiller heat was removed using the municipal water supply.

The chiller system's heat removal rate was matched with the heat input to the chiller system to maintain steady-state conditions in the test section. This was accomplished by using a false load heater in the antifreeze loop and maintaining an artificially low set point temperature for the chiller system which kept the compressor running at all times. An example describes how the process works. A temperature of 41°F in the test section is desired with 7000 Btu/hr of power added to the preheater and test section. The chiller set point temperature is set to 5°F and the actual temperature in the storage tank is 14°F. At this point, the chiller system can remove approximately 13,650 Btu/hr of heat based on load curves generated for the particular compressor in use. If no heat is added to the false load heater, the temperature of the refrigerant in the test section will drop. The false load heater is set to approximately 6650 Btu/hr to maintain a constant temperature in the test section. Adding additional heat will cause the antifreeze temperature and, hence, the refrigerant temperature in the test section to rise.

3.1.3. Horizontal, single-tube test sections

Four test sections were used to obtain heat transfer and pressure drop data. Table 3.1 gives a summary of the four test section dimensions. All copper tubes were commercially manufactured. Factory specifications were used for all diameter dimensions listed in Table 3.1. Calipers were used to check these dimensions at several different locations. Based on this measurement, the uncertainty of the inside diameter was estimated to be ±0.00315 in. Detailed descriptions of test sections 1 and 2 can be found in Wattelet [1990] and Panek [1992]. Test sections 3 and 4 will be described herein.

Table 3.1. Test section dimensions

Test section	Inside diameter	Wall thickness	Length
1	0.402 in	0.049 in	8 ft
2	0.277 in	0.049 in	8 ft
3	0.430 in	0.035 in	4 ft
4	0.305 in	0.035 in	4 ft

Heat input was provided to the test section using variac-controlled, surface-wrapped heaters. The silicone-rubber, surface-wrapped heaters manufactured by Minco had an aluminum foil backing attached to ensure even heating. Table 3.2 gives a more detailed description of the heaters used for the various test sections mentioned above. The heat rate was measured by an Ohio Semitronics Model PC5-49D watt transducer with a range of 0 to 17,000 Btu/hr. Output of the transducer is 0-10 VDC, and the uncertainty of the measurement is ±0.2% of the full scale reading. To reduce heat gain from the environment, the test section was covered with 2.0 in of foam insulation.

Table 3.2. Test section heater information

Test section	Dimensions, in x in	Resistance, Ohms	Number of heaters	Maximum power input, Btu/hr
1	1.5 x 12.0	42.8	8	8435
2	0.5 x 14.4	145.0	9	2491
3	0.375 x 18.0	126.2	12	4279
4	0.375 x 18.0	87.0	9	4668

Sixteen, thirty-gage, type T (copper-constantan) thermocouples were soldered in 0.015 in deep grooves cut longitudinally along the outside tube wall of the test section to measure the surface temperatures. Four thermocouples were mounted 90 degrees apart circumferentially at four different axial locations spaced evenly along the test section. Figure 3.6 shows the location of these thermocouples, and Fig. 3.7 shows how the heaters were mounted over the thermocouples. A thin, 0.003 in layer of copper tape was wrapped around the tube at these thermocouple locations with the heaters wrapped on top. This combination of thermocouples soldered in grooves of a thick copper tube wrapped with a thin layer of copper tape, in addition to the aluminum foil backing on the surface-wrapped heaters, prevented hot spots from occurring which have plagued many similar types of test sections in the past. Bulk fluid temperatures were measured at adiabatic locations at the inlet and outlet of the test section using type T thermocouples mounted on the outside of the tube. Preliminary testing was conducted to obtain the saturation temperature of the flowing refrigerants using thermocouple probes, a pressure transducer, and the externally mounted thermocouples. All three methods matched within ±0.38°F over a wide variation of conditions. The externally-mounted thermocouples were chosen to measure the saturation temperature at the inlet and outlet of the test section because the flow patterns entering and exiting the test section were least disturbed.

The absolute pressure transducer at the inlet of the test section provided a secondary check on the inlet saturation temperature. Both BEC Model GWP5-46AW 0 to 50 psia and 0 to 300 psia absolute pressure transducers were used, depending on the saturation pressure of the refrigerant. Pressure drop across the test section was measured using a differential pressure transducer as shown in Figs. 3.1 and 3.7. The differential pressure transducer was a Sensotec Model AD111AT with a range of 0-5 psid. For low flow rate testing, a Setra Model C228-1 with a range of 0-1 psid was used. These transducers, used along with the absolute pressure transducers, provided additional checks on the saturation temperature at the exit of the test section. Each of these transducers was calibrated using a dead weight tester. Uncertainties of the absolute and differential pressure measurements were estimated to be ±0.3% of the full scale reading. Pressure taps and connections were similar to those described in Sec. 3.1.1. The tap at the test section inlet was used as the tap for both the absolute pressure transducer and one half of the differential pressure transducer. The absolute pressure transducer was moved to the outlet of the test section during high speed pressure testing.

Sight glasses with the same inside diameter as the test section were installed at the inlet and outlet of the test section. The inside tube diameter of the glass tubes was within

0.004 in of the inside diameter of the test section, so perturbations due to the sight glasses were minimized. Flow visualization was enhanced using a strobe light. Videotape and high speed photography were used to gain additional insights on the flow patterns. For quick changes from one test section to the other, special zero clearance fittings were used to connect the test section with the rest of the refrigerant loop.

3.1.4. Data acquisition system

The data acquisition system hardware in this study consisted of a Macintosh II computer, four Strawberry Tree^{TM} data acquisition boards, and six Strawberry Tree^{TM} terminal panels. The system monitored and recorded analog input signals from temperature, pressure, flow, and watt transducers. Analog input signals included both 0-10 VDC signals and 4-20 mA current signals. In addition, the false load heater's power was controlled using a 0-10 VDC analog output signal from the data acquisition system. Figure 3.8 shows a schematic of the data acquisition system hardware. Signals from the transducers were sent through electrical wires to terminal panels. Current and voltage analog input signals were handled through the T-51 terminal panels while the thermocouple voltages were handled by T-21 terminal panels which had an isothermal plate with an integral cold junction sensor. The analog output signal to the false load heater was sent through a T-51 terminal panel.

The terminal panels were connected to the data acquisition boards through 50-wire ribbon connectors. These data acquisition boards are shown in Fig. 3.8. There were two 8 channel boards with analog output capability designated as ACM2-16-8A and ACM2-12-8A boards. The 12 and 16 stand for the bit precision of the boards. In addition, there were also two, sixteen channel analog output boards designated as ACM2-16-16 boards. The total system had 48 channels of analog input capability and 4 channels of analog output capability. A total of 40 channels were used for typical evaporation data runs. Data was scanned and was capable of being logged at 1 Hz for this combination of channels. When a smaller number of channels are sampled, each can be scanned and logged at a higher rate.

A canned data acquisition program created by Strawberry Tree^{TM} called Analog Connection Workbench^{TM} was used to display and record the data from the data acquisition hardware on the Macintosh II computer. This program is an icon driven program that uses a computer worksheet to read analog input signals and send analog output signals. An example of the icons used is shown in Fig. 3.9. Analog input signals were transformed into useful information such as pressures and wattages using calculation block icons. Using these calculation blocks, refrigerant thermodynamic and transport properties were determined from sources such as REFPROP [Morrison et al., 1991] using

curve fits based on monitored temperatures and pressures. Resulting values were shown on the screen using meters or logged to the hard disk using the log icon. Values were logged to files in tab-separated variable format for subsequent analysis using spreadsheets or post-data processing programs. For monitoring steady-state conditions, certain variables were shown on strip charts to monitor changes over time.

Higher sampling rates were required for pressure and pressure drop signals to obtain spectral and statistical information about the various flow patterns. Although the data acquisition system manuals claimed single-channel sampling speeds of above 1000 Hz, realistically achievable rates varied between 60 and 250 Hz. Trial and error led to a sampling rate of 100 Hz for the high speed pressure measurements.

3.2. System Operation

Before the system could be operated, several preparation and start-up tests were required. These included purging, evacuating, charging, and leak detection of the refrigerant portion of the apparatus. These steps will be discussed in Sec. 3.2.1. Operating procedures for a test will be discussed in Sec. 3.2.2. These include procedures for both evaporation and high speed pressure measurement tests. Finally, data verification tests will be discussed in Sec. 3.2.3. These include single-phase refrigerant tests to check energy balances and single-phase heat transfer coefficients and pressure drops. Initial two-phase tests were also run to check saturation temperature and saturation pressure correlation, subcooling, and quality measurements.

3.2.1. System preparation

Once the test section was mounted in place and the loop construction was completed, the refrigerant loop was purged using compressed air to remove dirt particles or contaminants from the system. The loop was then evacuated using a vacuum pump to dehydrate the system. The system was charged with compressed nitrogen and a soapy water solution was used to check fittings and connections for leaks. Bubble formation around a fitting or connection indicated that a leak was present. Fittings or connections were tightened or replaced until bubble formation ceased. The system was then evacuated again using a vacuum pump and was charged with R-134a gas. An electronic leak detector was used to check each of the fittings and connections for leaks. Leaks were eliminated by tightening or replacing ferrules in the compression fittings or applying Teflon tape to threaded connections. Resoldering of connections was done when necessary. Leaks were

much less of a problem than for the initial design due to the replacement of a large number of compression fittings with soldered connections.

After the electronic leak detector stopped indicating leaks, the refrigerant loop was evacuated using a vacuum pump and left to sit for a period of twenty-four hours. If the system held near the vacuum point (1 to 1.2 in water), the loop was subsequently charged with the desired refrigerant.

3.2.2. Operating procedure

When running either an evaporation or a high speed pressure measurement test, initial system testing was undertaken to ensure that all of the components and instrumentation were in proper working order. The computer data acquisition system was checked for functionality of both the analog input and analog output channels. The refrigerant pump was turned on and refrigerant was circulated around the loop. The chiller system was turned on and checked to see if it was lowering the antifreeze solution to the desired set point temperature. Heaters in the preheater and test section were turned on to make sure the heaters were operating and that the data acquisition system was reading appropriate values for each section. Temperature, pressure, and flow transducer signals fed into the data acquisition system were also checked for accuracy.

Parameters controlled during tests were mass flux, heat flux, inlet quality, and saturation temperature. Mass flux was first set through control of the variable-speed gear pump. Fine control was adjusted using the pump bypass tubing section. The refrigerant saturation temperature in the test section was adjusted by setting the antifreeze set point temperature in the chiller system several degrees below the desired value. Heat input rates to the preheater were set to control the inlet quality. Heat flux was then set in the test section. Once the temperature in the test section reached approximately the desired value, the false load heater was turned on to equate the heat added to the entire system with the heat removal rate of the compressor at the set point temperature. The various instruments described above were then further adjusted to meet the test specifications.

Steady-state conditions, reached in approximately 15 minutes to two hours, were assumed when the time variation of saturation temperature was less than 0.18°F for five minutes. The controlled parameters also had to be within the following range of target values: mass flux, ±5%; heat flux, ±5%; saturation temperature, ±0.9°F. Once steady-state conditions were achieved, the transducer signals were logged into a data acquisition output file. The channels were scanned once every second for a period of 60 seconds. The outlet pressure and differential pressure to the test section were then recorded at 100 Hz for 10 seconds during adiabatic high speed pressure tests. The data were then reduced using a

spreadsheet macro. Refrigerant transport and thermodynamic properties used during data collection and reduction were obtained from REFPROP [Morrison et al., 1991].

3.2.3. Data verification

Watt transducers were factory calibrated within ±34 Btu/hr, and this number was verified during single-phase energy balance testing. This testing was completed after each change of test section over a period of two and a half years. Heat gains to the test section were determined through single-phase energy balance testing. Table 3.3 shows the energy balance results for the test sections 3 and 4 for R-134a. The product of the mass flow rate times the change in enthalpy through the test section is labeled as q_{fluid}. The heat input rate measured from the watt transducer is labeled q_{power}. Heat gain from the environment is labeled q_{gain}. Energy balances were taken over a wide range of test section refrigerant temperature and the heat gains were curve fitted versus temperature difference between the test section and the environment and were included in the data acquisition software program. The sum of the heat input rate measured from the watt transducer and the calculated value of heat gain from the environment is labeled q_{total}.

Surface thermocouples were also checked during single-phase energy balance testing by comparing forced-convection constant heat flux testing with correlations from the literature such as Dittus-Boelter [1930], Petukov [1970], and Gnielinski [1976]. Values of single-phase heat transfer coefficients fell within ±10% of these correlations for Reynolds numbers above 4000. Mean deviations of the Gnielinski correlation, the Dittus-Boelter correlation, and the Petukov correlation compared with the experimental single-phase heat transfer coefficient data were 4.2%, 4.9%, and 9.8%, respectively. For the specific temperature range in which this single-phase testing took place, the resulting correlations were within 9% of each other. Figure 3.10 shows the experimental and predicted heat transfer coefficients using the three different correlations. These results indirectly substantiated pressure, temperature, mass flux, heat flux, and power measurements for the test facility. Single-phase pressure drop testing through the test section was also completed for various test sections, but the length of tube was not long enough to generate high enough pressure drops to indirectly determine the accuracy of the differential pressure transducers used. These single-phase pressure drops fell at or near the uncertainty of the measuring instrument, and could only be used for trend analysis purposes.

Table 3.3. Energy balances for test sections 3 and 4

Test section	q_{fluid} [Btu/hr]	q_{power} [Btu/hr]	q_{gain} [Btu/hr]	q_{total} [Btu/hr]	Δq [Btu/hr]
3	1374.4	1351.6	32.4	1384.0	9.6
3	704.3	684.8	30.7	715.6	11.3
3	30.4	0.0	31.4	31.4	1.0
3	21.8	0.0	23.9	23.9	2.0
3	691.7	689.3	34.8	724.1	32.4
4	689.6	688.6	0.0	689.6	1.0
4	14.3	0.0	0.0	14.3	14.3
4	1379.3	1392.6	8.5	1401.1	21.8
4	33.8	0.0	27.3	27.3	6.5
4	727.5	694.7	24.6	719.3	8.2

3.3. Test Envelope

The dissertation research consisted of three main areas for two-phase flow in a single-tube evaporator: flow pattern identification and evaluation of criteria to determine flow pattern transitions, evaluation and correlation of local heat transfer coefficients based on these flow patterns, and application of these results to evaporator design and simulation. Within each of these areas, several objectives are identified and are discussed below.

3.3.1. Experimental testing objectives

The following is a list of objectives for the experimental testing in regards to flow patterns, heat transfer coefficients, and design.

Flow Patterns

1. Evaluate flow maps developed for adiabatic flows for use with diabatic flows from subjective flow visualization at the test section sight glasses.
2. Examine objective flow regime criteria such as statistical and spectral analysis of high speed pressure and pressure drop measurements.

Heat transfer coefficients

1. Develop an empirical correlation for annular flow, examining the superposition of nucleate and convective boiling.
2. Determine a suitable method to predict the suppression of nucleate boiling.
3. Develop an empirical correlation for wavy flow, examining the effect of wall wetting and enhanced nucleate boiling presence.
4. Determine the dryout transition point, x_{cr}, for both annular and wavy flows.

Design

1. Combine the above-mentioned results into a design methodology scheme.
2. Analyze the effect of optimum tube diameter sizing using the developed heat transfer coefficient correlation for annular and wavy flow for a full refrigerant evaporator.

To develop the correlations, the data from the previous work conducted for the Air Conditioning and Refrigeration Center using R-134a, R-12, and R-22 were used. Also, additional tests were performed for both annular and wavy flow as described in Table 3.4. Refrigerants used in the test envelope included R-134a, R-12, R-22, and a 60%/40% azeotropic mixture of R-32/R-125. Four pipe diameters were tested ranging from inside diameters of 0.277 to 0.430 in. A wide range of mass fluxes allowed correlation of the data for wavy and annular subsets. In addition, the large heat flux range allowed a full examination of the effect of nucleate boiling on the heat transfer coefficient. The magnitudes of both convective and nucleate boiling for varying saturation temperature were examined. Additional evaporation testing was needed to fill in gaps within the database.

High speed pressure measurements were taken to determine objective flow regime criteria. Two wavy mass fluxes and two annular mass fluxes were used to map out the flow region with qualities varying from 20% to 80%. R-134a was used as the test fluid. Additional tests were performed in the transition flow pattern areas.

3.3.2. Basic matrices for heat transfer coefficient testing

The database of refrigerant heat transfer coefficients was built up over a three and a half year period in which several different objectives were accomplished. Four different test sections with varying tube diameters were used to obtain the data. The first test section described in Table 3.1 was a 8 ft long, 0.402 in inside diameter test section. Tests were conducted at automotive air conditioning evaporator mass fluxes and conditions as listed in Table 3.5. Refrigerants used were R-134a and R-12.

Table 3.4. Single-tube test envelope

Part I. Initial heat transfer testing

A. Low flow rate testing parameter ranges
   1. Mass flux: 19-75 klbm/ft^2-hr
   2. Heat flux: 640-3200 Btu/hr-ft^2
   3. Qualities: 10-90%
   4. T_{sat}: -4 to 41°F
   5. Tube D_i: 0.277 in, 0.403 in
   6. Refrigerants: R-134a, R-12

B. High flow rate testing parameter ranges
   1. Mass flux: 75-525 klbm/ft^2-hr
   2. Heat flux: 960-9600 Btu/hr-ft^2
   3. Qualities: 5-95%
   4. T_{sat}: 14 to 59°F
   5. Tube D_i: 0.277 in, 0.402 in, 0.430 in
   6. Refrigerants: R-134a, R-12, R-22

Part II. Additional heat transfer testing

A. Large diameter testing parameter ranges
   1. Mass flux: 38-225 klbm/ft^2-hr
   2. Heat flux: 640-12,800 Btu/hr-ft^2
   3. Qualities: 5-95%
   4. T_{sat}: 23 to 59°F
   5. Tube D_i: 0.430 in
   6. Refrigerants: R-32/R-125

B. Small diameter testing parameter ranges
   1. Mass flux: 38-225 klbm/ft^2-hr
   2. Heat flux: 640-12,800 Btu/hr-ft^2
   3. Qualities: 5-95%
   4. T_{sat}: 23 to 59°F
   5. Tube D_i: 0.305 in
   6. Refrigerants: R-22, R-32/R-125, R-134a

Part III. Additional specialty testing

A. High speed pressure measurements
   1. Mass flux: 38, 75, 150, 225 klbm/ft^2-hr
   2. Quality: 20, 40, 60, 80%
   3. T_{sat}: 41°F
   4. Tube D_i: 0.430 in
   5. Refrigerants: R-134a

B. Extra testing to fill in gaps in test plan above

The heat transfer coefficients were average values obtained over the entire length of the test section. Quality changes through the test section ranged from 5% to 50%, and, hence, the average heat transfer coefficients were fairly local in nature.

Table 3.5. Initial test matrix for R-134a and R-12 using test section 1

Saturation temperature, °F	Heat flux, Btu/hr-ft^2	Mass flux, klbm/ft^2-hr	Inlet quality, %
40.0	1620	100	20
40.0	3240	100	20
40.0	6480	100	20
40.0	1620	200	20
40.0	3240	200	20
40.0	6480	200	20
40.0	1620	300	20
40.0	3240	300	20
40.0	6480	300	20
40.0	1620	400	20
40.0	3240	400	20
40.0	6480	400	20

Next, R-134a and R-12 were used in a 8 ft long, 0.277 in inside diameter test section to simulate conditions in different sections of a household refrigerator evaporator. Table 3.6 shows the range of parameters used for these tests. Again, heat transfer coefficients were averaged over the entire test section with small quality changes occurring from the inlet to the outlet. The mass fluxes and heat fluxes were an order of magnitude below the values used for the automotive air conditioning evaporator testing.

The first two test sections provided an initial look at the various flow patterns encountered during two-phase evaporating flow. For the high flow rate testing, the predominant flow pattern was annular flow. For the low flow rate testing, the predominant flow pattern was wavy flow. The qualitative variation of heat transfer coefficient versus quality was observed for the different flow patterns. In addition, major improvements were made to the test sections which were introduced in test section 3 and 4. Thermocouple mounting techniques were improved along with better control of hot spots,

Table 3.6. Low flow rate test matrix for R-134a and R-12 in test section 2

Saturation temperature, °F	Heat flux, Btu/hr-ft^2	Mass flux, klbm/ft^2-hr	Inlet quality, %
41	640	19	20
41	640	26	20
41	640	38	20
41	640	38	40
41	640	38	60
41	640	38	80
41	960	38	20
41	960	38	40
41	960	38	60
41	960	38	80
41	1600	38	20
41	1600	38	40
41	640	56	20
41	640	56	40
41	640	56	60
41	640	56	80
41	960	56	20
41	960	56	40
41	960	56	60
41	960	56	80
41	1600	56	20
41	1600	56	40
41	960	75	20
41	960	75	40
41	960	75	60
41	960	75	80
41	1600	75	20
41	1600	75	40
41	1600	75	60
41	3200	75	20
41	3200	75	40

as was discussed in Sec. 3.1.3. System parameter ranges were also extended. Changes to the preheater, introduction of a Coriolis mass flow meter, and development of a pump bypass allowed higher quality testing to be achieved and created better system stability.

Table 3.7 shows the basic matrix of testing that was conducted using the 0.430 in and 0.305 in inside diameter test sections. This matrix encompassed the entire range of flow patterns encountered in the initial studies while expanding the heat flux and quality ranges. Refrigerants used were R-134a, R-12, R-22, and a 60%/40% azeotropic mixture of R-32/R-125. Table 3.13 gives a listing of thermodynamic and transport properties of the refrigerants at 41°F. Heat transfer coefficients were averaged over the entire test section with small quality changes occurring from the inlet to the outlet. These tests provided a basic map of the heat transfer coefficients encountered during evaporation inside smooth, horizontal tubes.

Table 3.7. Basic test matrix for test sections 3 and 4

Saturation temperature, °F	Heat flux, Btu/hr-ft^2	Mass flux, klbm/ft^2-hr	Inlet quality, %
41	640	38	20
41	640	38	40
41	640	38	60
41	640	38	80
41	960	38	20
41	960	38	40
41	960	38	60
41	960	38	80
41	1600	38	20
41	1600	38	40
41	1600	38	60
41	960	75	20
41	960	75	40
41	960	75	60
41	960	75	80
41	1600	75	20
41	1600	75	40
41	1600	75	60
41	1600	75	80

Table 3.7. cont'd

Saturation temperature, °F	Heat flux, Btu/hr-ft^2	Mass flux, klbm/ft^2-hr	Inlet quality, %
41	3200	75	20
41	3200	75	40
41	3200	75	60
41	1600	150	20
41	1600	150	40
41	1600	150	60
41	1600	150	80
41	3200	150	20
41	3200	150	40
41	3200	150	60
41	3200	150	80
41	6400	150	20
41	6400	150	40
41	6400	150	60
41	9600	150	20
41	9600	150	40
41	9600	150	60
41	1600	225	20
41	1600	225	40
41	1600	225	60
41	1600	225	80
41	3200	225	20
41	3200	225	40
41	3200	225	60
41	3200	225	80
41	6400	225	20
41	6400	225	40
41	6400	225	60
41	9600	225	20
41	9600	225	40
41	9600	225	60
41	3200	375	20

Table 3.7. cont'd

Saturation temperature, °F	Heat flux, Btu/hr-ft^2	Mass flux, klbm/ft^2-hr	Inlet quality, %
41	3200	375	40
41	3200	375	60
41	6400	375	20
41	6400	375	40
41	6400	375	60
41	9600	375	20
41	9600	375	40
41	9600	375	60

3.3.3. Specialty testing

In addition to the basic matrix of tests, additional tests were conducted to examine specific areas of interest. Refrigerant evaporator inlet qualities are typically near 20%. At qualities below this value, previous studies have shown more wavy flow patterns with slug flow occasionally superimposed on this flow pattern. A higher heat flux dependency, and, hence, nucleate boiling is more important in this area. Additional testing with the 0.430 in inside diameter and 0.305 in inside diameter test sections was conducted in this quality range, as shown in Table 3.8.

At higher qualities above 80%, the liquid layer becomes fairly thin for both wavy and annular flows. Eventually, the liquid layer completely evaporates, leaving only liquid droplets that are entrained in a vapor core. As discussed in Chap. 2, this flow pattern is called mist flow, and a study of where the transition quality between annular and mist flow and wavy and mist flow was also conducted. Table 3.9 shows the tests conducted to determine the dryout transition quality.

Table 3.8. Low quality test matrix

Saturation temperature, °F	Heat flux, Btu/hr-ft^2	Mass flux, klbm/ft^2-hr	Inlet quality, %
41	1600	225	5
41	1600	225	10
41	1600	225	15
41	3200	225	5
41	3200	225	10
41	3200	225	15
41	6400	225	5
41	6400	225	10
41	6400	225	15
41	9600	225	5
41	9600	225	10
41	9600	225	15

Table 3.9. Dryout transition quality test matrix

Saturation temperature, °F	Heat flux, Btu/hr-ft^2	Mass flux, klbm/ft^2-hr
41	960	75
41	1600	75
41	3200	75
41	1600	225
41	3200	225
41	6400	225
41	9600	225

Variation of saturation temperature and pressure also affects the heat transfer coefficient. Through examination of various heat transfer correlations discussed in Chap. 2, decreasing temperature tends to increase convective boiling and decrease nucleate boiling. Increasing temperature tends to decrease convective boiling and increase nucleate boiling. Saturation temperature was varied by 36°F and 45°F for a set of tests using R-134a for annular flow and wavy flow, respectively. Tests were conducted for wavy flow at -4°F using the matrix given in Table 3.6. Tests were conducted for annular flow at 23°F and 59°F as shown in Table 3.10.

Heat flux was also varied to examine the relative contributions of nucleate and convective boiling. Table 3.11 shows the additional heat fluxes tested for a typical set of flow rates and qualities. Low heat flux situations led to relatively high heat transfer coefficient uncertainties, but interesting trends were found in the data, as will be discussed in Chap. 5.

Table 3.10. High mass flux test matrix with variation of saturation temperature

Heat flux, Btu/hr-ft^2	Mass flux, klbm/ft^2-hr	Inlet quality, %
1600	225	20
1600	225	40
1600	225	60
1600	225	80
3200	225	20
3200	225	40
3200	225	60
3200	225	80
6400	225	20
6400	225	40
6400	225	60

Table 3.11. Low heat flux test matrix

Saturation temperature, °F	Heat flux, Btu/hr-ft^2	Mass flux, klbm/ft^2-hr	Inlet quality, %
41	960	225	10
41	960	225	20
41	960	225	30
41	960	225	40
41	960	225	50
41	960	225	60

Finally, high mass fluxes were run to examine the enhanced convective heat transfer effect. Due to high heat input requirements, testing was limited to qualities below 25% for the range of mass fluxes tested. Table 3.12 shows the tests conducted for R-134a.

Table 3.12. High mass flux test matrix

Saturation temperature, °F	Heat flux, Btu/hr-ft^2	Mass flux, klbm/ft^2-hr	Inlet quality, %
50	3200	525	20
50	3200	750	10

3.4. Data Reduction Techniques

In this section, data reduction techniques for heat transfer coefficients and energy balances will be described. In addition, methods used for statistical and spectral analysis of high speed pressure measurements will be outlined. Finally, an error analysis of the heat transfer coefficients will be conducted showing the effects of parameter uncertainties propagating through to the heat transfer coefficient.

3.4.1. Heat transfer coefficient and energy balance calculations

Experimental, local heat transfer coefficients were determined by the convective law of cooling using the circumferentially averaged values of surface temperatures, the linearly

interpolated values of bulk fluid temperature, the surface area of the test section, and the heat input rate to the test section as follows:

$$h = \frac{q / A_s}{(T_s - T_b)} \tag{3.1}$$

Since surface temperatures were measured inside grooves located along the external surface of the copper tube, the temperature drop across the tube wall needed to be considered. However, its value was determined to be negligibly small, and, therefore, it was disregarded. Axial heat conduction along the length of the tube was also neglected.

Heat gain from the environment was determined during single-phase energy balance testing. For the test section, these gains from the environment were generally small and were on the order of 17 to 34 Btu/hr. These gains, however, were important for low mass flux and heat flux tests. Energy balances were taken over a wide range of test section refrigerant temperatures, and the heat gains were curve fitted against temperature difference between the test section and the environment and were included in the data acquisition software program. Similar tests were taken for the preheater, which had heat gains on the order of 17 to 136 Btu/hr for the same range of refrigerant temperatures.

During an experimental run, heat was constantly being added to the test refrigerant at both the preheater and the test section. The preheater was used to heat the refrigerant from a subcooled state into the two-phase region. An energy balance was used to determine the inlet quality of the test refrigerant. The total energy of the preheater was divided into sensible and latent components as follows:

$$q_{preheater} + q_{environment} = q_{sensible} + q_{latent} \tag{3.2}$$

where

$$q_{sensible} = \dot{m}_r \bullet \left[i_l \left(T_{preheater,out} \right) - \left(T_{preheater,in} \right) \right] \tag{3.3}$$

and

$$q_{latent} = \dot{m}_r \bullet i_{lv} \bullet x_i \tag{3.4}$$

In Eq. 3.3 and 3.4, $\dot{m}_r$ is the mass flow rate of the refrigerant, i_l is the saturated liquid enthalpy of the refrigerant as a function of the refrigerant temperature, and x_i is the inlet quality to the test section. The enthalpy of vaporization was assumed to be the value of the average test section saturation temperature. The quality exiting the preheater was assumed to be the quality entering the test section. The heat input rate of the preheater was measured using a watt transducer, and the heat gain from the environment was determined through single-phase energy balance testing as discussed above. The subcooled refrigerant enthalpy was assumed to be approximately equal to the saturated liquid enthalpy at the same temperature. This approximation resulted in a negligibly small error to the resulting quality due to the domination of the enthalpy of vaporization term.

An energy balance performed on the test section determined the change in quality through the test section. The quality change was calculated by

$$\Delta x = \frac{q_{\text{test section}}}{\dot{m}_r \bullet i_{lv}} \tag{3.5}$$

where i_{lv} was the enthalpy of vaporization at the average saturation temperature of the refrigerant in the test section. Heat input to the test section was the sum of the value found using the watt transducer and the heat gain from the environment as determined from the single-phase energy balance testing. The outlet quality was the sum of the inlet quality to the test section and the change in quality through the test section.

Refrigerant properties used during data collection, data reduction, and post-data analysis were obtained from REFPROP [Morrison et al., 1991] and Jung and Radermacher [1990]. REFPROP uses the Carnahan-Starling-DeSantis (CSD) form for the equation of state. Comparison of values from REFPROP and other sources, such as ASHRAE Fundamentals [1989], yielded variation in properties of up to 5% for transport property data. Since data for R-32/R-125 were scarce, REFPROP was used as the main source of thermophysical property information for consistency purposes. Values of various thermodynamic and transport properties are shown in Table 3.13.

3.4.2. Spectral and statistical analysis of high speed pressure measurement

As discussed in Chap. 2, flow pattern identification is extremely subjective and can result in several different interpretations of the same flow pattern. In addition, flow pattern observation may not always be possible for certain types of evaporators, so determining certain peculiar, objective features of the flow could help in these situations.

Both statistical and spectral methods have been used in the past to examine pressure records of horizontal and vertical air-water flow. Some of these basic methods were applied to the two-phase, horizontal refrigerant flows in this study.

The methodology used in this study consisted of taking a series of high speed pressure and pressure drop measurements during two-phase flow of R-134a in horizontal flow, as described in Table 3.4. The pressure and pressure drop time traces were first examined. Next, calculations of power spectral density and probability density functions were performed from the digitally-sampled data. Subjective flow pattern identification was also recorded for each of the tests. The variations in the resulting graphs were then examined for possible objective flow regime indicators.

Table 3.13. Refrigerant properties at 41°F [Morrison et al., 1991]

Property	R-12	R-134a	R-22	R-32/R-125
Pressure	52.65 psia	50.76 psia	84.70 psia	139.67 psia
Reduced pressure	0.088	0.086	0.117	0.190
Molecular weight	120.9	102.0	86.5	67.3
Liquid thermal conductivity	0.046 Btu/hr-ft-°F	0.053 Btu/hr-ft-°F	0.054 Btu/hr-ft-°F	0.066 Btu/hr-ft-°F
Liquid viscosity	0.615 lb_m/ft-hr	0.653 lb_m/ft-hr	0.551 lb_m/ft-hr	0.480 lb_m/ft-hr
Liquid specific heat	0.224 Btu/lb_m-°F	0.324 Btu/lb_m-°F	0.280 Btu/lb_m-°F	0.312 Btu/lb_m-°F
Prandtl number	3.02	4.04	2.86	2.25
Liquid density	86.2 lb_m/ft^3	79.7 lb_m/ft^3	79.0 lb_m/ft^3	71.6 lb_m/ft^3
Vapor density	1.2 lb_m/ft^3	1.1 lb_m/ft^3	1.6 lb_m/ft^3	2.1 lb_m/ft^3

The pressure fluctuations in the system studied were essentially stationary because the displacement of the time origin left their statistical properties unaffected [Hubbard and Dukler, 1966]. These fluctuations are not well understood and are called random functions or processes. The pressure fluctuations can be examined both spectrally and statistically using the terms defined below.

The pressure fluctuations were discretely sampled through an analog to digital conversion process which approximated the true signal. The discrete sampling led to the potential for aliasing of the data. This is where discrete sampling at one frequency produces measurements that are the same as discretely sampling at another frequency [Adrian, 1993]. To avoid this problem, the data were sampled at a frequency greater than twice the maximum frequency of the signal. This is called the Nyquist criterion. Another way to avoid aliasing is to low pass filter the signal which cuts off the contributions of higher frequency information at a cutoff frequency.

The finite range Fourier transform of a real valued record is defined as [Bendat and Piersol, 1986]

$$X(f,T) = \int_0^T x(t)e^{-i2\pi ft}dt \tag{3.6}$$

where T is a finite sampling period. If a sampling rate of Δt is used over this period, the discrete Fourier transform can be given as

$$X(f,T) = \sum_{n=0}^{N-1} x_n e^{-j2\pi fn\Delta t} \tag{3.7}$$

Using MathCad, a numerical analysis computer program, the computationally efficient fast Fourier transform was used in place of Eq. 3.7. The spectral density for a given f can be estimated from

$$S_{xx} = \frac{1}{T}|X(f,T)|^2 \tag{3.8}$$

and can be normalized based on the total spectral power as

$$\hat{S}_{xx} = \frac{\frac{1}{T}|X(f,T)|^2}{\sum_{f=0}^{f_c}\frac{1}{T}|X(f,T)|^2} \tag{3.9}$$

The squared values of the pressure and pressure drop fluctuations were used by subtracting the mean value from each discretely sampled point and squaring the result. The power spectral density estimated the frequency distribution of the energy in these fluctuations.

The pressure and pressure drop records were also examined statistically. The following statistical parameters were used and are defined below. Definitions were obtained from Matsui [1986] and Bendat and Piersol [1986]. The mean value of a variable, x, is defined as

$$\bar{x} = \frac{\sum x_i}{N} \tag{3.10}$$

The standard deviation is

$$\sigma = \left[\frac{\sum (x_i - \bar{x})^2}{N}\right]^{0.5} \tag{3.11}$$

To define the asymmetry and degree of flatness of the resulting distributions, the n-th moment about the mean is given as

$$\mu_n = \frac{\sum (x_i - \bar{x})^n}{N} \tag{3.12}$$

The skewness is then defined as

$$\gamma_1 = \frac{\mu_3}{\sigma^3} \tag{3.13}$$

The skewness measures the asymmetry of a given distribution. For a positive value of skewness, the long tail will be on the positive side of the distribution. For a negative value

of skewness, the long tail will be on the negative side of the distribution. The kurtosis measures the degree of flattening of a curve near its center. It is defined as

$$\gamma_2 = \frac{\mu_4}{\sigma^4} - 3 \tag{3.14}$$

If the kurtosis is positive, the curve is relative tall and slim, and if the kurtosis is negative, the curve is smaller and more broad in nature. These terms are used to define the resulting statistical distribution of the data about a mean value. The histogram, or probability density function, is used to plot the data. It is estimated by the following equation:

$$P[x,W] = Prob\left[\left(x - \frac{W}{2}\right) \le x(t) \le \left(x + \frac{W}{2}\right)\right] = \frac{1}{T}\sum_i \Delta t_i \tag{3.15}$$

where the variable, x, assumes values in an interval W between x-W/2 and x+W/2, and Δt_i is the time spent by x(t) in the ith range.

Values for the statistical parameters above were calculated with a commercially available graphing package, KaleidaGraph, and the normalized probability density functions were also plotted using this software.

3.4.3. Uncertainty analysis

Uncertainties for the experimental heat transfer coefficients were determined using the method of sequential perturbation, as outlined by Moffat [1988] for single-sample data. The data were classified as single sample since the succession of readings during a test were taken under identical conditions by the same equipment and observer [ASHRAE Guidelines, 1986]. Uncertainties in each of the independent variables used to calculate the heat transfer coefficient from Eq. 3.1 were estimated based on calibration and examination of system-sensor interaction errors. Figure 3.11 shows the methodology for the calculation of uncertainty for each value of heat transfer coefficient. The inputs to the method of sequential perturbation were the heat flux, surface temperature, fluid temperature, and the estimated uncertainties of each value. First, a base case heat transfer coefficient was calculated using the obtained values from the experiment. Then, three additional cases were calculated with each parameter being individually perturbed by its estimated uncertainty. Three additional heat transfer coefficients were calculated. The difference of each of these heat transfer coefficients from the base case heat transfer coefficient was then calculated. Finally, the root-sum-square of the differences were calculated to determine the estimated uncertainty of the heat transfer coefficient from the following equation:

$$\delta h = \left\{\left(\frac{\partial h}{\partial q''}\partial q''\right)^2 + \left(\frac{\partial h}{\partial T_s}\partial T_s\right)^2 + \left(\frac{\partial h}{\partial T_f}\partial T_f\right)^2\right\}^{0.5} \tag{3.16}$$

Surface and fluid temperature thermocouples were calibrated in a thermostatic bath against a NIST-traceable thermometer. Estimated uncertainties of the thermocouple wire and the data acquisition system ranged between ±0.18°F and ±0.27°F. Thermocouples were then placed into the refrigeration flow loop and test section. Thermocouples in the test section were compared for steady-state two-phase flow with no heat applied to the test section and all thermocouples matched within ±0.36°F. These thermocouple readings were then checked against a dead-weight calibrated pressure transducer which indicated saturated pressures of the various refrigerants such as R-12. These values were compared against ASHRAE-tabulated pressure-temperature saturation curves [ASHRAE Fundamentals, 1989] and were within ±0.36°F. For a majority of tests, the estimated uncertainties in the surface and fluid temperatures were ±0.36°F. During low heat flux annular flow testing (960 to 1600 Btu/hr-ft^2), surface temperatures varied by about ±0.18°F, and this value was used as the estimated uncertainty for these tests. During high heat flux testing (9600 to 12,800 Btu/hr-ft^2), surface temperatures at each axial location did vary by more than this value due to slightly asymmetric heating from the electric resistance heaters. Estimated uncertainties for these cases were between ±0.54°F and ±0.90°F.

Wattage uncertainties in the test section were ±0.2% of the full scale reading of the watt transducer. For the 17,000 Btu/hr transducer, this corresponded to an uncertainty of ±34 Btu/hr. This value was verified during single-phase energy balance testing and was used to calculate the heat transfer coefficient uncertainties from Eq. 3.16.

Commercial values were used for the inside tube diameter. These values were verified using dial calipers. Commercial tube diameters were within ±0.003 in of the measured values. This value was used for the uncertainty of the inside tube diameter. The heated test section length was measured using a tape measure. These values were slightly different than the calculated values from the strip heaters due to overlap and the spiral wrapping effect. The measured length was within ±1.18 in of the strip heater length and this value was used for the estimated uncertainty of the heated length. Estimated axial conduction of the heat input of the electric resistance heaters fell within the estimated uncertainty value for test section length.

Uncertainties from a modified version of Eq. 3.16, including terms for the heat flux due to uncertainty of the tube diameter and length, were calculated for each value of heat transfer coefficient. These values are given in Appendix B, where the experimental data are tabulated. A discussion of the resulting values of experimental uncertainties for the heat transfer coefficients is given in Chap. 5. Test conditions resulting in high and low values of uncertainty will be discussed. Uncertainty estimation will be discussed as a design tool for selecting various equipment and setting up debugging procedures.

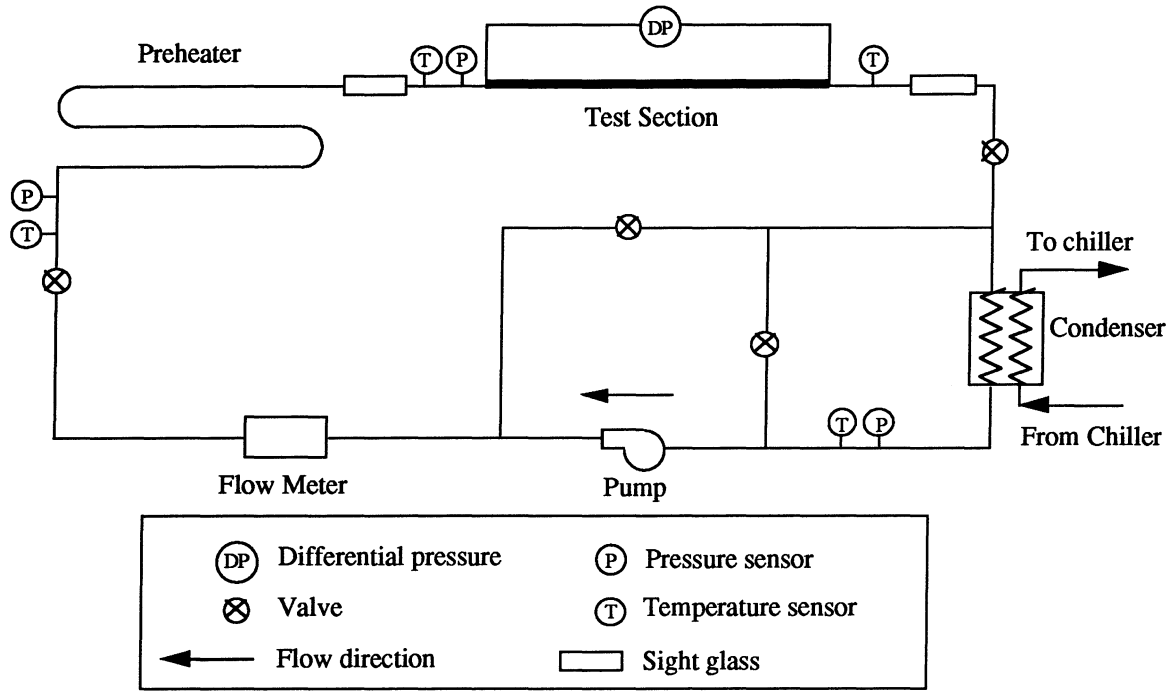

Figure 3.1. Experimental test facility.

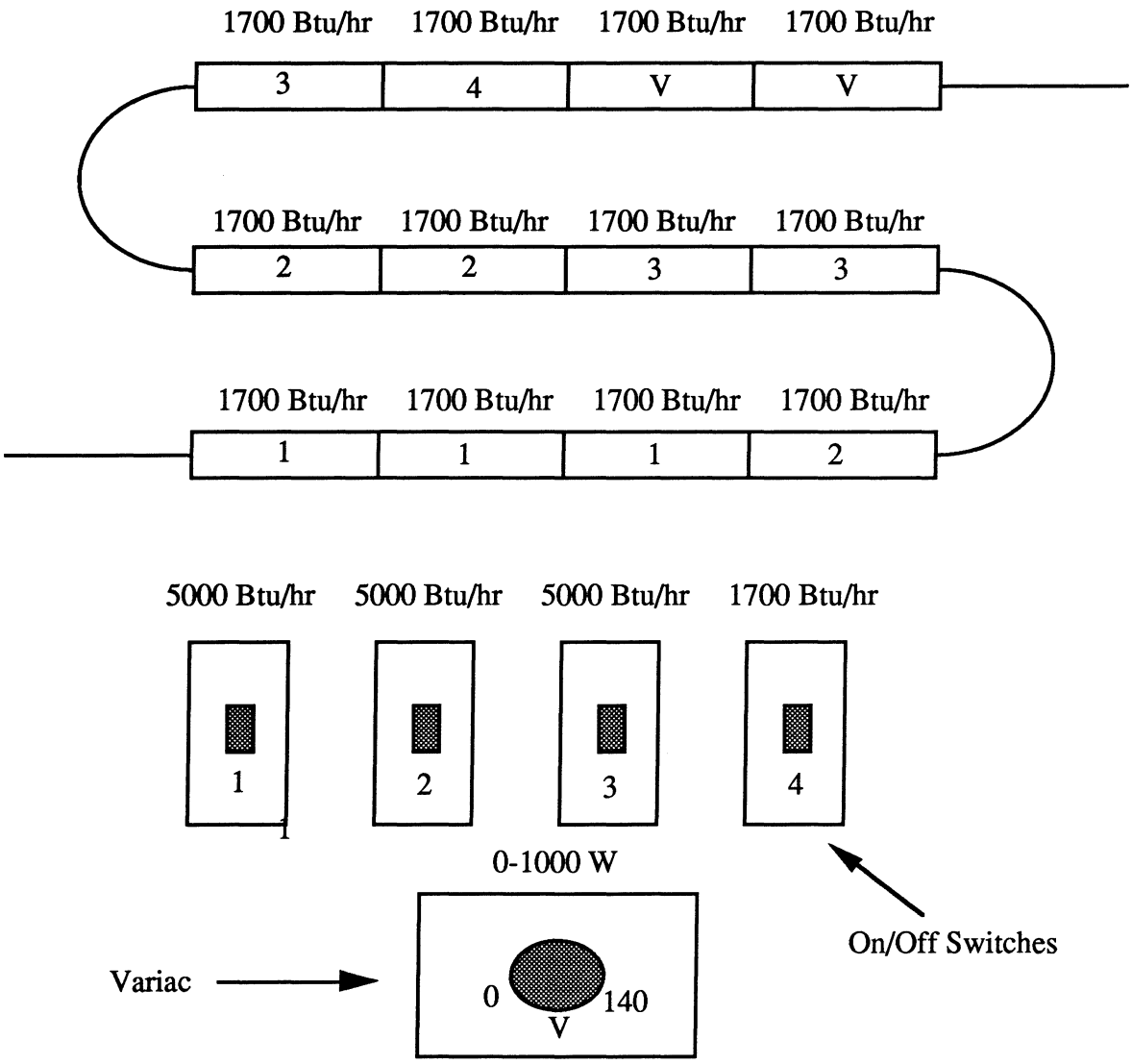

Figure 3.2. Preheater schematic.

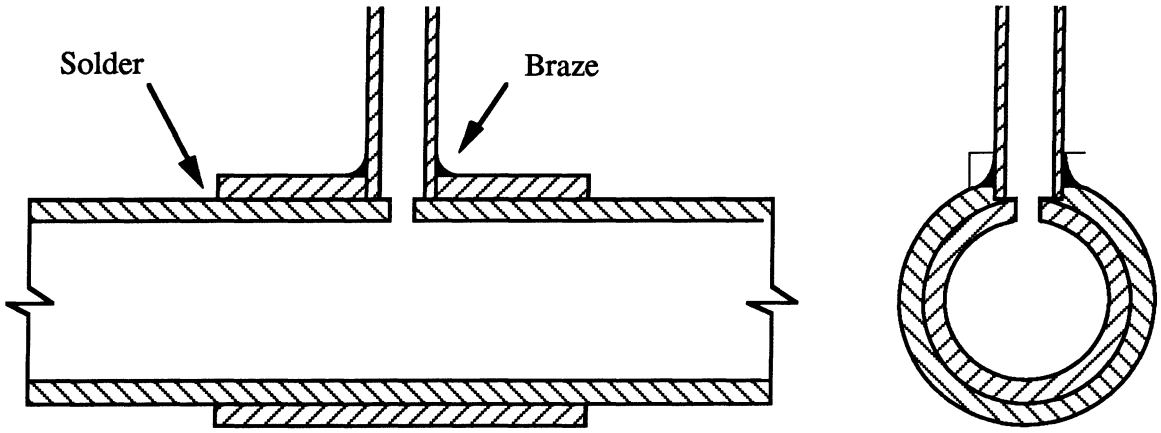

Figure 3.3. Pressure tap.

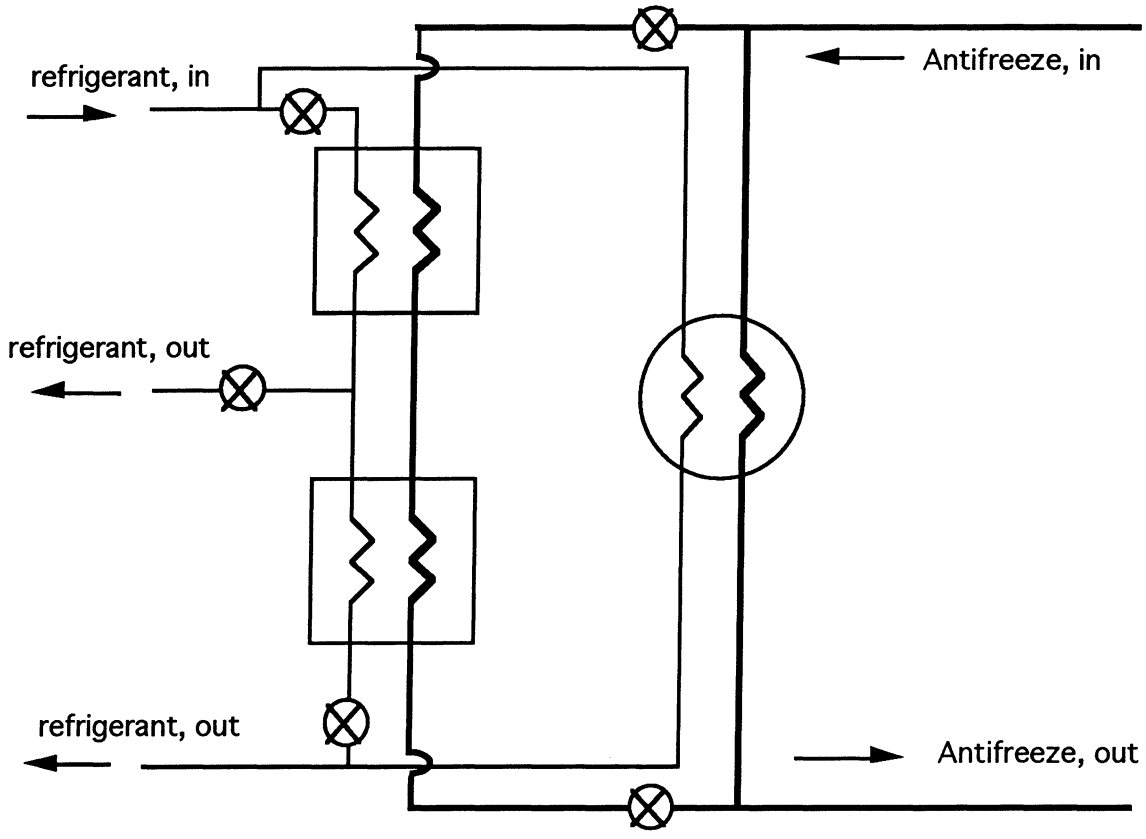

Figure 3.4. Condenser schematic.

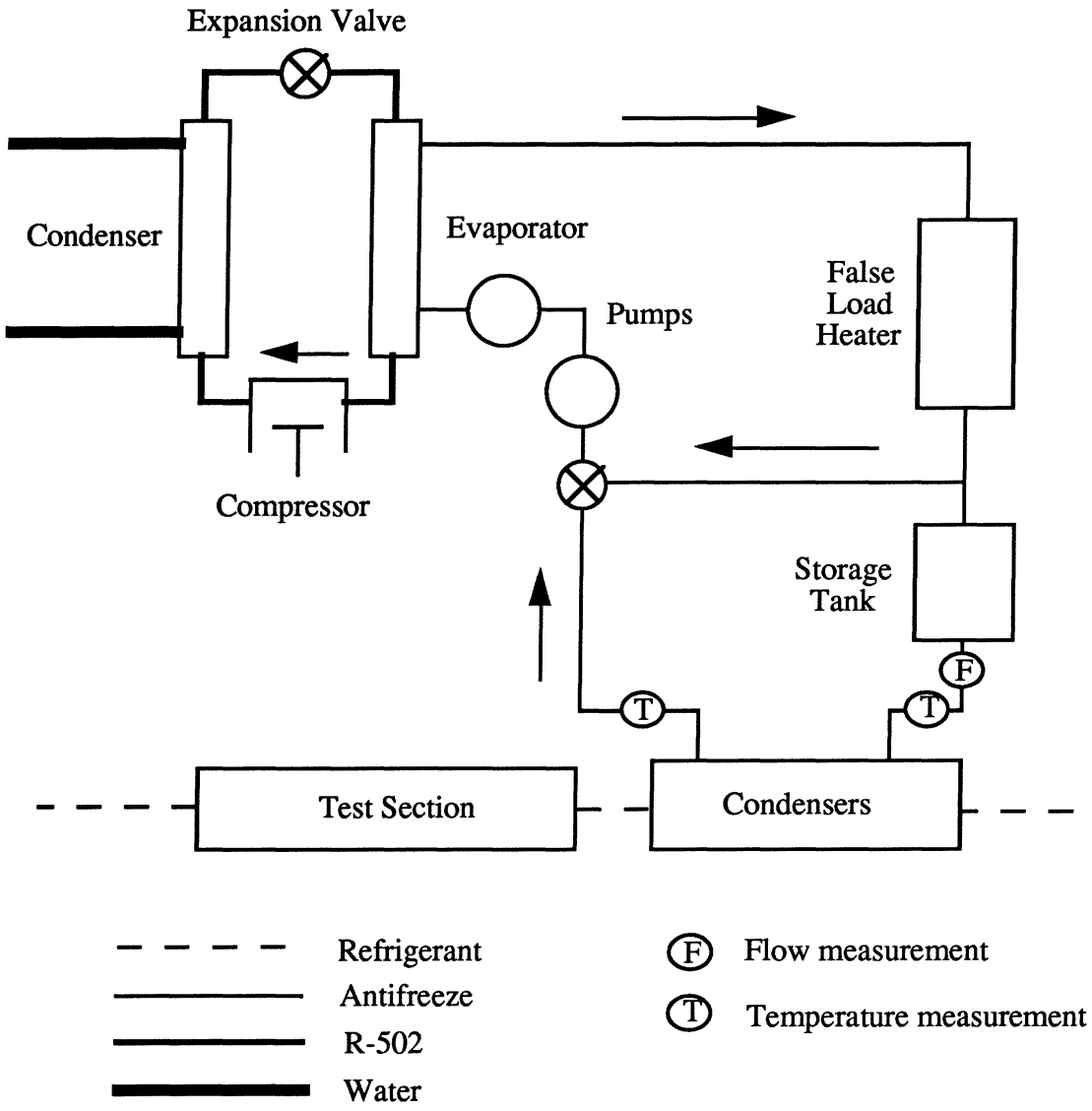

Figure 3.5. Chiller system.

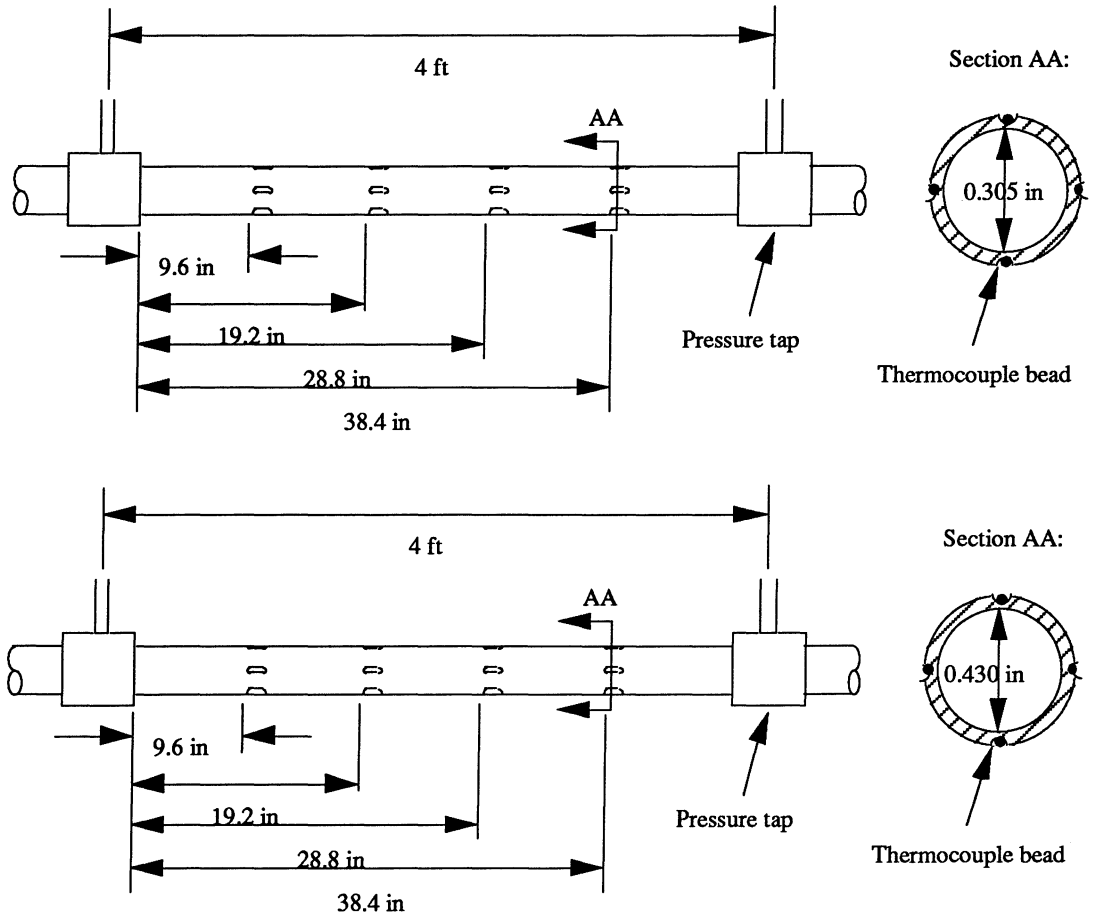

Figure 3.6. Test section thermocouple locations.

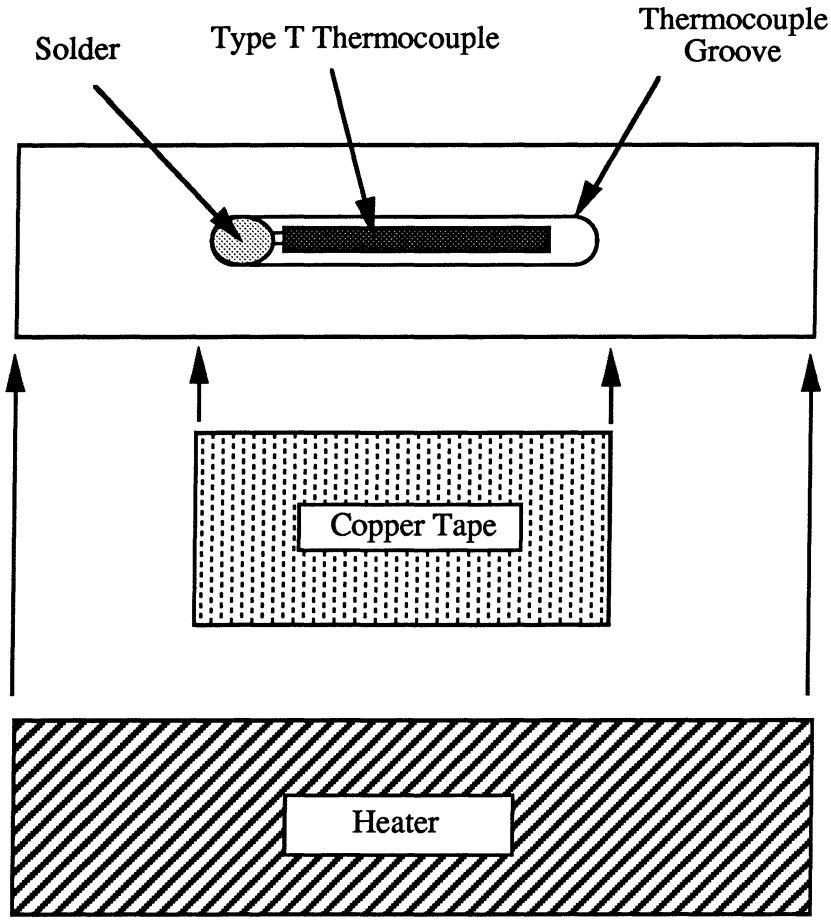

Figure 3.7. Test section fabrication.

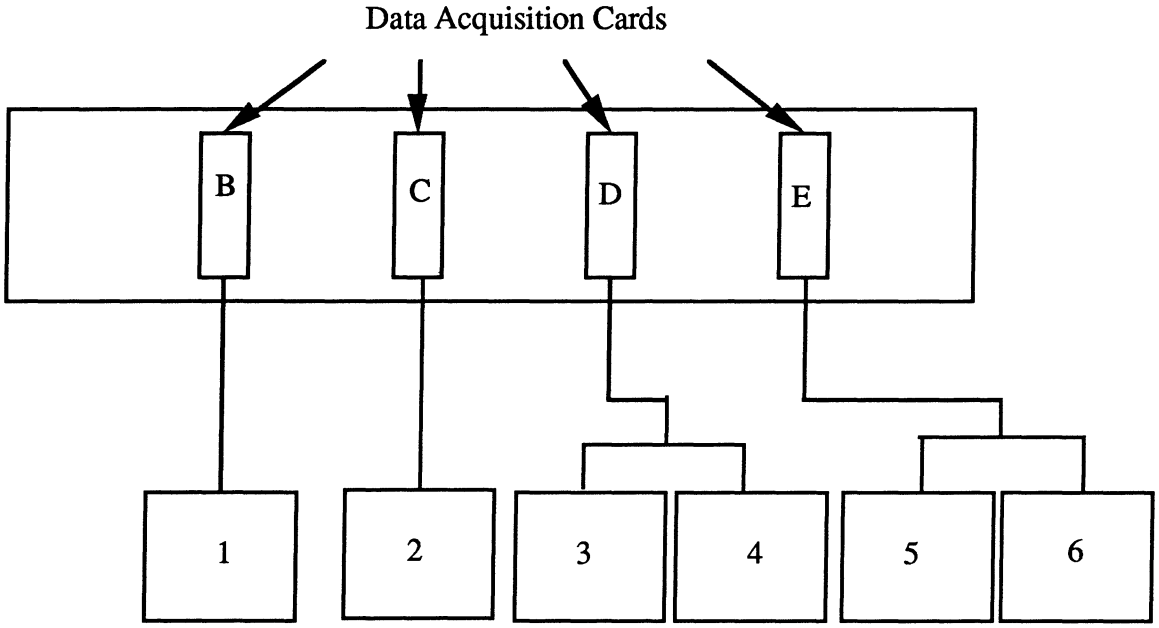

Terminal Panels

Slot	Data acquisition card	Terminal Panel	Channels
B	ACM2-12-8A	1: T-51, General Purpose Panel, (Flow, Pressure, Wattage)	1-8
C	ACM2-16-8A	2: T-21, Thermocouple Panel, (Fluid temperatures)	9-16
D	ACM2-16-16	3, 4: T-21, Thermocouple Panel, (Test section surface temperatures)	17-24 25-32
E	ACM2-16-16	5,6: T-51, General Purpose Panel, (Flow, Pressure, Wattage)	33-40 41-48

Figure 3.8. Data acquisition hardware.

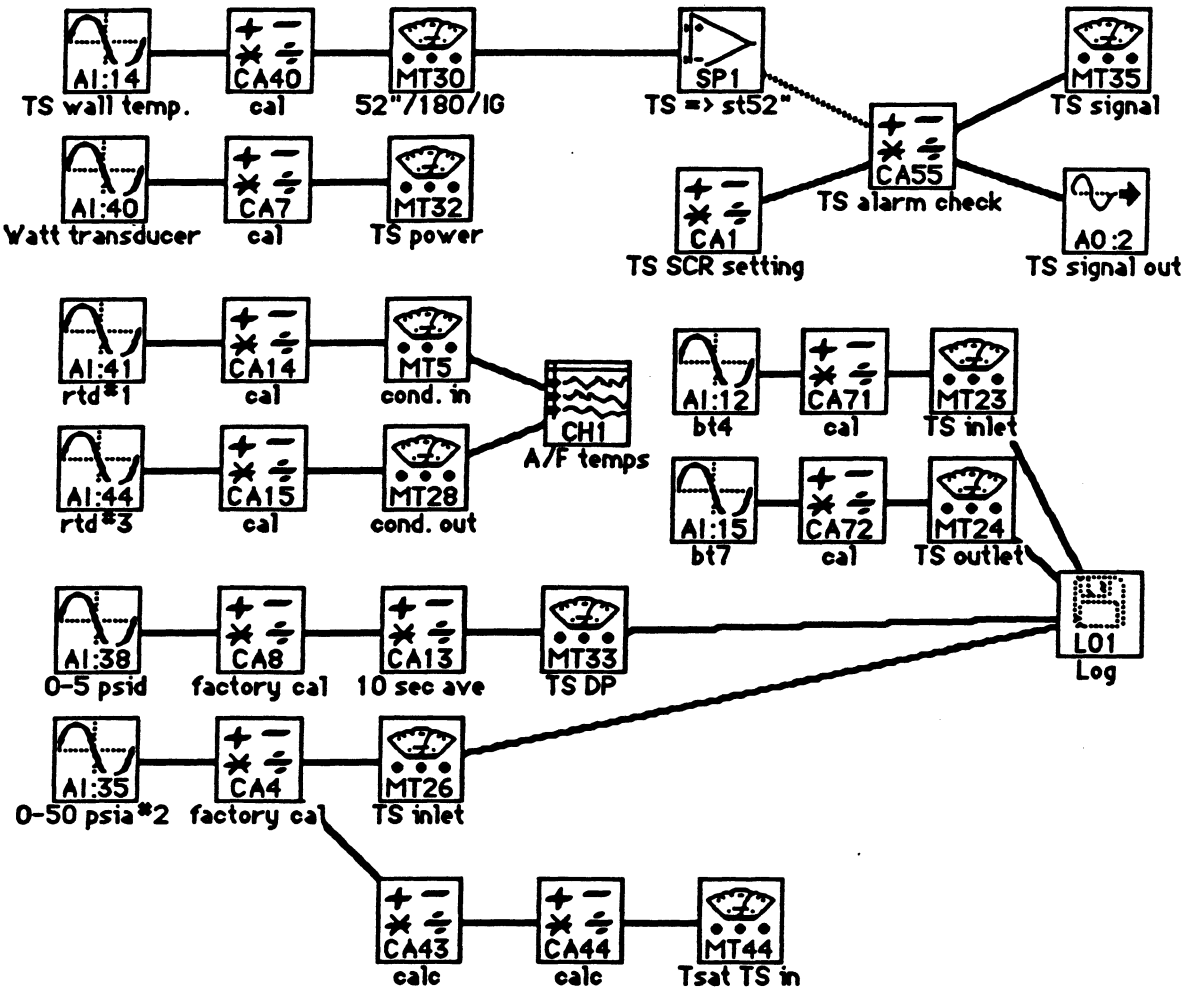

Figure 3.9. Software icons.

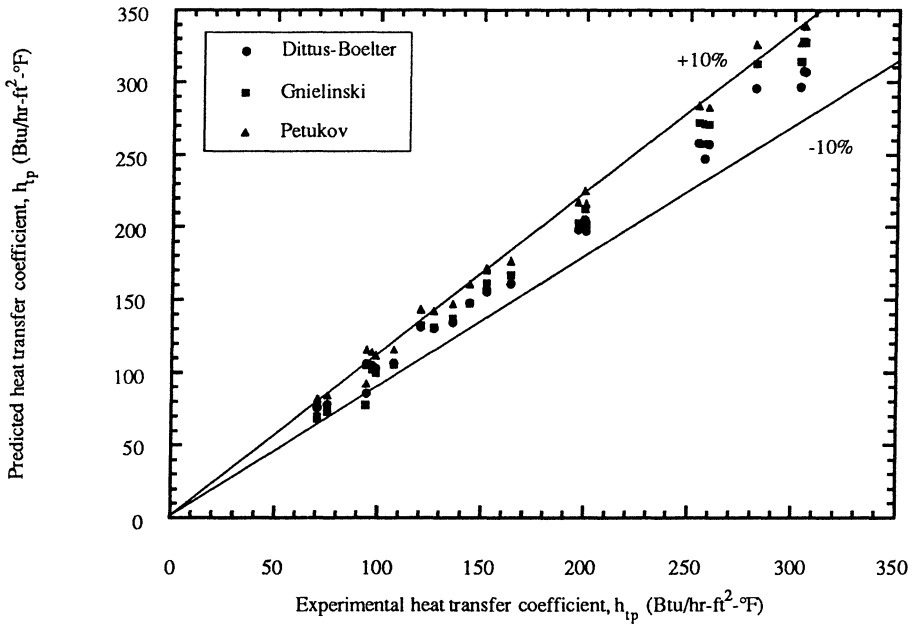

Figure 3.10. Experimental single-phase heat transfer coefficient versus single-phase heat transfer coefficient correlations for R-134a using various test sections.

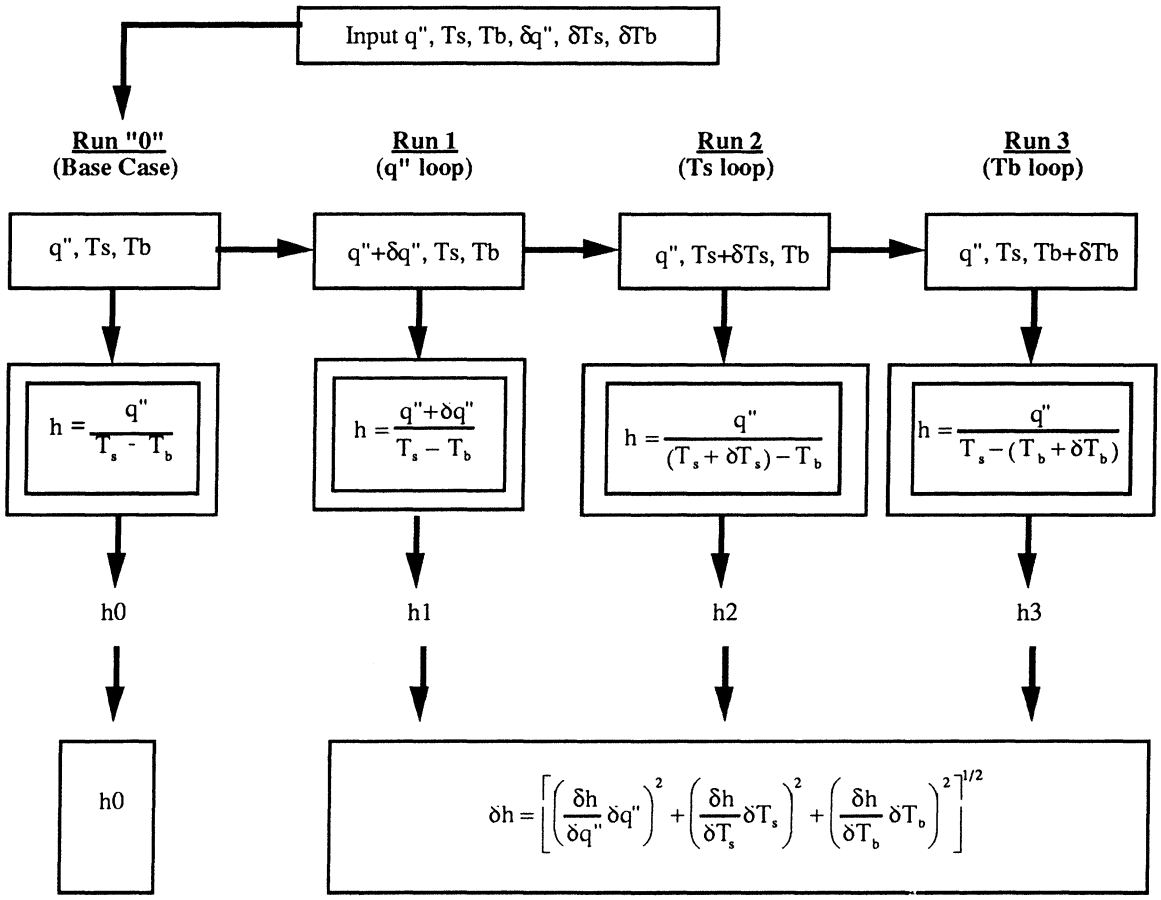

Figure 3.11. Method of sequential perturbation [Moffat, 1988].

CHAPTER 4. EXPERIMENTAL FLOW PATTERN RESULTS

The experimental results can be broken up into three main areas: flow patterns, objective flow regime criteria using high speed pressure and pressure drop measurements, and heat transfer coefficient data. This chapter will focus on the first two areas. In the first section, flow patterns will be discussed in terms of flow parameters. In addition, the results of the visual observations will be plotted on several flow regime maps discussed in Chap. 2. Next, the high speed pressure and pressure drop data will be examined both on spectral and statistical levels for potential objective flow regime criteria. Differences in power spectral densities and probability density functions will be examined for wavy flow, annular flow, slug flow, and mist flow, as observed visually at the sight glasses at the inlet and outlet of the test sections. A summary of the various flow pattern indicators and objective criteria will then be given for refrigerants.

4.1. Visual Identification of Flow Patterns

Several flow patterns were observed through the sight glasses at the inlet and outlet of the test section for the 0.430 in i.d. and 0.305 in i.d. test sections for the flow parameters given in Table 3.7. For mass fluxes of 150, 225, and 375 klb_m/ft^2-hr, the flow patterns were predominantly annular in nature. For low quality testing below 20%, as listed in Table 3.8, wavy and wavy-annular flows were also observed. Varying amounts of slugging were observed for flows at the lower qualities. For high quality testing above 95%, as listed in Table 3.9, mist flow was observed. Mist flow occurred when the annular liquid film on the wall began to completely evaporate. This was detected both by visual observation and a sudden decrease in the heat transfer coefficient due to a rise in the wall temperature for the constant heat flux boundary condition. The thermodynamic quality at this condition was less than unity, as droplets of liquid were still carried in the vapor core. It should be noted for this regime that annular flow was intermittently present with the dryout in an oscillatory pattern. In these horizontal tubes, dryout first occurred in the top region of the tube where the liquid layer is thinner. Variation of heat flux through the test section had little effect on the point at which mist flow could be observed.

Figure 4.1 shows the variation of flow patterns on a G-x map for both the 0.430 in i.d. and 0.305 in i.d. test sections for R-134a. No major variation of flow pattern was detected using the same test conditions for the different tube diameters. Saturation temperature variation also had very little effect on the flow patterns observed. In addition, changes of refrigerant had very little overall effect on the flow pattern variation.

For the lower mass fluxes of 38 and 75 klb_m/ft^2-hr, wavy flow was the predominant flow pattern. For high qualities and the 75 klb_m/ft^2-hr mass flux, promotion to wavy-annular and annular flow could be observed. Again, mist flow and annular-mist flow were observed for qualities above 95%. For mass fluxes between 19 and 38 klb_m/ft^2-hr, the waves on the surface of the liquid dissipated significantly, and nearly stratified flow was observed for a mass flux of 19 klb_m/ft^2-hr. Again, Fig. 4.1 shows the basic trends in the flow pattern variation with mass flux and quality.

In practical evaporators, inlet qualities are usually near 20%. Household refrigerator evaporators carry relatively low loads and require mass fluxes between 19 and 38 klb_m/ft^2-hr. Stationary air conditioning evaporators and automotive air conditioning evaporators require higher mass fluxes due to the higher loads imposed on these systems. Automotive air conditioning evaporators are mainly of the flat-plate type and the results in this study are only indirectly applicable. Mass fluxes per tube for stationary air conditioners usually range between 75 and 225 klb_m/ft^2-hr. The flow pattern variation makes a large difference in both the magnitude and trends of the heat transfer coefficient versus quality. This will ultimately affect the length of these evaporators, as will be discussed in Chap. 6.

The experimental flow pattern data of the various refrigerants were also plotted on the established flow pattern maps of Baker [1954], Mandhane [1974], and Taitel-Dukler [1976] in Figs. 4.2, 4.3, and 4.4, respectively. The predicted flow patterns of the various maps are also tabulated in Table 4.1 for R-134a. Identical flow pattern variation was found using the other refrigerants. Based on the mass flux / quality combinations shown in Table 4.1, the Baker map accurately predicted 42.1% of the flow pattern data, the Mandhane map predicted 21.1%, and the Taitel-Dukler map predicted 89.5%. As can be seen, the Taitel-Dukler map did the best job of predicting the resulting refrigerant flow patterns. Both the Baker and Mandhane maps predicted larger amounts of slug flow than were actually visually observed. For these maps to more accurately predict the refrigerant flow patterns, considerable shifting of the flow regime transition lines must occur. As will be discussed in the next section, even the slug flow predicted by the Taitel-Dukler map appeared to be pseudo-slug flow, as described by Lin and Hanratty [1989].

Table 4.1. Experimental flow regime / flow map comparison for R-134a

Mass flux (klb_m/ft^2-hr)	Quality	Experimental flow regime	Baker map	Mandhane map	Taitel-Dukler map
19	0.5	stratified	stratified	stratified	wavy
38	0.2	stratified	slug	stratified	wavy
38	0.5	wavy	slug	stratified	wavy
38	0.8	wavy	stratified	stratified	wavy
56	0.2	wavy	slug	stratified	wavy
56	0.5	wavy	slug	stratified	wavy
56	0.8	wavy	annular	stratified	wavy
75	0.2	wavy	slug	stratified	wavy
75	0.5	wavy	annular	stratified	wavy
75	0.8	wavy-annular	annular	stratified	wavy
150	0.2	wavy-annular	slug	stratified	annular
150	0.5	annular	annular	wavy	annular
150	0.8	annular	annular	wavy	annular
225	0.2	wavy-annular	slug	slug	annular
225	0.5	annular	annular	slug	annular
225	0.8	annular	annular	slug	annular
375	0.2	wavy-annular	annular	slug	annular
375	0.5	annular	dispersed	slug	annular
375	0.8	annular	dispersed	slug	annular

4.2. High Speed Differential Pressure Measurements

In addition to the visual identification of flow patterns, high speed differential pressure measurements were taken at a speed of 100 Hz for 10 seconds to examine potential objective flow regime criteria. Measurements were taken for mass fluxes of 38, 75, 150, and 225 klb_m/ft^2-hr, and the quality was varied between 0 and 80% in 20% increments. Additional sampling was conducted for low quality (below 20%) and high quality testing (above 90%). The resulting differential pressure measurements were plotted in a variety of different ways in an attempt to distinguish either spectral or statistical behavior that would separate the various flow patterns discussed above. First, the differential pressure-time traces were plotted for the various tests. Next, the probability distribution functions (histograms) were plotted for the various tests to examine potential changes in the mean, standard deviation, kurtosis, and skewness. Finally, the normalized power spectral densities were calculated to look for potential frequency variations in the data. High speed pressure measurements were also taken, but had similar trends compared to the high speed differential pressure measurements. In addition, the resolution of the differential pressure transducer was much better than the absolute pressure gages. For these reasons, the differential pressure measurements were used for a majority of the comparisons. However, for examination of the slug flow results, two absolute pressure transducers were used for cross-correlation analysis, which will be discussed below.

4.2.1. Spectral and statistical analysis

Figures 4.5 through 4.10 show the differential pressure-time trace, the normalized probability density function, and the normalized power spectral density for a typical annular flow and a typical wavy flow. For comparison purposes, the scales for each of the two flows in the various plots are the same. As can be seen from Figs. 4.5 and 4.6, the amplitudes of the differential pressure measurements for the two flow patterns differed quite a bit. However, these differences were mainly due to the magnitude of the mean pressure drop. The annular flow had a much higher mean pressure drop than the wavy flow (0.629 psid versus 0.013 psid). This trend was present throughout the data set.

Statistically, the standard deviation was also higher for the annular flow case. Figures 4.11 and 4.12 show the trend of the mean and standard deviation for mass flux and quality variation. Both the mean and the standard deviation decreased for a fixed mass flux as quality was decreased for qualities below 80%. The mean and standard deviation also decreased for a fixed quality as mass flux was decreased. No clear abrupt transition point was determined from the mean and standard deviation when plotted alone. However, the

normalized probability density function for the wavy flow case showed a much higher variation than the probability density function for the annular flow, as can be seen in Figs. 4.7 and 4.8. An interesting trend was found when the ratio of standard deviation to mean, $\sigma / \bar{x}$, was plotted. This is shown in Fig. 4.13. For $\sigma / \bar{x} < 0.10$, annular flow was observed for all of the tests conducted. For $\sigma / \bar{x} > 0.20$, wavy flow was observed for the tests conducted. A transition region occurred for $0.10 < \sigma / \bar{x} < 0.20$. The trend of this parameter was the exact opposite of the amplitude variation described above. Annular flow had the smallest value of this parameter, while the wavy flow data had the largest variation. This parameter has been verified for qualities above 5% and is useful for determining the transition between wavy and annular flow for these qualities.

Kurtosis and skewness were mixed for the various tests conducted. No clear trend could be determined from the data. Figures 4.14 and 4.15 show the erratic behavior of kurtosis and skewness for the variation of mass flux and quality.

The power spectral densities of pressure drop for wavy and annular flows showed very similar trends, as can be seen in Figs. 4.9 and 4.10. A majority of the power was found around zero frequency. This corresponded to the Hubbard and Dukler criterion [1966] for separated flow. Aliasing was not a problem since nearly 100% of the power was contained in frequencies below 50 Hz. Since both wavy and annular flows are part of the separated flow family, a distinction could not be determined between these two flow patterns using the normalized power spectral density of pressure drop.

4.2.2. Slug flow analysis

Varying amounts of slug flow were found at qualities below 20% based on a visual inspection. Tests were conducted at both 5 and 10% for a mass flux of 300 kg/m^2-s to examine the visually observed slug flow on a spectral basis. Figures 4.16 and 4.17 show the normalized power spectral densities for the two tests. Trends in the power spectra were again similar to the separated flow tests. No obvious spikes in the power spectrum occurred. The differential pressure-time trace also did not indicate slug flow. The $\sigma / \bar{x}$ ratio for the two tests showed values of 0.34 and 0.66, indicating more of a wavy-type flow. On the Taitel-Dukler map, these two tests fell at or near the slug flow transition line. All of these observations lead to a conclusion that although some amount of slug flow may be present at these lower qualities, these flows really can be classified according to the definition of pseudo-slug flow given by Lin and Hanratty [1989].

An additional test was run for the 225 klb$_m$/ft^2-hr mass flux and 5% quality test to determine whether pseudo-slug flow or slug flow was present. Two absolute pressure transducers were mounted at the inlet and outlet of the 0.305 in i.d. test section. High

speed pressure measurements were taken using both transducers sampling at 100 Hz. The cross-correlation of the two pressure-time traces were calculated using the following equation [Bendat and Piersol, 1986]:

$$R_{xy}(r\Delta t) = \frac{1}{N-r}\sum_{n=1}^{N-r}(x_n - \bar{x})(y_n - \bar{y}) \quad , r = 1,2,...m \qquad (4.1)$$

where $r\Delta t$ is the time delay and $m < N$, the number of observations in the time series. The cross-correlation was normalized through use of auto correlations, R_{xx} and R_{yy} as follows:

$$\rho_{xy}(r\Delta t) = \frac{R_{xy}(r\Delta t)}{\sqrt{R_{xx}(0)R_{yy}(0)}} \qquad (4.2)$$

The normalized cross-correlation has values between -1 and +1.

Figure 4.18 shows the cross-correlation for the 225 klb_m/ft^2-hr and 5% quality test. As can be noted from the plot, there is not a high degree of correlation, which is different from what can normally be seen from slug flow, as shown by Lin and Hanratty in Fig. 4.19. This plot, along with the other plots and observations discussed above, show that true slug flow is not found for these qualities and mass fluxes for refrigerants. Instead, a slug with vapor bubbles is formed, which does not cause large pressure fluctuations.

4.2.3. Mist flow analysis

As was discussed in Sec. 4.1, mist flow occurs for qualities at and above 95%. At these higher qualities, the liquid layer on the wall dries out and liquid droplets become entrained in the vapor core. As the liquid layer thins and more droplets become entrained in the vapor core, the mean pressure drop begins to decrease. The transition between annular and annular-mist flow using the maximum pressure drop value was first proposed by Chien and Ibele [1964] for air-water flow. In addition, the $\sigma / \bar{x}$ ratio begins to increase. Figure 4.20 is a plot of this ratio for R-134a at a mass flux of 225 klb_m/ft^2-hr including the higher quality tests. For detection of a transition to mist flow, the increase in surface temperature in the test section along with a corresponding decrease in the heat transfer coefficient appear to be the best criteria.

4.3. Flow Pattern Indicators and Criteria for Refrigerants

Based on the subjective, visual observations and the objective high speed pressure and pressure drop measurements, several conclusions can be drawn regarding the transitions found during two-phase horizontal flow of refrigerants. Under typical refrigerator evaporator conditions, stratified, wavy, annular, and mist flow were observed. Varying amounts of slug flow were superimposed on these basic flow patterns. For

qualities above 5%, the analysis of the slug flow through cross-correlation of high speed pressure measurements indicated that these slugs could be classified as pseudo-slugs, which are slugs with vapor bubbles showing little difference in pressure fluctuation with separated flows such as wavy and annular flow patterns.

Statistical and spectral indicators, such as the probability density function and the normalized power spectral density, did not adequately distinguish between wavy and annular flow. The normalized power spectral densities were similar between wavy and annular flow patterns with the majority of power located near zero frequency. The normalized probability density functions were much more spread out for wavy flows compared with annular flows. The main difference in statistical properties between wavy and annular flows occurred based on the magnitudes of the mean pressure drop. From the statistical analysis, the parameter which was most consistent in distinguishing between wavy and annular flows was the standard deviation to mean ratio of the differential pressure drop. For values below 0.10, annular flow was found to occur, while for values above 0.20, wavy flow was found to occur. Transition between the two flow patterns occurred between 0.10 and 0.20.

Transition from annular flow to annular-mist flow, where a significant amount of entrainment was present, was assumed to occur when the mean pressure drop decreased as quality increased for a fixed mass flux, and the standard deviation to mean pressure drop ratio increased as quality increased for a fixed mass flux. This assumption was based on a theory proposed by Chien and Ibele [1964] for air-water flow. Mist flow was detected when an increase in surface temperature occurred along with a corresponding decrease in the heat transfer coefficient.

Of the flow pattern maps, the Taitel-Dukler map predicted the observed flow patterns most accurately. However, the wavy-slug flow and annular-slug flow transition line should be shifted to higher X values, and an insertion of a pseudo-slug region should be included to accurately account for refrigerant flow patterns.

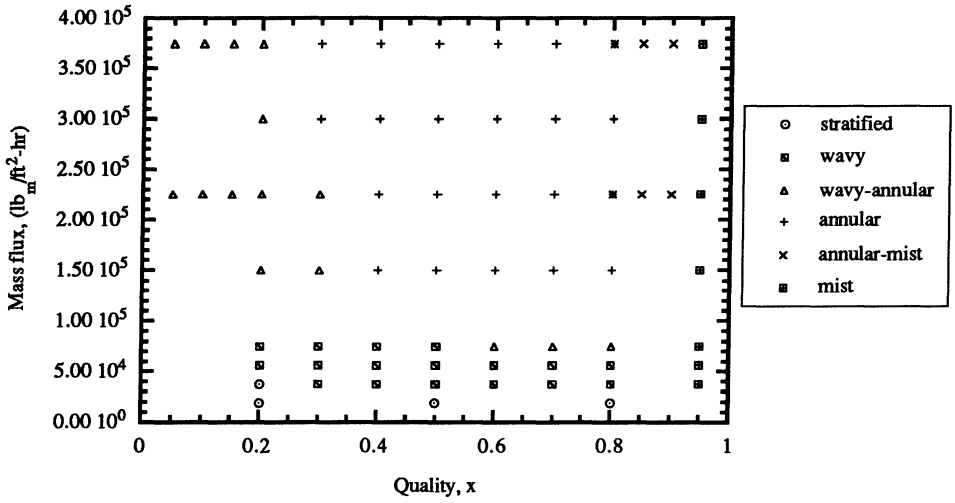

Figure 4.1. Experimental flow patterns on a G-x map for R-134a. Saturation temperature, 41°F; Tube diameter, 0.430 in.

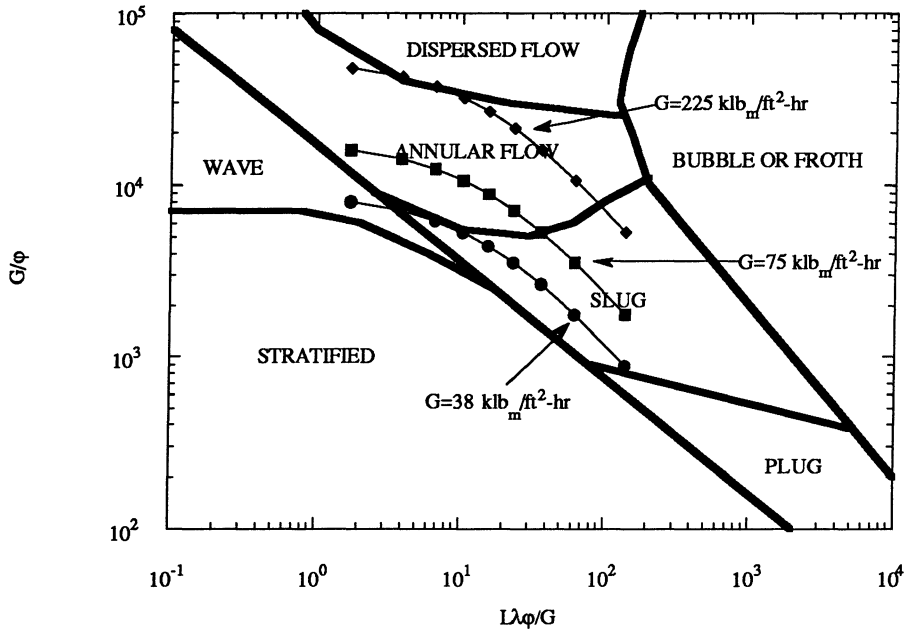

Figure 4.2. Experimental flow patterns on the Baker map for R-134a. Saturation temperature, 41°F; Quality, 10-90%; Tube diameter, 0.430 in.

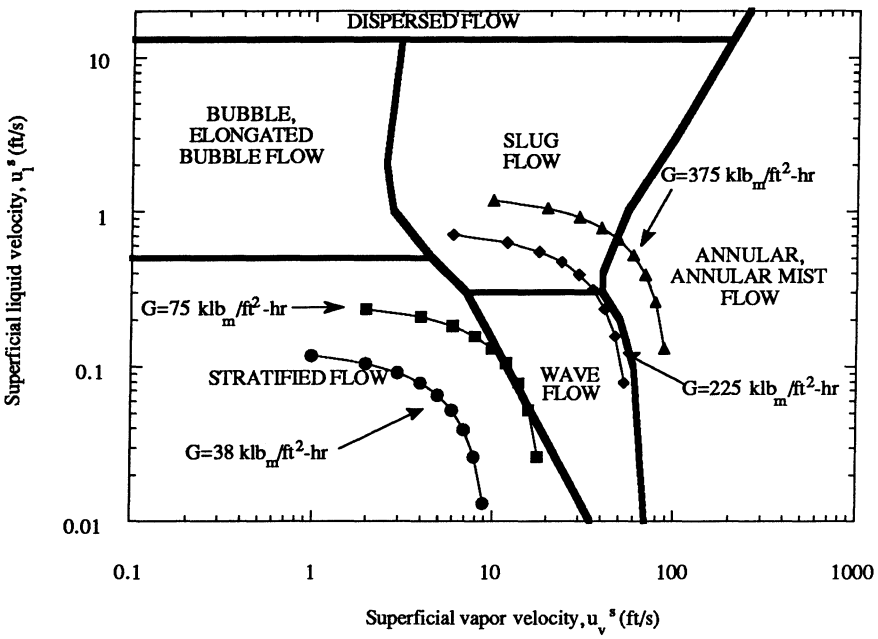

Figure 4.3. Experimental flow patterns on the Mandhane map for R-134a. Saturation temperature, 41°F; Quality, 10-90%; Tube diameter, 0.430 in.

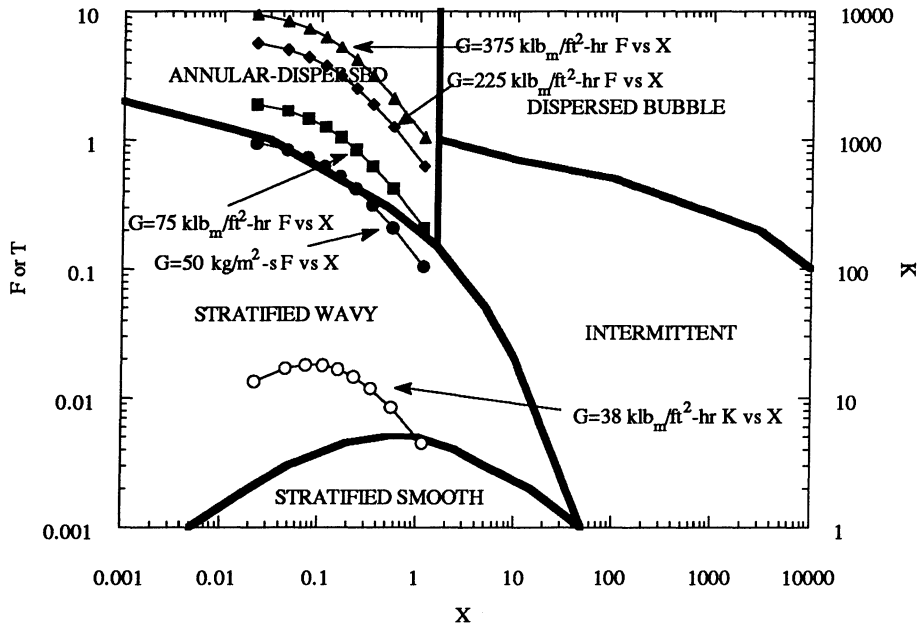

Figure 4.4. Experimental flow patterns on the Taitel-Dukler map for R-134a. Saturation temperature, 41°F; Quality, 10-90%; Tube diameter, 0.430 in.

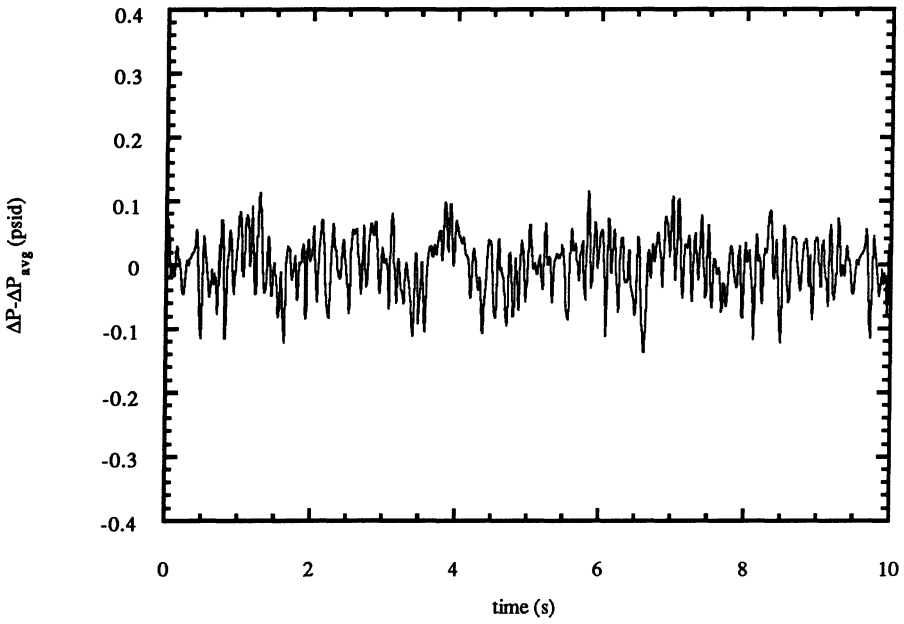

Figure 4.5. Differential pressure-time trace for annular flow for R-134a. Mass flux, 225 klb_m/ft^2-hr; Saturation temperature, 41°F; Quality, 40%; Tube diameter, 0.430 in.

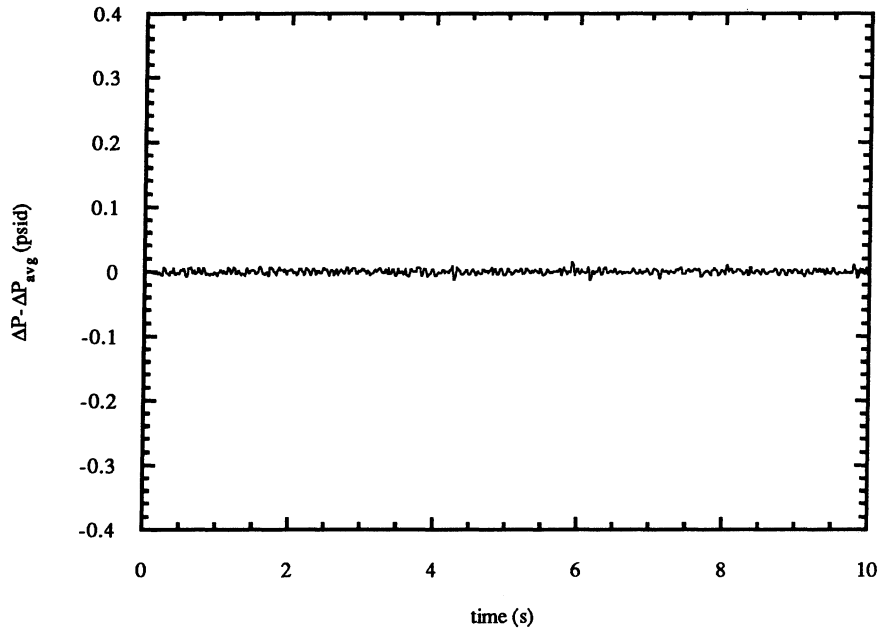

Figure 4.6. Differential pressure-time trace for wavy flow for R-134a. Mass flux, 38 klb_m/ft^2-hr; Saturation temperature, 41°F; Quality, 40% Tube diameter, 0.430 in.

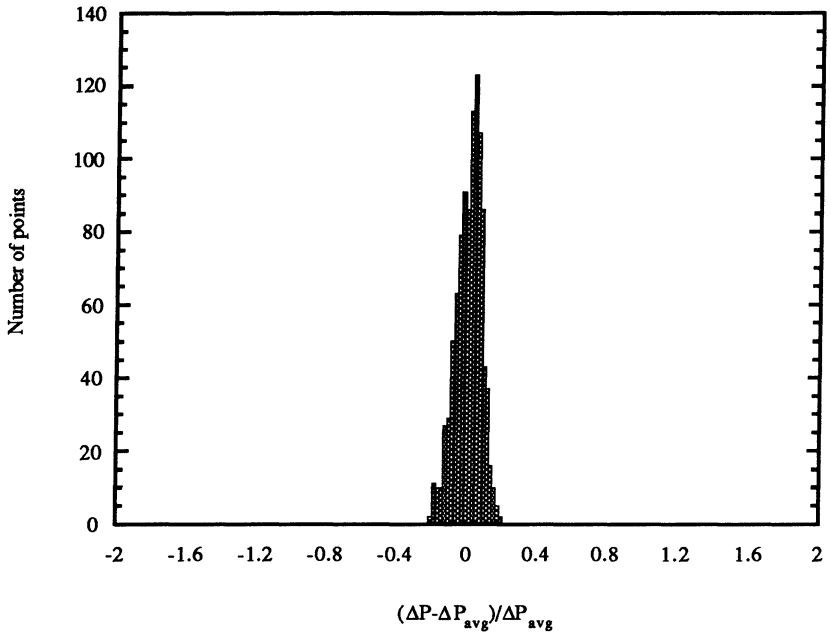

Figure 4.7. Normalized probability density function of pressure drop for annular flow for R-134a. Mass flux, 225 klb_m/ft^2-hr; Saturation temperature, 41°F; Quality, 40%; Tube diameter, 0.430 in.

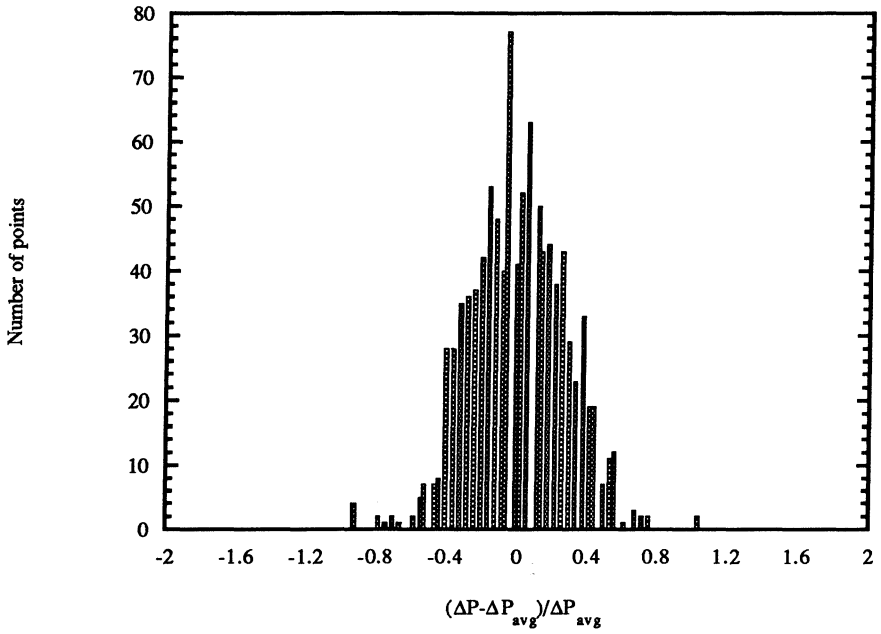

Figure 4.8. Normalized probability density function of pressure drop for wavy flow for R-134a. Mass flux, 38 klb_m/ft^2-hr; Saturation temperature, 41°F; Quality, 40%; Tube diameter, 0.430 in.

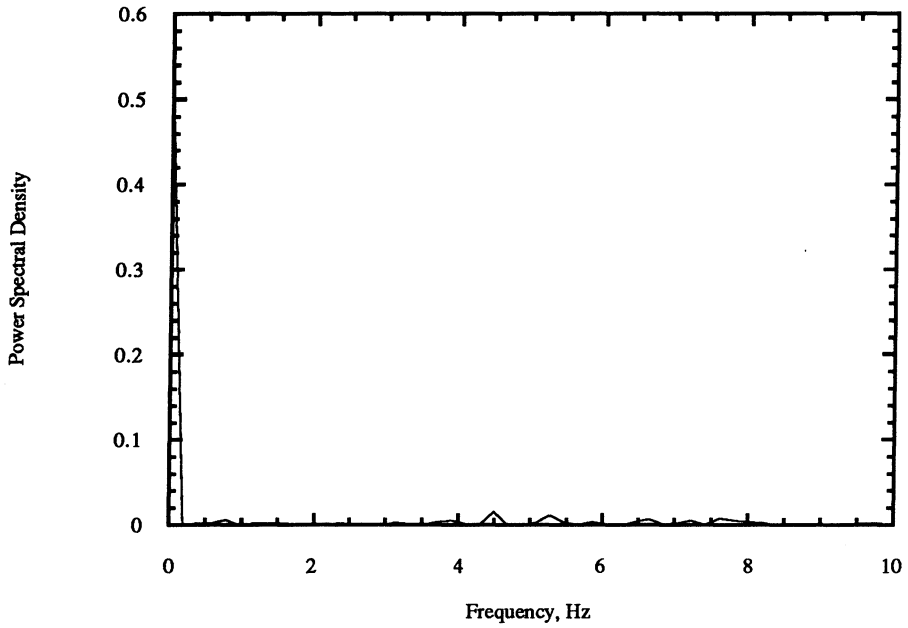

Figure 4.9. Normalized power spectral density of pressure drop for annular flow for R-134a. Mass flux, 225 klb_m/ft^2-hr; Saturation temperature, 41°F; Quality, 40%; Tube diameter, 0.430 in.

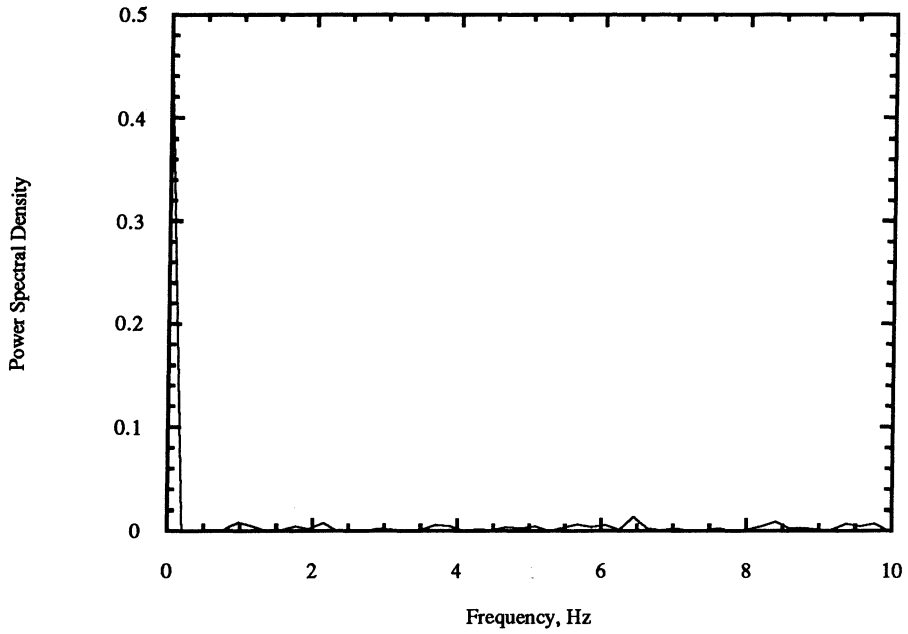

Figure 4.10. Normalized power spectral density of pressure drop for wavy flow for R-134a. Mass flux, 38 klb_m/ft^2-hr; Saturation temperature, 41°F; Quality, 40%; Tube diameter, 0.430 in.

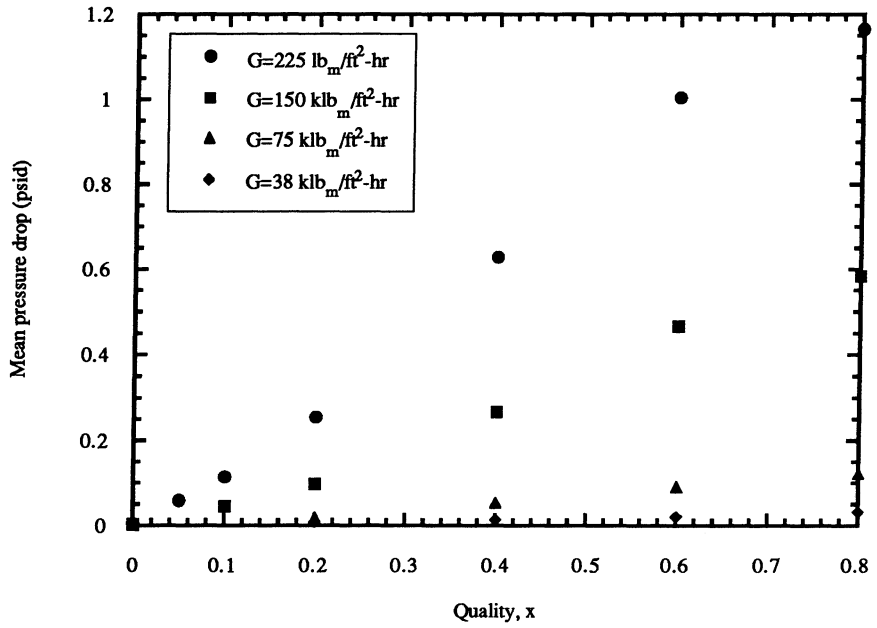

Figure 4.11. Mean pressure drop versus quality for varying mass flux for R-134a. Saturation temperature, 41°F; Tube diameter, 0.430 in.

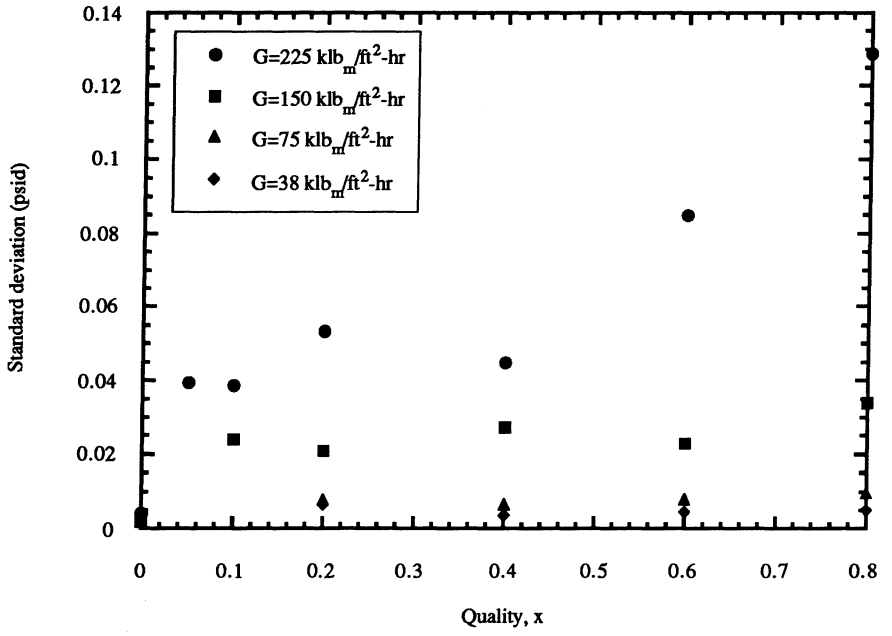

Figure 4.12. Standard deviation of pressure drop versus quality for varying mass flux for R-134a. Saturation temperature, 41°F; Tube diameter, 0.430 in.

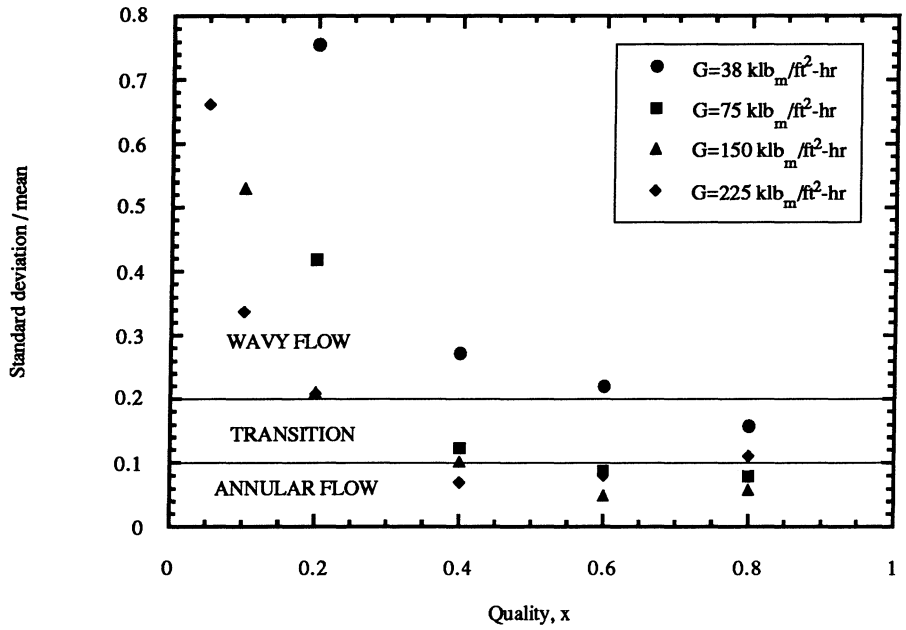

Figure 4.13. $\sigma / \bar{x}$ of pressure drop versus quality for varying mass flux for R-134a. Saturation temperature, 41°F; Tube diameter, 0.430 in.

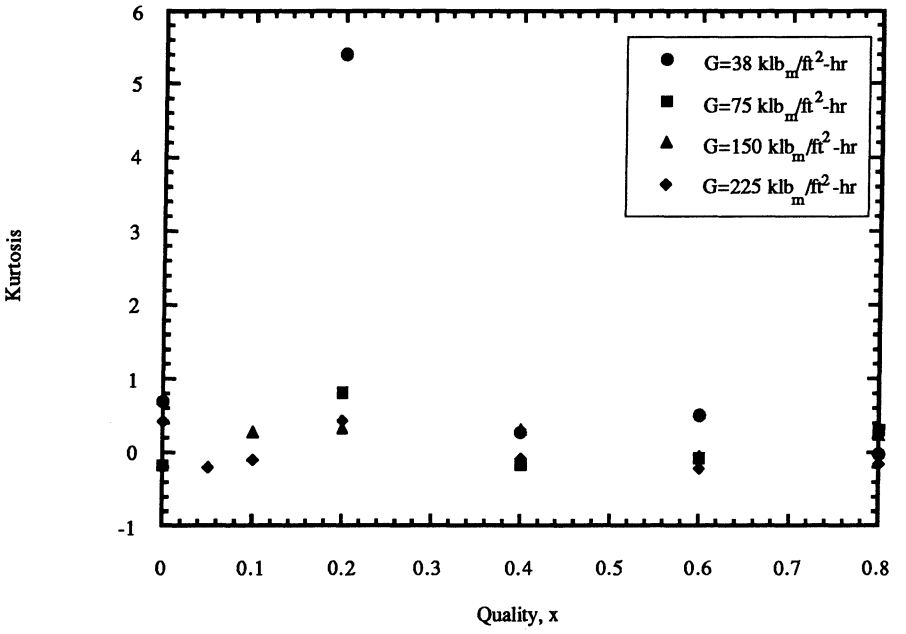

Figure 4.14. Kurtosis of pressure drop versus quality for varying mass flux for R-134a. Saturation temperature, 41°F; Tube diameter, 0.430 in.

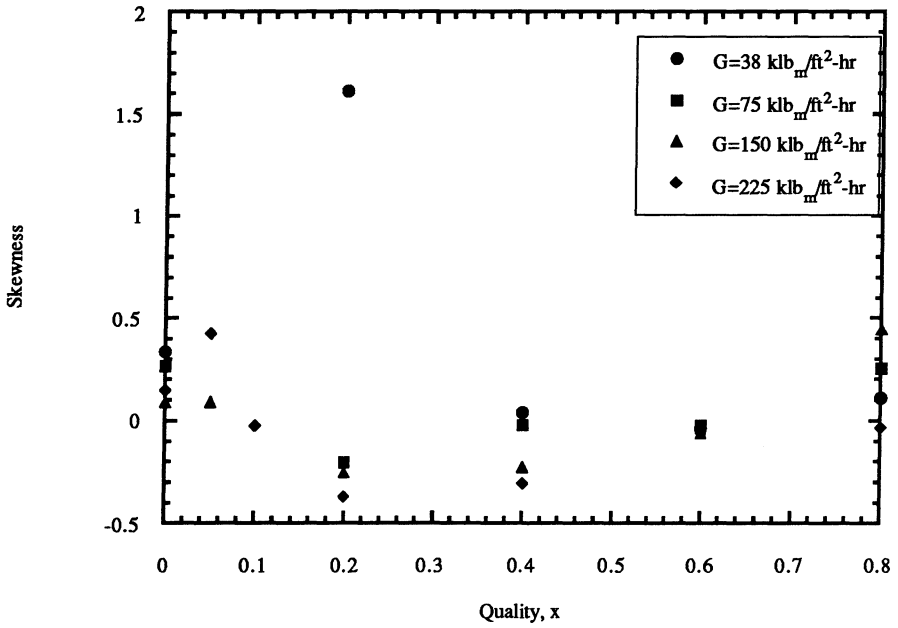

Figure 4.15. Skewness of pressure drop versus quality for varying mass flux for R-134a. Saturation temperature, 41°F; Tube diameter, 0.430 in.

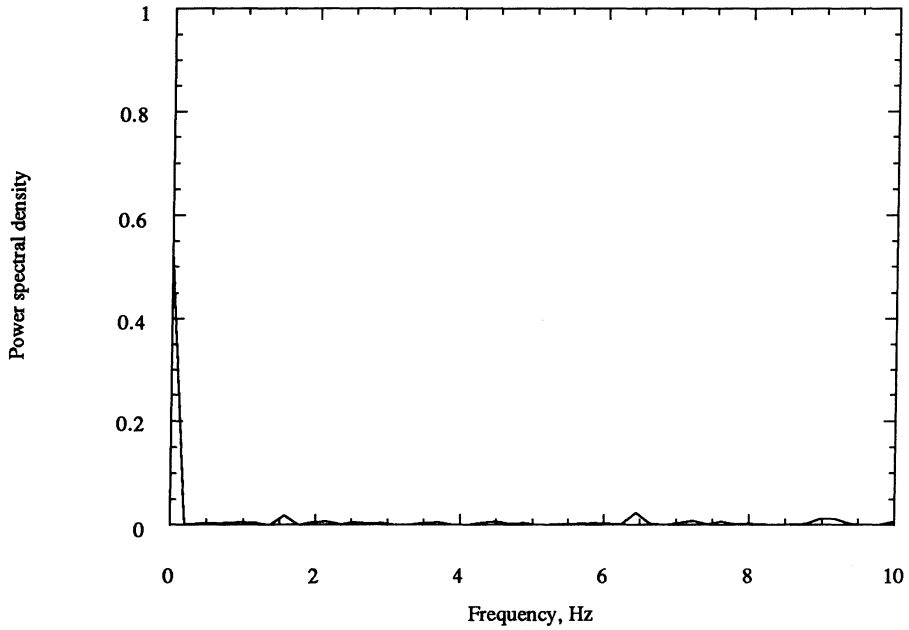

Figure 4.16. Normalized power spectral density for 5% quality case. Mass flux, 225 klb_m/ft^2-hr; Saturation temperature, 41°F; Tube diameter, 0.430 in.

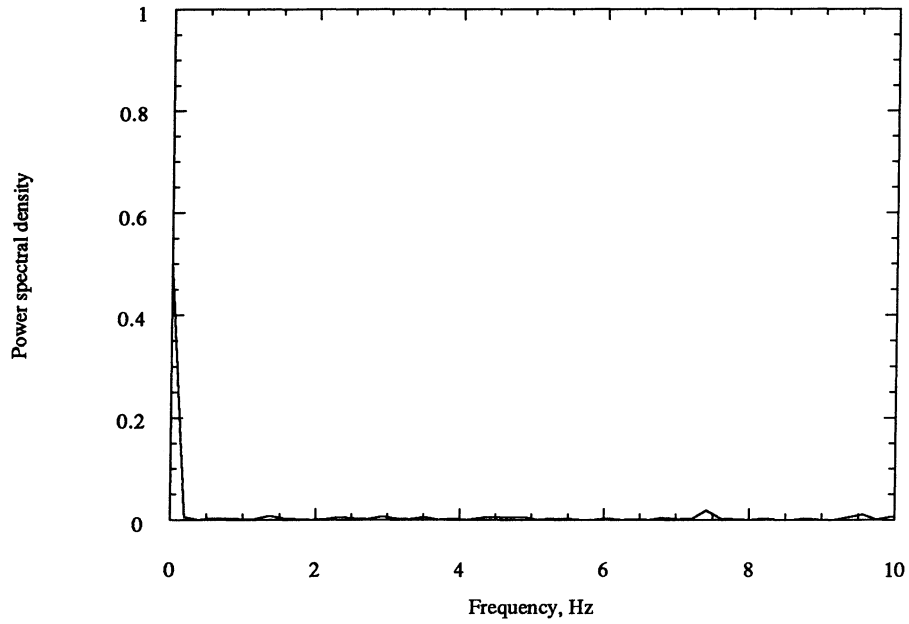

Figure 4.17. Normalized power spectral density for 10% quality case. Mass flux, 225 klb_m/ft^2-hr; Saturation temperature, 41°F; Tube diameter, 0.430 in.

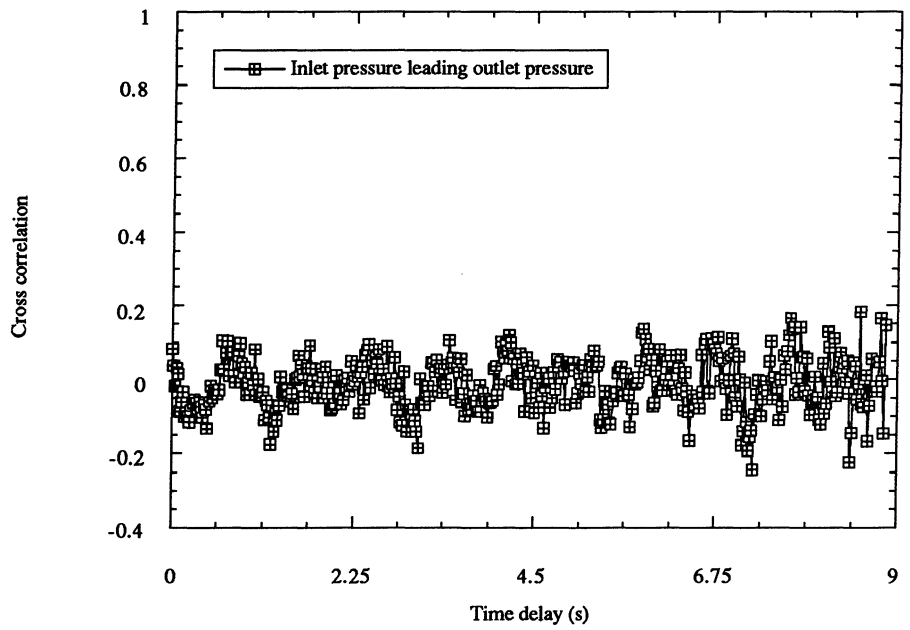

Figure 4.18. Cross-correlation of inlet and outlet absolute pressure signals for 0.305 in i.d. test section at 5% quality for R-134a. Mass flux, 225 klb_m/ft^2-hr; Saturation temperature, 41°F.

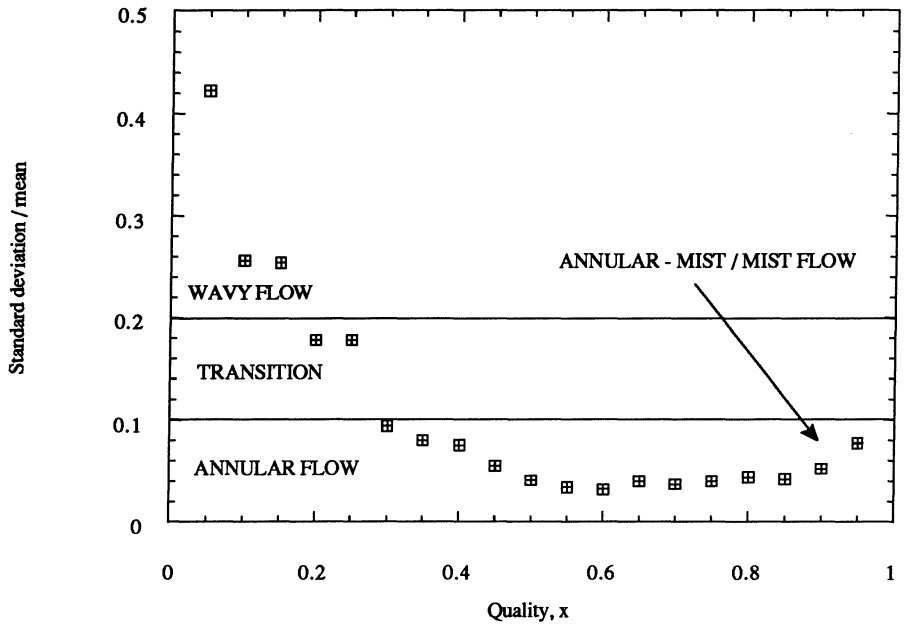

Figure 4.20. $\sigma / \bar{x}$ of differential pressure drop for annular-mist and mist flow. Mass flux, 225 klb_m/ft^2-hr; Saturation temperature, 41°F; Tube diameter, 0.430 in.

CHAPTER 5. EXPERIMENTAL HEAT TRANSFER RESULTS

In this chapter, the heat transfer coefficient data over the wide range of experimental parameters will be discussed. Differences between high mass flux annular flows and low mass flux wavy flows will be examined. The variation of heat transfer coefficient based on heat flux, refrigerant, and tube diameter will also be discussed. Wall superheats will be compared with the relations from Chap. 2 regarding the onset of nucleate boiling. The resulting experimental heat transfer coefficient data will be compared with selected correlations from the literature.

Utilizing the experimental heat transfer coefficient data, a correlation was developed by Project 01 of the Air Conditioning and Refrigeration Center to predict these heat transfer coefficients. The asymptotic form selected for this correlation will first be explained. The convective term will be developed through combination of the appropriate two-phase multiplier and single-phase heat transfer coefficient term. The nucleate boiling term will be selected based on the variation of the heat transfer coefficient with heat flux and pressure. Low mass flux effects will then be accounted for by adjusting the convective term through both the two-phase multiplier and single-phase heat transfer coefficient. The asymptotic value of n for the correlation will then be selected. Finally, the correlation will be compared to the complete set of experimental refrigerant data. The correlation will also be compared with data from several additional studies in the literature.

5.1. Experimental Heat Transfer Coefficient Test Data

The single-tube evaporator test facility was utilized by the Air Conditioning and Refrigeration Center to measure evaporation characteristics of CFC, HFC, and HCFC refrigerants. Testing was conducted for higher mass fluxes and heat fluxes similar to those found in automotive air conditioning and stationary air conditioning evaporators and for lower mass fluxes and heat fluxes similar to those found in household refrigerator evaporators.

The test sections consisted of 0.277, 0.305, 0.402, and 0.430 in inside diameter copper tubes. The 0.277 in i.d. and 0.430 in i.d. test sections were 8 ft in length, whereas the 0.305 in i.d. and 0.430 in i.d. test sections were 4 ft in length. Parameters for the testing, as summarized in Tables 3.4 through 3.12 of Chap. 3, were as follows: mass flux, 19-750 klb_m/ft^2-hr; heat flux, 640-12,800 Btu/hr-ft^2; quality, 5-95%; saturation temperature, -4 to 59°F. R-134a, R-12, R-22, and a 60%/40% azeotropic mixture of R-32/R-125 were used as test fluids. Flow patterns were determined by strobe-light

enhanced visual observation from sight glasses at the inlet and outlet of the test section. For higher mass flux testing, the predominant flow pattern was annular flow. For lower mass flux testing, the predominant flow pattern was wavy flow. Superimposed with these flow patterns were varying amounts of slug flow.

In the following sections, the experimental data from Table 3.7, the basic test matrix, will first be described in detail. These tests covered the parameter ranges most efficiently, and contained all of the basic trends in the data. Earlier tests results, as described in Tables 3.5 and 3.6, are summarized in several works by Wattelet et al. [1990, 1991, 1992] and Panek et al. [1992]. The results of these tests are presented in tabular form in Appendix B. The developed correlation presented later in this chapter will be compared with the earlier data. In addition, the results of the specialty testing, described in Tables 3.8 through 3.12, will be explored. These tests include low and high quality testing, variable saturation temperature testing, low heat flux testing, and high mass flux testing.

5.1.1. Basic test matrix — annular flow data

Figures 5.1 and 5.2 show the variation of heat transfer coefficient versus quality for annular flow tests with a fixed mass flux and varying heat flux for R-134a for 0.430 in i.d. and 0.305 in i.d. tubes, respectively. As can be noted, for low heat fluxes, the heat transfer coefficient increased with quality. Intense evaporation at the liquid-vapor interface diminished the liquid film thickness, reducing the thermal resistance, which was associated with heat conduction across the film. Nucleate boiling appeared to be largely suppressed for these low heat flux cases. As heat flux increased, the heat transfer coefficients increased in the lower quality region and eventually merged at higher qualities with the heat transfer coefficients for low heat flux cases. Nucleate boiling at these lower qualities enhanced the heat transfer coefficient. At higher qualities, nucleate boiling was again largely suppressed due to significant surface cooling promoted by the thinning of the annular film. Wall superheats for this set of data ranged from 1.8 to 10.8°F.

Similar results were found for refrigerants R-12, R-22, and R-32/R-125, as shown in Figs. 5.3 through 5.5, for the 0.430 in i.d. test section. However, some differences were noted, such as the effect of pressure on the heat transfer coefficient. Table 3.13 listed the various thermodynamic and transport properties for the refrigerants at 41°F. The reduced pressures of these refrigerants at 41°F are as follows: 0.086 for R-134a; 0.088 for R-12, 0.117 for R-22; and 0.190 for R-32/R-125. As the reduced pressure increased, the effect of heat flux and nucleate boiling became stronger. This was seen most dramatically by comparing the results of the R-12 and R-32/R-125 tests in Figs. 5.3 and

5.5. For R-12 and low heat fluxes, the magnitude of the heat transfer coefficient increased by a factor of 3 from 20 to 90%, showing a strong convective component. On the other hand, R-32/R-125 showed less than a two-fold increase in the magnitude of the heat transfer coefficient. At the higher reduced pressure, a larger nucleate boiling effect was found. The low heat flux plot is much flatter for R-32/R-125 than R-12. In addition, the thermal properties of R-32/R-125 are much better than R-12, resulting in both higher convective and nucleate boiling contributions to the heat transfer coefficient.

For the predominantly annular flow pattern testing, the heat transfer coefficient increased as mass flux was increased for a fixed heat flux and quality, as shown in Fig. 5.6 for R-134a in the 0.305 in i.d. test section. Figures 5.7 and 5.8 show the variation of heat transfer coefficient versus quality for R-134a and R-22, respectively, for high and low heat flux testing as mass flux is increased. Inertial effects increased turbulence in the flow as the mass flux increased, creating a more dominant convective term. Heat transfer coefficients for the high heat flux tests for a mass flux of 150 and 225 klb_m/ft^2-hr were fairly constant, indicating more of a nucleate boiling dominant situation. For a mass flux of 375 kg/m^2-s and a high heat flux of 9600 Btu/hr-ft^2, the heat transfer coefficients moved higher above 60%, indicating that the convective boiling contribution again became larger than the nucleate boiling contribution.

Inside tube diameter presented little change in the magnitude of the heat transfer coefficient for the same flow parameters. Comparison of all of the heat transfer coefficient data of the 0.430 in i.d. tube to the heat transfer coefficient data 0.305 in i.d. tube resulted in an overall increase of less than 10% for the 0.305 in i.d. tube, well within the statistical uncertainty of the data. More of a discussion on the variation of tube diameter on the heat transfer coefficient results will be given in the next section on wavy flow data.

Of the four refrigerants, R-32/R-125 had the highest overall heat transfer coefficients for the annular flow data. With a temperature glide of 0.07°F, the 60%/40% azeotropic mixture of R-32/R-125 had similar behavior to pure refrigerants for heat transfer and pressure drop. A high convective transport property ratio, $k_l^{0.6}c_{pl}^{0.4}/\mu_l^{0.4}$, which was derived from the single-phase Dittus-Boelter correlation and discussed in Chap. 2, combined with a relatively high reduced pressure to facilitate nucleate boiling, resulted in heat transfer coefficients that were 25 to 75% higher than R-12. R-22 and R-134a had similar heat transfer coefficients, with overall results within 10% of each other. R-134a had a slightly higher convective contribution, while R-22 had a slightly higher nucleate boiling contribution due to a higher reduced pressure at 41°F. R-12 had the lowest convective and nucleate boiling properties of the four refrigerants.

It should also be noted that, in a typical refrigerant evaporator for the same heat load, mass fluxes would be different for each refrigerant since the heat of vaporization also varies with refrigerant. R-32/R-125 has the highest heat of vaporization, followed by R-22, R-134a, and R-12. Mass fluxes would be increased or decreased to match a certain load requirement. This would inevitably bring the heat transfer coefficients closer together for this equivalent cooling capacity basis. The discussion above in the preceding paragraph was based on an equivalent mass flux. Additional comparisons based on these equivalencies will be given in the next chapter on evaporator design.

5.1.2. Basic test matrix — wavy flow data

For wavy tests, there was no major effect of quality on the circumferentially averaged heat transfer coefficients, as can be seen in Figs. 5.9 and 5.10 for R-134a in the 0.305 in i.d. and 0.430 in i.d. test sections. However, as the heat flux increased, the heat transfer coefficient also increased. Compared with the results in the annular flow regime, convective boiling was diminished while nucleate boiling did not appear to be suppressed at higher qualities or lower heat fluxes. The decrease in convective boiling can be attributed to the reduction in available surface area for convective boiling, a decrease in turbulence due to the decreased Reynolds numbers for the low mass fluxes, and a decrease in slip ratio between the vapor and liquid streams. Wall superheats for this set of data ranged from 3.6 to 9.0°F. Similar results were found for R-12, R-22, and R-32/R-125, and are shown in Figs. 5.11 through 5.13.

R-32/R-125 again had the highest heat transfer coefficients of the four refrigerants, followed by R-22, R-134a, and R-12, respectively. For these tests, the more dominant contribution came from the heat flux or nucleate boiling portion of the heat transfer coefficient. This resulted in a higher heat transfer coefficient for R-22 than R-134a for wavy flow, which was different from the similar heat transfer coefficients found for annular flow.

Tube diameter had a slightly larger influence for the wavy tests compared with the annular flow tests, although again the increases in magnitude were near the uncertainty limits. Again, the complete data sets of the 0.430 in i.d. and 0.305 in i.d. test sections were compared for the wavy tests. The heat transfer coefficients for the 0.305 in i.d tests were higher by 10% on average compared with the 0.430 in i.d. tests. There appeared to be a slightly larger effect of heat flux or nucleate boiling for the smaller tube diameter. The effect of tube diameter on the heat transfer coefficient will be discussed further in Sec. 5.2.

5.1.3. Low quality tests

Refrigerant evaporator inlet qualities are typically near 20%. At qualities below this value, previous studies have shown more wavy flow patterns with slug flow occasionally superimposed with this flow pattern. Figures 5.1 and 5.2 show the heat transfer coefficient variation versus quality for the low quality tests outlined in Table 3.8 for the 0.305 in i.d. and 0.430 in i.d. test sections. As can be noted, the heat transfer coefficients were relatively constant in this quality range, even for the low heat flux tests. This can be compared with the linear increase in heat transfer coefficient with quality for the higher quality and lower heat flux tests shown in Figs. 5.1 and 5.2. In the lower quality region, there was a higher heat flux dependency, indicating that nucleate boiling was more important. Wall superheats for these tests ranged from 5.4 to 10.8°F. Heat transfer coefficients in the low quality region for wavy flow also were highly dependent on heat flux, as shown in Fig. 5.10. This trend was similar to the pattern found for higher quality wavy flow.

5.1.4. High quality tests

At higher qualities above 80%, the liquid layer became fairly thin for both wavy and annular flows. Eventually, the liquid layer completely evaporated, leaving only liquid droplets that were entrained in a vapor core. As discussed in earlier chapters, this flow pattern is called mist flow, and a study of where the transition quality between annular and mist flow and wavy and mist flow was also conducted. Table 3.9 shows the tests conducted to determine the dryout transition quality.

For a constant mass flux, the transition to mist flow occurred for qualities above 95%. The transition quality was really a band of qualities over which mist flow began to occur. As described in Fig. 2.14 [Wedekind, 1971], the mist flow transition line oscillated over time. From the testing conducted, no major effect of heat flux was found on the transition quality band for a constant mass flux.

Figure 5.14 shows the changes in the heat transfer coefficient and pressure drop as quality was varied for a mass flux of 225 klb_m/ft^2-hr. The pressure drop had a maximum value at a quality of around 80%. This was the point where a visual indication of entrainment began, with liquid still coating the tube wall. It should be noted that the visual detection of entrainment was very difficult from the side view sight glasses used. This was the point where transition from annular to annular-mist flow began. The determination of this transition using the maximum pressure drop value was first proposed by Chien and Ibele [1964] for air-water flow. As quality increased, the liquid layer decreased until the wall partially and then completely dried out, leading to a decrease in the heat transfer

coefficient as complete mist flow was encountered above qualities of 95%. In some cases, mist flow was not completely observed until a quality of nearly 100%. In these cases, the heat transfer coefficient continued to rise throughout the entire quality range.

5.1.5. Tests on the variation of saturation temperature

Figures 5.15, 5.16, and 5.17 show the heat transfer coefficient versus quality plots for a 225 klb_m/ft^2-hr mass flux for R-134a at 23°F, 41°F, and 59°F, at heat fluxes of 1600, 3200, and 6400 $Btu/hr\text{-}ft^2$, respectively. The variation of saturation temperature had an effect on both the convective and nucleate boiling components of the heat transfer coefficient. As temperature increased, the convective contribution decreased due to decreased convective thermal properties ($k_l^{0.6} c_{p_l}^{0.4} / \mu_l^{0.4}$, as discussed in Chap. 2) and lower two-phase multiplier effects. More of a linear increase in heat transfer coefficient with quality could be found at 23 and 41°F than at 59°F, as indicated in Fig. 5.15 for a heat flux of 1600 $Btu/hr\text{-}ft^2$. In addition, the convective thermal properties at the lower temperatures were higher, resulting in increased heat transfer coefficients at the same quality. However, as the temperature increased, reduced pressure increased and helped to promote nucleate boiling which enhanced the heat flux effect on the heat transfer coefficient. At 59°F, the variation of the heat transfer coefficient with quality for fixed mass and heat fluxes was much less than at the lower temperatures.

For the 3200 $Btu/hr\text{-}ft^2$ tests shown in Fig. 5.16, the nucleate boiling effects became stronger at 59°F. The magnitudes of the heat transfer coefficients were much more similar than in Fig. 5.17 due to competing contributions between the nucleate boiling and convective boiling effects. In Fig. 5.17, the 59°F heat transfer coefficients became the highest compared with the 23°F and 41°F heat transfer coefficients due to the increased nucleate boiling effects for the 6400 $Btu/hr\text{-}ft^2$ tests. These were exactly opposite of the results for the low heat flux tests shown in Fig. 5.15.

Figs. 5.18 and 5.19 show similar effects for R-22 for heat fluxes of 1600, 3200, and 6400 $Btu/hr\text{-}ft^2$ at temperatures of 59°F and 23°F, respectively. In Fig. 5.18, the heat transfer coefficients at each heat flux were different, showing the increased nucleate boiling contribution as heat flux was increased. However, in Fig. 5.19, the heat transfer coefficients fell along a banded line, except for the 6400 $Btu/hr\text{-}ft^2$ points at low quality where nucleate boiling effects were still important. Here, convective boiling effects dominated with increased heat transfer coefficients at higher qualities compared with the results of Fig. 5.18 because of increased convective transport properties at the lower temperature.

Figure 5.20 shows the variation of heat transfer coefficient versus quality for a mass flux of 38 klb_m/ft^2-hr and saturation temperatures of 23°F and 41°F. There was more of a linear variation with quality for the 5°F tests compared with the 41°F tests. Again, this was due to an increased convective contribution and a decreased nucleate boiling contribution. It should be noted, however, that there was an increased uncertainty in the heat transfer coefficient at the lower saturation temperature due to the increased heat gain from the environment to both the preheater and test section. The heat gain was on the same order as the heat input.

5.1.6. Low heat flux tests

The convective contribution to the heat transfer coefficient was determined through a set of low heat flux tests, designed to reduce the contribution of the nucleate boiling term to an insignificant amount. The low heat flux testing, shown in Table 3.11, is plotted in Figs. 5.21 and 5.22 for R-12 and R-134a, respectively. Shown in these plots is the variation of heat transfer coefficient versus quality for 960, 1600, and 3200 $Btu/hr\text{-}ft^2$ heat fluxes. The 960 and 1600 $Btu/hr\text{-}ft^2$ tests merged around 60% quality, while the 3200 $Btu/hr\text{-}ft^2$ tests merged at near 80%. Differences in magnitude between the 960 and 1600 $Btu/hr\text{-}ft^2$ tests were below 10% for qualities under 60%. Uncertainties in these tests ranged between 10 and 25%. Based on these data, the low heat flux testing represented the approximate point where the convective contribution was the dominant mode of heat transfer. The 1600 $Btu/hr\text{-}ft^2$ tests for R-134a and R-12 were used as the data to calculate the convective contribution to the heat transfer coefficient correlation. This will be discussed in the following section.

Wall superheats for the 960 $Btu/hr\text{-}ft^2$ tests ranged from 1.1 to 3.6°F. Based on examination of all of the data above and comparison with the required wall superheats for the theoretical models described in Chap. 2, the conclusion can be drawn that nucleate boiling was present for all tests. However, for the low heat flux testing, the convective contribution dominated the nucleate boiling portion, making the contribution of the nucleate boiling term small compared to the overall two-phase flow boiling heat transfer coefficient.

5.1.7. Wall superheat and heat flux effects

Figures 5.23 through 5.25 show the heat transfer coefficient versus heat flux for mass fluxes of 38, 225, and 375 klb_m/ft^2-hr. For lower heat fluxes in Figs. 5.24 and 5.25, the points at each heat flux were different, indicating that the heat transfer coefficients were relatively independent of heat flux and contributions of nucleate boiling. As heat flux increased, the points moved toward each other, indicating more dependence on heat flux,

representing nucleate boiling. Values of the heat transfer coefficient for the 225 klb_m/ft^2-hr mass flux were almost identical at each value of quality for a heat flux of 9600 Btu/hr-ft^2, while heat transfer coefficients for the 375 klb_m/ft^2-hr and a heat flux of 9600 Btu/hr-ft^2 were independent of each other at each value of quality, still indicating a dominant convective presence. For a mass flux of 38 klb_m/ft^2-hr in Fig. 5.23, the points were close together at all heat fluxes and qualities and were strongly dependent on heat flux, indicating a strong nucleate boiling contribution for all points.

Figures 5.26 through 5.28 show the heat flux versus wall superheat for mass fluxes of 38, 225, and 375 klb_m/ft^2-hr. For low heat fluxes in Figs. 5.27 and 5.28, the points were independent of each other at each quality, indicating convective boiling was the dominant mode of heat transfer. As wall superheat increased, the points on each curve moved closer together, indicating increased presence of nucleate boiling. In Fig. 5.26, the curves were nearly identical for each heat flux, indicating that nucleate boiling was present for all points.

5.1.8. Comparison with other correlations

Three heat transfer correlations were selected from the literature to compare with the experimental values of the heat transfer coefficient. The correlations selected were the Shah [1982], Kandlikar [1990], and Jung-Radermacher [1989] correlations. Each of these correlations can be found in Table 2.4. The correlations of Shah and Kandlikar were selected because of their use of R-12 and R-22 as test fluids and the presence of a Froude number dependent term to account for wavy flow. The Shah correlation was the first generalized correlation developed and evaluates equations for the nucleate boiling, bubble suppression, and convective boiling dominated regimes, selecting the largest of the three values. The Kandlikar correlation uses the greater of the nucleate boiling and convective boiling dominated forms. It differs from the Shah correlation in its use of boiling number for both the nucleate boiling and convective boiling regimes. It also uses a fluid specific term to account for variations of the nucleate boiling component in each form.

The Jung-Radermacher correlation was selected because of its use of a pool boiling heat transfer coefficient term and its use of a reduced pressure term to account for the property ratios in the Lockhart-Martinelli parameter. Data for this correlation were obtained using refrigerants in an electrically-heated stainless steel test section. There appeared to be much less nucleate boiling in the data of their study using a stainless steel test section than in the data of this study using a copper test section.

Figures 5.29, 5.30, and 5.31 are plots of the predicted heat transfer coefficients for the four refrigerants used in this study from the correlations of Kandlikar, Shah, and Jung-

Radermacher, respectively, versus experimental heat transfer coefficients for the four refrigerants for annular and wavy flow. The mean deviations of the three correlations are given in Table 5.1 for both wavy and annular flow tests. The Kandlikar correlation did the best job predicting the heat transfer coefficient data. The presence of the Froude number dependent term accounted for stratification effects, and the fluid specific parameter helped to adjust the nucleate boiling contribution for each different fluid. A value of 3.3 was used for the fluid specific parameter for R-32/R-125. This value was determined using the data set in this study. The Shah correlation did an excellent job for convective dominated flows and also did adequately for wavy flows because of the Froude number dependent term. However, the lack of a heat flux dependent term for the quality range that Shah defines as convectively dominated caused large deviations when the Shah correlation was compared to the R-32/R-125 data and the high heat flux, low mass flux data. The Jung-Radermacher correlation did an excellent job in the annular flow region, but because of the correlation's lack of a Froude number dependent term, it should not be extrapolated to mass fluxes below 150 klb_m/ft^2-hr. Results for the annular data only are shown in the parentheses of Table 5.1 for the Jung-Radermacher correlation. In addition, the small nucleate boiling component to the correlation at higher qualities caused the correlation to severely underestimate the R-32/R-125 data.

Even with the Froude number dependent terms in the Shah and Kandlikar correlations, there was still a much higher standard deviation in the wavy flow region of tests than in the annular flow region of tests. Improvements in the correlations can definitely be made in this area. In addition, the trend of the heat transfer coefficient versus quality for a constant mass flux and heat flux differed substantially from correlation to correlation, as was shown in Chap. 2. Another look at combining the effects of the convective and nucleate boiling terms is also warranted.

Table 5.1. Comparison of mean deviation* between the various correlations and the experimental data for R-12, R-134a, R-22, and R-32/R-125

Correlation	R-12	R-134a	R-22	R-32/R-125
Kandlikar	14.8	12.6	13.5	14.0
Shah	12.9	16.2	20.2	38.1
Jung-Rad.	30.8 (16.7)	19.6 (15.5)	18.9 (18.4)	28.7 (28.7)

* Mean deviation is defined as the absolute value of the difference between the experimental and predicted heat transfer coefficients divided by the experimental heat transfer coefficient multiplied by 100%.

5.2. Heat Transfer Coefficient Correlation Development

In this section, the development of the heat transfer coefficient correlation will be discussed. Selection of the form of the correlation will first be justified. Next, the convective term will be examined using convective boiling dominated data to develop the two-phase multiplier for heat transfer. Selection of the single-phase heat transfer coefficient correlation used in the convective term will also be discussed. Stratification effects, which cause a loss of available convective surface area, will be accounted for through use of a Froude number dependent term. Next, a discussion on the selection of a nucleate boiling term will be given. The developed correlation will then be compared with the entire set of heat transfer coefficient data for the four refrigerants in Sec. 5.5. To broaden the applicability of the correlation, data from other studies in the literature will also be compared with the developed correlation in Sec. 5.5.

5.2.1. Asymptotic form

The superposition model, the "greater of the two" model, and the asymptotic model were all discussed earlier in the literature review. After extensive evaluation of these forms, the asymptotic model was chosen to be the best form to correlate the experimental data. Correlations from nucleate pool boiling can be used for the nucleate boiling term, while a convective form similar to the proposed form of Chen [1966] can be evaluated experimentally and used for the convective boiling term.

The main feature of this form is the "built in" suppression of the weaker component. The form of this correlation was given by Eq. 2.115 and is listed again below:

$$h_{TP} = \left[h_{nb}^{n} + h_{cb}^{n}\right]^{1/n} \tag{2.115}$$

Table 5.2 shows an example of the asymptotic form with n equal to 2.5. For a large convective component and a small nucleate boiling component, the total two-phase heat transfer coefficient is made up almost entirely of the convective boiling component. For a mixed situation where both nucleate boiling and convective boiling occur, the total two-phase heat transfer coefficient is made up of a combination of the two components. For a nucleate boiling dominated situation, the total two-phase heat transfer coefficient is made up almost entirely by the nucleate boiling component.

Table 5.2. Asymptotic form examples (n=2.5)

h (nucleate boiling)	h (conv. boiling)	h (two-phase)
5000	1000	5036
3000	3000	3959
1000	5000	5036

5.2.2. Convective boiling term

As previously discussed, the heat transfer coefficients obtained during low heat flux testing for R-134a and R-12 were convectively dominated. Using this set of points, a convective correlation was developed based on a single-phase heat transfer coefficient, h_l, and a two-phase multiplier, F. Based on the single-phase testing discussed in Chap. 3, the Dittus-Boelter correlation [1930] was found to be as accurate as the Gnielinski correlation [1976] over the range of Reynolds numbers tested (4.9% mean deviation versus 4.2% mean deviation) and was found to be more accurate than the Petukov correlation [1970]. In addition, due to its ease of evaluation and ability to be modified more easily for lower Reynolds numbers than the Gnielinski correlation, the Dittus-Boelter correlation was chosen as the single-phase heat transfer coefficient term.

A modified form of the convective term in the Chen correlation [1966] was selected for the convective term in the asymptotic correlating form of this study. Kenning and Cooper [1989] have shown this to be the appropriate form for the convective term. However, the Chen correlation has been found to underestimate their data and others. The convective boiling dominated experimental data in this paper were also underestimated by the Chen correlation. The form for the two-phase multiplier, F, in Eq. 5.2 below is approximately 10 to 30% higher than the Chen two-phase multiplier between qualities of 10 and 90% for refrigerants R-134a and R-12.

For the two-phase multiplier, either the Lockhart-Martinelli parameter or the convection number could be used. The convection number drops the viscosity ratio term in the Lockhart-Martinelli parameter and changes the dependence of the quality ratio slightly. Overall, this dimensionless number has worked fairly well in other correlations in accounting for convective effects. Matters can be simplified further, by replacing the property ratios in the Lockhart-Martinelli parameter by a function of the reduced pressure. The two-phase multiplier can then be determined by only knowing the quality and saturation temperature of the given refrigerant. Curve fitting as a function of reduced pressure for the refrigerants in Fig. 2.20, the property ratios can be represented by

$$\Omega = \left(\frac{\rho_v}{\rho_l}\right)^{0.5}\left(\frac{\mu_l}{\mu_v}\right)^{0.1} = 0.516P_r^{0.477} \tag{5.1}$$

The modified Lockhart-Martinelli parameter with the property ratio replaced by Ω will be used in the developed correlation.

Figure 5.32 is a plot of the heat transfer coefficient ratio, h_{TP}/h_l, versus the Lockhart-Martinelli parameter for the low heat flux tests for R-134a and R-12. Heat transfer coefficient ratio values for Lockhart-Martinelli parameter above 0.3 were used to determine the coefficients of the convective two-phase multiplier. These data fell along a straight line on a log-log plot, indicating convective boiling dominance. The data were curve fitted using the following form:

$$\frac{h_{TP}}{h_l} = 1 + C_1 X_{tt}^{C_2} \tag{5.2}$$

Using the newly calculated value for Ω, a nonlinear regression analysis was performed on the data which resulted in values of 1.925 for C_1 and -0.83 for C_2. The nonlinear regression was performed using the software program Engineering Equation Solver™ (EES), which optimized the coefficients based on minimizing the sum of the squares of the residuals.

5.2.3. Nucleate boiling term

Several nucleate pool boiling correlations have been developed over the past several decades. Many of these correlations have also been proposed for use in flow boiling situations. Initial correlations suggested by Chen [1966], such as the Forster-Zuber correlation [1955] for nucleate pool boiling, are difficult to calculate and require knowledge of data such as surface temperatures and surface tension, which are not always available. This lack of surface tension data may become even more important for correlating heat transfer coefficients for zeotropic mixtures.

Two recent pool boiling correlations have been developed that are more accurate than some of the original correlations and are easier to evaluate. The Cooper correlation [1984] is based on reduced pressure, heat flux, and molecular weight and is of the same order of accuracy as the Forster-Zuber correlation, but is much easier to evaluate. The other recent correlation developed in the literature is that of Stephan and Abdelsalam [1980]. It is used in the Jung-Radermacher correlation [1989]. However, the Stephan and Abdelsalam correlation uses the bubble departure diameter, which is currently under scrutiny for use in flow boiling correlations [Klausner, 1993]. The Stephan and Abdelsalam correlation also requires surface tension, which is not always readily available for newly developed refrigerants and refrigerant mixtures. Both correlations have been

determined to be fairly accurate in representing the present flow boiling data. After weighing all of these competing factors, the Cooper correlation was selected for the nucleate boiling term.

However, the Cooper correlation requires the heat flux to be given in W/m^2. An attempt was made to nondimensionalize the heat flux to allow easier use of the correlation in English units. In the literature, a diameter dependence for the nucleate boiling heat transfer coefficient has been suggested [Steiner and Taborek, 1993]. The suggested dependence is $h_{nb} \propto d^{-0.4}$. A nondimensional number similar to the term used in the Stephan and Abdelsalam correlation was suggested for correlating the data of this study by replacing the bubble departure diameter with the inside tube diameter. However, using this method, the mean deviation of the overall data set actually increased and the dimensionless heat flux was abandoned in favor of the original Cooper correlation as follows:

$$h_{nb} = 55q''^{0.67} M^{-0.5} P_r^{0.12} \left[-\log_{10} P_r\right]^{-0.55} \tag{5.3}$$

5.2.4. Low mass flux effects

To account for the decease in convective heat transfer due to loss in convective boiling surface area and a loss of turbulence for lower Reynolds number flows, a Froude number dependent term and a loss of turbulence term were attempted to be added to the convective term in the correlation developed in this study. The loss of turbulence term takes effect at Reynolds numbers below 10,000. This offsets the overestimation of the single-phase liquid heat transfer coefficient through use of the Dittus-Boelter correlation [1930] for tests with Reynolds numbers below 10,000. Kandlikar [1990] and others have recently suggested using the Gnielinski correlation [1976] for test conditions with Reynolds numbers below 10,000. However, the Gnielinski correlation only works for Reynolds numbers above 4,000 and is not suggested for extrapolation below this value because of the presence of a (Re_{lo}-1000) term in the correlation. Many practical uses of refrigerants inside horizontal tubes, such as in household refrigerator evaporators, have Reynolds numbers below 4,000. Because the form of the Dittus-Boelter correlation is more tractable to modification, this correlation was selected for use in the convective boiling term.

The loss of turbulence term was designed to approximate the Gnielinski correlation while removing the Re_{lo}-1000 term. This was done by adding a Reynolds number dependence term to the Dittus-Boelter equation. Using the physical properties of the four refrigerants studied, the Dittus-Boelter and Gnielinski correlations were plotted for Reynolds numbers between 4,000 and 10,000. A Reynolds number term was added to the Dittus-Boelter correlation as follows:

$$L_T = C_3 Re_{lo}^{C_4} \tag{5.4}$$

A nonlinear regression analysis was used to determine the constant so the modified Dittus-Boelter equation matched the Gnielinski correlation. Values of 0.157 and 0.2 were determined for C_3 and C_4, respectively. The modified Dittus-Boelter correlation was then extrapolated below 4,000 to determine the Froude number dependent term to account for loss of convective area due to stratification of the flow.

Wavy-stratified heat transfer coefficient data were used to develop a Froude number dependent term which was added to the overall convective term. This power law term was selected as

$$R = C_5 Fr_l^{C_6} \tag{5.5}$$

where Fr_l is defined as

$$Fr_l = \frac{G^2}{\rho_l^2 g D} \tag{5.5a}$$

From an analysis of the flow pattern data and an examination of the heat transfer coefficient data, the Froude number where the predominant flow pattern became wavy was 0.08. R at this point was set equal to 1. From the heat transfer coefficient data, the value for C_6 was found to be 1.1. From this value for the slope of this term, the corresponding value for C_5 equating R to 1 at Fr_l was 16.01.

However, a fairly high overall value of mean deviation (over 20%) was generated for the 7.04 mm data sets. This was very different than the good agreement using only a Froude number dependent term for tests with a Froude number below 0.25. The loss of turbulence term was therefore abandoned in favor of a reduction parameter based only on the Froude number. This Froude number dependent term was as follows:

$$R = C_7 Fr_l^{C_8} \tag{5.6}$$

For Fr_l above 0.25, R was set equal to 1. For Fr_l below 0.25, C_7 was found to be equal to 1.32 with C_8 equal to 0.2. What this seems to indicate is that the reduction in heat transfer for wavy flows or even wavy-annular flows is more of an effect of the stratification rather than a loss of turbulence.

5.3. The Overall Correlation

Bringing all of the terms discussed in Sec. 5.2 together, the overall heat transfer coefficient correlation is given by the following set of equations:

$$h_{TP} = \left[h_{nb}^n + h_{cb}^n\right]^{1/n}, \quad n = 2.5 \tag{5.7}$$

$$h_{nb} = 55q''^{0.67} M^{-0.5} P_r^{0.12} [-\log_{10} P_r]^{-0.55} \quad (5.8)$$

$$h_{cb} = F h_l R \quad (5.9)$$

$$F = 1 + 1.925 X_{tt}^{-0.83} \quad (5.10)$$

$$h_l = 0.023 \frac{k_l}{D} Re_l^{0.8} Pr_l^{0.4} \quad (5.11)$$

$$R = 1.32 Fr_l^{0.2}, \text{ for } Fr_l < 0.25 \quad (5.12a)$$

$$R = 1, \text{ for } Fr_l \geq 0.25 \quad (5.12b)$$

5.4. Wall Superheat Required for Nucleation in Flow Boiling

As was discussed in the literature review, the superheat required for the onset of nucleation in flow boiling varies based on the cavity size distribution. Using Eq. 2.86 with an infinite cavity size distribution for R-134a and a heat flux of 1600 Btu/hr-ft^2 at 41°F, the necessary wall superheat is 1.15°F. For 9600 Btu/hr-ft^2, the necessary wall superheat is 2.81°F. The other possibility is that cavity size is limited, and Eq. 2.101 can determine the necessary wall superheat. The wall superheat for onset of nucleate boiling is extremely sensitive to the r_{max} term in this equation. Davis and Anderson [1966] suggest a maximum cavity radius of 4 x 10^{-5} in. Hino and Ueda [1986] suggest a value of 1.1 x 10^{-5} in for a stainless steel tube. Collier [1981], in his book *Convective Boiling and Condensation*, suggests a value of 2 x 10^{-5} in. Brown [1967], in a Ph.D. study from MIT, found that reasonable cavity distributions are only found below 4 x 10^{-4} in for metal tubes. Based on Eq. 2.101, Table 5.3 indicates the various values of wall superheat versus cavity radius for a convective heat transfer coefficient of 616 Btu/hr-ft^2-°F for R-134a.

Table 5.3. Wall superheat required for nucleation during flow boiling of R-134a

Cavity radius	Wall superheat
1.1 x 10^{-5} in	6.66°F
2 x 10^{-5} in	3.69°F
4 x 10^{-5} in	1.92°F
4 x 10^{-4} in	0.30°F

The assumptions of infinite cavity size and limited cavity size yield similar results between 4 x 10^{-5} and 4 x 10^{-4} in. Our experimental heat transfer coefficient data suggest that this maximum cavity radius is between 4 x 10^{-5} and 4 x 10^{-4} in, or in a sense, an

infinite cavity size distribution is approached. This would validate Bergles and Rohsenow's statement that commercially produced surfaces usually do have cavities over a wide range of sizes, and the results of the Bergles and Rohsenow model should be applicable to many real systems [Carey, 1992].

Based on this brief analysis, the data of this study showed that there can be nucleate boiling for many of our conditions. For low heat fluxes in annular flow, this contribution was small and may be considered to be negligible compared with the dominant convective heat transfer. The asymptotic model that was developed in Sec. 5.2 properly accounted for this. For higher heat fluxes in annular flow, both convective and nucleate boiling occurred and the asymptotic model again accounted for this. For wavy flows, the convective term was diminished and both nucleate boiling and convective boiling contributed to the heat transfer. Again, the asymptotic model accounted for this.

5.5. Comparison with Experimental Data

Figure 5.33 is a comparison of the predicted values of Eq. 5.7 and experimental values of heat transfer coefficient for annular and wavy flow data for R-134a, R-12, R-22 and R-32/R-125. The mean deviations of the correlation compared with the experimental data are shown in Table 5.4. These results compare very favorably to those of the other correlations shown in Table 5.1, and should give much credibility to the asymptotic form used in Eq. 5.7.

Table 5.4. Mean deviation between the developed correlation, Eq. 5.7, and the experimental data for R-12, R-134a, R-22, and R-32/R-125

Correlation	R-12	R-134a	R-22	R-32/R-125
Equation 5.7	13.3	11.2	10.7	12.1

To demonstrate the applicability of Eq. 5.7 over a wider range of conditions, the asymptotic correlation was also compared with the R-134a and R-12 data of Eckels and Pate [1991], shown in Fig. 5.34, and R-12 and R-22 data of Jung [1989], shown in Fig. 5.35. It should be noted that the Eckels and Pate data were average heat transfer coefficient data and the correlation was integrated over the corresponding quality range assuming a linear variation of quality over the test section. Compared with the Eckels and Pate data, the correlation had a mean deviation of 7.3% for R-134a and 17.5% for R-12. Compared

with the Jung and Radermacher R-12 and R-22 data, the correlation had a mean deviation of 9.4% for R-12 and 12.1% for R-22..

Additional studies were conducted with water by Kenning and Cooper [1989] in heated vertical tubes and by Wambsganss [1992] using R-113 in small tubes at high heat fluxes. Figures 5.36 and 5.37 show the comparison of Eq. 5.7 with the experimental data for the Kenning and Cooper and Wambsganss studies, respectively. For the Kenning and Cooper data, the correlation had a mean deviation of 9.9% for water. For the Wambsganss data, the correlation had a mean deviation of 14.6% for R-113.

5.6. Uncertainty Analysis

As discussed in Chap. 3, uncertainties for the experimental heat transfer coefficients were determined using the method of sequential perturbation, as outlined by Moffat [1988] for single-sample data. Figure 3.11 showed the methodology for the calculation of uncertainty for each value of heat transfer coefficient. Two additional terms were added to the root sum square of the uncertainty terms of Eq. 3.16 for the experimental data in this chapter. One term added the uncertainty of the heat flux due to the diameter, and the other term added the uncertainty of the heat flux due to the length of the test section. Uncertainty values are given in Appendix B, where the experimental data are tabulated.

Estimated uncertainties ranged from 5 to 30% for the experimental heat transfer coefficient data in this study. Different terms of Eq. 3.16 accounted for a majority of the uncertainty of the experimental heat transfer coefficients depending on the flow conditions tested. The uncertainties of the length and diameter of the test sections led to less than 3% of the overall uncertainty for all tests conducted. For many low heat flux annular flow tests, the difference in temperature between the surface and fluid temperature (wall superheat) was between 1.8 and 3.6°F. With uncertainties of each temperature measurement between 0.18 and 0.36°F, uncertainties in the heat transfer coefficient were near 20% for many tests. For higher heat flux testing, the variation of surface temperature increased the uncertainty of these measurements to 0.54 to 0.90°F. However, the wall superheats were on the order of 5.4 to 10.8°F, and led to uncertainties between 5 and 20%. For wavy flow tests, the wall superheats were above 3.6°F for most tests, but the heat input rates to the test section were less than 341 Btu/hr. With an estimated uncertainty of 34 Btu/hr for the heat input rate of the test section, this resulted in uncertainties near 20% for many of these tests.

The uncertainties in the wall temperature measurements coupled with the high thermal conductivity of the copper tubes also made it difficult to determine trends in the

circumferential temperature distribution. These circumferential temperatures varied between 0 and 1.8°F for the range of tests encountered, with smaller differences occurring for low heat flux tests. These smaller differences were also found for wavy flow tests, which might be expected to have higher circumferential temperature variation than the annular flow tests.

The values of uncertainty for each of the variables in an experimental calculation play an important role in the ability of a researcher to accurately predict the obtained data. Before an experiment is designed, the equipment used should be examined for the uncertainties in their respective measurements, and these values should be combined in a root sum square fashion to determine estimated uncertainties of the desired quantity being measured in the experiment. From the standpoint of experimental heat transfer coefficient measurements, the temperature measurement is the most important value. To achieve meaningful heat transfer coefficient data in this study, thermocouple wire with special limits of error were ordered and extensive calibration was conducted to ensure as low an uncertainty as possible with the computer data acquisition equipment used.

When the experimental system was debugged, such as in the case of single-phase testing, values of experimental single-phase heat transfer coefficients were obtained. For these tests, the wall superheats were fairly high (above 9°F) and calculated uncertainties were fairly low (less than 5%). Correlations from the literature are fairly accurate for these single-phase heat transfer coefficients, and these single-phase heat transfer coefficients acted as another check on the system that it was operating properly. If the values of the experimental heat transfer coefficient were 20 or 30% different than the correlations, this would be an indication that something in the system was wrong because the calculated uncertainties were small due to the large wall superheats. In summary, the calculation of uncertainties can help tremendously in the design, debugging, and data analysis portions of an experimental study. However, a note of caution is also given. For single sample experiments, the uncertainty of the values for parameters such as temperature and heat input rate are to a large extent estimations and are based on judgment or experience. Values of uncertainty for certain parameters can easily be underestimated or overestimated, which can propagate into the calculated value such as the heat transfer coefficient. The data must be carefully examined, and as parameters are extended beyond the range of initial conditions studied, the values of estimated uncertainties should be reevaluated.

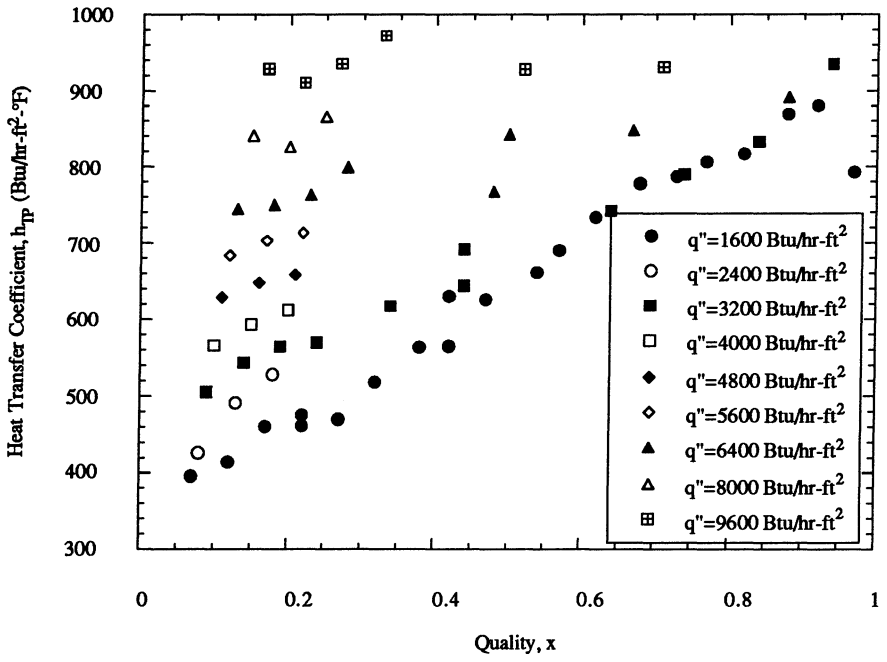

Figure 5.1. R-134a heat transfer coefficient versus quality for annular flow in 0.430 in i.d. test section. Mass flux, 225 klb_m/ft^2-hr; Saturation temperature, 41°F.

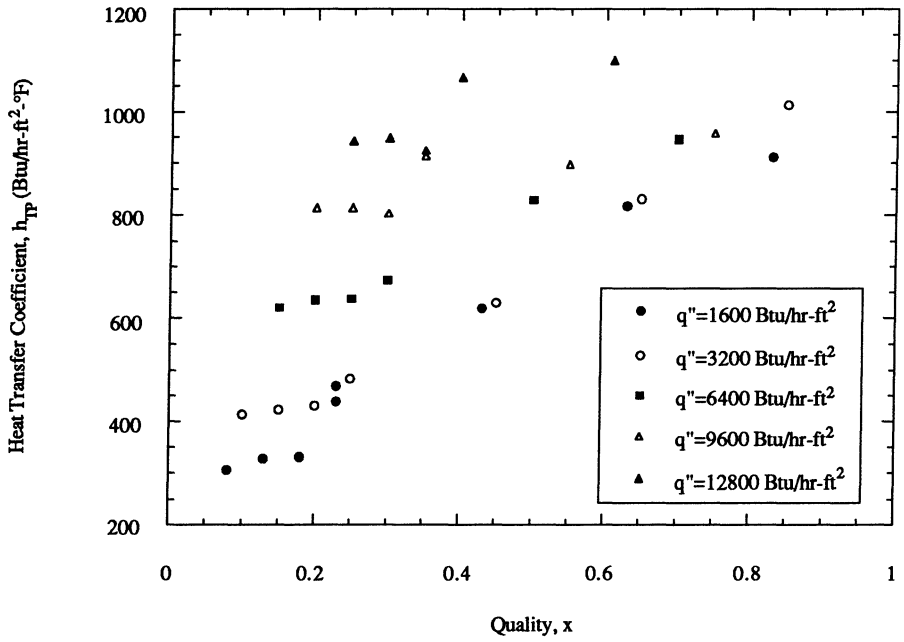

Figure 5.2. R-134a heat transfer coefficient versus quality for annular flow in 0.305 in i.d. test section. Mass flux, 225 klb_m/ft^2-hr; Saturation temperature, 41°F.

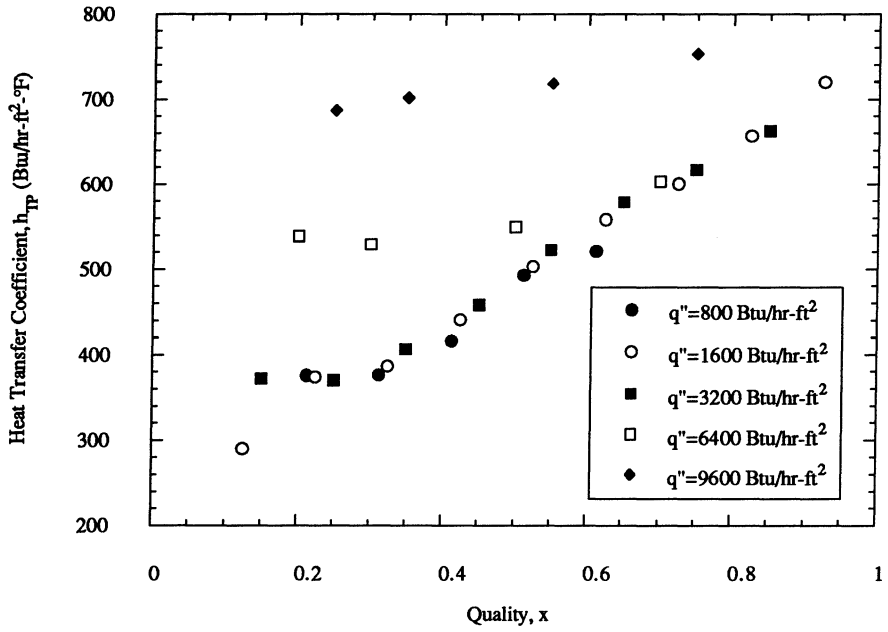

Figure 5.3. R-12 heat transfer coefficient versus quality for annular flow in 0.430 in i.d. test section. Mass flux, 225 klb_m/ft^2-hr; Saturation temperature, 41°F.

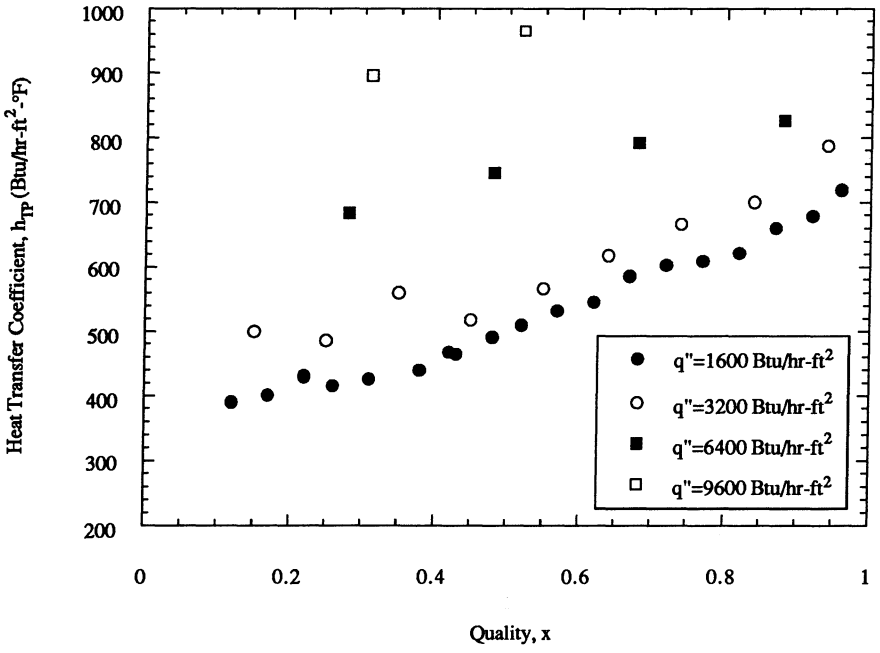

Figure 5.4. R-22 heat transfer coefficient versus quality for annular flow in 0.430 in i.d. test section. Mass flux, 225 klb_m/ft^2-hr; Saturation temperature, 41°F.

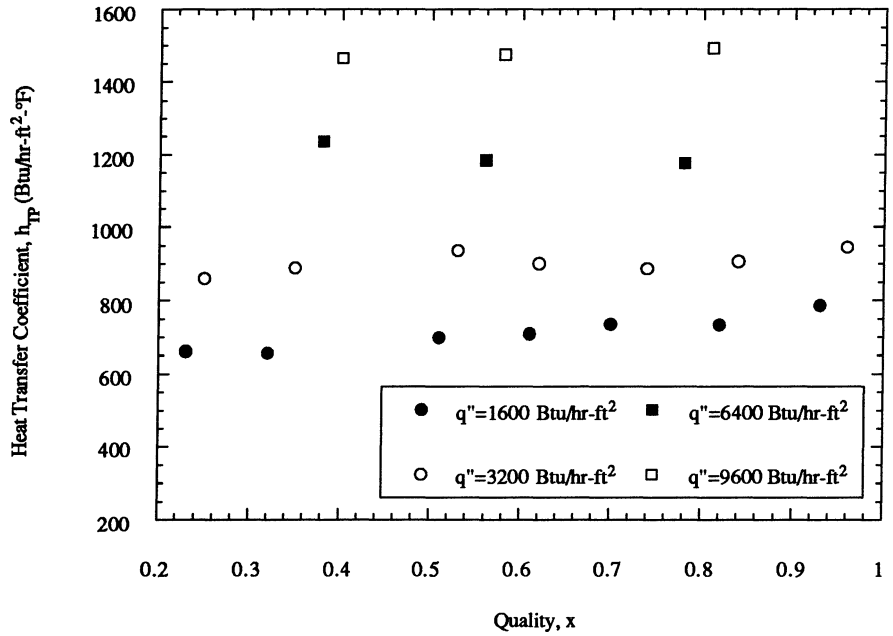

Figure 5.5. R-32/R-125 heat transfer coefficient versus quality for annular flow in 0.430 in i.d. test section. Mass flux, 225 klb$_m$/ft^2-hr; Saturation temperature, 41°F.

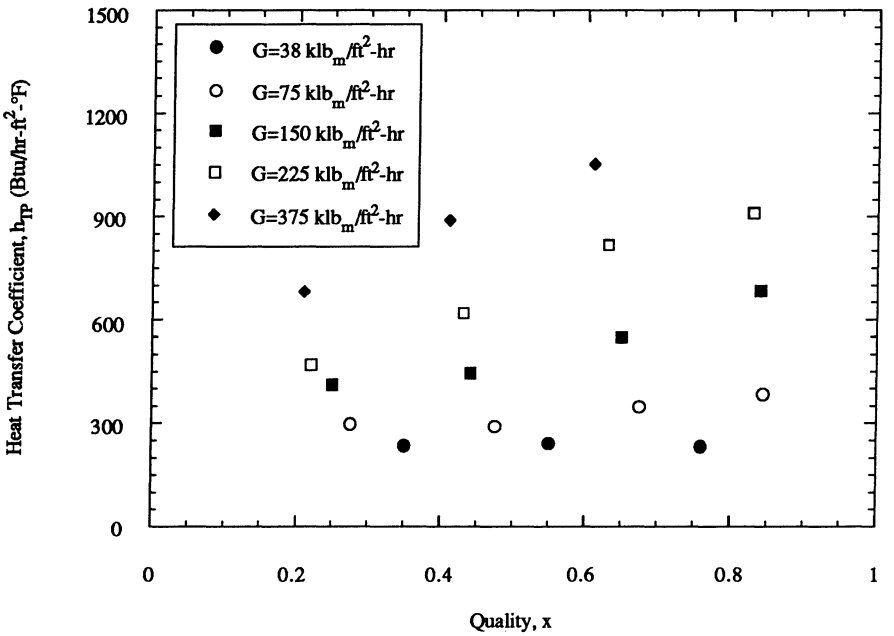

Figure 5.6. R-134a heat transfer coefficient versus quality for annular flow in 0.305 in i.d. test section for varying mass fluxes. Heat flux, 1600 Btu/hr-ft^2; Saturation temperature, 41°F.

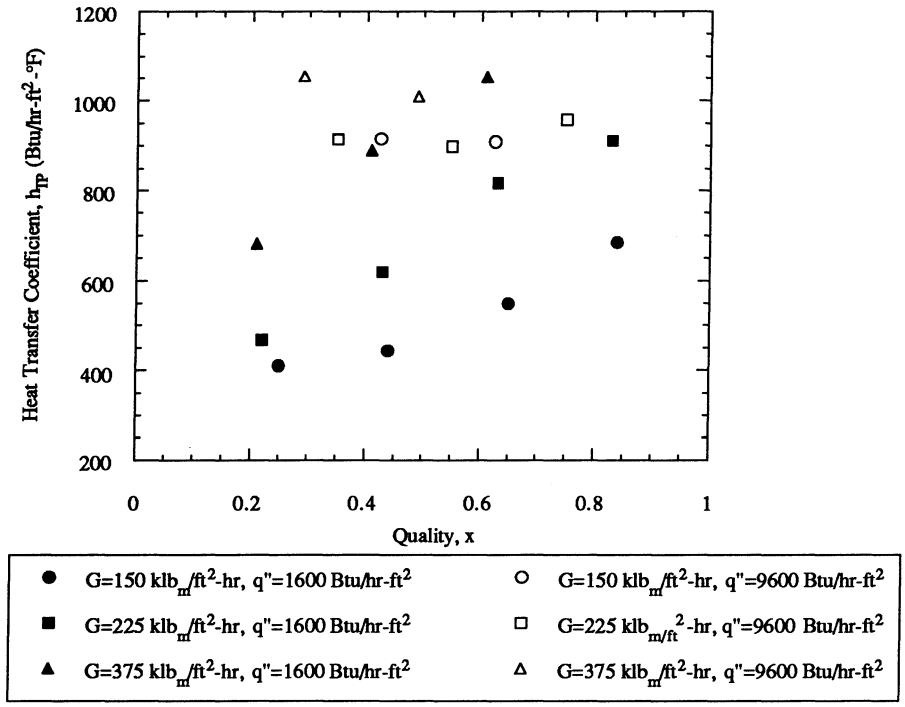

Figure 5.7. R-134a heat transfer coefficient versus quality for low heat flux and high heat flux tests in 0.305 in i.d. test section for varying mass fluxes. Saturation temperature, 41°F.

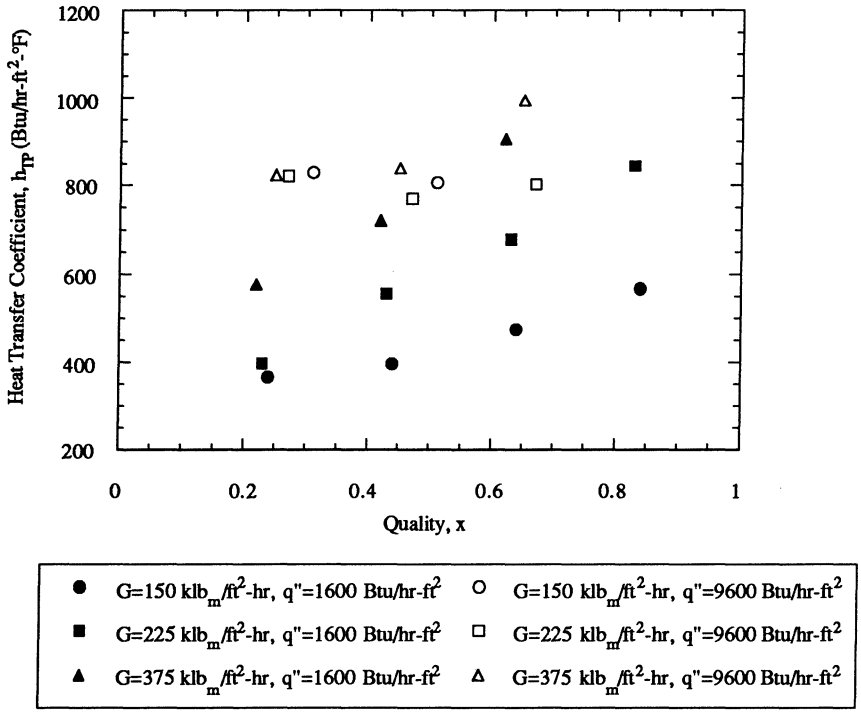

Figure 5.8. R-22 heat transfer coefficient versus quality for low heat flux and high heat flux tests in 0.305 in i.d. test section for varying mass fluxes. Saturation temperature, 41°F.

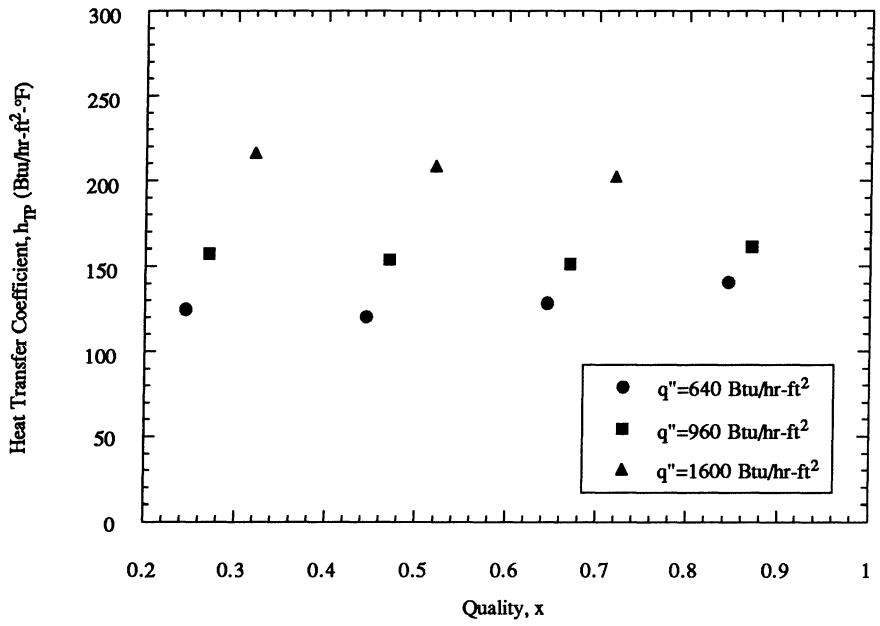

Figure 5.9. R-134a heat transfer coefficient versus quality for wavy flow in 0.430 in i.d. test section. Mass flux, 38 klb_m/ft^2-hr; Saturation temperature, 41°F.

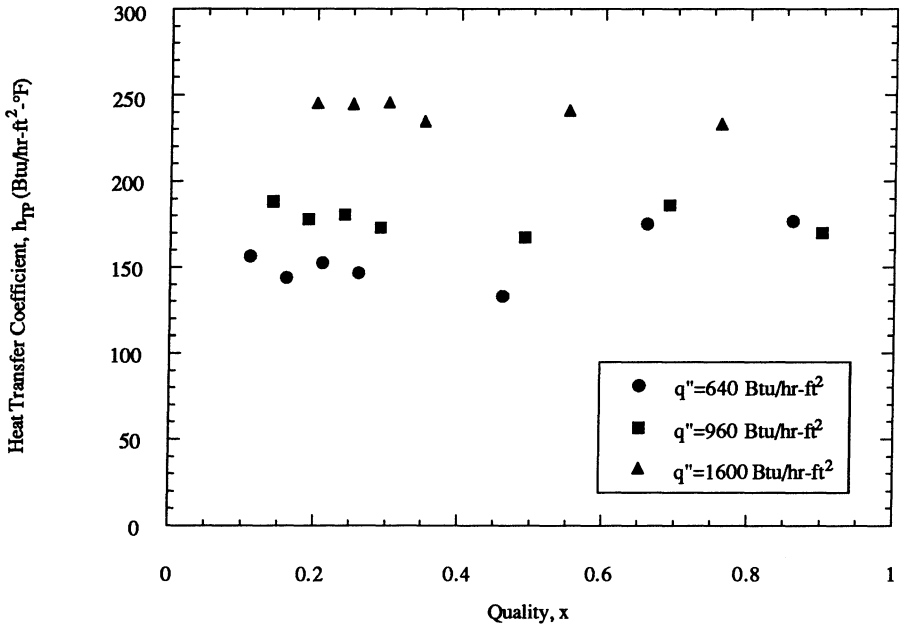

Figure 5.10. R-134a heat transfer coefficient versus quality for wavy flow in 0.305 in i.d. test section. Mass flux, 38 klb_m/ft^2-hr; Saturation temperature, 41°F.

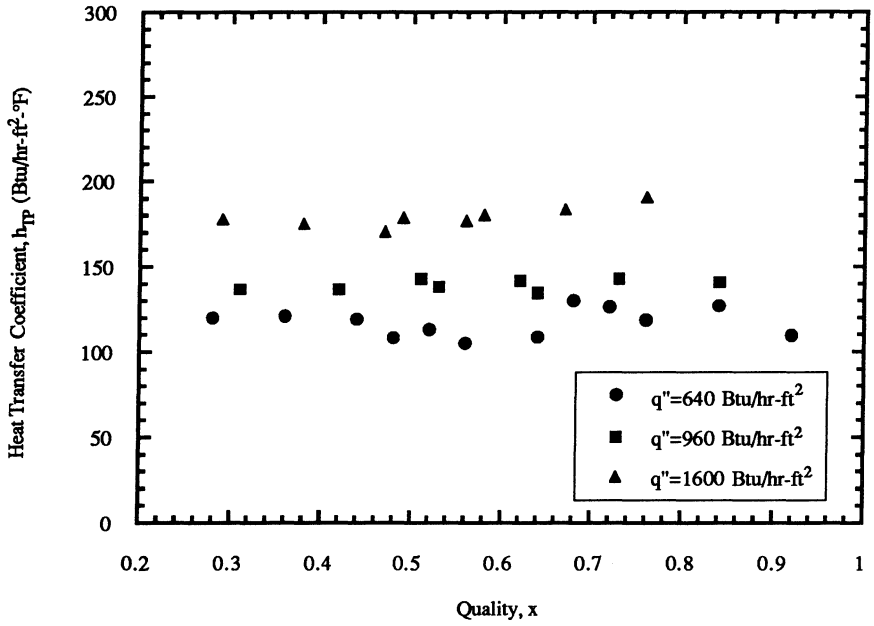

Figure 5.11. R-12 heat transfer coefficient versus quality for wavy flow in 0.430 in i.d. test section. Mass flux, 38 klb_m/ft^2-hr; Saturation temperature, 41°F.

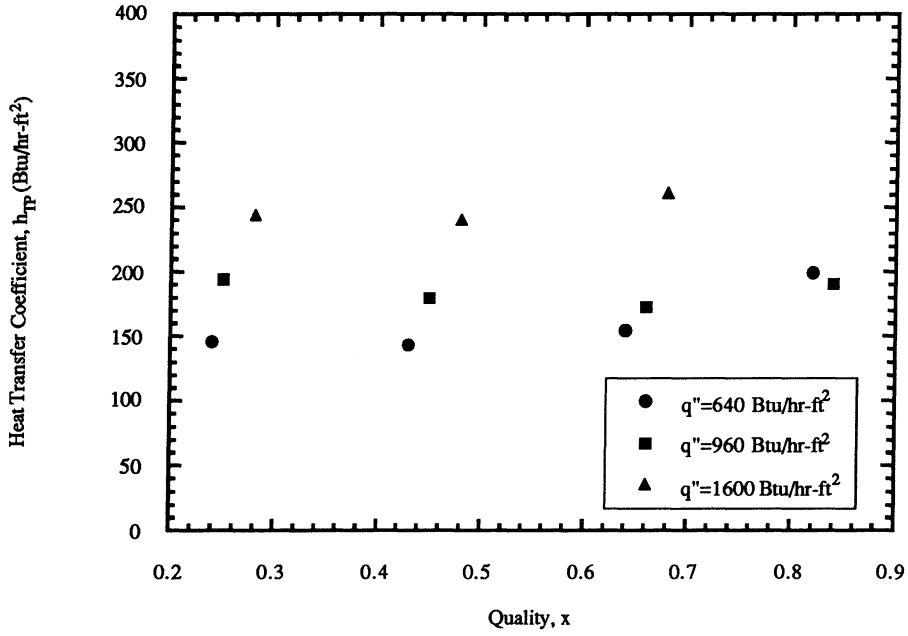

Figure 5.12. R-22 heat transfer coefficient versus quality for wavy flow in 0.430 in i.d. test section. Mass flux, 38 klb_m/ft^2-hr; Saturation temperature, 41°F.

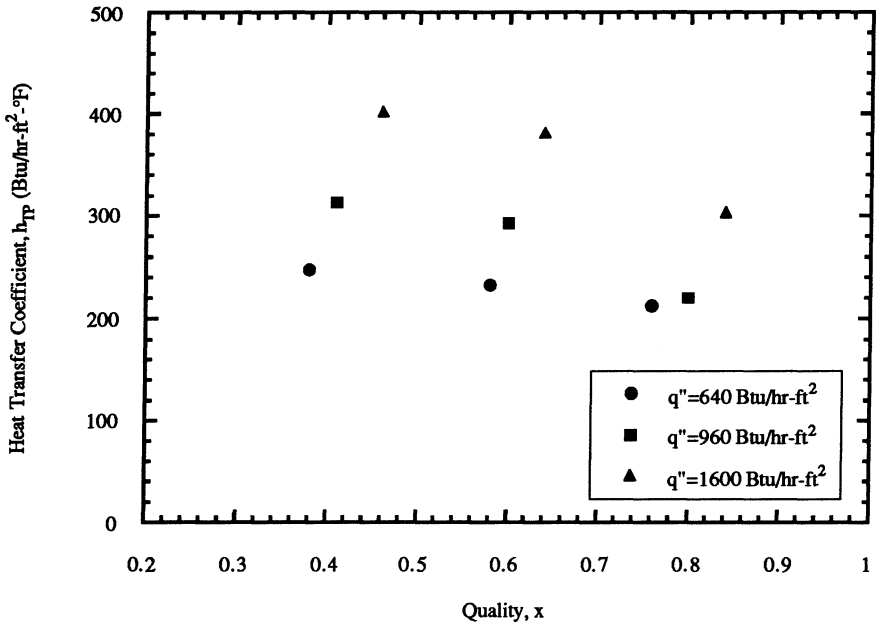

Figure 5.13. R-32/R-125 heat transfer coefficient versus quality for wavy flow in 0.430 in i.d. test section. Mass flux, 38 klb_m/ft^2-hr; Saturation temperature, 41°F.

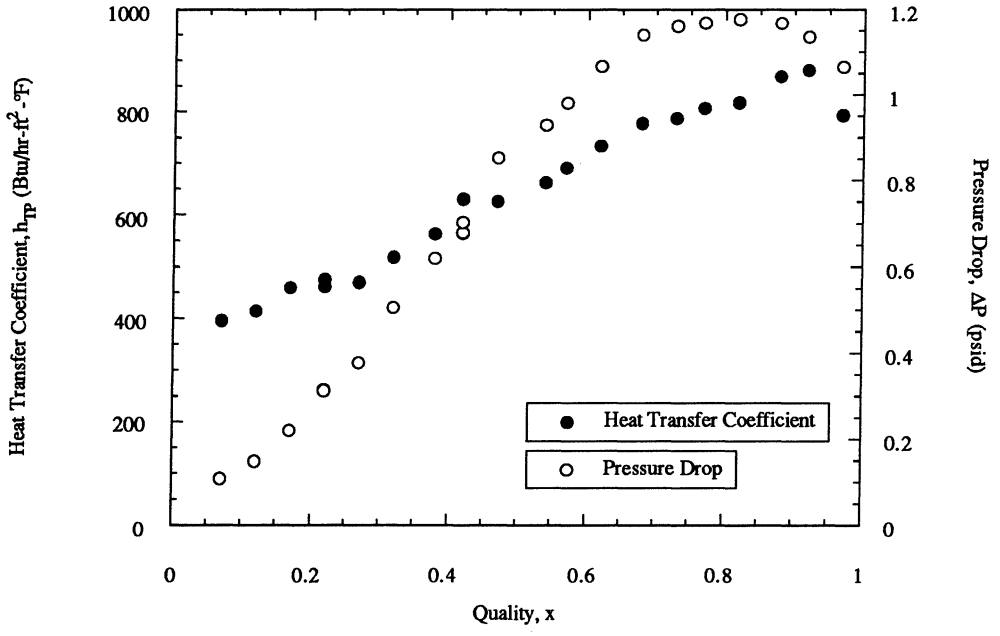

Figure 5.14. Heat transfer coefficient and pressure drop variations versus quality during transitions from annular to annular-mist flow to mist flow for R-134a. Mass flux, 225 klb_m/ft^2-hr; Heat flux, 1600 Btu/hr-ft^2; Saturation temperature, 41°F. Tube diameter, 0.430 in.

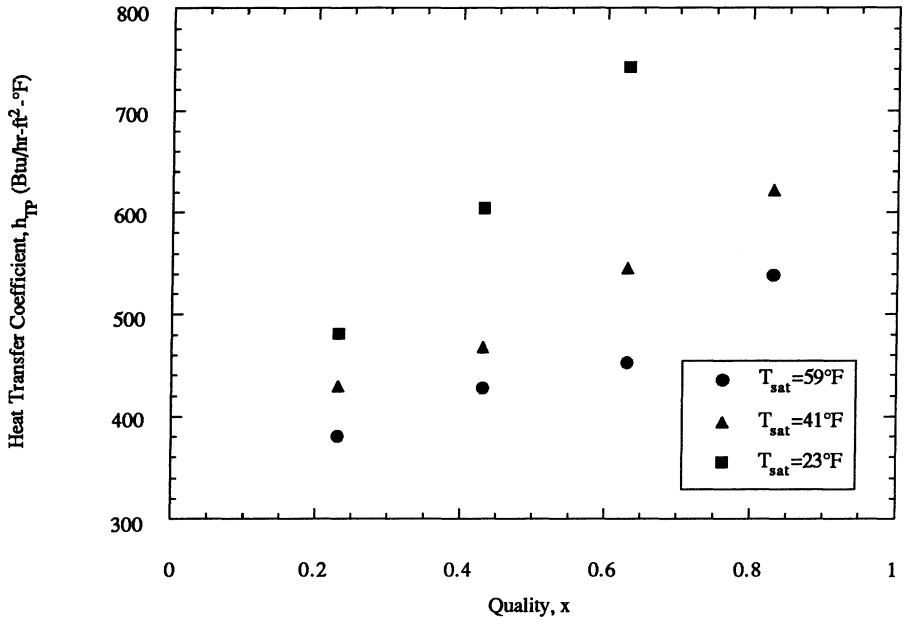

Figure 5.15. R-134a heat transfer coefficient versus quality for annular flow in 0.305 in i.d. test section at 23°F, 41°F, and 59°F. Mass flux, 225 klb_m/ft^2-hr; Heat flux, 1600 Btu/hr-ft^2.

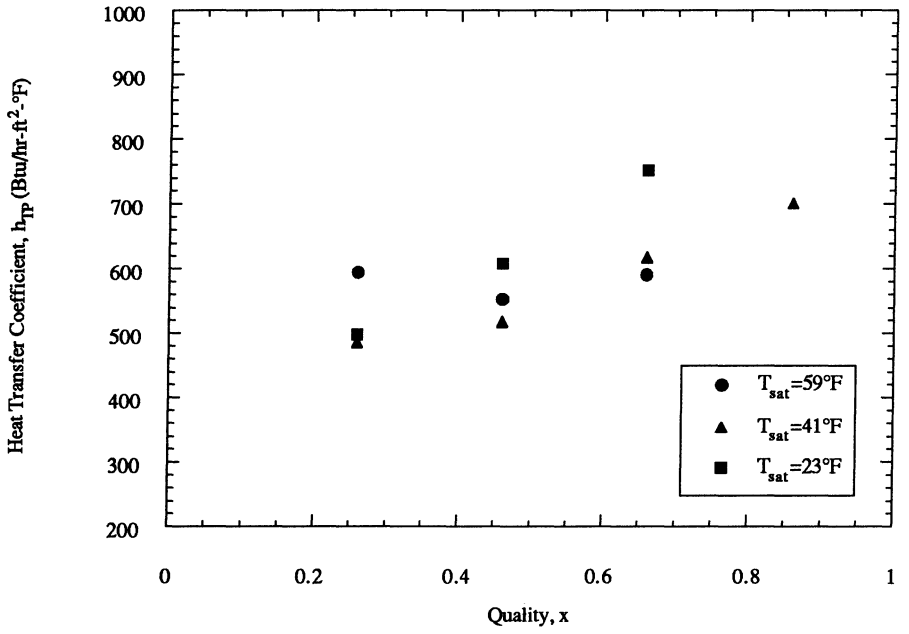

Figure 5.16. R-134a heat transfer coefficient versus quality for annular flow in 0.305 in i.d. test section at 23°F, 41°F, and 59°F. Mass flux, 225 klb_m/ft^2-hr; Heat flux, 3200 Btu/hr-ft^2.

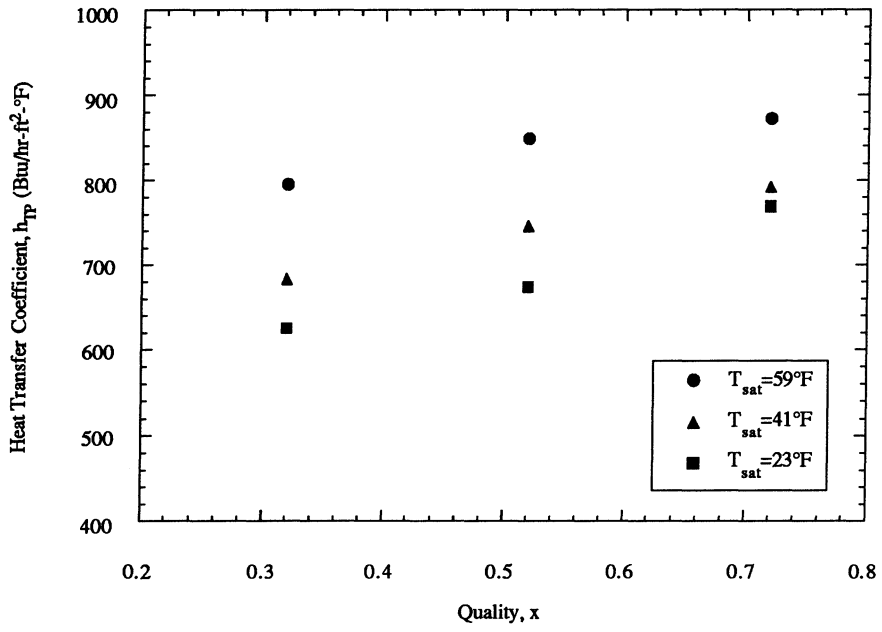

Figure 5.17. R-134a heat transfer coefficient versus quality for annular flow in 0.305 in i.d. test section at 23°F, 41°F, and 59°F. Mass flux, 225 klb_m/ft^2-hr; Heat flux, 6400 Btu/hr-ft^2.

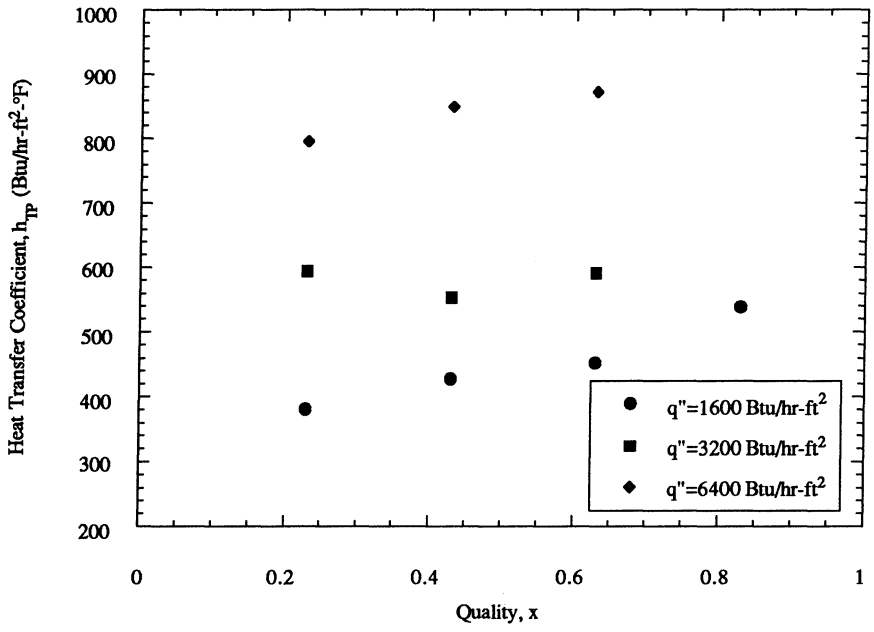

Figure 5.18. R-22 heat transfer coefficient versus quality for annular flow in 0.430 in i.d. test section at 59°F. Mass flux, 225 klb_m/ft^2-hr.

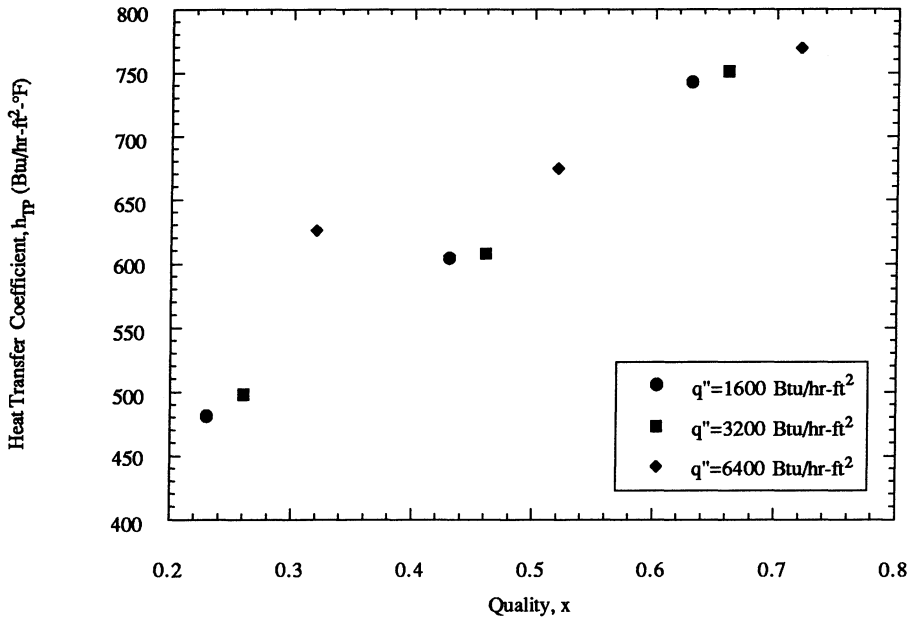

Figure 5.19. R-22 heat transfer coefficient versus quality for annular flow in 0.430 in i.d. test section at 23°F. Mass flux, 225 klb_m/ft^2-hr.

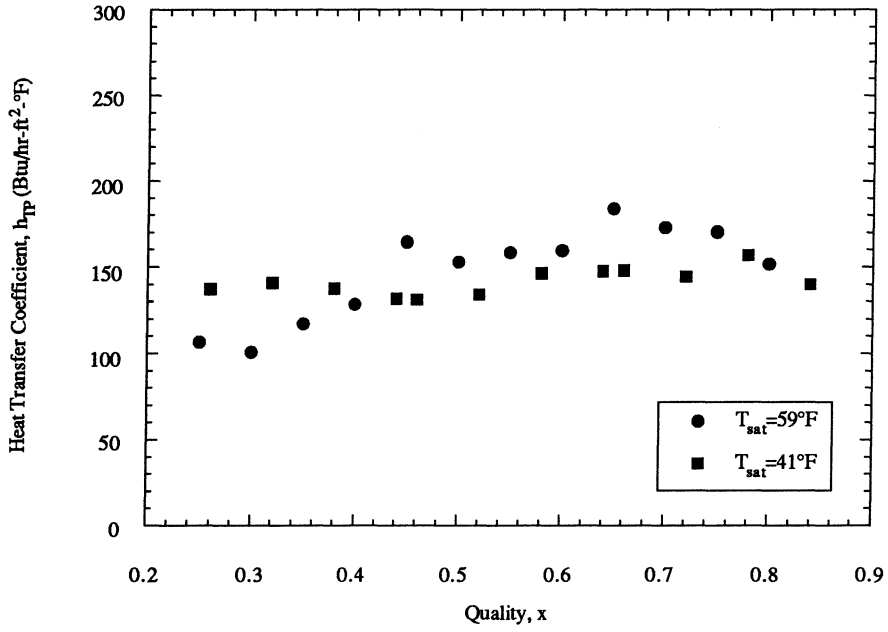

Figure 5.20. R-134a heat transfer coefficient versus quality for annular flow in 0.277 in i.d. test section at 5°F and 41°F. Mass flux, 38 klb_m/ft^2-hr; Heat flux, 640 Btu/hr-ft^2.

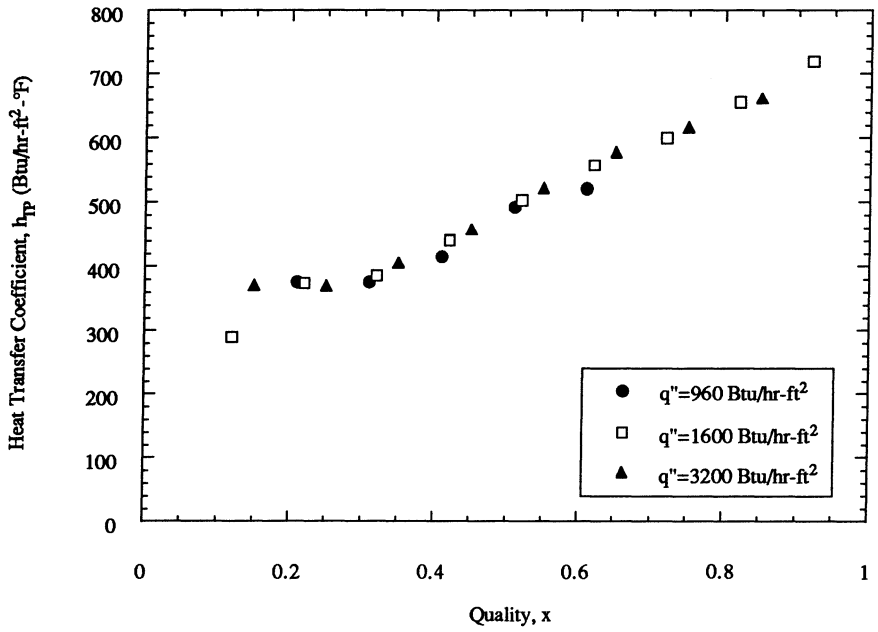

Figure 5.21. R-12 heat transfer coefficient versus quality for annular flow in 0.430 in i.d. test section. Mass flux, 225 klb_m/ft^2-hr; Saturation temperature, 41°F.

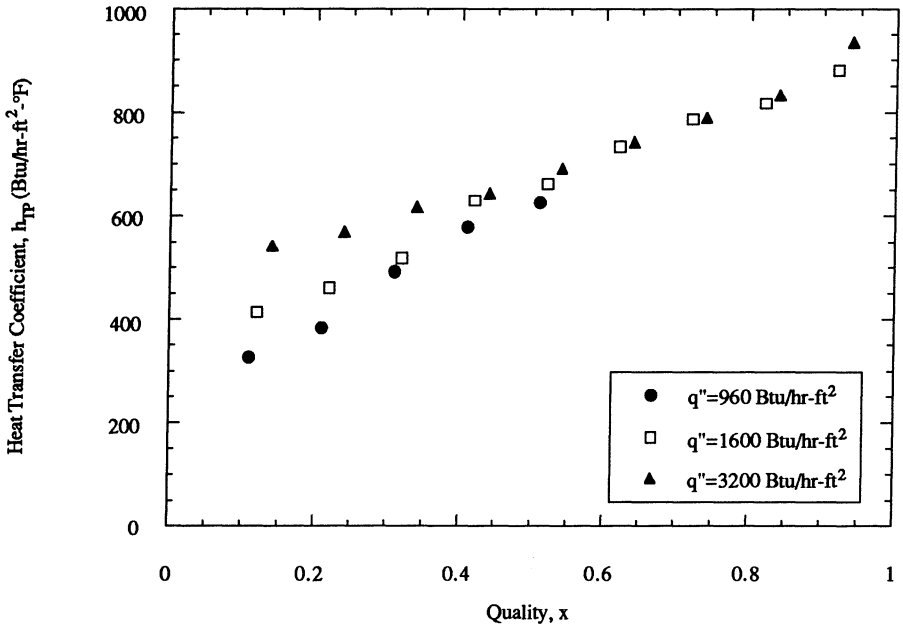

Figure 5.22. R-134a heat transfer coefficient versus quality for annular flow in 0.430 in i.d. test section. Mass flux, 225 klb_m/ft^2-hr; Saturation temperature, 41°F.

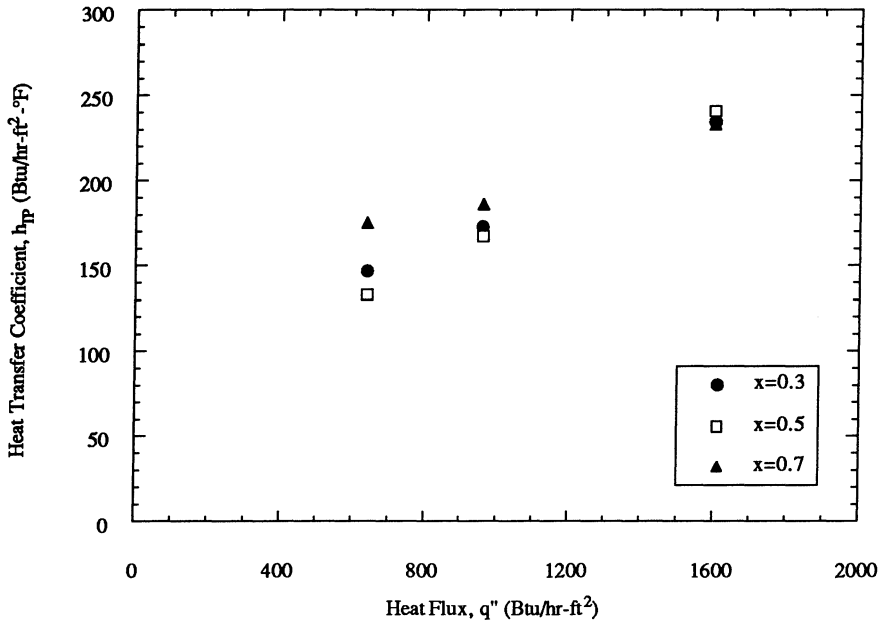

Figure 5.23. R-134a heat transfer coefficient versus heat flux at 38 kg/m^2-s in 0.305 in i.d. test section. Saturation temperature, 41°F.

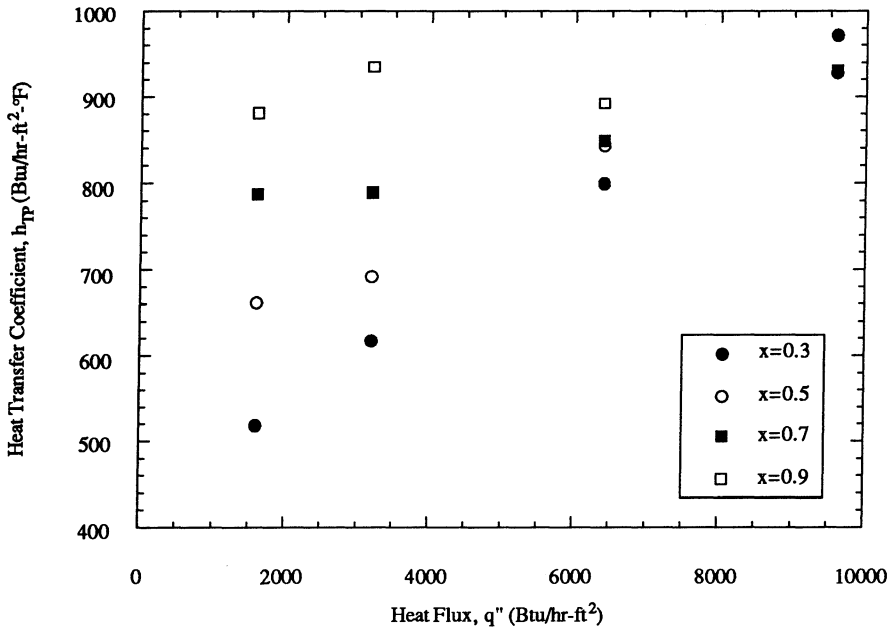

Figure 5.24. R-134a heat transfer coefficient versus heat flux at 225 klb$_m$/ft^2-hr in 0.305 in i.d. test section. Saturation temperature, 41°F.

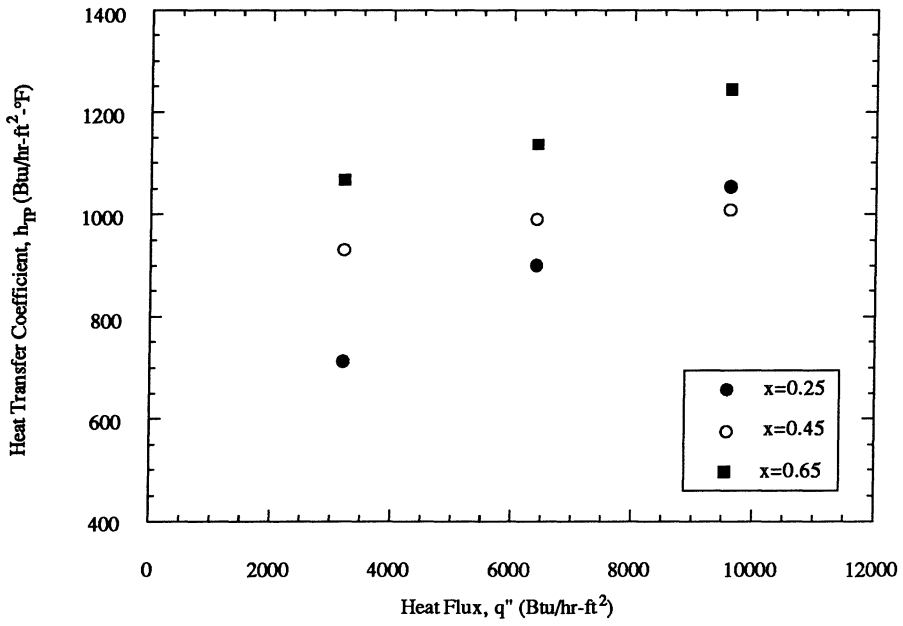

Figure 5.25. R-134a heat transfer coefficient versus heat flux at 375 klb_m/ft^2-hr in 0.305 in i.d. test section. Saturation temperature, 41°F.

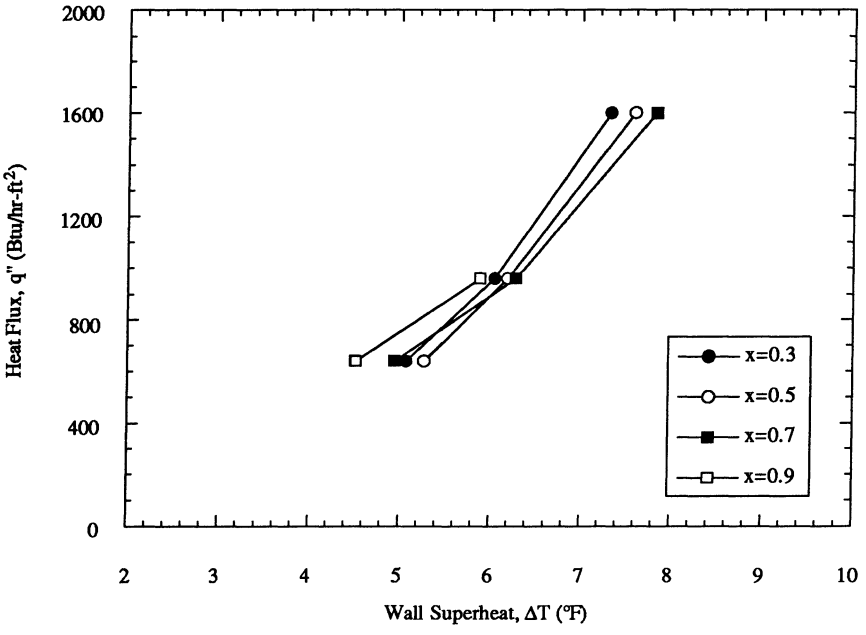

Figure 5.26. R-134a heat flux versus wall superheat at 38 klb_m/ft^2-hr in 0.305 in i.d. test section. Saturation temperature, 41°F.

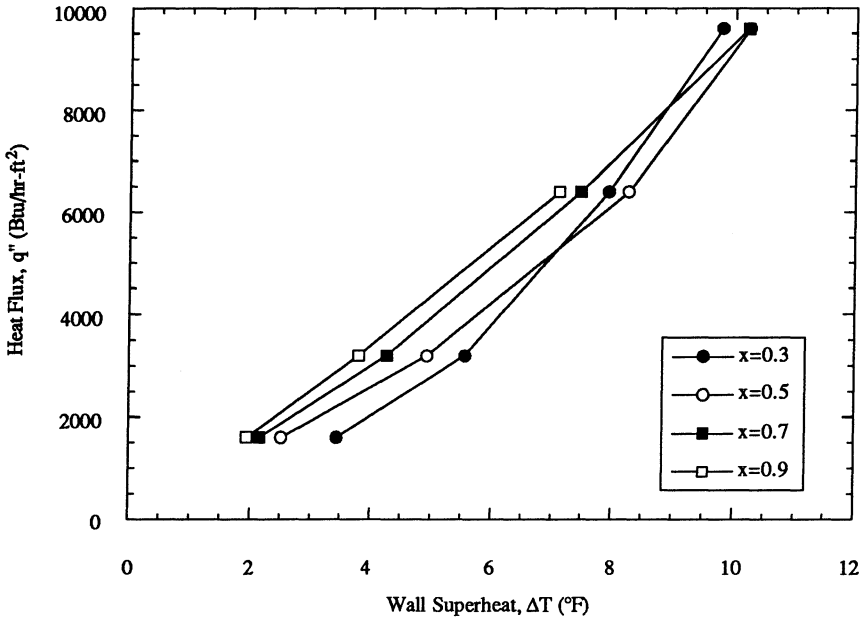

Figure 5.27. R-134a heat flux versus wall superheat at 225 klb_m/ft^2-hr in 0.305 in i.d. test section. Saturation temperature, 41°F.

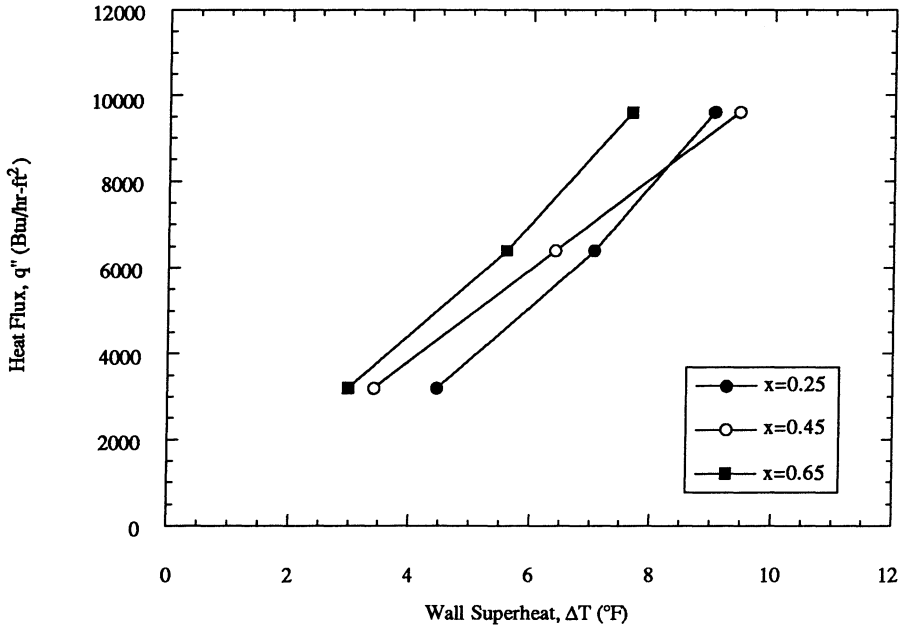

Figure 5.28. R-134a heat flux versus wall superheat at 375 klb_m/ft^2-hr in 0.305 in i.d. test section. Saturation temperature, 41°F.

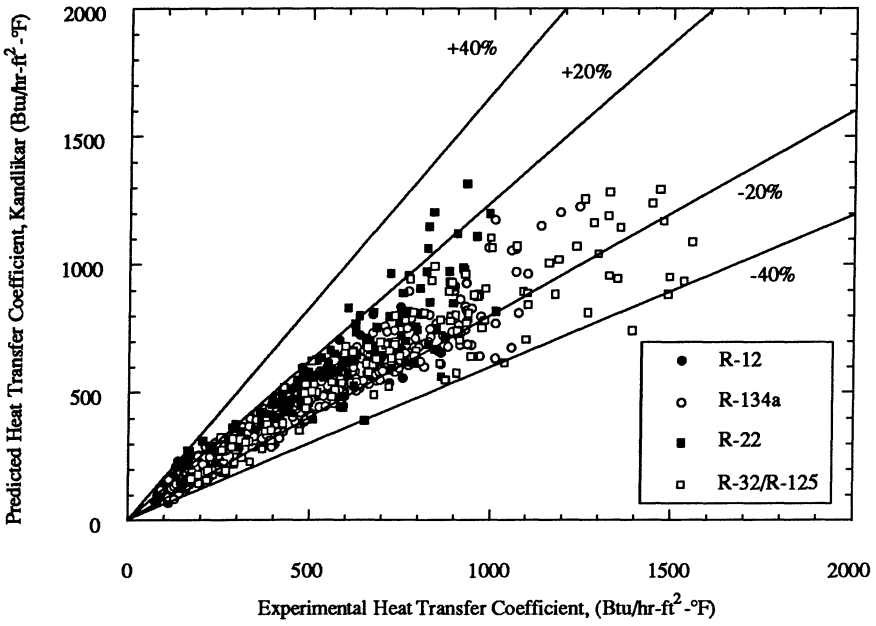

Figure 5.29. Predicted heat transfer coefficient using Kandlikar correlation [1990] versus experimental heat transfer coefficient for R-12, R-134a, R-22, and R-32/R-125.

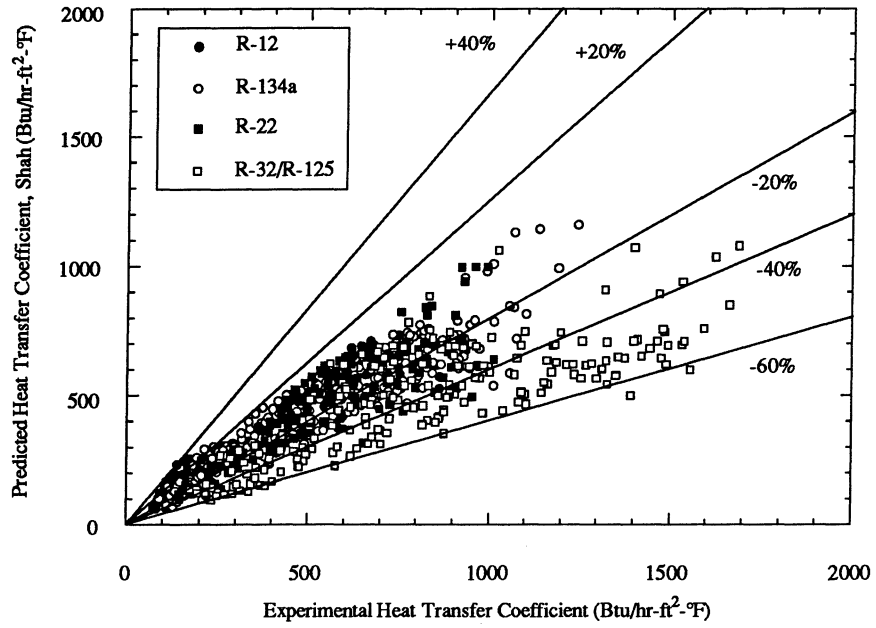

Figure 5.30. Predicted heat transfer coefficient using Shah correlation [1982] versus experimental heat transfer coefficient for R-12, R-134a, R-22, and R-32/R-125.

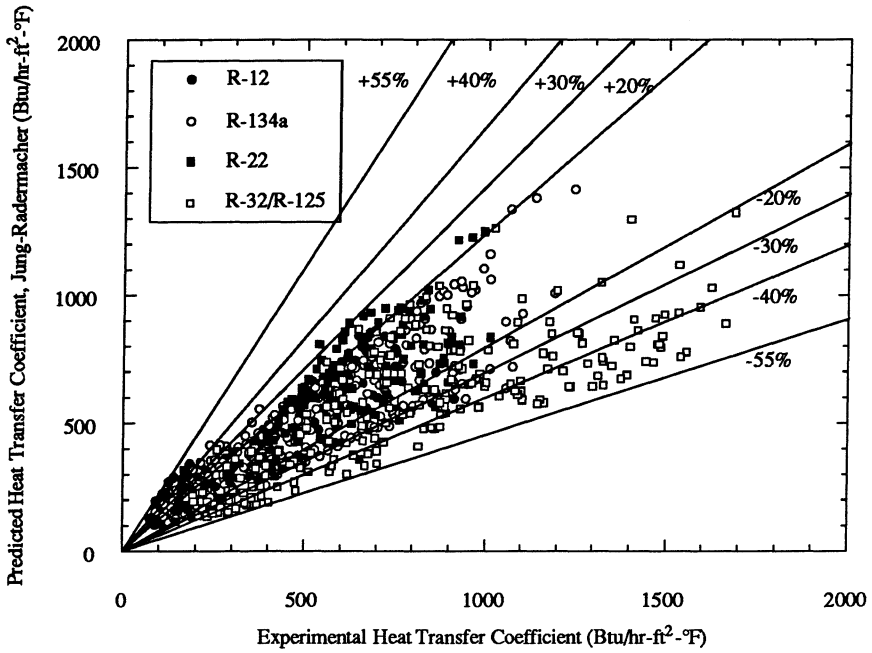

Figure 5.31. Predicted heat transfer coefficient using Jung-Radermacher correlation [1989] versus experimental heat transfer coefficient for R-12, R-134a, R-22, and R-32/R-125.

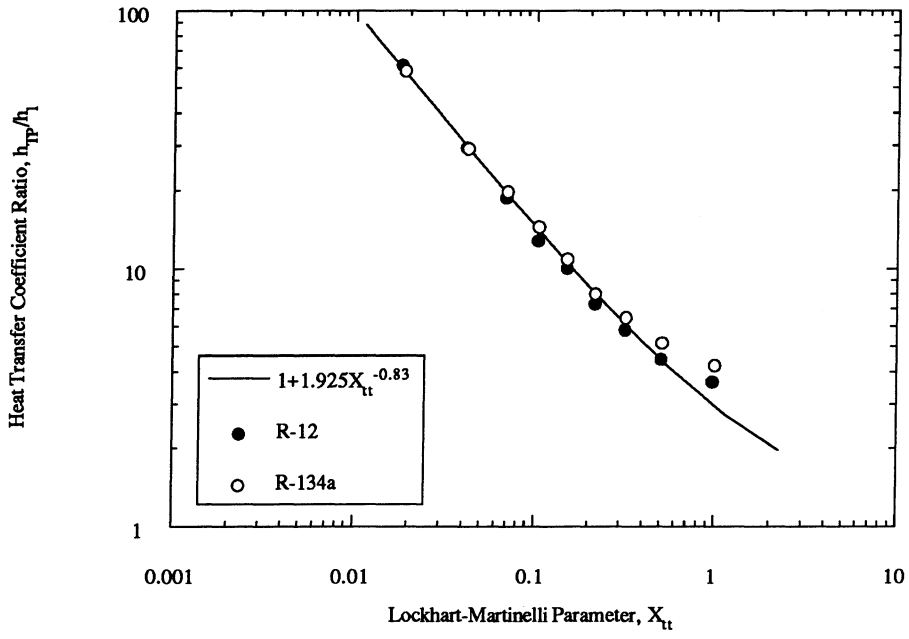

Figure 5.32. Heat transfer coefficient ratio for R-134a and R-12 versus Lockhart-Martinelli parameter at low heat flux. Mass flux, 225 klb_m/ft^2-hr; Heat flux, 1600 Btu/hr-ft^2; Saturation temperature, 41°F; Tube diameter, 0.430 in.

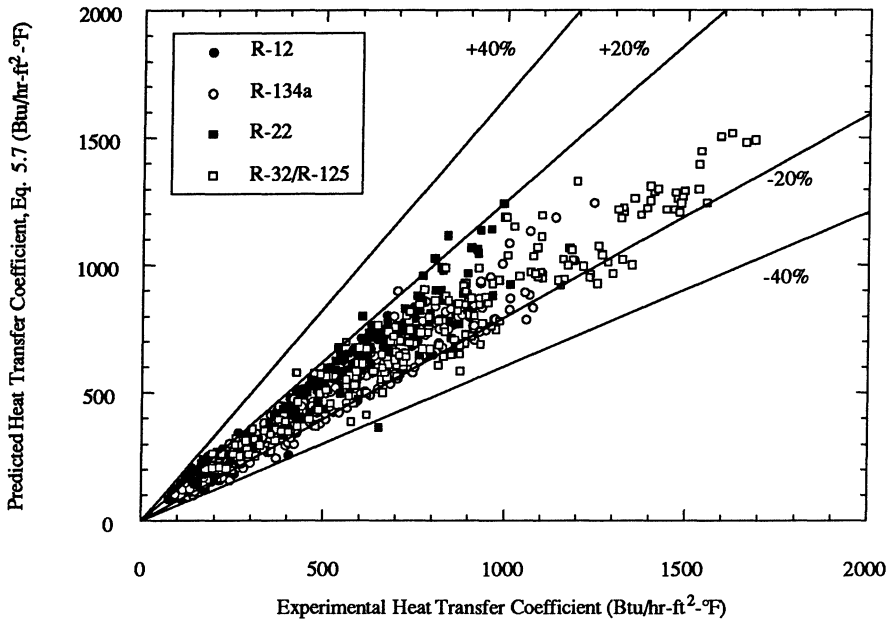

Figure 5.33. Predicted heat transfer coefficient using Eq. 5.7 versus experimental heat transfer coefficient for R-12, R-134a, R-22, and R-32/R-125.

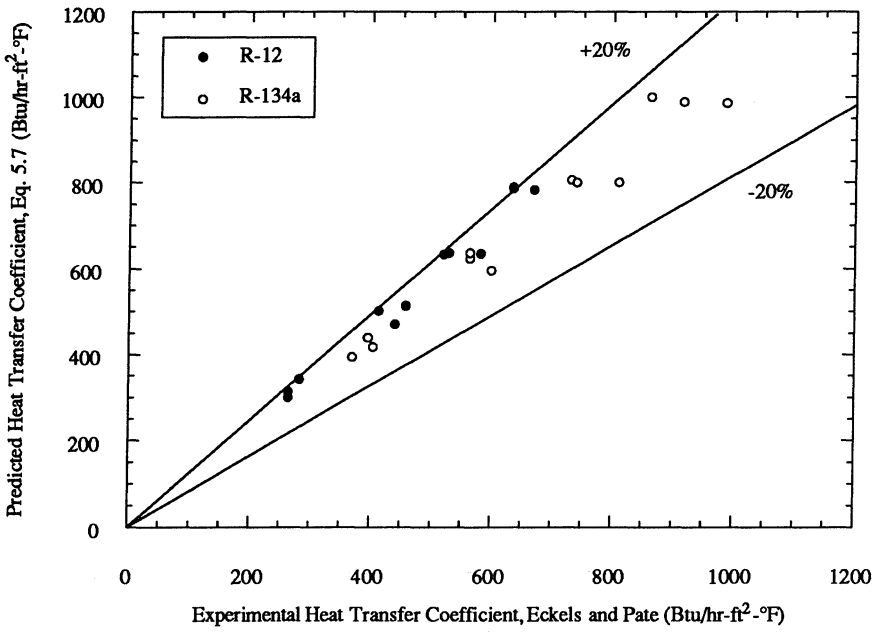

Figure 5.34. Predicted heat transfer coefficient using Eq. 5.7 versus experimental heat transfer coefficient of R-134a and R-12 from Eckels and Pate [1991].

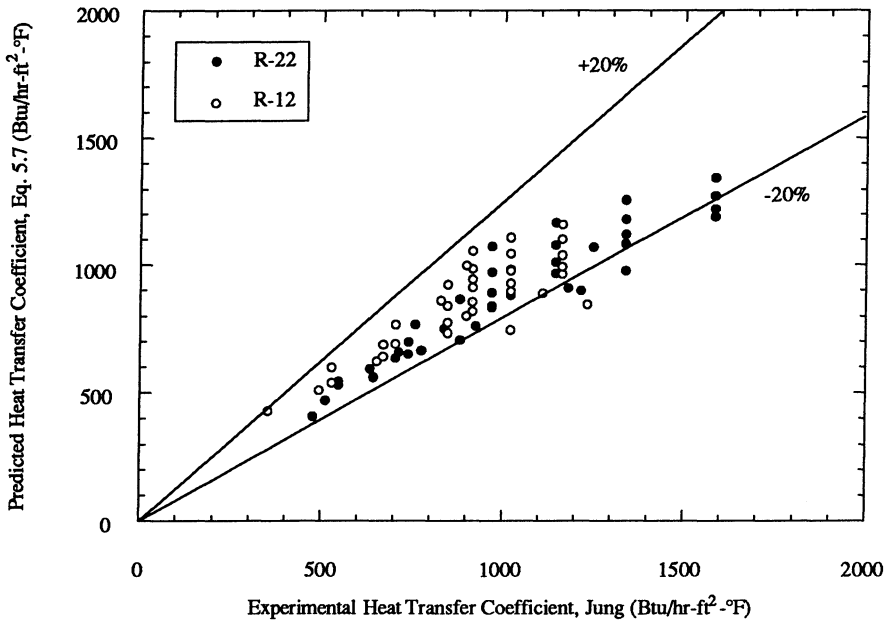

Figure 5.35. Predicted heat transfer coefficient using Eq. 5.7 versus experimental heat transfer coefficient of R-22 and R-12 from Jung [1989].

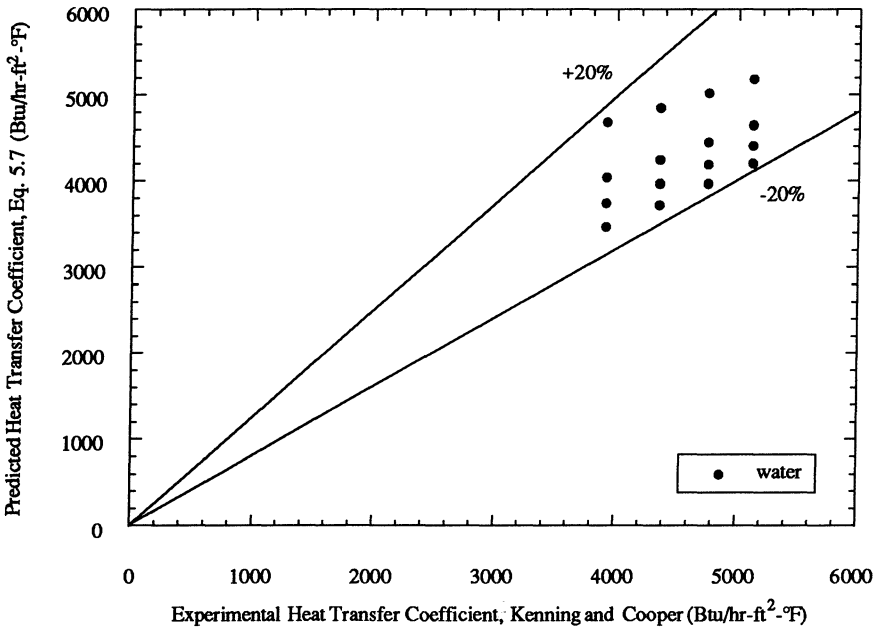

Figure 5.36. Predicted heat transfer coefficient of Eq. 5.7 versus experimental heat transfer coefficient of water from Kenning and Cooper [1989].

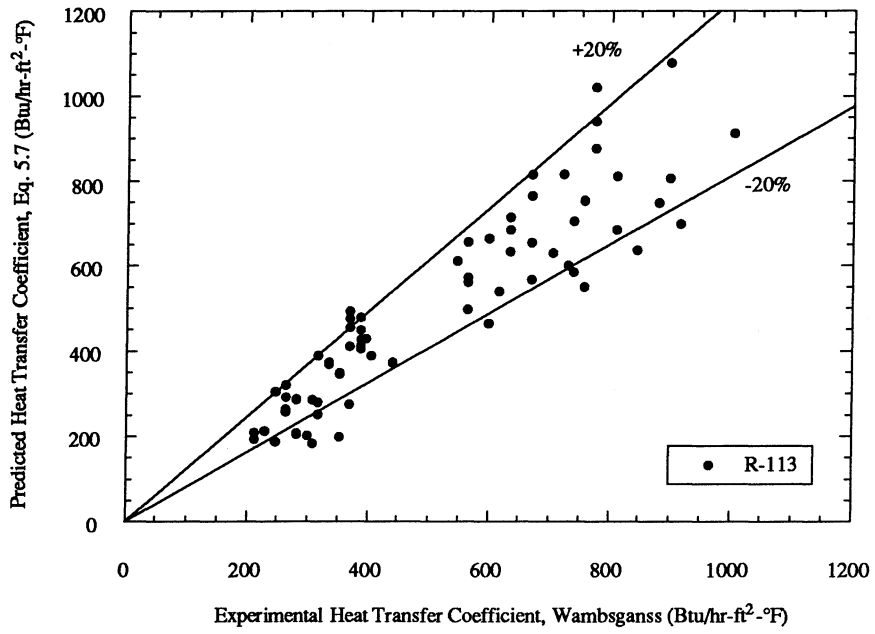

Figure 5.37. Predicted heat transfer coefficient of Eq. 5.7 versus experimental heat transfer coefficient of R-113 from Wambsganss [1993].

CHAPTER 6. EVAPORATOR SIMULATION

The previous chapters have been devoted to describing the localized two-phase heat transfer behavior of refrigerants. Using the flow pattern and heat transfer data, a semi-theoretical heat transfer coefficient correlation was developed to be applied over a wide range of evaporator conditions. The goal of this chapter is to apply the developed heat transfer coefficient correlation to different design scenarios. To achieve this, a computer simulation of an evaporator has been developed using a simple spreadsheet format. Details of the program and corresponding algorithm will be discussed in this chapter. Additional information can be found in ACRC Technical Report 42 [Dobson, Wattelet, and Chato, 1993].

For designers, the performance of a heat exchanger is based on a combination of heat transfer and pressure drop tradeoffs. Pressure drop correlations, although not examined as part of this dissertation, have also been developed during adiabatic and diabatic two-phase flow studies as part of Project 01 of the Air Conditioning and Refrigeration Center. A pressure drop correlation was developed for horizontal, evaporating flow in smooth, straight tubes and was presented in ACRC Technical Report 25 [Souza et al., 1992]. This correlation will be used to account for pressure drop in the computer simulation, along with a correlation developed for return bend pressure drop which was outlined in ACRC Technical Report 47 [Christoffersen et al., 1993].

Several different design scenarios will be presented in this chapter. First, a study was conducted to determine what tube diameter is optimum for a given mass flow rate, air-side resistance, and driving temperature difference. As tube diameter is decreased, the heat transfer coefficient increases due to the inversely proportional relationship between tube diameter and heat transfer coefficient. In addition, a much stronger effect on pressure drop occurs when the diameter is decreased, again due to the inversely proportional relationship between pressure drop and tube diameter. Keeping the outlet pressure of the evaporator fixed so that saturated vapor can be fed to the compressor, the increase in pressure drop decreases the temperature difference between the refrigerant and air streams, which reduces the heat transfer of the evaporator. The decreased tube diameter also results in decreasing the heat transfer area per unit length. These competing effects suggest, at least qualitatively, that an optimum tube diameter might exist for each set of operating conditions. This optimum diameter will be determined by minimizing the evaporator length or area for each set of operating conditions.

Two different sets of operating conditions will be examined. A low cooling capacity case typical of conditions found in a household refrigerator evaporator will be

examined for both R-134a and R-12. A higher cooling capacity case will also be considered which is indicative of flow found in a unitary air conditioner evaporator. Refrigerants used for this simulation will be R-134a, a 60%/40% azeotropic mixture of R-32/R-125, and R-22. Because of different heats of vaporization for each refrigerant, the mass flux for each refrigerant will be different. Comparisons will be made for each refrigerant based on the optimum tube diameter determined through the computer simulation.

6.1. Description of the Computer Model

Heat transfer can be discussed in terms of thermal resistances for steady-state, one-dimensional heat transfer with constant properties. If the thermal resistance of the high conductivity tube wall is neglected along with neglecting fouling factors on the inside and outside surfaces of the tube, the following equation can be used to determine the heat transfer through the heat exchanger:

$$q = \frac{L \bullet \Delta T}{R'_{AIR} + R'_{REF}} \tag{6.1}$$

where

$$R'_{REF} = \frac{1}{\pi D h_{REF}} \tag{6.2}$$

and is defined as the heat transfer resistance per unit length. To focus on the effects of the refrigerant-side heat transfer coefficient, the air-side resistance will be held constant throughout the various computer simulations. The πDh term in the refrigerant-side resistance is the heat transfer coefficient times the perimeter. Based on an examination of Eqs. 6.1 and 6.2, keeping both the temperature driving potential, ΔT, and the quantity hD as large as possible are the primary focuses when optimizing a certain parameter, such as evaporator length, for a given set of operating conditions. The coupling of the heat transfer coefficient with the perimeter indicates that decreasing the heat exchanger length by decreasing the tube diameter requires a larger percentage increase in heat transfer coefficient than the corresponding percentage decrease in tube diameter.

Simulating a real heat exchanger, however, requires integrating the heat transfer coefficient and pressure drop correlations over the length of the heat exchanger as the quality is varied. A spreadsheet was developed that would accept inputs concerning the operating conditions of the heat exchanger and compute the length of the various regions of the heat exchanger as output. Since tube length is required for the straight tube pressure

drop correlation, iteration was required which could easily be done using a spreadsheet program. Refrigerant properties were then curve fitted over the desired temperature range and were fed into the spreadsheet using a macro. These properties were evaluated by the spreadsheet using function calls to the property macros. Property macros were developed for R-12, R-134a, R-22, and R-32/R-125 using information from REFPROP [Morrison et al., 1991].

The required inputs to the spreadsheet were mass flow rate, inside tube diameter, air temperature, air-side thermal resistance per unit length, inlet quality, and outlet pressure. The length of the evaporator was calculated using the differential version of Eq. 6.1 as follows:

$$\Delta L = \frac{\delta q \bullet (R'_{REF} + R'_{AIR})}{(T_{REF} - T_{AIR})} \tag{6.3}$$

The heat transfer coefficient, pressure drop, and thermal resistance were computed for quality increments of 5% from the given inlet quality to the saturated vapor point. The differential heat transfer rate was calculated through an energy balance on the element of the heat exchanger as follows:

$$\delta q = \dot{m}\, i_{lv} \Delta x \tag{6.4}$$

Saturation temperature / pressure relationships from REFPROP were used to calculate the temperature drop through the heat exchanger element from the calculated pressure drop. Iteration was required since the pressure drop was a function of the length of the heat exchanger element. For each quality increment, the resulting values from the spreadsheet were the outlet pressure, outlet saturation temperature, and required length. The refrigerant temperature in Eq. 6.3 was assumed to be equal to the arithmetic mean of the inlet and outlet values. Summing each of the differential lengths, the required length of heat exchanger was determined. For evaporators, the superheat section is a small part of the total heat transfer area, and this section of a typical evaporator was neglected in this analysis.

6.2. Pressure Drop Correlations

In this section, correlations for pressure drop during evaporating flow in horizontal, smooth tubes and pressure drop in return bends will be outlined. These correlations were used to compute the pressure decrement for each quality increment of the evaporator as discussed in Sec. 6.1.

6.2.1. Friction pressure drop correlation

Pressure drop in horizontal evaporating flow is comprised of two components: friction pressure drop and acceleration pressure drop. As discussed in Chap. 2, a variation of the Lockhart-Martinelli [1947] method is commonly used to compute friction pressure for horizontal separated flows. Their basic hypothesis was that the two-phase pressure gradient was equal to the pressure drop of the liquid or vapor phase times a two-phase multiplier, ϕ^2. Using the liquid phase, the resulting form of the correlation was

$$\Delta P_f = \Delta P_l \phi_l^2 \tag{6.5}$$

with the single-phase pressure drop defined as

$$\Delta P_l = \frac{2 f_l G^2 (1-x)^2 L}{\rho_l D} \tag{6.6}$$

and the friction factor given as

$$f_l = \frac{0.079}{Re_l^{0.25}} \tag{6.7}$$

A correlation for the two-phase multiplier was developed for horizontal, evaporating flow in smooth, straight tubes and was presented in ACRC Technical Report 25 [Souza et al., 1992]. The two-phase multiplier for friction pressure drop was found to be a function of the Lockhart-Martinelli parameter and is defined as follows:

$$\phi_l^2 = 1.376 + C_1 X_{tt}^{C_2} \tag{6.8}$$

where C_1 and C_2 are functions of mass flux. The mass flux dependence of the coefficients was accounted for using the Froude number as follows:

For $0 < Fr_l \leq 0.7$,

$$\begin{aligned} C_1 &= 4.172 + 5.48 Fr_l - 1.564 Fr_l^2 \\ C_2 &= 1.773 - 0.169 Fr_l \end{aligned} \tag{6.9}$$

For $Fr_l > 0.7$,

$$\begin{aligned} C_1 &= 7.242 \\ C_2 &= 1.655 \end{aligned} \tag{6.10}$$

This correlation was tested for all of the refrigerants used in this study, with mean deviations under ±20% for all tests conducted in both annular and wavy flows.

6.2.2. Acceleration pressure drop correlation

The acceleration pressure drop results from acceleration of the flow due to the evaporation phase-change process. Using appropriately averaged velocities for each phase and a constant tube-diameter, the acceleration pressure drop was determined using a simplified, one-dimensional momentum equation given in Eq. 2.41. The resulting equation

for acceleration pressure drop for a section with inlet properties denoted by the subscript i and outlet properties denoted by the subscript o for a constant flow rate was

$$\Delta P_a = \frac{16\dot{m}^2}{\pi^2 D^4}\left\{\left[\frac{x_o^2}{\rho_v \alpha_o} + \frac{(1-x_o)^2}{\rho_l(1-\alpha_o)}\right] - \left[\frac{x_i^2}{\rho_v \alpha_i} + \frac{(1-x_i)^2}{\rho_l(1-\alpha_i)}\right]\right\} \tag{6.11}$$

Void fraction was calculated using the correlation of Zivi [1964] as follows:

$$\alpha = \frac{1}{1+\left(\frac{1-x}{x}\right)\left(\frac{\rho_v}{\rho_l}\right)^{0.67}} \tag{6.12}$$

6.2.3. Return bend pressure drop correlation

A correlation developed for return bend pressure drop was outlined in ACRC Technical Report 47 [Christoffersen et al., 1993]. Using the premise of Pierre [1964], the adiabatic pressure drop associated with a bend was broken down into two parts: a pressure drop related to friction and a pressure drop related to turning the flow. This is shown as follows:

$$\Delta P_b = \Delta P_f + \Delta P_t \tag{6.13}$$

Frictional pressure drop was calculated from Eq. 6.5. The pressure drop due to turning the flow was based on a dimensionless resistance factor defined as

$$\varepsilon = \frac{2\Delta P_t}{G^2 v_{ave}} \tag{6.14}$$

where v_{ave} is given as

$$v_{ave} = (1-x)v_l + xv_v \tag{6.15}$$

In ACRC Technical Report 47 [Christoffersen et al. 1993], the dimensionless resistance factor was determined to be a function of liquid Reynolds number and Lockhart-Martinelli parameter as follows:

$$\frac{2\varepsilon}{\delta Re_l} = C_3 X_{tt}^{C_4} \tag{6.16}$$

where C_3 is $6.93\text{x}10^{-5}$ and C_4 is -0.712. The parameter δ is defined as $\sqrt{D/D_{RB}}$.

6.3. Optimum Tube Diameter Simulations

Based on the correlations presented above, an optimum diameter may exist since decreasing the diameter enhances heat transfer while also dramatically increasing the pressure drop, which reduces the driving temperature difference. This type of situation often results in an optimum value in which the two competing effects are balanced.

Changing the evaporator's inside tube diameter would normally result in many changes propagating through the refrigeration system. To isolate the effects to the evaporator, the exit pressure of the evaporator, and, hence, the inlet pressure to the compressor, was kept fixed. As discussed above, the air-side resistance was also fixed. For simplicity, a return bend was used for each 5 percent quality increment. The length of each quality increment module included the length of the return bend, which was arbitrarily set at 0.5 ft. A somewhat complicated but more realistic way of including return bend effects would be to add a return bend when the quality increment exceeds a certain length.

Two sets of conditions were simulated for an evaporator: a high flow rate case that would be applicable for unitary systems and a low flow rate case that would be applicable for refrigerators. The test conditions for the evaporator using R-134a as the refrigerant are listed in Tables 6.1. For each case, the inputs were made to the spreadsheet and the diameter was varied over a wide range. The required length of heat exchanger to complete the phase-change process was computed for each diameter. A lower limit on diameter was eventually reached where the pressure drop became so great that the temperature driving potential was nearly eliminated.

Table 6.1. Input parameters for evaporation optimum diameter simulations for R-134a

Quantity	High Flow Rate Case	Low Flow Rate Case
Mass Flow Rate	80 lb_m/hr	10 lb_m/hr
Inlet Quality	20%	20%
Outlet Saturation Temp.	41°F	-4°F
Air Temperature	73°F	14°F
Air Side Resistance/Length	0.073 ft-°F-hr/Btu	0.43 ft-°F-hr/Btu

In addition to the high and low flow rate tests for R-134a, comparison tests were conducted for the additional refrigerants used in this study. The computer simulation was also run for R-12 at the same cooling capacity as R-134a for the low flow rate case. Adjustments were made in the spreadsheet to input cooling capacity instead of mass flow rate. For R-12, this resulted in a flow rate of 13 lb_m/hr. Also, the computer simulation was run for R-22 and R-32/R-125 at the same cooling capacity as R-134a for the high flow rate case. For R-22 and R-32/R-125, this resulted in flow rates of 78 lb_m/hr, and 67 lb_m/hr, respectively.

6.3.1. Results for R-134a

The results of the evaporation simulations for R-134a are presented in Figs. 6.1 and 6.2, which show the required heat exchanger length for the phase-change process as a function of the inside tube diameter. Figure 6.1 shows the comparison between the computer simulation with and without the inclusion of bend pressure drop. The trends of the two curves were the same, with the additional pressure drop from the return bends shifting the curve to a slightly higher length for each respective diameter. The optimum point also occurred at a higher diameter. Since the trends were the same and the bend pressure drop setting was highly arbitrary, bend pressure drop was neglected for the remainder of the plots.

In Fig. 6.2, both high and low mass flow rate cases are shown. For decreasing inside tube diameter, the required length of heat exchanger slowly increased until eventually the curve took a sharp upward turn. As inside tube diameter was decreased, both the heat transfer coefficient and pressure drop in the evaporator increased. For larger tube diameters, the pressure drop in the evaporator remained relatively low and did not destroy much of the temperature difference between the refrigerant stream and the air stream. Therefore, the length of the heat exchanger required to transfer the given heat load remained relatively constant, increasing only marginally. When the inside tube diameter was further decreased to a critical value, the pressure drop increased, eventually becoming large enough to destroy a substantial portion of the temperature difference between the refrigerant stream and air stream. The length of the evaporator necessary to transfer the required heat increased substantially at this point.

The minimum inside diameter for the low flow rate case was smaller than for the high flow rate case, as can be seen in Fig. 6.2. The refrigerant-side resistance was much smaller compared to the air-side resistance for the low flow rate case than the high flow rate case. In addition, the pressure drop in the evaporator was highly dependent on mass flow rate and was substantially reduced for a wavy flow pattern, which was the predominant flow pattern for the low flow rate case. Pressure drop was much higher for the annular flow pattern found in the high mass flow rate case. Both of these kept the temperature driving potential higher for the low flow rate case than the high flow rate case for the same diameter. This resulted in a lower inside tube diameter for the sharp upward turn of the curve in Fig. 6.2 for the low flow rate case.

6.3.2. Results for equivalent cooling capacity tests

As indicated above, equivalent cooling capacity tests were conducted for both the high and low flow rate cases for R-134a. For the low flow rate case, R-12 was compared

with R-134a. For the high flow rate case, R-22 and R-32/R-125 were compared with R-134a. Figure 6.3 shows the evaporator length versus inside tube diameter curves for the high flow rate case. Although the trends in the curves were similar, R-32/R-125 had the lowest optimum tube diameter, followed by R-22 and R-134a. Although R-32/R-125 had the lowest mass flow rate of the three refrigerants for the equivalent cooling capacity simulations, its superior thermal properties kept the heat transfer coefficients similar to its R-22 and R-134a counterparts. However, its low pressure drop kept the temperature driving potential higher than the other two refrigerants at the lower tube diameters and pushed the optimum tube diameter to a lower level. R-134a and R-22 had similar heat transfer coefficients at equivalent cooling capacity conditions. Again, the lower pressure drop for R-22 kept the temperature driving potential higher than R-134a and caused the optimum tube diameter for R-22 to be lower than R-134a.

Figure 6.4 shows the equivalent cooling capacity tests for the low flow rate case for R-134a and R-12. R-12 has an approximately 23% lower heat of vaporization than R-134a and, therefore, had a higher flow rate than R-134a for the equivalent cooling capacity simulation. This caused the heat transfer coefficients to be similar for the two refrigerants. Pressure drop was slightly higher for R-12. Overall, the optimum tube diameters for the two refrigerants were almost identical.

6.3.3. Minimum surface area results for Fig. 6.2

The optimum diameter also may be defined in terms of material costs as the one that requires the minimum surface area. The data from Fig. 6.2 are presented in this fashion in Fig. 6.5. If the optimum tube diameter is based on the minimum surface area criterion, as shown in Fig. 6.5, a distinct optimum is observed for both the low flow rate and high flow rate cases. The optimum values in Fig. 6.5 are very near the sharp change in slope of the curves in Fig. 6.2. From a design standpoint, the best sizing rule would be to select the first commercially available size that is larger than the optimum value.

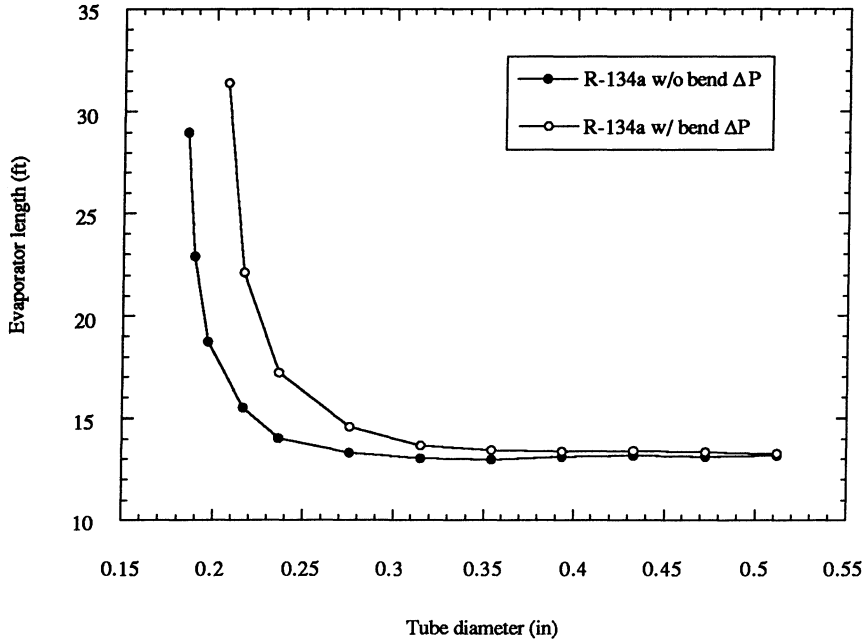

Figure 6.1. Evaporator length versus inside tube diameter for R-134a with and without return bend pressure drop.

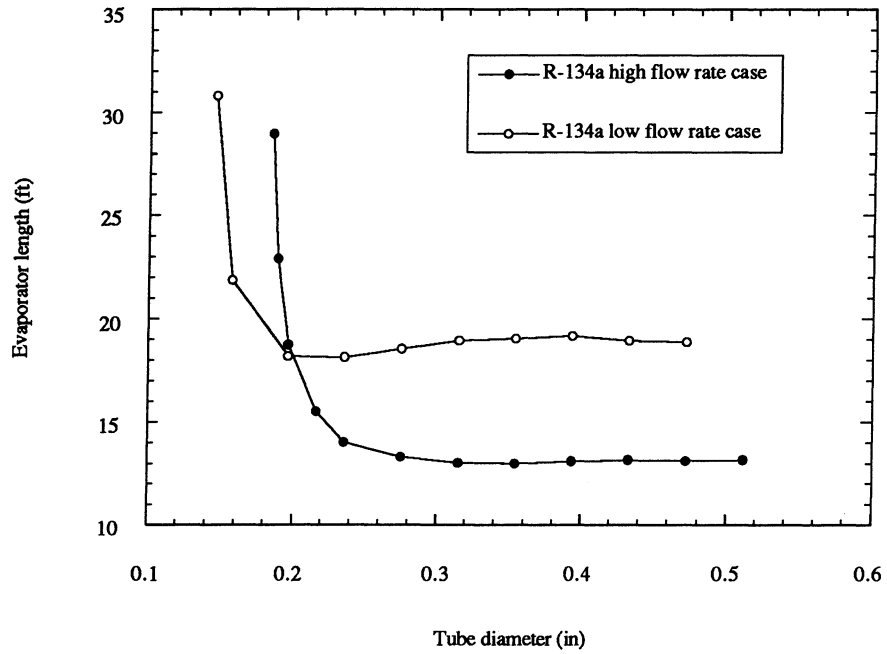

Figure 6.2. Evaporator length versus inside tube diameter for R-134a for high and low flow rate cases.

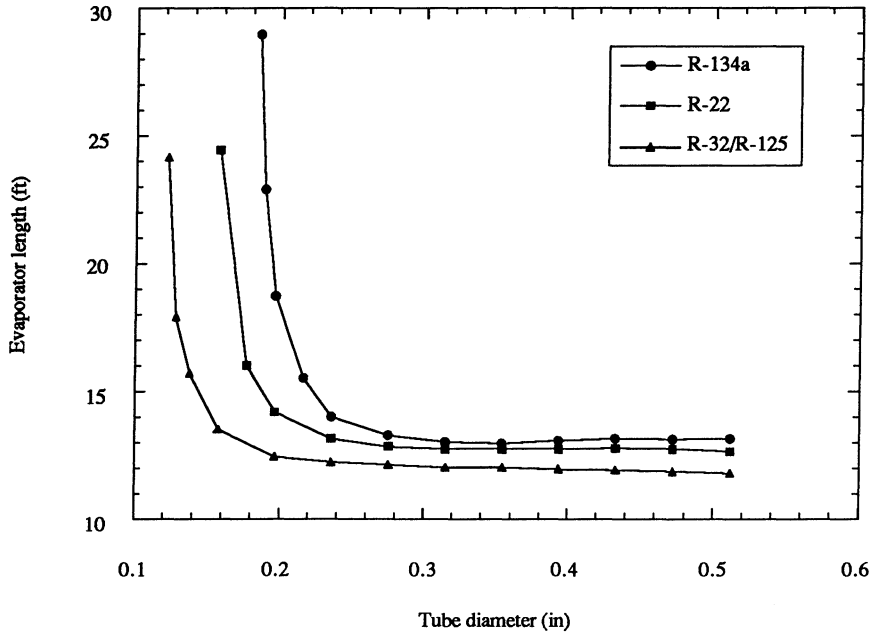

Figure 6.3. Evaporator length versus inside tube diameter for R-134a, R-22, and R-32/R-125 for unitary air conditioning evaporator cooling capacity.

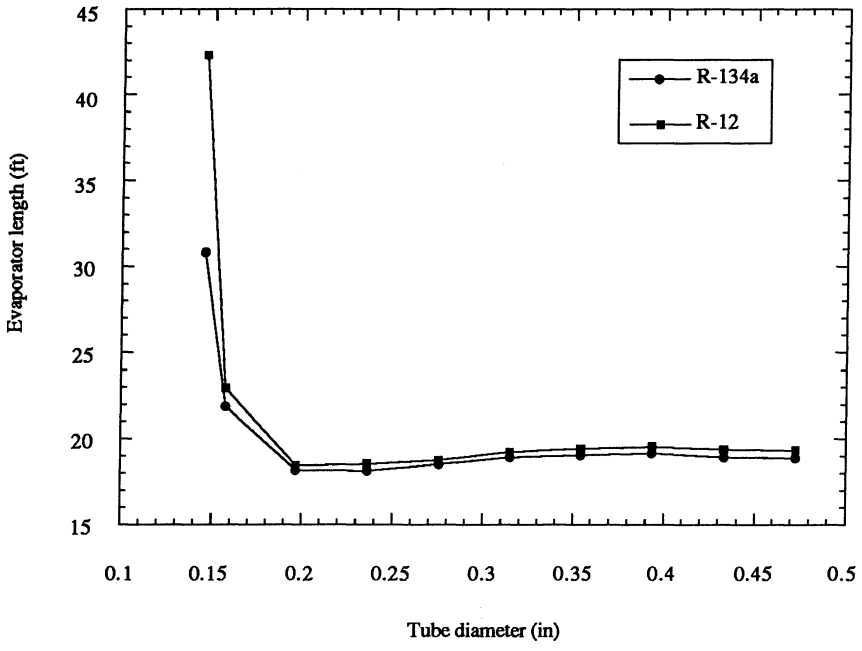

Figure 6.4. Evaporator length versus inside tube diameter for R-134a and R-12 for household refrigerator evaporator cooling capacity.

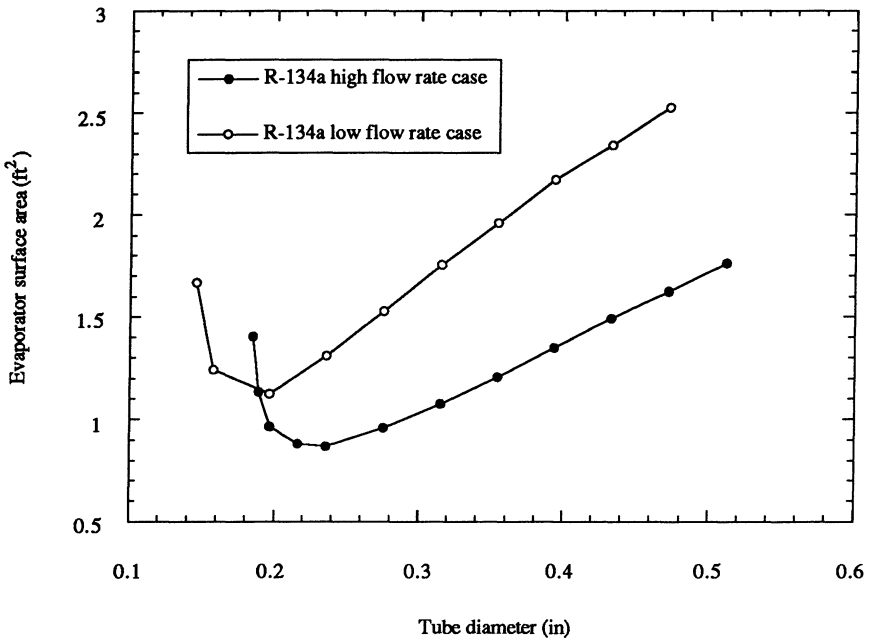

Figure 6.5. Evaporator surface area versus inside tube diameter for R-134a for high and low mass flow rates.

CHAPTER 7. CONCLUSIONS AND RECOMMENDATIONS

This dissertation consisted of three main areas for two-phase flow in a single-tube evaporator: flow pattern identification and evaluation of criteria to determine flow pattern transitions; evaluation and correlation of local heat transfer coefficients for refrigerants; and application of these results to evaporator design. Within each of these areas, several conclusions were drawn and are discussed below.

7.1. Conclusions

7.1.1. Flow patterns

The two main flow regimes found during objective and subjective evaluation of the flow patterns during adiabatic and diabatic flows in smooth, horizontal tubes were wavy and annular flow. The differences in these flow patterns were of major importance in correlating the resulting heat transfer coefficients. Slug and mist flow were found to be of minor importance for typical qualities found in a refrigerant evaporator.

Of the three flow maps examined, the Taitel-Dukler [1976] flow map was found to be the most accurate. Its use of analytically determined dimensionless parameters for the axes of the flow map proved to be superior to the superficial velocity type coordinates of the Baker [1954] and the Mandhane [1974] maps. An additional flow pattern, a kind of combination of slug and separated flow patterns discussed by Lin and Hanratty [1989] called pseudo-slug flow, was also identified for horizontal, two-phase refrigerant flow using objective high speed pressure and differential pressure measurement techniques. This pushes the actual slug flow region indicated on the Taitel-Dukler map to the right, to higher Lockhart-Martinelli parameter values or lower qualities.

High speed pressure and differential pressure measurements were taken for a variety of mass flux and quality combinations. These measurements were analyzed both statistically and spectrally, using methods outlined by Hubbard and Dukler [1966] and Matsui [1984, 1986]. Spectrally, the resulting normalized power spectral density of the high speed pressure and pressure drop measurements indicated patterns typically found for separated flow of air-water flows. These patterns had sharp spikes near zero frequency, with the majority of power occurring at this value. Even low quality flows, which appear to be slug flow based on visual observation at the sight glasses at the inlet and outlet of the test section, had a separated flow signature indicated by the normalized power spectral density plots. Cross-correlations of high speed pressure measurements at the inlet and outlet of the test section showed little correlation, indicative of pseudo-slug flow, in which

the visually observed slugs had vapor bubbles distributed in them, causing only minor pressure fluctuations compared with true slug flow.

Statistically, normalized probability density functions showed wider normalized variations for wavy flows than for annular flows. Plots of the standard deviation divided by the mean pressure drop for the high speed differential pressure measurements indicated that wavy flow occurred for values of this parameter above 0.20, while annular flow occurred for values below 0.10. A transition between the two flow patterns occurred for values between 0.10 and 0.20.

Examining the heat transfer coefficient and pressure drop trends versus quality, a transition from annular to annular-mist flow was observed when the pressure drop curve achieved a maximum value, usually around 80 percent quality for the tests conducted in this study. This transition, using the maximum pressure drop value, was first proposed by Chien and Ibele [1964] for air-water flow. Visually, it was difficult to tell the difference between annular flow without entrainment and annular-mist flow using the sight glasses in this study, and further confirmation of this transition is needed, possibly using visual techniques perpendicular to the flow or by physically measuring entrainment in the vapor core. Examining the heat transfer coefficient versus quality plots, mist flow was encountered when there was a sudden drop in heat transfer coefficient, caused by the dryout of the tube wall. For the constant heat flux boundary condition in this study, the decrease in heat transfer coefficient caused the wall temperatures to become very large. This transition occurred at qualities above 95 percent for the tests conducted, and played little role in its effect on the overall heat transfer coefficient in two-phase flow for typical refrigerant evaporator conditions.

7.1.2. Heat transfer coefficients

Heat transfer to the various refrigerants tested was broken down based on the major flow patterns discussed above: annular and wavy flow. For annular flow at low heat fluxes, convective boiling was the dominant mode of heat transfer. The heat transfer coefficients increased with quality. Intense evaporation at the liquid-vapor interface diminished the liquid film thickness, reducing the thermal resistance, which is associated with heat conduction across the film. Nucleate boiling appeared to be largely suppressed for these low heat flux cases. As heat flux increased, the heat transfer coefficients increased in the lower quality region and eventually merged at higher qualities with the heat transfer coefficients for the low heat flux cases. Nucleate boiling at these lower qualities enhanced the heat transfer coefficients. At higher qualities, nucleate boiling was again

largely suppressed due to significant surface cooling promoted by the thinning of the annular film. Wall superheats for this set of data ranged from 1.8 to 10.8°F.

For wavy flows, there was no major effect of quality on the circumferentially averaged heat transfer coefficients. However, as the heat flux increased, the heat transfer coefficient also increased. Compared with the results in the annular flow regime, convective boiling was diminished while nucleate boiling did not appear to be suppressed at higher qualities or lower heat fluxes. The decrease in convective boiling was attributed to the reduction in available surface area for convective boiling and a decrease in slip ratio between the vapor and liquid streams. Wall superheats for this set of data ranged from 3.6 to 9°F.

The asymptotic model combined the "greater of the two" and superposition models and handled the combination of the nucleate and convective boiling well. It was chosen as the model to correlate the empirical data of this study. The asymptotic model automatically suppressed either term based on the magnitudes of the convective and nucleate boiling term, thereby eliminating the need for a nucleate boiling suppression term. The data showed that there can be nucleate boiling for many of our conditions. For low heat fluxes in annular flow, this contribution was small and may be considered to be negligible compared with the dominant convective heat transfer. The asymptotic model that was developed in this study properly accounted for this. For higher heat fluxes in annular flow, both convective and nucleate boiling occurred, and the model also accounted for this. For wavy flows, the convective term was diminished, and both nucleate boiling and convective boiling contributed to the heat transfer. Again, the asymptotic model accounted for this.

Convective boiling was well correlated by the combination of the single-phase heat transfer coefficient based on liquid alone flowing in the tube and a two-phase multiplier for heat transfer based on the Lockhart-Martinelli parameter. Variations on the Lockhart-Martinelli parameter, such as replacing the property ratios by a reduced pressure term or by the convection number, also worked well. The Dittus-Boelter correlation worked well for heat transfer coefficients in the annular flow regime. A Froude number dependent term accounted for the stratification effects of the wavy flows better than a combination of a Froude number dependent term and a loss of turbulence term. Also, the Gnielinski correlation, although regarded as more accurate than the Dittus-Boelter correlation in the 4000-10000 Reynolds number range, has a (Re-1000) term, which caused correlating problems below a Reynolds number of 4000, making it ill-suited for correlating the heat transfer coefficient data for wavy flow.

The heat flux was the most important parameter in characterizing nucleate boiling effects, but was not enough to correlate data accurately for different pressures or different

fluids. Experimental data developed in this and other studies were combined to show that molecular weight can account well for these fluid specific effects. Temperature variation also affected the heat transfer coefficient data, and a reduced pressure term was shown to account well for these effects.

Overall, the developed correlation, Eq. 5.7, accounted for data over a wide range of mass and heat fluxes, from 38-750 klb_m/ft^2-hr and 640-96,000 $Btu/hr\text{-}ft^2$, respectively. Fluids tested include R-12, R-134a, R-22, and a 60%/40% azeotropic mixture of R-32/R-125. Additional data for R-113 and water from other studies in the literature were well correlated by Eq. 5.7. The limits of the correlation have been well thought out, and it is hoped that this correlation will be robust enough to be used for fluids not presently examined, such as other refrigerants or hydrocarbons.

7.1.3. Evaporator simulation

Two-phase heat transfer and pressure drop correlations developed in this study were combined into a computer simulation spreadsheet which allowed simulation of the two-phase portion of evaporators. The spreadsheet allowed simulation with four refrigerants: R-12, R-134a, R-22, and a 60%/40% azeotropic mixture of R-32/R-125. The spreadsheet was used to study the effect of altering the diameter of heat exchangers while keeping the air-side resistance and refrigerant mass flow rate constant. Simulations were performed for both a high and a low flow rate for evaporators. The results of all the simulations were similar. The required length of heat exchanger remained relatively constant as the tube diameter was decreased over a wide range. As the diameter became sufficiently small, though, the required length of heat exchanger began to increase greatly as the diameter was decreased further. This occurred because a substantial portion of the driving temperature difference between air and refrigerant streams was eliminated by pressure drop. This optimum diameter was smaller for the low flow rate cases than for the high flow rate cases because of decreased pressure drop for the low flow rate cases.

7.2. Recommendations

This study has provided a sound basis for future studies regarding two-phase flow heat transfer in refrigerant evaporators. Listed here are some recommendations for the direction of these future studies. Several different areas need to be addressed regarding two-phase flow heat transfer in refrigerant evaporators. These include micro-fin studies and other surface enhancements, alternative geometries, such as flat plates, zeotropic refrigerants, effect of lubricating oils, electrohydrodynamic enhancement techniques, and microchannel evaporation. As discussed above, the asymptotic model correlation

developed in this study should be used as the basic template for future correlating work. Modifications can be made on different terms of the correlation, incorporating differences due to zeotropic refrigerants or surface enhancements.

Several suggestions can be made regarding micro-fin tube studies. The advantages of micro-fins are that these fins increase the surface area for the same outside tube diameter and increase surface wetting. In the correlation, the reduction parameter term in Eq. 5.7, which accounts for stratification effects, can virtually be eliminated. Initial correlations have been suggested in ACRC Technical Report 47 [Christoffersen et al., 1993]. An examination of the tradeoffs between the improvement in heat transfer and the increase in pressure drop needs to be conducted for the micro-fin tubes. For example, these tradeoffs can be closely examined using the heat exchanger simulation spreadsheet developed in this study. The results of substituting the heat transfer and pressure drop correlations into the computer simulation for a micro-fin tube and a smooth tube for a typical unitary air conditioning flow rate can be seen in Fig. 7.1. For a wide range of tube diameters, the micro-fin evaporator has a shorter length than the smooth tube evaporator. However, its optimum diameter is slightly higher than the smooth tube optimum diameter. These are the type of tradeoffs that need to be addressed regarding micro-fins.

Experimentally, the different micro-fin parameters must be isolated in order to address optimization of the micro-fin design. This includes examining a range of helix angles, fin heights, etc. One basic tube type should be used, not a smorgasbord of tubes which will not allow parameters to be isolated while other parameters are held constant.

Alternative geometries also need to be examined, such as flat plates. This is very important to the automotive industry, which widely use flat plate evaporators. First, a smooth flat plate should be tested. The use of a hydraulic diameter for correlating purposes should be considered. Later, more specific geometries used by industry, such as bumped and ribbed surfaces, should be examined as differences compared to round tubes are determined.

Zeotropic refrigerants should be examined in detail. A reduction of nucleate boiling in annular flow and a reduction of convective and nucleate boiling in wavy flow have been shown to occur for a ternary blend of refrigerants [Wattelet et al., 1994]. Many zeotropic refrigerants of R-32, R-134a, and R-125 are being examined as potential replacements to R-22, an HCFC refrigerant. For correlating purposes, binary mixtures should first be used. Experimentally, the saturation temperature / saturation pressure relationship must be identified for the quality range studied. Assumption of a linear temperature drop through the test section as used in this study for pure and azeotropic refrigerants may not be

justified for zeotropic mixtures. Measuring concentrations in the liquid layer in the test section should also be considered.

A large number of tests have been run for refrigerant-oil mixtures [Panek et al., 1992]. However, due to a lack of thermophysical property information, the data has not been correlated. With accurate thermophysical property information for the oils, the properties of the refrigerant-oil mixtures can be modified and may be used directly with existing correlations. Again, the apparent superheat of the refrigerant-oil mixtures causes saturation temperature / saturation pressure discrepancies, which affect the heat transfer coefficient data at high qualities. This may actually account for the apparent degradation in heat transfer coefficient at high qualities that is commonly observed.

Additional, novel heat transfer enhancement should also be examined. These include microchannel evaporation using laminar flow of refrigerants and electrohydrodynamic enhancement of heat transfer coefficients. These topics indicate some of the future directions in which refrigerant heat transfer research is headed.

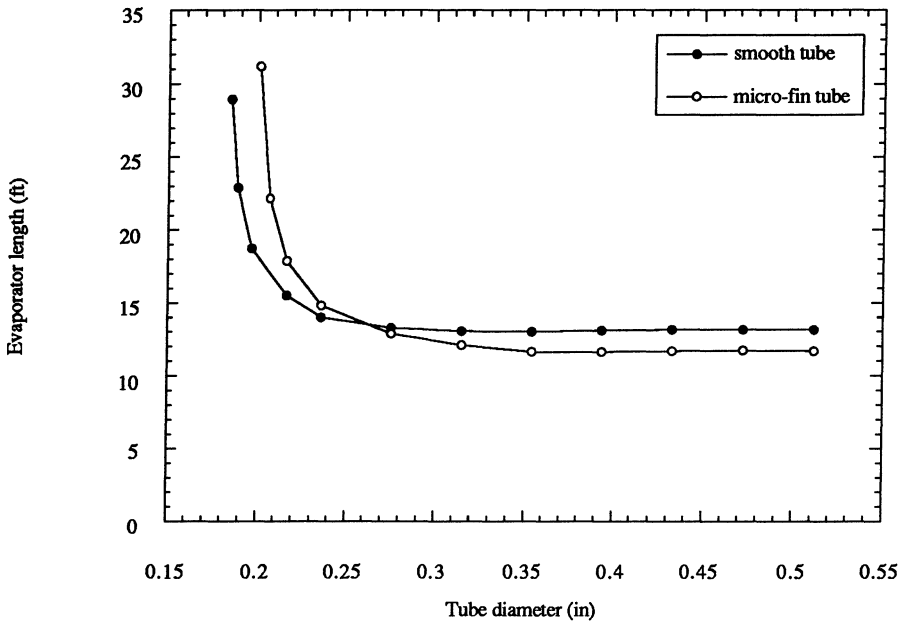

Figure 7.1. Comparison of micro-fin and smooth tubes using evaporator simulation for R-134a and the high flow rate conditions described in Table 6.1.

BIBLIOGRAPHY

Adrian, R., TAM 437 notes, 1993.

Andrisotos, N., L. Williams, and T.J. Hanratty, "Effect of liquid viscosity on the stratified-slug transition in horizontal pipe flow," International Journal of Multiphase Flow, 15(6), 877-892, 1989.

ASHRAE Fundamentals, American Society of Heating, Refrigerating, and Air Conditioning Engineers, 1989.

"ASHRAE guidelines: guide for engineering analysis of experimental data," ANSI/ASHRAE Standard 41.5-75R, 1986.

Baker, O., "Simultaneous flow of oil and gas," Oil & Gas Journal, 53, 185-195, 1954.

Barnea, D., O. Shoham, and Y. Taitel, "Flow pattern transition for gas-liquid flow in horizontal and inclined pipes," International Journal of Multiphase Flow, 6, 217-226, 1980.

Barnhart, J, "An experimental investigation of flow patterns and liquid entrainment in a horizontal-tube evaporator," PhD thesis, University of Illinois, 1992.

Baroczy, C.J., "A systematic correlation for two-phase pressure drop," Chemical Engineering Progress Symposium Series -- Heat Transfer, 62(64), 232-249, 1966.

Bendat, J.S. and A.G Piersol, *Random Data*, 2nd edition, John Wiley & Sons, 1986.

Bennett, D.L and J.C. Chen, "Forced convective boiling in vertical tubes for saturated pure components and binary mixtures," American Institute of Chemical Engineering Journal, 26, 454-461, 1980.

Bergles, A.E., and W.M. Rohsenow "The determination of forced convection surface boiling," Journal of Heat Transfer, 86, 365-372, 1964.

Brauner, N. and D. Moalem Maron, "Identification of the range of 'small diameter' conduits regarding two-phase flow pattern transitions," International Communications in Heat and Mass Transfer, 19(1) 29-39, 1992.

Brown, W.T., "A study of flow surface boiling," PhD thesis, MIT, Mechanical Engineering Department, 1967.

Butterworth, D., "A comparison of some void-fraction relationships for co-current gas liquid flow," International Journal of Multiphase Flow, 1, 845-850, 1975.

Butterworth, D., "A visual study of mechanisms in horizontal, air-water flow," AERE Report M2556, Harwell, England, 1972.

Carey, V.P, *Liquid-Vapor Phase Change Phenomena*, Hemisphere, New York, 1992.

Chaddock, J.B. and J.A. Noerager, "Evaporation of refrigerant 12 in a horizontal tube with constant wall heat flux," ASHRAE Transactions, 12(1), 90-103, 1966.

Chen, J.C., "A correlation for boiling heat transfer to saturated fluid in convective flow," Industrial Engineering Chemical Process Design and Development, 5(3), 322-329, 1966.

Chien, S.F, and W. Ibele, "Pressure drop and liquid film thickness of two-phase annular and annular-mist flows," Journal of Heat Transfer, 89-96, 1964.

Chisholm, D., "The influence of mass velocity on friction pressure gradients during steam-water flow," Proceedings of the Institute of Mechanical Engineers, 182(3), 336-341, 1968.

Christoffersen, B.C., "Heat transfer and flow characteristics of R-22, R-32/R-125, and R-134a in smooth and micro-fin tubes," M.S. thesis, University of Illinois at Urbana-Champaign, 1993.

Christoffersen, B., J.C. Chato, and J.P. Wattelet, "Evaporation of R-22 and its alternatives in horizontal smooth and micro-fin tubes," ACRC Technical Report, 1993.

Churchill, S.W. and R. Ugasi, "A general expression for the correlation of rates of transfer and other phenomena," A.I. Ch. E. Journal, 18(6), 1121-1128, 1972.

Colburn, A.P., Transactions of the American Institute of Chemical Engineers, 29, 174, 1933.

Cole, R. and W.M. Rohsenow, "Correlation of bubble departure diameters for boiling of saturated liquids," Chemical Engineering Progress Symposium Series, 65, 211-213, 1969.

Collier, J.G., *Convective Boiling and Condensation*, 2nd edition, McGraw-Hill, New York, 1981.

Cooper, M.G., "Saturation pool boiling--A simple correlation," International Chemical Engineering Symposium Series, 86, 785-792, 1984.

Damianides, C.A., "Horizontal two-phase flow of air-water mixtures in small diameter tubes and compact heat exchangers," PhD thesis, Department of Chemical Engineering, University of Illinois, 1987.

Damianides, C.A. and J.W. Westwater, "Two-phase flow patterns in a compact heat exchanger and in small tubes," Second UK Conference on Heat Transfer, Institute of Mechanical Engineers, 2, 1257-1268, 1988.

Davis, E.J. and G.H. Anderson, "The incipience of nucleate boiling in forced convection flow," American Institute of Chemical Engineering Journal, 12, 774-780, 1966.

Denglor, C.E. and J.N. Addoms, "Heat transfer mechanism for vaporization of water in a vertical tube," Chemical Engineering Progress Symposium Series, 52(18), 95-103, 1956.

Dittus, F.W. and L.M.K. Boelter, University of California Publications on Engineering, 2, 443, 1930.

Dobson, M.K., J. P. Wattelet, J.C. Chato, "Optimal sizing of two-phase heat exchangers," ACRC Technical Report 42, 1993.

Dukler, A.E., M. Wicks, and R.G. Cleveland, "Frictional pressure drop in two-phase flow: an approach through similarity analysis," American Institute of Chemical Engineering Journal, 10(1), 44, 1964.

Eckels, S.J., and M.B. Pate, "An experimental comparison of evaporation and condensation heat transfer coefficients for HFC-134a and CFC-12," International Journal of Refrigeration 14(2), 70-77, 1990.

Forster, H.K. and N. Zuber, "Dynamics of vapor bubbles and boiling heat transfer," American Institute of Chemical Engineering Journal, 1(4), 531-535, 1955.

Fritz, W., "Berechnung des Maximalvolumens von Dampfblasen," Physik. Zeitschr, 36, 379-384, 1955.

Frost, W. and G.S. Dzakowic, "An extension of the methods of predicting incipient boiling on commercially finished surfaces," 1967 National Heat Transfer Conference, 67-HT-61, 1967.

Galbiati, L. and P. Andreini, "The transition between stratified and annular regimes for horizontal two-phase flow in small diameter tubes," International Communications in Heat and Mass Transfer, 19(2), 185-190, 1992.

Gnielinski, V., "New equations for heat and mass transfer in turbulent pipe and channel flow," International Chemical Engineering, 16, 359-368, 1976.

Groothius, H. and W.P. Hendal, "Heat transfer in two-phase flow," Chemical Engineering Science, 11, 212, 1959.

Guerrieri, S.A. and R.D. Talty, "A study of heat transfer to organic liquids ins single-tube, natural circulation, vertical tube boilers," Chemical Engineering Progress Symposium Series, 52(18), 69-77, 1956.

Gungor, K.E., and R.H.S. Winterton, "A general correlation for flow boiling in tubes and annuli," International Journal of Heat and Mass Transfer, 29(3), 351-358, 1986.

Hino, R. and T. Ueda, "Studies on heat transfer and flow characteristics in subcooled flow boiling -- part 1: boiling characteristics," International Journal of Heat and Mass Transfer, 29(4), 637-640, 1986.

Hsu, Y.Y., "On the size of range of active nucleation cavities on a heating surface," Journal of Heat Transfer, 84, 1962.

Hubbard, M.G. and A.E. Dukler, "The characterization of flow regimes for horizontal two-phase flow: statistical analysis of wall pressure fluctuations," Proceedings of the 1966 Heat Transfer and Fluid Mechanics Institute, 100-121, 1966.

Incropera, F.P., and D.P. DeWitt, *Fundamentals of Heat and Mass Transfer*, 3rd ed., Wiley, New York, 1990.

Jabardo, J.M.S., ME 497 notes, 1991.

Jeffreys, H., "On the formation of water waves by wind," Proceedings of the Royal Society, A107, 189, 1925.

Jeffreys, H., "On the formation of water waves by wind," Proceedings of the Royal Society, A110, 241, 1926.

Jones, O.C. and N. Zuber, "The interrelation between void fraction fluctuations and flow patterns in two-phase flow," International Journal of Multiphase Flow, 2, 273-306, 1975.

Jung, D.S., M. McLinden, R. Radermacher, and D. Didion, "A study of flow boiling heat transfer with refrigerant mixtures," International Journal of Heat and Mass Transfer, 32(9), 1751-1764, 1989.

Jung, D.S. and R. Radermacher, "Transport properties and surface tension of pure and mixed refrigerants," ASHRAE Transactions, 97(1), 90-99, 1990.

Kandlikar, S.G., "A general correlation for saturated two-phase flow boiling heat transfer inside horizontal and vertical tubes," Journal of Heat Transfer, 112, 219-228, 1990.

Kedzierski, M.A., "Simultaneous visual and calorimetric measurements of R11, R123, and R123/alkylbenzene nucleate flow boiling," 29th National Heat Transfer Conference, 243, 27-33, 1993.

Kenning, D.B and M.G. Cooper, "Saturated flow boiling of water in vertical tubes," International Journal of Heat and Mass Transfer, 32(3), 445-458, 1989.

Klausner, J.F., R. Mei, D.M. Bernhard, and L.Z. Zeng, "Vapor bubble departure in forced convection boiling," International Journal of Heat and Mass Transfer, 36(3), 651-662, 1993.

Kutateladze, S.S., "Boiling heat transfer," International Journal of Heat and Mass Transfer, 4, 3-45, 1961.

Lin, P.Y. and T.J. Hanratty, "Detection of slug flow from pressure measurements," International Journal of Multiphase Flow, 15(2), 209-226, 1989.

Lin, P.Y. and T.J. Hanratty, "Prediction of the initiation of slugs with linear stability theory," International Journal of Multiphase Flow, 12(1), 79-98, 1986.

Liu, Z. and R.H.S. Winterton, "Wet wall flow boiling correlation with explicit nuclear term," 5th Miami International Symposium of Multiphase Transport and Particulate Phenomena, 1988.

Lockhart, R.W. and R.C. Martinelli, "Proposed correlation of data for isothermal two-phase , two-component flow in pipes," Chemical Engineering Progress, 45(1), 39-48, 1947.

Mandhane, J.M., G.A. Gregory, and K. Aziz, "A flow pattern map for gas-liquid flow in horizontal and inclined pipes," International Journal of Multiphase Flow 1, 537-553, 1974.

Martinelli, R.C. and B. Nelson, "Prediction of pressure drop during forced-circulation boiling of water," ASME Transactions, 70, 695-702, 1948.

Matsui, G. "Identification of flow regimes in vertical gas-liquid two-phase flow using differential pressure fluctuations," International Journal of Multiphase Flow, 10(6), 711-720, 1984.

Matsui, G., "Automatic identification of flow regimes in vertical two-phase flow using differential pressure fluctuations," Nuclear Engineering Design, 95, 221-231, 1986.

Mikic, B.B and W.M. Rohsenow, "New correlations of pool boiling data including the effect of heating surface characteristics," Journal of Heat Transfer, 91, 245-250, 1969.

Moffat, R.J, "Describing the uncertainties in experimental results," Experimental Thermal and Fluid Science 1, 3-17, 1988.

Morrison, G., M. McLinden, and J. Ely, "NIST thermodynamic properties of refrigerants and refrigerant mixtures database, (REFPROP)" National Institute of Standards and Technology, 1991.

Panek, J.S., "Evaporation heat transfer and pressure drop in ozone-safe refrigerants and refrigerant-oil mixtures," M.S. thesis, University of Illinois at Urbana-Champaign, 1992.

Pierre, B., "Coefficient of heat transfer for boiling freon-12 in horizontal tubes," Heating and Air Treatment Engineer, 19, 302-310, 1956.

Pierre, B. "Flow resistance with boiling refrigerants -- Part I," ASHRAE Journal, 6(9), 58-65, 1964.

Pierre, B. "Flow resistance with boiling refrigerants -- Part II," ASHRAE Journal 6(10), 73-77.

Petukov, B.S., *Advances in Heat Transfer*, Academic, New York, 6, 503-564, 1970.

Prandtl, L. *Guide to Flow Theory*, Vieweg and Son, Braunschweig, 359, 1944.

Rhee, B.W., "Heat transfer to boiling refrigerants R-12 and R-22 flowing inside a plain copper tube," PhD thesis, University of Michigan, 1972.

Rohsenow, W.M., "A method of correlating heat transfer data for surface boiling of liquids," ASME Transactions," 74, 969-976, 1952.

Rohsenow, W.M., Department of Mechanical Engineering Technical Report 8767-21, MIT, 1962.

Sato, T. and M. Matsumura, Bulletin of the Japanese Society of Mechanical Engineers, 7, 392, 1964.

Shah, M.M., "A new correlation for heat transfer during boiling flow through pipes," ASHRAE Transactions, 82(2), 66-86, 1976.

Shah, M.M, "Chart correlation for saturated boiling heat transfer: equations and further study," ASHRAE Transactions, 88(1), 185-196, 1982.

Shah, R.K., *Handbook of Heat Transfer*, McGraw-Hill, New York, 1981.

Steiner, D. and J. Taborek, "Flow boiling heat transfer of single components in vertical tubes," Heat Transfer Engineering 13(2), 43-69, 1992.

Shrock, V.E. and L.M. Grossman, "Forced convection boiling in tubes," Nuclear Science and Engineering, 12(4), 474-481, 1962.

Souza, A.L, J.C. Chato, and J.P. Wattelet, "Pressure drop during two-phase flow of refrigerants in horizontal smooth tubes," ACRC-TR-25, 1992.

Stephan, K. and M. Abdelsalam, "Heat transfer correlations for natural convection boiling," International Journal of Heat and Mass Transfer, 23, 73-80, 1980.

Sthapak, B.K., H.K. Varma, and C.P. Gupta, "Heat transfer coefficients in dry-out region of horizontal tube water heated R-12 evaporator," ASHRAE Transactions, 82(2), 47-55, 1976.

Taitel, Y., and A.E. Dukler, "A model for predicting flow regime transitions in horizontal and near-horizontal gas-liquid flow," American Institute of Chemical Engineering Journal, 22(1), 47-55, 1976.

Wambsganss, M.W., D.M. France, J.A Jendrzejczyk, T.N. Tran, "Boiling heat transfer of refrigerant R-113 in a small diameter, horizontal tube," Argonne National Laboratory, ANL-92/12, 1992.

Wattelet, J.P., "Design, building, and baseline testing of an apparatus used to measure evaporation characteristics of ozone-safe refrigerants," M.S. thesis, University of Illinois at Urbana-Champaign, 1990.

Wattelet, J.P, J.C. Chato, J.M.S. Jabardo, J.S. Panek, J.P. Renie, "An experimental comparison of evaporation characteristics of HFC-134a and CFC-12," XVIIIth International Congress of Refrigeration, Montreal, Canada, 1991.

Wattelet, J.P., J.M.S. Jabardo, J.C. Chato, J.S. Panek, and A.L. Souza, "Experimental evaluation of convective boiling of refrigerants HFC-134a and CFC-12," 28th National Heat Transfer Conference, San Diego, California, 1992.

Wattelet, J.P., J.C. Chato, A.L. Souza, and B.R. Christoffersen, "Evaporative characteristics of R-134a, MP-39, and R-12 at low mass fluxes," ASHRAE Transactions, 1994.

Wedekind, G.L., "An experimental investigation into the oscillatory motion of the mixture-vapor transition point in horizontal evaporating flow," Journal of Heat Transfer, 93, 47-54, 1971.

Weisman, J., D. Duncan, J. Gibson, and T. Crawford, "Effects of fluid properties and pipe diameter on two-phase flow patterns in horizontal lines," International Journal of Multiphase Flow, 5, 437-462, 1979.

Whalley, P.B., *Boiling, Condensation, and Gas-Liquid Flow*, Clarendon Press, Oxford, 1987.

Zahn, W.R., "A visual study of two-phase flow while evaporating in horizontal tubes," Journal of Heat Transfer, 86(3), 417-429, 1964.

Zivi, S.M., 1964, "Estimation of steady-state steam void fraction by means of the principle of minimum entropy generation," Journal of Heat Transfer, 86, 247-252.

APPENDIX

EVAPORATION TEST DATA

The tables of the evaporation test data listed in Appendix B are organized under the following headings with the units of these headings given in parenthesis: T, saturation temperature at the inlet of the test section (°F); q", test section heat flux (kBtu/hr-ft^2); G, mass flux (klb$_m$/ft^2-hr); xin, inlet quality to the test section; xout, outlet quality of the test section; hexp, experimental average heat transfer coefficient over the test section (Btu/hr-ft^2-°F); dP, pressure drop through the test section (psid); hpred, predicted heat transfer coefficient using Eq. 5.7 (Btu/hr-ft^2-°F); %error, the percent error of the predicted heat transfer coefficient using Eq. 5.7 compared with the experimental heat transfer coefficient; %dh, estimated experimental uncertainty of the heat transfer coefficient.

Table A.1. R-12 data for the 0.277 in diameter test section

T	q"	G	xin	xout	hexp	dP	hpred	%error	%dh
-4.7	0.6	19.0	0.20	0.91	74	0.06	87	16.41	10.99
-3.8	0.6	37.4	0.20	0.55	93	0.09	107	15.03	11.76
3.9	0.6	55.3	0.20	0.44	163	0.16	131	19.80	15.20
5.7	1.0	56.3	0.20	0.55	152	0.19	154	1.47	9.97
5.0	1.0	74.5	0.20	0.47	201	0.32	186	7.60	11.86
14.0	0.6	18.7	0.20	0.91	81	0.03	85	4.57	11.25
13.6	0.6	26.3	0.20	0.71	82	0.03	90	10.93	11.27
14.2	0.6	37.7	0.20	0.56	97	0.05	102	5.78	11.93
14.5	0.6	37.1	0.39	0.75	116	0.11	115	0.70	12.80
14.2	0.6	37.2	0.59	0.95	134	0.16	127	4.83	13.70
14.2	1.0	37.8	0.20	0.74	128	0.09	126	1.22	9.10
14.2	1.0	37.5	0.40	0.94	135	0.15	137	1.16	9.37
14.0	0.6	56.7	0.20	0.44	175	0.12	129	26.15	15.86
14.0	0.6	55.8	0.40	0.64	214	0.24	158	26.24	17.95
14.0	0.6	56.3	0.59	0.83	254	0.34	184	27.79	20.17
14.2	1.0	56.7	0.20	0.56	162	0.16	151	6.79	10.36
14.4	1.0	56.0	0.39	0.75	191	0.27	175	8.43	11.46
14.4	1.0	74.5	0.19	0.46	211	0.24	178	15.82	12.25
14.0	1.0	75.4	0.20	0.47	207	0.26	182	11.90	12.07
14.4	1.0	74.3	0.40	0.67	268	0.47	223	16.77	14.48
14.4	1.0	74.4	0.60	0.87	405	0.66	259	36.04	19.82
14.2	1.6	75.6	0.20	0.65	238	0.38	222	6.70	8.28
14.2	1.6	75.5	0.40	0.85	282	0.59	259	8.06	9.39
40.6	0.6	19.0	0.20	0.95	111	0.02	83	25.10	12.58
41.2	0.6	26.6	0.20	0.80	110	0.03	92	16.96	12.54
40.8	0.6	37.9	0.20	0.58	118	0.04	103	12.67	12.93
41.0	0.6	37.7	0.40	0.78	112	0.06	117	4.65	12.63
41.2	0.6	37.7	0.61	0.98	121	0.09	140	15.44	13.08
40.6	1.0	39.6	0.20	0.77	136	0.07	113	17.12	9.41
41.2	1.0	37.7	0.39	0.97	138	0.10	121	11.86	9.45
41.0	0.6	56.1	0.20	0.45	134	0.08	107	20.01	13.69
41.0	0.6	56.3	0.40	0.65	164	0.16	125	23.92	15.28
41.0	0.6	56.0	0.60	0.85	176	0.21	140	20.03	15.88
41.2	1.0	56.1	0.20	0.58	160	0.11	129	19.35	10.28
41.2	1.0	55.1	0.40	0.78	160	0.18	143	10.92	10.29
41.5	1.0	75.3	0.20	0.48	192	0.17	153	20.47	11.51
40.8	1.0	75.2	0.40	0.68	186	0.29	181	2.62	11.26
41.5	1.0	74.0	0.60	0.88	214	0.38	204	4.75	12.34
41.0	1.6	75.2	0.20	0.67	230	0.25	192	16.65	8.07
41.0	1.6	74.9	0.40	0.87	228	0.36	214	6.36	8.02

Table A.2. R-12 data for the 0.402 in diameter test section

T	q"	G	xin	xout	h	dP	hpred	%error	%dh
40	1.6	100	0.21	0.40	177	0.15	238	34.50	6.57
40	3.2	100	0.19	0.55	279	0.28	341	22.01	4.91
40	6.5	100	0.20	0.74	396	0.36	515	30.12	3.63
40	1.6	200	0.20	0.29	351	0.45	349	0.69	10.93
40	3.2	200	0.19	0.36	398	0.62	425	6.72	6.48
40	6.5	200	0.20	0.56	567	0.99	592	4.44	4.75
40	1.6	300	0.20	0.26	446	1.12	444	0.46	13.33
40	3.2	300	0.19	0.31	507	1.39	506	0.27	7.94
40	6.5	300	0.19	0.43	686	1.81	650	5.17	5.56
40	1.6	400	0.20	0.24	561	1.94	534	4.91	16.16
40	3.2	400	0.19	0.28	643	2.28	587	8.69	9.76
44	6.5	400	0.20	0.38	735	2.77	722	1.79	5.90

Table A.3. R-12 data for the 0.430 in diameter test section

T	q"	G	xin	xout	h	dP	hpred	%error	%dh
41.0	0.7	37.4	0.20	0.32	88	0.01	112	26.95	12.12
41.2	0.6	36.8	0.40	0.53	83	0.01	114	38.09	12.64
40.8	0.6	37.7	0.61	0.72	98	0.02	121	22.62	12.80
40.8	0.6	37.5	0.81	0.93	92	0.03	125	35.87	12.73
41.2	1.0	37.7	0.19	0.37	117	0.01	143	22.62	8.63
40.8	1.0	37.7	0.40	0.57	114	0.02	144	27.00	8.87
41.0	1.0	38.6	0.59	0.77	116	0.02	152	31.01	8.63
40.6	1.6	38.0	0.21	0.50	170	0.02	195	14.74	7.54
41.0	1.6	38.0	0.40	0.69	164	0.02	198	20.96	7.40
41.0	1.6	38.0	0.59	0.89	159	0.03	203	27.46	7.19
41.0	0.6	56.3	0.20	0.28	87	0.01	118	36.06	12.68
41.0	0.6	56.2	0.40	0.48	106	0.03	133	26.01	12.89
41.0	0.6	56.4	0.59	0.67	110	0.05	148	34.25	12.94
40.8	0.6	57.1	0.81	0.88	126	0.06	162	28.65	13.15
41.0	1.0	56.0	0.20	0.32	123	0.02	150	21.73	8.69
40.8	1.0	56.3	0.40	0.52	133	0.03	161	21.46	8.78
41.2	1.0	55.9	0.60	0.72	120	0.05	170	41.48	8.93
40.6	0.9	56.9	0.80	0.91	126	0.06	179	41.35	9.27
40.6	1.6	56.0	0.21	0.40	181	0.02	200	10.82	7.76
40.6	1.6	57.2	0.40	0.59	183	0.04	209	14.14	7.81
40.6	1.6	56.8	0.59	0.78	167	0.06	216	29.57	7.47
41.0	1.0	76.5	0.40	0.48	133	0.06	183	37.94	9.05
40.3	1.0	75.3	0.61	0.69	139	0.08	206	48.47	8.84
40.6	1.0	75.2	0.79	0.88	183	0.11	220	20.58	9.60
40.6	1.6	75.8	0.40	0.54	180	0.07	226	25.65	7.74
40.5	1.6	76.0	0.61	0.75	181	0.10	242	33.57	6.21
41.0	1.6	74.7	0.80	0.95	184	0.12	255	38.63	7.69
41.4	3.1	75.1	0.20	0.49	301	0.06	316	4.85	5.86
40.6	3.2	75.1	0.40	0.69	290	0.10	327	12.77	5.69
41.7	3.2	75.8	0.61	0.91	302	0.13	340	12.50	5.79
40.8	1.6	150.8	0.20	0.28	222	0.11	282	26.84	8.53
40.8	1.6	150.0	0.40	0.47	353	0.22	349	1.11	11.81
41.2	1.6	150.4	0.60	0.67	401	0.39	413	2.84	12.99
40.8	1.6	149.5	0.80	0.87	480	0.51	456	4.89	14.91
40.6	3.2	151.4	0.20	0.35	336	0.15	369	9.72	6.25
40.8	3.2	150.5	0.40	0.55	386	0.27	421	9.14	6.88
41.0	3.2	150.5	0.60	0.75	436	0.44	471	8.19	7.51
40.8	3.1	149.1	0.80	0.94	502	0.51	502	0.11	8.45
41.0	6.4	150.2	0.20	0.50	546	0.24	535	1.99	5.04
41.2	6.3	150.5	0.40	0.70	587	0.42	566	3.60	5.36
40.6	6.3	150.5	0.60	0.88	598	0.56	598	0.02	5.43
40.8	9.6	149.5	0.20	0.65	743	0.36	682	8.10	4.64
41.4	9.5	149.9	0.40	0.84	757	0.54	702	7.19	4.75

Table A.3. R-12 data for the 0.430 in diameter test section

T	q"	G	xin	xout	h	dP	hpred	%error	%dh
41.4	0.8	226.1	0.20	0.23	376	0.21	325	13.50	14.88
41.0	0.8	224.8	0.30	0.33	376	0.34	391	3.96	14.88
40.8	0.8	225.8	0.40	0.43	416	0.52	453	8.90	15.70
40.8	0.8	225.8	0.50	0.53	493	0.72	508	2.98	17.33
40.8	0.8	226.2	0.60	0.63	521	0.90	557	6.89	17.94
40.3	1.6	225.7	0.10	0.15	290	0.11	289	0.37	10.28
41.2	1.6	227.0	0.20	0.25	374	0.22	356	4.89	8.04
41.4	1.6	224.0	0.30	0.35	386	0.37	415	7.44	12.62
41.0	1.6	225.4	0.40	0.45	441	0.54	473	7.33	13.96
41.2	1.6	226.1	0.50	0.55	504	0.73	526	4.56	15.48
41.4	1.6	226.0	0.60	0.65	558	0.91	574	2.70	16.52
40.8	1.6	225.4	0.70	0.75	601	1.03	613	2.01	17.81
41.0	1.6	225.5	0.80	0.85	657	1.08	645	1.78	19.13
40.8	1.6	224.9	0.90	0.95	720	1.02	657	8.70	12.19
40.8	3.2	223.4	0.10	0.20	372	0.18	376	1.13	6.69
40.6	3.2	224.3	0.20	0.30	370	0.28	426	15.18	6.67
41.2	3.2	225.5	0.30	0.40	407	0.44	478	17.49	7.14
41.2	3.2	227.3	0.40	0.50	458	0.63	529	15.36	7.81
40.8	3.2	225.1	0.50	0.60	523	0.82	572	9.44	8.57
41.2	3.1	225.6	0.60	0.70	579	0.96	613	5.91	9.47
40.8	3.1	225.5	0.70	0.80	617	1.08	649	5.21	9.98
41.0	3.2	226.1	0.80	0.90	663	1.10	678	2.40	10.48
41.0	6.3	224.4	0.10	0.30	539	0.29	541	0.41	5.03
41.0	6.4	226.2	0.20	0.40	529	0.45	579	9.32	4.94
41.2	6.3	225.2	0.40	0.60	550	0.77	647	17.60	5.11
41.0	6.3	224.9	0.60	0.80	603	1.07	714	18.37	5.44
41.0	9.5	225.6	0.10	0.40	687	0.42	689	0.21	4.45
41.0	9.5	222.5	0.20	0.50	701	0.60	714	1.77	4.50
41.2	9.6	224.0	0.40	0.70	718	0.94	772	7.50	4.54
40.8	9.4	225.5	0.60	0.90	753	1.20	821	9.06	4.74
41.2	1.6	301.9	0.20	0.24	398	0.44	428	7.33	12.69
40.5	1.6	302.5	0.40	0.44	551	1.01	584	5.95	16.64
41.0	1.6	299.8	0.60	0.64	648	1.48	707	9.16	18.93
41.0	3.1	301.7	0.20	0.28	425	0.51	487	14.66	7.44
40.5	3.2	300.9	0.40	0.48	551	1.06	626	13.48	9.02
41.2	3.2	299.1	0.60	0.67	681	1.53	738	8.41	10.63
41.0	6.3	298.7	0.20	0.36	587	0.67	619	5.42	5.36
41.0	6.3	302.0	0.41	0.56	638	1.25	734	14.96	5.67
40.3	9.6	299.6	0.20	0.43	768	0.89	755	1.66	4.74
41.0	9.5	300.1	0.40	0.62	748	1.40	837	11.85	4.69
40.1	1.6	376.9	0.21	0.24	486	0.77	504	3.82	9.32
40.6	1.6	374.6	0.40	0.43	619	1.39	683	10.31	17.94
41.2	3.2	376.1	0.21	0.27	488	0.79	556	14.00	8.19

Table A.3. R-12 data for the 0.430 in diameter test section

T	q"	G	xin	xout	h	dP	hpred	%error	%dh
40.6	3.2	373.4	0.39	0.45	669	1.46	710	6.23	10.47
40.3	6.3	376.1	0.20	0.32	580	0.95	666	14.81	5.32
41.4	6.4	373.1	0.39	0.51	674	1.58	802	18.92	5.88
40.8	9.5	376.3	0.21	0.38	749	1.16	792	5.75	4.71
58.8	1.0	75.5	0.40	0.49	155	0.04	187	20.80	9.27
59.0	1.6	75.2	0.40	0.55	214	0.05	241	12.92	8.34
59.0	1.6	150.1	0.20	0.28	256	0.09	286	11.47	9.30
59.0	1.6	151.1	0.40	0.47	265	0.16	344	29.73	9.51
59.2	1.6	151.4	0.60	0.67	391	0.27	398	1.92	12.50
58.6	1.6	225.5	0.21	0.26	354	0.17	352	0.54	11.83
58.8	1.6	225.8	0.40	0.45	386	0.36	449	16.25	12.39
59.0	1.6	224.0	0.61	0.66	491	0.64	534	8.78	14.92
58.6	1.6	224.4	0.80	0.85	577	0.81	593	2.78	17.25
59.0	3.2	224.9	0.20	0.30	457	0.20	436	4.63	7.72
59.0	3.1	225.0	0.39	0.49	423	0.40	508	20.12	7.41
58.6	3.2	225.0	0.60	0.70	508	0.67	586	15.25	8.39
58.8	3.2	224.4	0.80	0.90	595	0.83	636	6.99	9.59
59.0	6.4	225.5	0.20	0.40	677	0.30	610	10.02	5.90
59.2	6.3	225.0	0.40	0.60	672	0.53	661	1.53	5.89
58.8	6.3	225.0	0.59	0.79	661	0.78	710	7.48	5.82
58.8	9.5	225.8	0.19	0.49	854	0.42	766	10.24	5.14
58.8	9.5	226.2	0.39	0.69	863	0.68	804	6.77	5.20
58.8	9.5	224.6	0.60	0.90	861	0.91	846	1.81	5.17

Table A.4. R-134a data for the 0.277 in diameter test section

T	q"	G	xin	xout	h	dP	hpred	%error	%dh
5.4	0.6	18.7	0.20	0.74	112	0.04	96	13.90	12.63
4.6	0.6	26.5	0.20	0.57	92	0.05	105	13.76	11.71
4.6	0.6	37.6	0.20	0.47	113	0.08	122	7.65	12.68
4.8	0.6	36.5	0.40	0.68	159	0.17	142	10.76	14.99
4.5	0.6	37.4	0.60	0.88	171	0.24	164	3.77	15.62
4.6	1.0	37.1	0.21	0.62	162	0.14	147	9.19	10.35
5.2	1.0	37.6	0.40	0.81	163	0.21	166	1.87	10.39
4.8	0.6	55.9	0.20	0.38	242	0.18	158	34.74	19.50
5.0	0.6	56.6	0.40	0.58	279	0.37	206	26.15	21.49
5.2	0.6	56.2	0.61	0.78	369	0.55	244	33.92	26.24
5.0	1.0	56.3	0.20	0.47	207	0.23	182	11.86	12.07
5.5	1.0	56.2	0.40	0.67	274	0.42	223	18.71	14.73
5.0	1.0	76.2	0.21	0.41	281	0.41	232	17.63	15.01
5.0	1.0	75.4	0.39	0.60	340	0.77	290	14.59	17.31
5.9	1.0	74.6	0.60	0.80	412	1.06	342	16.97	20.12
5.4	1.6	74.2	0.20	0.54	292	0.54	265	9.27	9.66
5.2	1.6	75.2	0.40	0.74	372	0.92	325	12.58	11.71
40.8	0.6	18.7	0.20	0.80	129	0.02	94	27.51	13.47
40.8	0.6	26.1	0.20	0.62	142	0.03	99	30.18	14.11
41.0	0.7	37.5	0.20	0.50	137	0.05	114	16.91	13.23
41.0	0.6	37.2	0.40	0.69	140	0.08	126	9.91	14.00
41.0	0.6	37.5	0.60	0.90	147	0.12	141	4.69	14.39
40.8	1.0	37.5	0.21	0.64	176	0.07	137	21.86	10.87
40.8	1.0	37.4	0.40	0.85	169	0.10	151	10.66	10.28
40.8	1.4	38.2	0.20	0.82	221	0.11	168	23.85	9.03
41.0	0.6	56.3	0.20	0.40	176	0.09	141	20.05	15.91
40.8	0.6	56.6	0.40	0.59	183	0.19	174	5.22	16.29
41.0	0.6	56.3	0.60	0.79	194	0.26	201	3.63	16.85
40.8	1.0	56.1	0.20	0.50	207	0.12	163	20.95	12.07
40.8	1.0	56.3	0.40	0.70	212	0.22	192	9.13	12.26
41.0	1.0	74.9	0.20	0.42	233	0.20	197	15.55	13.10
41.4	1.0	75.2	0.20	0.42	226	0.19	197	12.55	12.81
41.2	1.0	76.1	0.34	0.61	252	0.36	241	4.33	13.43
41.0	1.0	75.0	0.40	0.62	266	0.36	244	8.14	14.40
41.4	1.0	75.0	0.60	0.82	318	0.49	283	10.95	16.48
41.0	1.6	75.5	0.20	0.56	279	0.27	238	14.60	9.32
41.0	1.6	75.2	0.20	0.56	278	0.28	239	14.18	9.14
41.4	1.6	75.4	0.40	0.76	296	0.43	278	6.05	9.76
41.0	2.7	75.0	0.20	0.82	402	0.44	304	24.27	7.66
41.0	1.3	112.1	0.10	0.30	281	0.26	251	10.83	11.26
40.8	1.3	112.1	0.20	0.40	295	0.46	298	0.88	11.44
41.2	1.3	112.1	0.30	0.50	315	0.66	340	7.91	12.30

Table A.4. R-134a data for the 0.277 in diameter test section

T	q"	G	xin	xout	h	dP	hpred	%error	%dh
41.0	1.3	112.3	0.40	0.60	382	0.92	380	0.45	14.33
41.2	1.3	112.7	0.40	0.60	336	0.94	381	13.54	12.94
41.5	1.3	113.8	0.49	0.69	420	1.11	418	0.26	15.47
40.6	1.3	112.1	0.50	0.70	354	1.13	415	17.24	13.49
40.6	1.3	112.4	0.60	0.80	465	1.24	447	3.73	16.81
41.0	1.3	112.1	0.60	0.80	375	1.28	446	18.90	14.14
41.2	4.0	112.7	0.20	0.80	517	1.01	445	13.89	6.67
40.8	1.7	150.3	0.10	0.30	332	0.54	326	1.99	9.80
41.4	1.7	149.9	0.15	0.35	352	0.72	357	1.35	10.27
41.2	1.7	150.2	0.20	0.40	364	0.93	388	6.75	10.54
41.5	1.7	149.3	0.25	0.45	390	1.12	416	6.75	11.15
40.6	1.7	150.1	0.30	0.50	403	1.37	446	10.50	11.47
41.5	1.7	150.1	0.35	0.56	417	1.59	475	13.99	11.79
41.0	1.7	149.5	0.40	0.60	440	1.79	497	12.91	12.34
40.5	3.5	149.3	0.39	0.80	527	2.12	568	7.68	7.64
41.0	5.2	150.1	0.20	0.80	601	1.92	567	5.64	5.91

Table A.5. R-134a data for the 0.305 in diameter test section

T	q"	G	xin	xout	h	dP	hpred	%error	%dh
22.1	1.0	228.2	0.20	0.23	594	1.13	469	21.09	18.46
21.9	1.8	226.8	0.20	0.25	581	1.15	491	15.53	16.52
22.6	3.3	226.7	0.20	0.28	589	1.22	540	8.39	9.67
23.0	6.3	225.9	0.20	0.36	625	1.42	657	5.10	5.92
23.5	9.4	227.6	0.20	0.45	771	1.70	780	1.13	5.10
40.8	0.6	37.8	0.20	0.32	147	0.02	113	22.86	19.44
40.8	0.6	36.8	0.40	0.52	133	0.03	125	6.49	19.30
41.4	0.6	37.5	0.60	0.72	175	0.05	138	21.09	19.77
41.4	0.6	38.4	0.80	0.92	177	0.07	151	14.88	19.79
41.0	1.0	37.5	0.20	0.38	173	0.02	144	16.75	12.94
40.6	1.0	38.0	0.40	0.58	167	0.04	152	9.38	13.30
40.8	1.0	37.9	0.60	0.78	186	0.06	162	13.12	13.46
41.4	1.0	37.7	0.81	0.99	170	0.07	169	0.68	13.32
41.0	1.6	38.1	0.20	0.50	234	0.03	193	17.66	10.63
41.0	1.6	38.4	0.40	0.70	241	0.05	202	15.85	10.56
40.8	1.6	37.1	0.61	0.91	233	0.07	205	11.75	10.60
41.4	1.0	76.1	0.40	0.49	274	0.13	233	15.10	13.94
40.8	1.0	74.6	0.61	0.70	346	0.19	269	22.37	14.82
41.2	1.0	76.1	0.79	0.88	418	0.24	300	28.36	16.30
41.0	1.6	75.2	0.20	0.35	297	0.08	227	23.74	11.91
41.0	1.6	75.7	0.40	0.55	290	0.15	264	9.18	11.77
41.0	1.6	75.2	0.59	0.74	347	0.21	294	15.15	12.98
40.8	1.6	76.7	0.77	0.92	383	0.25	323	15.54	13.53
40.8	3.2	73.8	0.20	0.50	409	0.13	323	20.91	7.80
41.2	3.2	75.2	0.41	0.71	421	0.20	350	17.00	7.94
40.8	3.2	75.1	0.60	0.90	397	0.25	372	6.31	7.59
41.0	1.6	148.7	0.21	0.29	410	0.25	353	13.78	14.39
41.2	1.6	150.7	0.40	0.48	444	0.58	464	4.47	14.89
41.0	1.6	150.1	0.61	0.69	549	0.87	559	1.89	17.54
40.8	1.6	148.7	0.80	0.88	684	0.95	618	9.66	20.24
41.0	3.2	149.0	0.20	0.35	504	0.33	420	16.63	8.95
41.2	3.2	150.2	0.41	0.56	531	0.66	521	1.88	9.20
41.4	3.1	150.9	0.60	0.75	598	0.93	599	0.21	10.20
41.2	3.2	150.6	0.80	0.95	683	0.95	656	3.98	11.09
41.2	6.3	151.1	0.20	0.50	710	0.55	570	19.72	6.43
41.0	6.3	149.6	0.41	0.71	721	0.87	640	11.16	6.49
41.4	6.4	149.9	0.60	0.90	697	1.03	700	0.35	6.32
40.8	9.5	150.2	0.20	0.65	915	0.79	706	22.81	5.63
41.2	9.6	150.4	0.40	0.85	908	1.06	762	16.07	5.57
41.4	12.7	151.0	0.20	0.80	1076	0.98	833	22.55	5.12
41.0	1.0	224.6	0.20	0.23	453	0.51	426	5.92	16.30
40.8	1.6	225.9	0.20	0.25	468	0.56	448	4.24	15.71

Table A.5. R-134a data for the 0.305 in diameter test section

T	q"	G	xin	xout	h	dP	hpred	%error	%dh
40.8	1.6	226.4	0.20	0.25	438	0.56	449	2.47	15.03
41.4	1.6	224.3	0.41	0.45	619	1.30	615	0.56	18.79
41.2	1.6	225.6	0.60	0.65	817	1.83	749	8.33	23.50
41.2	1.6	224.2	0.80	0.85	911	1.88	844	7.34	25.48
41.0	3.2	224.9	0.20	0.30	482	0.67	508	5.35	8.60
41.4	3.2	224.0	0.40	0.50	630	0.76	655	3.96	10.42
41.4	3.2	224.6	0.60	0.70	831	1.88	780	6.11	13.04
41.2	3.2	224.5	0.80	0.90	1013	1.91	869	14.20	15.30
41.2	6.3	224.8	0.20	0.40	673	0.93	635	5.72	6.22
41.2	6.4	223.7	0.40	0.60	829	1.48	754	9.04	7.16
41.2	6.4	224.2	0.60	0.80	946	2.01	860	9.06	7.92
40.6	9.5	224.7	0.20	0.50	914	1.28	763	16.48	5.62
41.4	9.5	224.6	0.40	0.70	898	1.66	862	3.98	5.55
41.4	9.5	226.0	0.60	0.90	958	2.08	952	0.54	5.80
41.0	12.7	225.7	0.20	0.60	1067	1.59	883	17.28	5.11
41.0	12.7	224.2	0.41	0.80	1101	1.94	969	11.94	5.19
41.2	3.2	376.4	0.21	0.27	713	1.75	700	1.78	11.45
40.8	3.2	373.4	0.41	0.47	931	3.13	938	0.78	14.29
41.4	3.2	375.1	0.60	0.66	1067	3.59	1132	6.03	15.84
40.5	6.3	374.5	0.21	0.33	900	2.08	797	11.42	7.65
41.4	6.4	374.6	0.40	0.52	991	3.40	1006	1.49	8.15
40.3	6.2	373.9	0.60	0.72	1137	3.68	1186	4.32	9.37
41.0	9.3	375.1	0.21	0.38	1054	2.41	894	15.22	6.34
41.4	9.5	375.5	0.40	0.57	1009	3.59	1085	7.51	6.02
41.7	9.3	376.2	0.59	0.76	1244	3.73	1244	0.01	7.18
40.3	12.8	375.8	0.21	0.46	1191	2.89	1018	14.55	5.46
49.5	3.2	527.6	0.19	0.23	806	2.40	848	5.15	12.73
50.0	3.2	752.6	0.11	0.13	779	2.56	858	10.17	12.28
67.8	3.2	225.5	0.20	0.29	585	0.37	517	11.64	9.86
68.5	3.2	226.0	0.40	0.49	630	0.76	672	6.79	10.51
68.0	3.2	224.2	0.60	0.69	693	1.15	799	15.36	11.20
68.0	3.2	226.1	0.80	0.89	702	1.28	898	27.92	11.32
67.8	4.8	223.5	0.20	0.33	694	0.44	574	17.29	7.98
67.8	4.7	226.1	0.40	0.53	733	0.85	717	2.15	8.36
68.0	4.7	225.9	0.60	0.73	805	1.23	838	4.07	8.99

Table A.6. R-134a data for the 0.402 mm diameter test section

T	q"	G	xin	xout	h	dP	hpred	%error	%dh
40	1.6	100	0.20	0.34	212	0.16	269	26.97	7.41
40	3.2	100	0.20	0.48	308	0.25	379	23.09	5.28
40	6.5	100	0.20	0.76	447	0.45	569	27.29	3.96
40	1.6	200	0.20	0.27	489	0.54	412	15.74	14.40
40	3.2	200	0.20	0.34	507	0.71	494	2.58	7.94
40	6.5	200	0.20	0.48	707	1.1	659	6.81	5.71
40	1.6	300	0.20	0.25	622	1.28	535	13.91	17.60
40	3.2	300	0.20	0.29	694	1.57	598	13.92	10.44
40	6.5	300	0.20	0.39	800	2.03	744	7.04	6.34
40	1.6	400	0.19	0.23	720	1.96	640	11.10	19.91

Table A.7. R-134a data for the 0.430 in diameter test section

T	q"	G	xin	xout	h	dP	hpred	%error	%dh
41.2	0.6	37.6	0.20	0.29	125	0.01	120	3.84	13.14
41.2	0.6	37.4	0.40	0.49	120	0.02	128	6.51	13.08
41.2	0.6	37.8	0.60	0.69	128	0.03	138	7.35	13.18
41.4	0.6	37.4	0.80	0.89	140	0.03	144	2.70	13.36
41.0	1.0	37.5	0.20	0.34	157	0.01	153	2.48	9.30
40.8	1.0	37.7	0.40	0.54	154	0.02	159	3.72	9.26
40.8	1.0	37.9	0.60	0.74	151	0.03	166	9.99	9.23
41.0	1.0	37.5	0.80	0.94	162	0.04	171	5.90	9.35
41.0	1.6	37.4	0.20	0.44	216	0.02	209	3.26	6.48
40.8	1.6	37.8	0.40	0.64	209	0.03	214	2.42	6.42
40.6	1.6	37.5	0.60	0.84	203	0.04	218	7.46	6.37
40.8	1.0	75.2	0.20	0.27	190	0.03	184	3.25	9.40
41.2	1.0	75.6	0.40	0.47	194	0.07	216	10.97	9.74
40.8	1.0	75.3	0.60	0.67	213	0.11	246	15.47	9.99
41.0	1.0	75.0	0.80	0.87	283	0.13	269	5.02	11.02
41.0	1.6	75.9	0.20	0.32	248	0.04	236	5.09	9.12
41.0	1.6	74.8	0.40	0.52	247	0.07	255	3.07	6.75
40.3	1.6	75.7	0.41	0.53	235	0.08	262	11.22	8.82
40.8	1.6	74.9	0.59	0.71	241	0.11	282	17.23	8.94
41.0	1.6	74.8	0.60	0.72	252	0.12	279	10.73	6.80
41.4	1.6	74.9	0.80	0.92	267	0.14	298	11.68	6.94
40.3	1.6	74.5	0.81	0.93	240	0.14	301	25.50	8.93
41.0	3.2	74.9	0.20	0.44	375	0.07	347	7.31	6.73
41.0	3.1	75.8	0.40	0.64	369	0.11	360	2.65	6.78
40.6	3.1	74.8	0.60	0.84	383	0.15	374	2.53	6.96
40.8	4.7	75.2	0.20	0.56	471	0.10	444	5.63	5.76
41.4	4.7	74.9	0.40	0.76	485	0.14	455	6.19	5.89
41.0	1.6	150.1	0.20	0.26	301	0.12	332	10.52	10.53
41.0	1.6	150.1	0.20	0.26	361	0.13	332	7.92	12.00
41.2	1.6	150.2	0.40	0.46	480	0.31	431	10.21	14.90
40.8	1.6	150.0	0.40	0.46	468	0.29	430	8.03	14.62
41.2	1.6	148.7	0.60	0.66	539	0.49	510	5.30	16.05
41.0	1.6	151.3	0.80	0.86	639	0.62	582	8.96	18.71
41.0	3.2	150.7	0.20	0.32	437	0.17	421	3.59	7.53
41.0	3.2	149.4	0.20	0.32	482	0.17	421	12.66	8.04
41.0	3.2	150.1	0.40	0.52	505	0.34	497	1.58	8.42
41.0	3.2	150.5	0.41	0.53	490	0.37	502	2.46	8.22
41.5	3.1	150.5	0.60	0.72	588	0.56	568	3.36	9.59
41.0	3.2	150.9	0.60	0.72	588	0.55	571	2.95	9.51
41.0	3.2	149.9	0.60	0.72	603	0.54	568	5.74	9.62
41.5	3.2	149.9	0.80	0.92	662	0.61	619	6.58	10.48
40.8	3.2	150.1	0.80	0.92	665	0.62	619	6.84	10.51

Table A.7. R-134a data for the 0.430 in diameter test section

T	q"	G	xin	xout	h	dP	hpred	%error	%dh
41.2	6.3	149.3	0.20	0.44	693	0.28	590	14.82	6.03
41.2	6.3	150.8	0.20	0.44	734	0.27	592	19.45	6.31
41.0	6.3	149.9	0.40	0.64	772	0.47	643	16.71	6.56
41.0	6.4	150.1	0.60	0.84	815	0.66	695	14.73	6.81
41.0	9.5	150.3	0.20	0.56	914	0.40	746	18.37	5.41
41.2	9.5	151.0	0.20	0.56	946	0.38	746	21.19	5.57
41.0	9.5	150.2	0.40	0.76	1057	0.60	786	25.67	6.04
40.8	9.5	150.6	0.60	0.96	1012	0.75	825	18.45	5.83
40.8	1.6	226.9	0.05	0.09	395	0.11	294	25.53	12.62
41.0	1.6	225.5	0.10	0.14	414	0.15	339	18.09	13.07
41.0	1.6	227.6	0.15	0.19	460	0.22	386	16.20	14.18
41.0	1.6	225.8	0.20	0.24	461	0.31	426	7.60	14.20
41.4	1.6	225.2	0.20	0.24	475	0.31	425	10.45	14.53
41.5	1.6	225.2	0.25	0.29	469	0.38	466	0.81	14.40
40.8	1.6	224.6	0.30	0.34	518	0.50	503	2.84	15.56
41.2	1.6	224.1	0.36	0.40	563	0.62	546	2.97	16.63
41.5	1.6	223.4	0.40	0.44	564	0.68	573	1.54	16.66
41.0	1.6	225.4	0.40	0.44	630	0.70	576	8.53	18.50
40.8	1.6	226.4	0.45	0.49	626	0.85	612	2.15	18.09
41.0	1.6	223.1	0.52	0.56	662	0.93	649	1.86	19.24
41.0	1.6	223.6	0.55	0.59	690	0.98	668	3.15	19.91
41.2	1.6	223.7	0.60	0.64	734	1.07	698	4.89	20.55
40.6	1.6	222.0	0.66	0.70	777	1.14	725	6.70	21.53
40.8	1.6	223.8	0.71	0.75	787	1.16	754	4.24	21.75
41.5	1.6	224.6	0.75	0.79	806	1.17	773	4.14	22.18
40.1	1.6	223.4	0.80	0.84	817	1.18	789	3.50	22.41
41.5	1.6	221.3	0.86	0.90	869	1.17	798	8.16	23.93
41.4	1.6	221.9	0.90	0.94	881	1.13	803	8.76	24.18
41.0	1.6	222.3	0.95	0.99	969	1.06	788	18.70	26.07
40.6	2.4	227.0	0.05	0.11	426	0.13	344	19.28	9.48
40.8	2.3	223.8	0.10	0.16	490	0.18	379	22.75	10.71
41.0	2.4	228.3	0.15	0.21	528	0.26	424	19.58	11.09
41.0	3.2	227.4	0.05	0.13	505	0.15	396	21.69	8.35
41.0	3.1	222.9	0.10	0.18	543	0.20	423	22.09	8.99
40.6	3.2	227.0	0.15	0.23	564	0.28	462	18.11	9.19
41.0	3.1	221.7	0.20	0.28	570	0.37	489	14.08	9.35
41.0	3.2	226.8	0.30	0.38	617	0.56	564	8.56	9.89
40.8	3.2	226.1	0.40	0.48	644	0.78	627	2.56	10.24
40.8	3.2	226.0	0.40	0.48	692	0.77	627	9.33	10.87
40.3	3.2	224.9	0.60	0.68	742	1.12	739	0.32	11.42
40.6	3.2	221.9	0.70	0.78	789	1.18	779	1.28	12.03
41.0	3.2	223.1	0.80	0.88	833	1.21	818	1.76	12.59

Table A.7. R-134a data for the 0.430 in diameter test section

T	q"	G	xin	xout	hexp	dP	hpred	%error	%dh
40.5	3.2	224.7	0.90	0.98	935	1.16	832	10.97	14.01
40.6	3.9	227.4	0.05	0.15	566	0.17	440	22.16	7.65
40.8	4.0	223.4	0.10	0.20	593	0.23	469	20.91	7.89
41.0	4.0	226.1	0.15	0.25	612	0.30	504	17.62	7.98
40.8	4.8	227.6	0.05	0.17	629	0.20	489	22.28	7.08
41.0	4.8	226.8	0.10	0.22	647	0.26	515	20.51	7.24
41.2	4.8	225.5	0.15	0.27	658	0.34	542	17.72	7.34
40.6	5.5	226.7	0.05	0.19	684	0.22	533	22.05	6.65
41.0	5.5	227.0	0.10	0.24	703	0.29	556	20.97	6.83
41.5	5.6	224.3	0.15	0.29	713	0.35	582	18.37	6.84
41.2	6.4	226.0	0.05	0.21	745	0.27	577	22.47	6.35
41.2	6.4	225.5	0.10	0.26	750	0.30	599	20.11	6.38
41.2	6.4	223.3	0.15	0.31	763	0.41	623	18.28	6.42
40.8	6.5	222.4	0.20	0.36	799	0.50	648	18.98	6.63
40.1	6.3	227.1	0.40	0.56	767	0.93	747	2.57	6.52
40.6	6.4	222.1	0.42	0.58	843	0.92	750	10.98	7.00
41.4	6.4	221.6	0.59	0.75	848	1.21	828	2.39	6.98
41.0	6.3	221.8	0.80	0.96	892	1.19	891	0.11	7.42
41.4	7.9	224.9	0.05	0.25	841	0.30	656	21.95	5.87
40.5	7.9	223.7	0.10	0.30	826	0.40	676	18.13	5.78
41.7	7.9	225.3	0.15	0.35	866	0.48	697	19.45	5.99
40.8	9.6	223.1	0.05	0.29	929	0.36	738	20.51	5.45
41.2	9.5	221.9	0.10	0.34	911	0.41	753	17.34	5.38
40.5	9.5	223.4	0.15	0.39	935	0.56	769	17.81	5.52
41.0	9.4	223.5	0.21	0.45	972	0.65	787	18.98	5.73
40.1	9.4	227.2	0.40	0.64	928	1.07	869	6.40	5.52
40.6	9.4	221.6	0.59	0.83	931	1.33	930	0.05	5.54
40.8	1.6	302.2	0.20	0.23	443	0.51	515	16.26	14.01
41.4	3.1	301.8	0.20	0.26	578	0.59	572	1.12	9.46
41.0	3.2	299.1	0.20	0.26	480	0.58	570	18.60	8.10
40.8	3.2	301.6	0.39	0.45	733	1.12	745	1.70	11.30
41.0	6.3	299.3	0.20	0.32	706	0.72	702	0.58	6.14
40.6	1.6	377.2	0.20	0.22	598	0.83	599	0.20	17.75
40.8	3.2	374.7	0.20	0.24	639	0.89	644	0.86	10.17

Table A.8. R-22 data for the 0.305 in diameter test section

T	q"	G	xin	xout	h	dP	hpred	%error	%dh
41.2	0.6	37.4	0.21	0.27	146	0.01	143	2.37	19.43
41.0	0.6	39.0	0.40	0.46	143	0.02	152	5.72	19.40
41.4	0.6	37.2	0.61	0.67	155	0.02	158	1.90	19.53
41.2	0.6	37.5	0.79	0.85	200	0.04	164	17.72	20.08
41.0	1.0	37.9	0.20	0.29	194	0.02	187	3.51	13.12
40.6	1.0	37.4	0.40	0.49	180	0.02	189	4.79	13.41
41.0	1.0	37.1	0.61	0.70	173	0.02	194	12.40	13.35
41.5	1.0	37.7	0.80	0.88	191	0.04	199	4.52	13.50
41.0	1.6	37.4	0.20	0.35	244	0.02	255	4.48	10.82
41.0	1.6	36.6	0.40	0.55	241	0.02	258	7.13	10.76
41.5	1.6	37.4	0.60	0.75	262	0.04	262	0.15	11.17
41.2	1.0	76.2	0.39	0.44	245	0.08	240	1.77	14.05
41.4	1.0	76.1	0.60	0.64	306	0.12	272	11.32	14.77
40.8	1.0	73.9	0.79	0.84	302	0.12	288	4.59	14.71
40.8	1.5	75.6	0.20	0.27	280	0.05	267	4.77	9.33
41.2	1.6	75.7	0.40	0.47	293	0.09	298	1.46	11.62
41.0	1.6	75.8	0.60	0.67	320	0.12	316	1.25	9.47
40.8	3.2	74.6	0.20	0.35	419	0.08	413	1.46	7.92
41.5	3.2	74.6	0.39	0.54	410	0.11	425	3.66	7.81
41.0	3.2	74.3	0.59	0.74	387	0.12	438	13.10	7.54
41.0	1.6	151.6	0.20	0.24	367	0.17	357	2.51	13.42
41.2	1.6	150.5	0.40	0.44	396	0.34	447	12.86	13.83
41.4	1.6	149.7	0.61	0.65	474	0.51	526	10.89	15.85
40.8	1.6	151.2	0.80	0.84	567	0.55	586	3.42	17.64
41.2	3.1	149.3	0.20	0.28	481	0.21	466	3.11	8.73
41.5	3.2	151.0	0.40	0.47	466	0.40	533	14.52	8.48
40.8	3.2	150.6	0.60	0.67	512	0.56	596	16.47	9.04
40.8	3.2	148.7	0.80	0.87	621	0.41	640	3.02	10.40
40.6	6.3	150.2	0.20	0.35	665	0.36	681	2.33	6.14
41.0	6.4	150.0	0.40	0.55	654	0.53	723	10.58	6.05
41.2	6.4	150.0	0.60	0.75	629	0.53	765	21.57	5.90
41.4	9.5	150.5	0.20	0.42	829	0.49	869	4.84	5.29
40.6	9.5	151.6	0.40	0.62	806	0.58	902	11.93	5.18
41.2	12.7	150.7	0.20	0.49	924	0.56	1046	13.17	4.66
41.0	1.6	224.7	0.21	0.24	397	0.36	445	12.28	14.09
41.0	1.6	224.9	0.39	0.42	555	0.79	572	2.97	17.38
40.8	1.6	223.7	0.60	0.63	678	1.18	692	2.04	20.10
41.0	1.6	225.4	0.80	0.83	844	1.29	783	7.30	23.68
40.8	3.2	224.7	0.20	0.25	479	0.45	529	10.62	8.56
41.0	3.2	223.7	0.40	0.45	556	0.90	640	15.05	9.59
40.8	3.2	227.3	0.60	0.64	655	1.27	748	14.10	10.83
41.0	3.2	224.3	0.80	0.85	763	1.22	821	7.57	12.19

Table A.8. R-22 data for the 0.305 in diameter test section

T	q"	G	xin	xout	h	dP	hpred	%error	%dh
41.2	6.3	225.2	0.20	0.30	636	0.66	718	12.88	5.99
41.0	6.3	225.2	0.40	0.50	605	1.12	800	32.18	5.77
40.8	6.4	223.6	0.61	0.71	765	1.28	881	15.23	6.72
41.0	9.6	224.4	0.20	0.34	820	0.88	902	10.00	5.22
41.0	9.5	223.7	0.39	0.54	771	1.22	958	24.33	5.03
41.0	9.6	226.6	0.60	0.74	802	1.28	1028	28.10	5.13
40.8	12.7	226.1	0.19	0.39	905	1.08	1069	18.15	4.60
40.8	3.2	376.7	0.20	0.23	626	1.19	671	7.15	10.46
41.4	3.2	377.2	0.40	0.43	756	2.20	880	16.48	11.99
40.8	3.2	377.0	0.61	0.64	922	2.99	1062	15.18	14.18
41.2	6.3	374.0	0.21	0.27	722	1.32	829	14.90	6.50
40.8	6.3	378.2	0.40	0.46	824	2.50	991	20.36	7.18
41.2	6.3	377.9	0.60	0.65	959	3.21	1141	18.89	8.04
41.2	9.5	375.5	0.20	0.29	826	1.55	979	18.59	5.28
40.6	9.5	373.6	0.40	0.49	839	2.63	1115	32.99	5.31
41.2	9.5	372.8	0.60	0.69	994	3.27	1243	25.05	5.96
41.2	12.7	374.0	0.20	0.32	930	1.84	1137	22.32	4.67
58.8	1.6	225.4	0.20	0.23	424	0.24	400	5.83	14.72
58.8	1.6	225.2	0.40	0.43	480	0.53	512	6.61	15.98
58.8	1.6	226.4	0.60	0.63	577	0.83	609	5.53	18.18
58.8	1.6	224.2	0.80	0.83	678	0.93	675	0.41	20.10
59.4	3.2	224.6	0.20	0.25	544	0.29	499	8.24	9.35
58.8	3.2	225.2	0.41	0.46	532	0.61	589	10.70	9.29
58.6	3.2	226.3	0.60	0.65	603	0.91	669	10.98	10.08
58.5	3.2	225.0	0.80	0.86	696	0.88	728	4.61	11.25
59.0	6.4	225.2	0.21	0.31	718	0.43	703	2.16	6.45
59.2	6.3	223.2	0.40	0.50	718	0.75	752	4.74	6.50
58.8	6.4	226.1	0.61	0.71	749	0.95	819	9.36	6.64
59.4	9.6	224.3	0.20	0.36	883	0.58	889	0.66	5.47
58.6	9.5	225.4	0.40	0.56	886	0.90	929	4.84	5.50
59.0	9.5	223.9	0.60	0.76	895	0.88	969	8.27	5.55

Table A.9. R-22 data for the 0.430 in diameter test section

T	q"	G	xin	xout	h	dP	hpred	%error	%dh
23.5	1.0	75.8	0.41	0.47	163	0.06	226	38.58	9.09
22.8	1.6	75.8	0.40	0.51	205	0.07	271	32.01	8.30
23.2	1.6	150.0	0.20	0.25	295	0.10	339	14.89	10.40
22.6	1.6	149.2	0.40	0.45	476	0.27	433	8.88	14.80
22.8	1.6	148.8	0.60	0.65	571	0.46	516	9.68	16.81
23.0	1.6	224.4	0.20	0.24	481	0.26	434	9.68	14.68
23.2	1.6	224.4	0.41	0.44	604	0.64	588	2.71	17.90
22.6	1.6	225.5	0.60	0.63	743	1.00	710	4.37	20.76
23.5	3.2	225.5	0.20	0.28	498	0.30	515	3.47	8.25
23.4	3.2	224.7	0.40	0.47	608	0.70	638	5.06	9.76
23.2	3.2	224.7	0.60	0.67	751	1.03	753	0.23	11.54
23.2	6.4	224.4	0.20	0.35	626	0.42	679	8.43	5.57
22.6	6.3	225.0	0.40	0.55	674	0.81	772	14.49	5.93
23.0	6.3	225.0	0.60	0.74	769	1.09	861	11.94	6.54
41.0	1.0	75.0	0.20	0.27	162	0.02	186	14.94	9.35
40.8	1.0	75.0	0.40	0.47	167	0.04	213	26.92	9.42
41.0	1.0	75.5	0.60	0.66	168	0.07	238	41.54	9.43
41.2	1.6	75.3	0.40	0.51	232	0.05	263	13.07	8.91
40.8	3.2	75.3	0.20	0.42	374	0.05	370	0.98	6.72
41.0	1.6	150.3	0.10	0.16	307	0.06	284	7.27	10.68
41.0	1.6	150.2	0.20	0.26	287	0.09	328	14.24	10.20
41.0	1.6	150.0	0.40	0.46	362	0.18	411	13.40	12.03
41.0	1.6	150.9	0.61	0.67	441	0.31	491	11.26	13.49
40.8	1.6	148.9	0.80	0.86	499	0.40	533	6.68	15.12
41.0	1.6	151.1	0.90	0.95	585	0.38	549	6.12	17.44
40.8	3.2	149.9	0.10	0.21	438	0.08	397	9.34	7.55
41.0	3.2	150.2	0.20	0.31	423	0.12	427	0.88	7.35
41.0	3.2	150.9	0.40	0.51	446	0.22	491	10.02	7.65
40.8	3.2	150.1	0.61	0.72	498	0.35	552	10.83	8.19
41.4	3.2	149.5	0.81	0.92	563	0.41	590	4.86	9.10
41.2	6.3	150.4	0.20	0.43	652	0.17	618	5.27	5.76
41.0	6.4	150.2	0.40	0.63	697	0.29	659	5.41	6.03
40.8	6.4	150.5	0.60	0.83	726	0.43	700	3.58	6.20
41.2	9.4	150.8	0.40	0.73	910	0.38	814	10.59	5.42
40.8	9.7	151.1	0.60	0.94	952	0.50	853	10.45	5.51
40.1	1.6	228.2	0.10	0.14	390	0.10	335	13.99	8.21
41.2	1.6	225.1	0.15	0.19	401	0.13	372	7.18	12.98
41.0	1.6	223.7	0.20	0.24	429	0.17	407	5.18	13.67
41.2	1.6	225.0	0.20	0.24	431	0.18	408	5.32	13.72
40.6	1.6	224.9	0.24	0.28	416	0.24	435	4.64	8.50
41.2	1.6	225.1	0.29	0.33	426	0.30	469	10.20	8.62
41.0	1.6	222.6	0.36	0.40	439	0.35	512	16.51	13.68

Table A.9. R-22 data for the 0.430 in diameter test section

T	q"	G	xin	xout	h	dP	hpred	%error	%dh
41.7	1.6	224.7	0.40	0.44	468	0.43	539	15.26	14.61
41.2	1.6	226.4	0.41	0.45	464	0.45	548	18.06	14.52
40.3	1.6	224.9	0.46	0.50	491	0.53	574	16.77	9.39
41.0	1.6	226.4	0.50	0.54	510	0.60	599	17.44	9.61
41.0	1.6	226.3	0.55	0.59	532	0.67	625	17.55	9.88
40.5	1.6	225.0	0.60	0.64	546	0.74	649	18.83	16.50
41.4	1.6	226.9	0.65	0.69	586	0.80	676	15.34	10.53
41.2	1.6	226.4	0.70	0.74	603	0.85	697	15.55	17.87
40.3	1.6	225.8	0.75	0.79	609	0.91	715	17.31	18.02
41.4	1.6	226.6	0.80	0.84	622	0.90	733	17.83	18.32
41.0	1.6	227.3	0.85	0.89	660	0.91	747	13.14	18.89
41.0	1.6	225.2	0.90	0.94	679	0.87	745	9.75	19.65
41.9	1.6	228.2	0.94	0.98	719	0.79	743	3.35	20.58
41.0	3.2	224.9	0.11	0.18	500	0.15	437	12.50	8.35
41.0	3.2	224.6	0.21	0.28	486	0.23	494	1.72	8.09
40.5	3.1	222.5	0.31	0.38	560	0.36	544	2.82	9.22
40.8	3.1	224.6	0.41	0.48	518	0.50	600	15.90	8.66
40.8	3.2	225.7	0.51	0.58	566	0.64	653	15.35	9.22
41.0	3.2	225.7	0.60	0.68	618	0.77	698	12.95	9.81
40.8	3.2	225.2	0.70	0.78	667	0.88	736	10.41	10.54
41.0	3.2	224.6	0.80	0.87	701	0.92	764	9.09	10.98
41.4	3.2	225.2	0.90	0.97	787	0.82	776	1.47	12.11
40.6	6.3	226.7	0.20	0.35	683	0.32	659	3.57	5.99
40.8	6.4	224.4	0.40	0.55	746	0.59	738	1.05	6.35
41.0	6.3	224.8	0.60	0.75	792	0.41	811	2.42	6.69
41.9	6.3	224.9	0.80	0.95	826	0.94	864	4.57	6.92
40.1	9.5	227.3	0.20	0.42	895	0.43	822	8.14	5.32
41.2	9.5	224.0	0.40	0.63	965	0.69	881	8.73	5.62
40.6	9.2	224.0	0.60	0.82	1012	0.97	924	8.68	6.00
58.6	1.0	74.7	0.20	0.27	166	0.02	183	10.05	9.40
58.8	0.9	75.6	0.40	0.47	160	0.04	204	27.66	9.63
59.5	1.6	76.0	0.40	0.52	225	0.04	259	14.81	8.75
59.4	3.2	75.9	0.40	0.63	350	0.06	378	8.17	6.42
59.2	1.6	151.1	0.20	0.26	310	0.07	319	2.83	10.76
59.0	1.6	151.4	0.61	0.67	427	0.21	462	7.98	13.63
59.4	1.6	150.6	0.80	0.86	452	0.28	503	11.28	14.23
59.2	1.6	150.9	0.91	0.96	510	0.28	510	0.08	15.64
59.0	3.2	150.8	0.20	0.32	461	0.09	425	7.89	7.71
57.7	3.2	150.3	0.40	0.52	486	0.16	474	2.53	8.17
58.3	3.2	151.1	0.61	0.72	589	0.24	527	10.50	9.52
58.8	3.3	149.6	0.81	0.93	593	0.30	563	5.06	9.32
58.8	6.2	149.6	0.20	0.43	630	0.13	606	3.84	5.68

Table A.9. R-22 data for the 0.430 in diameter test section

T	q"	G	xin	xout	h	dP	hpred	%error	%dh
58.1	6.3	150.3	0.41	0.64	762	0.21	647	15.13	6.49
59.0	6.4	149.6	0.60	0.84	862	0.29	678	21.28	7.13
58.8	1.6	228.3	0.20	0.24	381	0.13	393	3.27	12.48
59.4	1.6	224.8	0.82	0.86	539	0.62	676	25.46	16.34
59.5	3.2	225.5	0.21	0.28	594	0.17	477	19.75	9.59
58.6	3.2	223.9	0.40	0.48	553	0.33	567	2.56	9.04
59.0	3.2	225.2	0.61	0.69	591	0.54	658	11.33	9.38
58.5	6.3	225.6	0.20	0.35	795	0.23	647	18.65	6.71
58.5	6.4	226.5	0.40	0.55	849	0.42	715	15.81	7.05
59.4	6.2	226.1	0.59	0.74	872	0.60	769	11.80	7.32

Table A.10. R-32/R-125 data for the 0.305 in diameter test section

T	q"	G	xin	xout	h	dP	hpred	%error	%dh
40.8	0.6	35.9	0.33	0.43	248	0.02	197	20.41	20.79
41.0	0.6	37.4	0.53	0.63	233	0.03	204	12.22	20.56
41.0	0.6	38.0	0.71	0.81	212	0.03	210	0.95	20.26
41.5	1.0	37.1	0.33	0.48	313	0.02	254	18.75	14.85
41.2	1.0	37.6	0.52	0.67	293	0.03	259	11.68	14.60
41.0	1.0	37.1	0.72	0.87	220	0.03	262	19.05	13.79
41.0	1.6	36.8	0.33	0.58	403	0.03	349	13.44	10.19
40.8	1.6	37.6	0.52	0.76	382	0.03	351	7.94	10.00
41.2	1.6	37.2	0.71	0.96	303	0.04	358	18.05	12.04
40.8	1.0	74.3	0.32	0.40	357	0.05	290	18.71	15.43
41.4	1.0	74.2	0.52	0.60	366	0.08	316	13.68	15.55
41.2	1.0	74.6	0.72	0.80	353	0.10	339	3.96	15.38
41.4	1.6	74.1	0.32	0.44	474	0.06	377	20.32	15.83
40.8	1.6	75.7	0.51	0.64	461	0.09	398	13.67	15.53
41.0	3.2	76.1	0.32	0.56	668	0.09	577	13.54	10.89
41.0	3.2	76.0	0.50	0.75	636	0.11	584	8.27	10.59
40.6	1.6	148.7	0.32	0.39	568	0.18	487	14.36	17.98
41.0	1.6	149.7	0.43	0.49	584	0.25	530	9.21	18.02
41.2	1.6	149.6	0.71	0.77	604	0.46	616	1.93	12.24
41.2	1.6	149.6	0.90	0.96	708	0.44	646	8.73	20.75
41.0	3.1	150.0	0.32	0.45	829	0.22	642	22.53	13.13
41.0	3.2	149.6	0.42	0.55	771	0.29	670	13.07	12.29
41.2	3.1	149.6	0.72	0.84	766	0.49	736	3.87	12.33
41.4	6.4	150.8	0.32	0.57	1161	0.32	946	18.50	9.29
41.0	6.3	150.6	0.42	0.66	1089	0.39	953	12.49	8.93
40.8	6.3	150.2	0.70	0.95	925	0.53	989	6.94	7.88
41.0	9.4	150.2	0.31	0.68	1375	0.41	1197	12.90	7.68
41.0	9.6	150.1	0.41	0.79	1312	0.49	1218	7.16	7.32
41.2	12.7	148.3	0.32	0.82	1538	0.51	1447	5.92	6.59
40.8	1.6	223.9	0.01	0.05	576	0.09	387	32.81	18.16
41.2	1.6	223.5	0.05	0.09	618	0.12	414	33.04	19.10
41.0	1.6	224.7	0.11	0.16	582	0.16	459	21.13	18.29
41.0	1.6	226.4	0.32	0.36	661	0.41	599	9.43	20.07
41.0	1.6	223.0	0.54	0.58	690	0.74	721	4.40	20.72
40.8	1.6	225.6	0.91	0.95	869	0.88	850	2.18	24.61
40.8	3.2	222.6	0.01	0.09	875	0.14	585	33.14	13.48
40.5	3.2	227.0	0.32	0.40	889	0.49	729	17.97	13.65
41.0	3.1	225.4	0.53	0.61	867	0.82	821	5.30	13.61
41.2	3.2	225.5	0.72	0.81	889	1.03	898	1.01	13.77
41.2	3.2	225.8	0.89	0.98	963	0.89	928	3.60	14.44
41.4	6.6	223.6	0.01	0.18	1254	0.22	928	25.98	9.65
41.2	6.4	225.0	0.32	0.49	1215	0.61	996	18.06	9.68

Table A.10. R-32/R-125 data for the 0.305 in diameter test section

T	q"	G	xin	xout	h	dP	hpred	%error	%dh
40.6	6.4	223.3	0.53	0.70	1182	0.93	1060	10.36	9.43
41.2	6.4	225.4	0.73	0.90	1098	1.11	1112	1.19	8.92
41.2	9.5	224.9	0.32	0.57	1485	0.73	1243	16.24	8.12
41.0	9.5	226.6	0.52	0.77	1411	1.05	1290	8.55	7.80
41.4	9.5	226.4	0.73	0.98	1197	1.08	1330	11.10	6.83
41.2	12.8	225.0	0.31	0.65	1662	0.85	1482	10.83	6.98
40.3	12.6	227.3	0.51	0.84	1592	1.17	1506	5.45	6.83
41.0	3.2	373.5	0.20	0.25	725	0.69	802	10.51	11.61
40.8	3.2	375.2	0.40	0.45	832	1.42	989	18.86	13.06
41.0	3.1	376.3	0.60	0.65	1023	2.13	1152	12.60	15.56
41.2	6.3	377.0	0.19	0.29	1005	0.83	1039	3.36	8.38
40.8	6.4	373.8	0.40	0.50	1320	1.58	1185	10.18	10.37
40.8	6.3	374.1	0.60	0.70	1400	2.25	1312	6.32	10.94
41.0	9.5	375.3	0.20	0.35	1470	1.00	1287	12.45	8.06
41.2	9.5	376.2	0.40	0.55	1533	1.77	1397	8.89	8.32
41.0	9.5	372.9	0.59	0.74	1687	2.42	1491	11.63	9.00
41.0	12.7	375.8	0.20	0.40	1623	1.17	1518	6.48	6.87
58.8	1.0	75.1	0.21	0.29	355	0.03	272	23.45	15.41
59.2	1.6	74.6	0.20	0.33	477	0.03	369	22.52	15.62
59.2	3.2	74.5	0.20	0.47	701	0.04	565	19.36	11.41
59.2	3.2	150.8	0.21	0.34	815	0.13	607	25.53	12.84
58.6	3.2	149.7	0.40	0.54	851	0.19	649	23.70	13.17
59.2	3.2	148.8	0.61	0.74	816	0.29	688	15.75	12.75
58.8	6.4	151.4	0.20	0.47	1152	0.18	922	19.95	9.23
58.8	6.4	150.8	0.39	0.66	1144	0.26	942	17.72	9.22
59.0	6.4	150.6	0.60	0.86	1082	0.36	967	10.57	8.77
59.0	1.6	225.9	0.20	0.25	617	0.18	498	19.25	19.09
59.2	1.7	224.2	0.41	0.45	605	0.37	613	1.31	17.87
58.6	1.6	227.0	0.59	0.63	559	0.58	698	24.72	17.47
59.0	1.6	224.6	0.80	0.84	648	0.74	764	17.93	19.43
59.0	3.2	225.2	0.20	0.29	874	0.22	651	25.47	13.57
59.0	3.3	223.9	0.41	0.50	832	0.42	739	11.10	12.72
59.2	3.4	224.8	0.60	0.69	735	0.60	817	11.20	11.15
58.8	3.3	225.2	0.80	0.89	805	0.75	861	6.96	12.39
59.0	6.4	223.9	0.21	0.39	1231	0.30	952	22.70	9.75
59.2	6.4	226.7	0.40	0.58	1172	0.51	1000	14.71	9.36
59.2	6.3	225.3	0.59	0.77	1076	0.69	1036	3.68	8.84
59.0	9.5	226.4	0.20	0.46	1480	0.38	1207	18.42	8.10
59.2	9.7	226.2	0.39	0.66	1401	0.61	1253	10.50	7.65
59.0	9.9	223.4	0.60	0.88	1422	0.79	1300	8.58	7.61

Table A.11. R-32/R-125 data for the 0.430 in test section

T	q"	G	xin	xout	h	dP	hpred	%error	%dh
40.3	0.6	37.7	0.32	0.40	207	0.01	195	5.95	14.53
40.3	0.6	37.9	0.52	0.60	205	0.01	200	2.51	14.48
40.3	0.6	38.0	0.71	0.79	175	0.01	204	16.89	13.92
40.3	1.0	37.7	0.32	0.44	263	0.01	252	4.17	10.71
40.5	1.0	38.0	0.52	0.64	250	0.01	261	4.25	10.20
40.5	1.0	37.9	0.72	0.83	194	0.02	264	36.02	9.45
40.5	1.6	37.6	0.32	0.52	342	0.01	356	4.09	11.34
40.1	1.6	37.9	0.52	0.71	299	0.02	354	18.11	10.50
40.3	1.0	75.9	0.32	0.38	289	0.02	280	3.31	11.12
40.3	1.0	75.0	0.51	0.57	256	0.04	298	16.38	10.60
40.3	1.0	75.5	0.71	0.77	309	0.06	317	2.75	11.43
40.5	1.0	74.3	0.90	0.96	258	0.06	323	25.21	10.63
40.3	1.6	75.4	0.32	0.42	380	0.03	365	3.95	8.11
40.6	1.6	75.2	0.52	0.62	383	0.05	379	0.89	8.13
40.3	1.6	75.5	0.71	0.80	376	0.07	396	5.15	12.37
40.5	3.2	74.8	0.32	0.51	512	0.04	567	10.75	8.50
40.3	3.1	74.6	0.53	0.72	494	0.07	571	15.44	8.35
40.5	3.1	75.0	0.73	0.92	424	0.08	577	36.28	7.42
40.3	1.6	149.5	0.23	0.28	486	0.08	435	10.39	15.06
40.3	1.6	149.8	0.31	0.35	428	0.09	465	8.49	13.41
40.5	1.6	150.5	0.41	0.46	489	0.12	499	2.01	15.13
40.8	9.5	149.1	0.49	0.78	1327	0.27	1210	8.82	7.24
40.3	1.6	149.9	0.51	0.56	561	0.15	530	5.55	16.88
40.3	1.6	152.2	0.60	0.64	585	0.19	563	3.72	17.13
40.5	1.6	150.2	0.69	0.74	587	0.23	582	0.87	17.50
40.8	1.6	149.9	0.79	0.84	718	0.27	603	16.00	20.55
40.6	1.6	149.3	0.88	0.93	677	0.28	611	9.71	19.60
40.6	3.2	149.5	0.23	0.32	700	0.10	607	13.29	10.98
40.5	3.2	150.2	0.32	0.42	694	0.12	629	9.46	10.90
40.5	3.2	150.5	0.41	0.51	659	0.14	650	1.45	10.44
40.5	3.2	150.5	0.50	0.60	792	0.17	670	15.40	12.17
40.3	3.2	149.3	0.52	0.61	617	0.18	672	8.83	9.89
40.6	3.2	149.7	0.60	0.70	748	0.21	693	7.33	11.50
40.3	3.2	149.9	0.69	0.79	858	0.26	708	17.53	13.03
40.5	3.2	150.4	0.78	0.88	905	0.29	723	20.12	13.62
40.3	6.4	150.4	0.32	0.51	891	0.17	930	4.44	7.32
40.3	6.3	150.8	0.49	0.68	1101	0.22	948	13.96	8.81
40.1	6.3	150.5	0.69	0.88	1097	0.31	974	11.17	8.74
40.5	9.5	149.8	0.31	0.60	997	0.21	1189	19.26	5.79
40.6	9.5	148.8	0.68	0.98	1392	0.34	1225	11.99	7.53
40.6	1.6	223.7	0.21	0.25	662	0.14	501	24.25	19.25
40.5	1.6	223.5	0.30	0.34	657	0.19	552	16.03	11.41

Table A.11. R-32/R-125 data for the 0.430 in test section

T	q"	G	xin	xout	h	dP	hpred	%error	%dh
40.6	1.6	224.9	0.32	0.35	506	0.20	565	11.66	15.54
40.3	1.6	225.3	0.41	0.44	595	0.27	616	3.52	17.68
40.6	1.6	224.9	0.49	0.53	698	0.35	660	5.51	20.10
40.6	1.6	225.2	0.52	0.56	598	0.38	676	12.89	17.76
40.5	1.6	224.1	0.59	0.62	709	0.44	704	0.65	20.34
40.6	1.6	225.7	0.68	0.71	735	0.54	746	1.49	20.95
40.3	1.6	225.2	0.71	0.74	695	0.56	757	8.93	20.01
40.8	1.6	223.9	0.80	0.83	734	0.63	783	6.68	20.91
41.0	1.6	224.5	0.91	0.95	787	0.61	797	1.34	22.11
40.6	3.2	224.6	0.21	0.28	859	0.16	655	23.72	12.93
40.3	3.2	224.8	0.31	0.38	734	0.23	695	5.34	11.42
40.5	3.1	224.0	0.32	0.38	888	0.23	694	21.91	13.53
40.6	3.2	225.6	0.40	0.47	785	0.30	737	6.10	11.97
40.3	3.2	224.9	0.50	0.56	936	0.39	772	17.49	14.03
40.3	3.2	224.9	0.52	0.58	814	0.41	783	3.87	12.35
40.3	3.2	224.5	0.59	0.65	900	0.48	807	10.39	13.57
40.3	3.2	224.4	0.70	0.76	761	0.56	846	11.18	11.67
40.5	3.2	224.8	0.70	0.77	887	0.59	847	4.55	13.40
40.8	3.2	223.9	0.80	0.87	906	0.65	871	3.84	13.63
41.4	3.2	223.9	0.92	0.99	945	0.57	874	7.48	14.01
40.5	6.3	225.1	0.31	0.44	1236	0.28	966	21.80	9.72
40.5	6.4	225.2	0.33	0.45	1070	0.30	975	8.82	8.52
40.8	6.4	226.2	0.49	0.62	1185	0.45	1021	13.85	9.30
40.3	6.3	225.3	0.51	0.64	1160	0.48	1023	11.81	9.17
40.8	6.3	225.4	0.70	0.83	1088	0.62	1069	1.77	8.69
41.0	6.3	224.4	0.71	0.84	1177	0.64	1067	9.33	9.33
40.5	9.5	226.7	0.30	0.49	1465	0.35	1219	16.79	7.91
40.5	9.5	224.7	0.32	0.51	1326	0.37	1227	7.47	7.23
41.0	9.6	223.4	0.48	0.68	1475	0.50	1260	14.56	7.88
40.3	9.5	224.0	0.51	0.71	1356	0.55	1262	6.96	7.39
40.8	9.4	224.6	0.71	0.90	1494	0.68	1291	13.58	8.06
41.2	9.5	225.1	0.72	0.92	1532	0.69	1300	15.17	8.16
40.5	3.2	301.1	0.32	0.36	984	0.41	781	20.60	14.50
40.8	3.2	301.4	0.48	0.52	834	0.63	878	5.29	12.72
40.5	3.2	300.5	0.52	0.57	775	0.69	905	16.72	11.85
40.6	6.3	299.6	0.31	0.41	1323	0.47	1022	22.74	10.26
40.3	3.2	374.9	0.31	0.35	843	0.57	861	2.08	12.83
58.6	0.6	37.6	0.37	0.45	233	0.01	195	16.34	15.04
58.3	0.6	37.7	0.57	0.66	220	0.01	199	9.67	14.77
58.6	0.7	37.4	0.77	0.85	195	0.01	207	6.38	13.64
58.6	1.0	38.0	0.36	0.48	291	0.01	252	13.28	11.14
58.6	1.0	37.7	0.56	0.68	269	0.01	254	5.60	10.81

Table A.11. R-32/R-125 data for the 0.430 in test section

T	q"	G	xin	xout	h	dP	hpred	%error	%dh
58.3	1.0	37.5	0.76	0.89	217	0.01	256	18.28	10.04
58.1	1.6	37.7	0.36	0.57	369	0.01	356	3.59	11.99
58.6	1.6	37.6	0.56	0.77	336	0.01	353	5.03	11.39
58.5	1.0	75.3	0.37	0.43	333	0.02	278	16.42	11.84
58.5	1.0	76.0	0.56	0.63	324	0.04	296	8.76	11.69
58.3	1.0	76.1	0.75	0.81	285	0.05	313	9.68	10.73
58.5	1.6	75.3	0.37	0.47	427	0.03	369	13.57	13.62
58.6	1.6	74.6	0.57	0.68	394	0.04	384	2.59	12.58
58.3	1.6	75.2	0.74	0.85	394	0.05	388	1.46	12.81
58.5	3.2	74.8	0.37	0.57	570	0.04	566	0.66	9.27
58.5	3.2	74.9	0.56	0.77	490	0.05	572	16.80	8.21
58.3	3.2	75.3	0.74	0.94	472	0.06	576	22.18	7.98
59.0	4.8	75.7	0.36	0.67	676	0.05	740	9.38	7.46
58.5	1.6	149.3	0.36	0.41	518	0.08	458	11.58	15.84
58.3	1.6	149.9	0.55	0.60	505	0.12	510	0.89	15.53
59.0	1.6	149.9	0.73	0.79	561	0.16	551	1.71	16.86
58.5	3.2	149.6	0.35	0.46	719	0.10	621	13.56	11.22
58.1	3.2	149.3	0.54	0.64	724	0.13	657	9.34	11.19
58.6	3.2	149.7	0.74	0.84	874	0.19	684	21.75	13.24
58.5	6.3	149.6	0.35	0.56	883	0.13	920	4.16	7.33
58.6	6.3	149.9	0.54	0.74	982	0.17	941	4.11	7.97
58.5	6.3	148.9	0.73	0.94	1038	0.22	956	7.89	8.35
58.3	9.5	149.7	0.35	0.65	1001	0.17	1188	18.61	5.80
58.1	9.4	151.2	0.53	0.83	1099	0.21	1196	8.88	6.26
58.1	1.6	225.9	0.37	0.40	673	0.18	561	16.65	19.18
58.5	1.6	226.0	0.55	0.58	725	0.28	640	11.71	20.37
58.8	1.6	225.6	0.73	0.76	683	0.39	702	2.84	19.74
58.3	3.1	224.9	0.37	0.44	932	0.20	690	25.99	14.09
58.6	3.1	224.0	0.55	0.62	975	0.29	749	23.18	14.64
58.5	3.2	224.3	0.74	0.80	913	0.42	803	12.12	13.73
58.3	6.4	226.7	0.36	0.50	1296	0.24	968	25.31	10.04
58.6	6.3	224.6	0.54	0.68	1350	0.35	1002	25.79	10.45
58.6	6.4	224.9	0.73	0.86	1268	0.46	1040	17.99	9.81
58.5	9.5	225.9	0.36	0.56	1445	0.28	1219	15.62	7.79
58.6	9.5	225.2	0.53	0.74	1555	0.39	1245	19.96	8.29
58.5	9.5	226.6	0.71	0.92	1489	0.50	1269	14.78	7.99
58.3	3.2	299.9	0.34	0.40	961	0.31	760	20.85	14.21
58.8	3.2	300.7	0.53	0.58	952	0.49	852	10.50	14.22
58.5	6.4	300.9	0.34	0.44	1283	0.37	1011	21.21	9.95
58.5	3.2	374.6	0.35	0.40	928	0.46	847	8.76	13.92
58.8	6.3	375.2	0.36	0.44	1258	0.51	1075	14.59	9.83